ABSTRACT

Title of Document: ANALYSES OF MULTIPLE GLOBAL AND REGIONAL AEROSOL PRODUCTS: INVESTIGATION OF AEROSOL EFFECTS AND ARTIFACTS

Myeong Jae Jeong, Doctor of Philosophy, 2005

Directed By: Professor Zhanqing Li, Department of Atmospheric and Oceanic Science/Earth System Science Interdisciplinary Center

Multiple aerosol products derived from satellite, ground-based, and air-borne instruments were analyzed with a focus on satellite-based aerosol products. Aerosol measurements based on different techniques were utilized to investigate the effects and the artifacts of aerosols and clouds by taking advantages of respective techniques.

The global aerosol products derived from Advanced Very High Resolution Radiometer (AVHRR) and Total Ozone Mapping Spectrometer (TOMS), were analyzed for extracting synergic information. Global distributions of dominant aerosol type(s) were derived and the two products were combined to acquire an extended spatial coverage of aerosol optical thickness (AOT) at a common wavelength (0.55μm). It was shown that the derived AOT agreed reasonably with AOT from the state-of-the-art Moderate Resolution Imaging Spectroradiometer (MODIS).

In-depth comparison of aerosol products derived from the MODIS and the AVHRR was performed. New insights and understanding were gained for the discrepancies between the two prominent aerosol products, allowing for bridging the current and past products. Several factors causing the discrepancies were investigated. Cloud-screening techniques and aerosol models employed by the retrieval algorithms were found to be the most important factors explaining the observed discrepancies.

The column aerosol humidification effect (AHE) was investigated. The column AHE was shown to be sensitive to changes in relative humidity (RH). Six methods to infer the column AHE were introduced. The knowledge of the AHE helps investigate aerosol properties and retrievals near clouds, enabling separation of aerosol real effects from artifacts associated with clouds.

Finally, apparent correlations between AOT and cloud amount from ground- and satellite-based measurements were investigated. Several factors including air convergence, cloud contamination and uncertainty in cloud cover estimation, the AHE, cloud-processed/new particle genesis were studied to explain the correlations. We showed that the correlation found in ground-based measurements is mostly due to real effects while satellite-based measurements are significantly influenced by artifacts caused by clouds.

ANALYSES OF MULTIPLE GLOBAL AND REGIONAL AEROSOL PRODUCTS: INVESTIGATION OF AEROSOL EFFECTS AND ARTIFACTS

By

Myeong Jae Jeong

Dissertation submitted to the Faculty of the Graduate School of the
University of Maryland, College Park, in partial fulfillment
of the requirements for the degree of
Doctor of Philosophy
2005

Advisory Committee:
Professor Zhanqing Li, Chair /Advisor
Professor Russell R. Dickerson
Professor Robert Hudson
Professor Rachel T. Pinker
Professor Si-Chee Tsay
Professor Xiangdong Ji, Dean's Representative

Statement of Originality

The original scientific contributions made in this study include:

(1) Synthetic analyses of the global aerosol products derived from two long-lasting sensors, AVHRR and TOMS. Regional features of the aerosols, which have not been reported in the literature, were reported. A new algorithm was proposed to classify aerosol types by taking advantage of the synergy of the two sensors. Global distribution of dominant aerosol type(s) was derived. A new global (ocean and land) AOT product was developed by combining data from the two sensors at a common wavelength (0.55μm), while previous products were exclusively available over oceans.

(2) In depth inter-comparison between the global aerosol products derived from AVHRR and MODIS was performed, providing an anchor for linking the long historical AVHRR products with the modern MODIS products. The factors that may cause discrepancies between the two aerosol products were discussed in detail. The impact of aerosol models employed by respective algorithms on the observed discrepancies between them were substantiated. Implications associated with cloud-screening and uncertainties in radiometric calibration were discussed.

(3) Effect of relative humidity on the aerosol optical thickness was investigated. Several methods to estimate humidity effects on AOT were suggested and compared.

(4) Numerous factors affecting the remote sensing of aerosols from radiometric instruments deployed in spacecraft (MODIS) and on the ground (Cimel sun photometer) were investigated in detail. The effects of air convergence, aerosol

humidification, cloud contamination, and cloud-processed / new particles under cloudy skies were substantiated together with discussions concerning the uncertainties in cloud detection from the Total Sky Imager and MODIS.

Two chapters (2 and 3) of the thesis have been published in following journal articles:

1. Jeong, M.-J. and Z. Li (2005), Quality, compatibility and synergy analyses of global aerosol products derived from the advanced very high resolution radiometer and total ozone mapping spectrometer, *J. Geophys. Res.*, 110, D10S08, doi:10.1029/2004JD004647.
2. Jeong, M.-J., Z. Li, D.A. Chu, and S.-C. Tsay (2005), Quality and compatibility analyses of global aerosol products derived from the advanced very high resolution radiometer and moderate resolution imaging spectroradiometer, *J. Geophys. Res.*, 110, D10S09, doi:10.1029/2004JD004648.

The author of the thesis contributed the idea, the method, the analysis of the data and the writing of drafts, while Professor Zhanqing Li guided the studies and revised the final versions of the papers submitted for publications. The co-authors provided scientific guidance and partial support.

Acknowledgements

It is hard to express my sincere thanks to my advisor, Professor Zhanqing Li, for his excellent guidance, encouragement and support throughout the study. Without his thoughtful help, I might not be able to complete my dissertation.

I am very grateful to Dr. Fu-Lung Chang and Ms. Maureen Cribb for their help to get me accustomed to radiative transfer calculations and remote sensing, and for many constructive discussions and comments concerning my work. A special thanks goes to Dr. Si-Chee Tsay for his support and encouragement during my study. I benefited from discussions with Dr. D. Allen Chu and his comments on my work.

Many thanks go to Dr. Yingtao Ma for his help in using the Total Sky Imager data, and I appreciate many useful discussions with my officemates Tianle Yuan and Brian Vant-Hull. I cannot numerate all the helps, concerns, cares from many other fellow graduate students, but I sincerely thank them.

During my study here, I deeply benefited from excellent lectures and guidance provided by the faculty members of the department, and especially, I would like to thank my former advisor professor Robert Ellingson, and professors Russell Dickerson, Robert Hudson, Eugenia Kalnay, Raghu Murtugudde, Kenneth Pickering, Rachel Pinker, Owen Thompson, Ning Zeng, Da-Lin Zhang, and Drs. Arnold Gruber and Warren Wiscombe.

I would like to give my sincerest thanks to my dear wife, Kyung-Me, for her love, patience and support. I also thank my daughter, Sony, who used to bring me a smile when I was spending hard times. I am very grateful to my father and mother for

their supports and encouragements during the long period of my study. A special note of thanks goes to all the family members for their concerns and cares.

Finally, I greatly appreciate the graduate assistantship provided by the research grants awarded to Professor Zhanqing Li by the US Dept of Energy, NSF, NASA and NOAA during my Ph.D study.

Table of Contents

List of Tables

List of Figures

Chapter 1: Introduction

1.1. Background

The surface temperature of the earth has increased by 0.6 K during the last century (Intergovenmental Panel on Climate Change [IPCC], 2001). This warming trend has been attributed to the changes in the radiative balance in the earth system due to increasing anthropogenic greenhouse gases (GHGs) (Intergovernmental Panel on Climate Change, IPCC, 2001; Crowley, 2000). The warming effect of GHGs is well constrained because their quantity and radiative effects are well understood due to their rather homogeneous spatio-temporal distribution, invariant optical properties and long lifetime in the atmosphere. On the other hand, the effects of anthropogenic aerosols on climate and climate change remain one of the largest sources of uncertainties in climate studies (IPCC, 2001). The radiative forcing of GHGs is estimated at 2.5±0.3 Wm^{-2} while the aerosol radiative forcing (ARF) for sulfates has been estimated at –1.4±1.5 Wm^{-2} and could be –2.5±2 Wm^{-2} when the effects of organic aerosols are incorporated (Houghton et al., 1996). Moreover, model calculations of aerosol radiative forcing from different methods- forward calculations based on aerosol physics and chemistry and inverse calculations inferring aerosol forcing from the total forcing required to match climate model simulations with observed temperature changes- have revealed large discrepancies with large uncertainties (Anderson et al., 2003). Inverse calculations constrain aerosol forcing to around -1 Wm^{-2} with uncertainties ranging from -1 to -1.9 Wm^{-2}, while forward

calculations suggest aerosol forcing equal to about –1.5 Wm^{-2} with an uncertainty beyond -3 Wm^{-2} (Anderson et al., 2003). Such large uncertainties in aerosol forcing and their dependence on the calculation methods clearly indicates the lack of knowledge concerning aerosols and makes it difficult to accurately assess their impact on climate and climate change.

Aerosols influence the climate system in many ways. Aerosols scatter and absorb shortwave radiation and absorb longwave radiation; which is referred to as direct radiative forcing (Liou et al., 1978; Coakley et al., 1983). Scattering of shortwave radiation by aerosols enhances the shortwave radiation reflected back to space and results in the cooling of the atmosphere and the surface. On the other hand, absorption of shortwave and longwave radiation by aerosols introduces changes in the thermal structure of the atmosphere-surface system and may contribute to changes in the atmospheric circulation. More complicated aerosol forcings to the climate system comes in the form of indirect effects. Aerosols play an important role as cloud condensation nuclei (CCN; IPCC, 2001). Increasing the number of aerosols can modify the optical properties of clouds by increasing the number of cloud droplets. This, in turn, results in the reduction of cloud droplet size since both cloud droplets and aerosol particles compete for the limited amount of water vapor required for their growth. Therefore, the increased number of aerosols in the atmosphere is expected to cause enhanced cloud reflectance, thereby increasing the albedo of the climate system (Twomey, 1977; Twomey et al., 1984; Coakley et al., 1987; Kaufman and Nakajima, 1993; Kaufman and Fraser, 1997; Ramanathan et al., 2001). Furthermore, since smaller cloud droplets are inefficient in producing precipitation, an enhanced aerosol

population would increase the lifetime of clouds and ultimately suppress precipitation (Albrecht, 1989; Rosenfeld, 1999 and 2000). On the other hand, some absorbing aerosols like soot and urban pollutants may affect clouds in a quite different way. The presence of such absorbing aerosols reduces shortwave radiation arriving at the surface (Li, 1998; Li and Kou, 1998). This results in less evaporation from the surface, a more stable and drier atmosphere, and consequently less cloud formation (Hansen et al., 1997). In addition, when heating due to absorption of solar radiation by aerosols reaches its maximum around the top of the boundary layer, stabilization of the boundary layer occurs, suppressing convective activity and preventing cloud formation (Ackerman et al., 2000; Koren et al., 2004).

As described above, the effects of aerosols are diverse and may result in quite different consequences, depending on the properties and spatio-temporal distribution of aerosols and environmental conditions. Therefore it is very important to obtain the distributions of aerosol optical/chemical properties, as well as the quantity of aerosols in space and time, as accurately as possible in order to correctly assess the impact of aerosols on the climate system. The use of satellites in the global monitoring of aerosols is a critical tool in this regard. However, the information content that can be extracted from satellite-based observations of upwelling radiances at the top of the atmosphere is limited and subject to various errors. Some properties of aerosols can be characterized from in situ measurements, and the amount of aerosols can be accurately measured from ground-based observations. Therefore, the analyses of aerosols from diverse sources of measurements are essential in order to obtain a comprehensive understanding of aerosols and their effects on the climate system.

1.2. Aerosol Retrievals from Satellites

To date, many satellite sensors have been used for aerosol retrievals and even more numerous retrieval algorithms with a variety of characteristics have been developed (see Table 1.1 and 1.2); King et al. (1999) presented a detailed review of these. An updated summary of some satellite sensors and aerosol retrieval algorithms of importance follows here.

Table 1.1. Selected sensors and satellites making significant contributions to aerosol remote sensing.

Sensor	Satellite	Period	Channel(s) for Aerosol Retrieval[&] (μm)	Sensor Resolution (km)	Swath (km)
AVHRR	NOAA-7, 9, 11, 14, 16, 17	1981~ Present	0.63, 0.83, 1.61[@]	1.1(LAC[*]) 4.4(GAC[#])	2800
TOMS	Nimbus-7, Meteor-3, ADEOS, Earth Probe, QuikTOMS	1978~ Present	0.340 0.380	50	3000
POLDER	ADEOS ADEOS II	1996~ 1997 2002~ Present	0.443, 0.765, 0.865	7	2200
SeaWiFS	OrbView 2	1997~ Present	0.765, 0.865	1.1(LAC) 4.5(GAC)	2800
MODIS	Terra Aqua	1999~ Present 2001~ Present	0.66(B1), 0.87(B2), 0.47(B3), 0.55(B4), 1.23(B5), 1.63(B6), 2.13(B7)	0.25 (B1, B2) 0.50 (B3~B7)	2330
MISR	Terra	1999~ Present	0.446, 0.558, 0.672, 0.866	1.1	360
GLI	ADEOS II	2002~ Present	0.380, 0.412, 0.678, 0.865	0.25-1	1600

[@]1.61μm channel is available for AVHRR/3 aboard NOAA-16 and 17.
[*]LAC: Local Area Coverage; [#]GAC: Global Area Coverage
[&]Provided channels are those used by operational or representative algorithms listed in Table 1.2. More channels from respective sensors may be utilized for aerosol retrieval.

Table 1.2. Major global aerosol products derived from satellites.

Satellite Sensor	Aerosol Product (or References)	Retrieved Parameters	Aerosol Microphysics/ Assumptions	Data Availability
AVHRR	GACP/AVHRR (Mishchenko et al., 1999; Geogdzhayev et al., 2002)	AOT, Angstrom exponent (AE) over ocean	Type of Aerosol size distribution (SD), refractive index (RI), ocean surface reflectance, water-leaving radiance, whitecaps, spherical particle	1983-2000
	PATMOS/AVHRR (Stowe et al., 2002)	AOT over ocean	Mono-modal log-normal size distribution, spherical particle, RI	1981-1999
TOMS	TOMS Aerosol Index (AI) (Herman et al., 1997)	AI over land and ocean	No assumption about aerosol property	1979-Present
	TOMS AOT (Torres et al., 1998 and 2002)	AOT over land and ocean	Mono-modal log-normal SD, surface reflectance, RI, aerosol types, spherical particle	1979-2000
MODIS	MODIS Ocean (Tanre et al., 1997)	AOT, AE, Fine-Mode Fraction (FMF), Effective Radius (r_{eff}) over ocean	20 composites of aerosol models with bi-modal SD, spectrally varying RI, ocean surface bi-directional reflectance distribution function (BRDF), water-leaving radiance, spherical particle	2000-Present
	MODIS Land (Kaufman et al., 1997)	AOT, AE, FMF over land	Aerosol types, multi-modal log-normal SD varying with aerosol loading, correlation of visible surface reflectance with NIR surface reflectance, single scattering albedo	2000-Present
MISR	Diner et al. (1998, 2001), Khan et al. (1998, 2001)	AOT, Aerosol types	24 mixtures of 1-3components, non-spherical mineral dust, angular surface reflectance shape/scene contrast	2000-Present
POLDER	Deuzé et al. (2000)	AOT, AE, r_{eff}, RI, single scattering albedo (SSA) over ocean	Bi-modal SD, surface reflectance/polarization, spherical/nonspherical particles	1996-1997 2003
	Deuzé et al. (2001)	AOT, AE, RI over land	Bi-modal SD, surface BRDF/polarization, spherical particle	1996- 1997 2003
SeaWiFS	Gordon and Wang (1994), Wang et al. (2000a, b)	AOT over ocean	Shettle and Fenn (1979) aerosol model with bi-modal log-normal SD	1997-Present

1.2.1. Satellite Sensors Used for Aerosol Retrievals

Remote sensing of aerosols from space began a few decades ago and was accomplished using satellite sensors that were not originally planned for aerosol retrievals, which included the Advanced Very High Resolution Radiometer (AVHRR), the Total Ozone Mapping Spectrometer (TOMS), the Sea-viewing Wide Field-of-view Sensor (SeaWiFS), and the Along Track Scanning Radiometer 2 (ATSR-2). The AVHRR aboard the NOAA polar orbiting satellites was designed to determine sea surface temperature and the vegetation index. It is a cross-track scanning radiometer with five channels in the visible, near infrared, and thermal infrared and has monitored the earth since 1978. The AVHRR has a reasonable spatial resolution for aerosol remote sensing (1 km at nadir), but no onboard calibration in the visible channel, which is the most important channel in aerosol retrievals. The TOMS was intended for monitoring total ozone so its channels span the ultraviolet (UV) spectrum where strong and weak ozone absorption bands (Hartley-Huggins bands) exist. The TOMS was flown on the Nimbus-7 satellite in 1978, and then was placed aboard the Meteor-3 satellite, the ADvanced Earth Observing Satellite (ADEOS), and the Earth Probe. Since this instrument has a large field of view (~50 km at nadir), sub-pixel cloud contamination becomes the greatest problem in its application to aerosol retrievals. Given the long record of measurements from the AVHRR and TOMS instruments, application of these measurements to aerosol retrievals are beneficial in studying the effects of aerosols on climate. The original use of the SeaWiFS was for global ocean color monitoring for the fishery industry and was launched by NASA and OrbImage in 1997. It has eight

narrow channels spanning the visible and near infrared and is designed to avoid sun glint, which helps in acquiring more data for surface and aerosol remote sensing. But they suffer from lacking on-board calibration and thermal channel. The ATSR-2 was launched on the ERS-2 platform by the ESA in 1995. It is similar to the AVHRR in terms of its channels, but its capability to observe the same location at two different viewing angles is expected to improve aerosol retrievals by improving the corrections for the effects of the surface and some atmospheric constituents other than aerosols. This sensor has yet to be applied to global aerosol retrievals.

Given the importance of aerosols in the climate system, a number of satellite sensors specifically designed for aerosol retrievals have been developed and launched. The POLarization and Directionality of the Earth's Reflectances (POLDER; Deschamps et al., 1994) instrument aboard the ADEOS-I and ADEOS-II platforms is the first satellite sensor developed with aerosol retrievals in mind. The capability of measuring polarized radiances in addition to intensities helps to retrieve additional aerosol properties (e.g., refractive index) over land as well as over ocean. Again, there is no capability for on-board calibration and thus additional effort is required in post-launch calibrations. Unfortunately, data from POLDER are available for only eight months due to the failure of the solar panel on the ADEOS platform. The MODerate resolution Imaging Spectroradiometer (MODIS; Salmonson et al., 1989; King et al., 1992) on the Terra and Aqua platforms and the Multiangle Imaging Spectroradiometer (MISR; Diner et al., 1989) on the Terra brought significant improvements in aerosol remote sensing. The MODIS and the MISR aboard the Terra spacecraft were launched in 1999 and the MODIS on Aqua, in 2002 by NASA. The

MODIS has 36 spectral bands (including 7 bands dedicated to aerosol retrievals) with variable spatial resolutions (0.25, 0.5, and 1 km at nadir). This spectral capability led to major improvements in cloud and shadow detection (Ackerman et al., 1998; King et al., 1998). In addition, the on-board calibrating system of MODIS distinguishes itself from the earlier sensors. The major characteristic of the MISR lies in its ability to acquire measurements from multiple viewing angles for the same target. It has nine cameras to view forward, backward and nadir directions at four bands. By virtue of this multi-angle viewing capability, it is expected to retrieve aerosol types as well as aerosol optical thicknesses over both ocean and land. Drawbacks of the MISR are its narrow swath width (~360 km compared to 2300 km for the MODIS) and long duration required to acquire measurements on a global scale (2-9 days, depending on latitude, compared to 1~2 days for the MODIS). Measurements taken by the MISR may be combined with MODIS measurements for further improvements in aerosol retrievals. POLDER and the GLobal Imager (GLI; Nakajima et al., 1998) on ADEOS-II were launched by the National Space Development Agency of Japan in 2002. Similar to MODIS, the GLI has 36 spectral bands, but also includes UV (380 nm) and deep blue (412 nm) bands dedicated to aerosol retrievals, which will be an advantage over prior sensors in characterizing aerosols over land (e.g., Hsu et al., 2004). These modern sensors are expected to deliver the characteristics of aerosol over the globe with an unprecedented accuracy.

1.2.2. Aerosol Retrieval Algorithms and Uncertainties

In principle, aerosol retrievals are performed using the reflected radiance at single or multiple wavelengths (channels or bands) at the altitudes of the satellite sensors. The reflection function for a cloud-free atmosphere over a non-Lambertian surface can be approximated as follows:

$$\rho^*(\mu_0,\mu_v,\phi_r) = \rho^R(\mu_0,\mu_v,\phi_r) + \rho^a(\mu_0,\mu_v,\phi_r) + \frac{r_{sfc}(\mu_0,\mu_v,\phi_r)}{1-\overline{r_{sfc}}\cdot\overline{r_{atm}}}\cdot T(\mu_0,\phi_r)\cdot T(\mu_v,\phi_r) \quad (1.1)$$

where ρ^*, ρ^R and ρ^a are apparent reflectance, and specific reflectances due to Rayleigh scattering and aerosol scattering, respectively. $r_{sfc}(\mu_0,\mu_v,\phi_r)$, $\overline{r_{sfc}}$, $\overline{r_{atm}}$, $T(\mu_0,\phi_r)$, and $T(\mu_v,\phi_r)$ are the bi-directional surface reflectance, the effective surface reflectance, the spherical albedo of the atmosphere, and the downward and upward transmittances, respectively. μ_0, μ_v and ϕ_r stand for the cosine of solar zenith angle, the satellite viewing zenith angle and the relative azimuth angle. In Eq. (1.1), reflectance due to aerosol scattering and transmittances are functions of aerosol optical thickness (AOT) and single scattering albedo, which are implicitly associated with the aerosol size distribution and refractive indices. Most aerosol retrieval algorithms for satellites are based on Eq. (1.1) or its variation but with different assumptions for aerosol properties (size distribution, refractive indices, sphericity, etc.) and for surface reflectance, depending on the characteristics and capabilities of the sensors and the developer's preference and philosophy. Such assumptions are inevitable, given that Eq. (1.1) implies that there are more unknowns (e.g., spectral

surface reflectance, spectral refractive indices for aerosols, aerosol size distribution parameters, aerosol number density, etc.) than the number of equations.

Given the large number of retrieval algorithms and products generated and used (see King et al., 1999), our focus is placed on three satellite sensors, namely, AVHRR, TOMS and MODIS. For climate studies, long-term observations from the AVHRR and TOMS instruments are useful, as they are available for more than two decades of near-global coverage. On the other hand, MODIS-based aerosol products are much more reliable, thanks to the sophisticated on-board calibration and unprecedented spectral coverage. The launch of CALIPSO and CLOUDSAT (scheduled in Sep 2005) will mark the beginning of a new era in aerosol-climate studies in virtue of the well-coordinated observing system consisting of an array of other satellite sensors flown in formation in the so called "A-Train" (Afternoon satellites constellation; NASA, 2003). Recently many researches evaluating and comparing different global aerosol products from satellites began to emerge (e.g., Kinne et al., 2001 and 2003; Myhre et al., 2004; Ichoku et al., 2005). It has been reported that the major challenges in satellite aerosol retrievals are associated with uncertainties in radiometric calibration of a sensor, cloud screening, and surface reflectance estimation in addition to large variability of aerosol properties such as size distribution, single scattering albedo (SSA), and corresponding phase function (King et al., 1999; Mishchenko et al., 1999; Kinne et al., 2001; Myhre et al., 2004). Thus, it is necessary to analyze satellite data with such uncertainties in mind, and to go further to quantify any uncertainties and to improve satellite-based retrievals.

1.3. Ground-based and Air-borne Aerosol Measurements

As discussed above, satellite-based retrievals are subject to numerous sources of uncertainty; therefore, accurate measurements and additional information about aerosol optical, microphysical, chemical properties from ground-based and air-borne measurements are crucial to evaluate and improve satellite retrievals if exploited appropriately.

One of most popular techniques to monitor the aerosols from ground is sun photometry. Ever since Volz (1959, 1974) developed the first hand-held instrument, significant improvements have been made for sun photometers. Modern digital units of laboratory quality can collect data accurately and quickly, and even a sun photometer can be carried by an aircraft or a ship for measurements (Holben et al., 1998; Schmid et al., 1997). Sun-photometry utilizes the direct beam of solar radiation transmitted through the cloud-free atmosphere based on the Beer-Bouguer-Lambert law in the form of:

$$I_\lambda^n(\theta_0) = d_0^2 I_{0,\lambda}^n(\theta_0) \exp[-\tau_\lambda m(\theta_0)] \tag{1.2}$$

, where I_λ^n, $I_{0,\lambda}^n$, d_0, θ_0, τ_λ, and m are measured direct normal solar irradiance, extraterrestrial solar irradiance, ratio of the average to the actual Earth-Sun distance, solar zenith angle, total optical thickness of the atmosphere, and relative optical air mass, respectively. Specific wavelengths with minimal interference from gas absorption are selected for optimized aerosol retrievals. For such wavelengths, the product of total atmospheric optical thickness and relative optical air-mass, $\tau_\lambda \cdot m$, can be rewritten as:

$$\tau_\lambda \cdot m = \tau_\lambda^R m_R + \tau_\lambda^a m_a + \tau_\lambda^{O3} m_{O3} \tag{1.3}$$

, where τ_λ^R, τ_λ^a, τ_λ^{O3}, m_R, m_a, and m_{O3} denote molecular, aerosol, and ozone optical thicknesses and relative optical air masses for air molecules, aerosols, and ozone, respectively. Relative optical air mass for molecules and ozone can be calculated accurately from standard profiles of air density and ozone considering atmospheric refraction and curvature of the earth (Lenoble, 1993; Kasten and Young, 1989). However, since aerosol vertical distributions are quite variable and rarely available, aerosol optical air mass used to be assumed to follow the molecular air masses (e.g., Iqbal, 1983; Porter et al., 2001). Thus, AOT estimation from sun photometry is straightforward as shown in the Eq. (1.2) and (1.3), thereby, sources of error are well defined: sensor calibration, gaseous/molecular optical thickness, relative optical air masses. Calibration issues have been carefully addressed in the recent sun photometry programs such as NASA's Sensor Intercomparison and Merger for Biological and Interdisciplinary Ocean Studies (SIMBIOS; Mueller et al., 1998) and Aerosol Robotic Network (AERONET; Holben et al., 1998). Errors in corrections for molecular and gaseous absorption and relative optical air masses are generally small. As such, the overall AOT errors due to these factors are known to be less than 0.02 (Porter et al., 2001; Rainwater and Gregory, 2005). However, an implicit but important uncertainty lies in cloud-screening, since AOT from sun photometry requires cloud-free condition. Therefore, sophisticated cloud-screening algorithms (e.g., Smirnov et al., 2000) were developed for automated retrieval of AOT (e.g., AERONET) and worked well in general (Kaufman et al., 2005). Nevertheless, uncertainty due to cloud-screening has yet been quantified thoroughly.

Although AOT is one of the aerosol parameters that can be estimated accurately from sun photometric measurements, it is difficult to relate AOT to aerosol number concentration and to separate contribution of absorption from that of scattering, which are very important to study numerous aerosol effects on the climate system. Besides, it is important but difficult to obtain the profiles of aerosol scattering, absorption, size, and hygroscopic property. Occasionally, aerosol profiling was made in some special field campaigns (e.g., Hegg et al., 1996; Sheridan and Ogren, 1999; Öström and Noone, 2000; Russell and Heintzenberg, 2000; Sheridan et al., 2002). These measurements do not resolve aerosol temporal variability, nor does it allow assessment of the representative for a general condition. Among few exception are the routine measurements made by flying an instrumented light aircraft (Cessna C-172N) over the Department of Energy Atmospheric Radiation Measurement Program (DOE/ARM) Southern Great Plains (SGP) cloud and radiation test bed (CART) site (36.6°N, 97.5°W) near Lamont, Oklahoma, USA (Andrews et al., 2004). The aircraft carrying integrating nephelometers (Model 3563, TSI Inc.) and particle soot absorption photometer (PSAP, Radiance Research) flew several times a week to measure the profiles of aerosol scattering and absorption coefficients at low relative humidity (~40%) and aerosol scattering coefficients at high relative humidity (~85%), from which the profiles of aerosol hygroscopicity and single scattering albedo can be derived. Major factors contributing to uncertainties in these measurements are associated with instrument calibration and noise. As for absorption, uncertainties also result from instrument accuracy and instrument-to-instrument variability. The uncertainties are well documented in the literature (Anderson and Ogren, 1998; Bond

et al., 1999; Anderson et al., 1999). Overall, the uncertainties are estimated 10~40% for scattering coefficients and 20~50% for absorption, depending on the amount of aerosols. In addition, sampling is another important issue since these measurements are based on small samples collected through the inlet of the aircraft. Normally, large particles (e.g., aerodynamic diameter >1μm) are difficult to intake due to an aerodynamic effect (Baron and Willeke, 2001). Consequently, submicron particles have been the main target for airborne sampling (e.g., Andrews et al., 2004). In spite of many sources of uncertainties, Andrews et al. (2004) reported good agreement between the AOT integrated from aircraft measurements and the AOT measured from a sun photometer (i.e., Cimel CE-318, Cimel Electronique) and a radiometer (i.e., Multifilter Rotating Shadowband Radiometer; MFRSR, Yankee Environmental Systems, Inc.). The agreement guarantees a combined use of ground-based and air-borne measurements to better characterize the aerosols.

1.4. Objectives and Outline of This Study

It is evident from the above discussions that satellite monitoring is crucial in the investigation of the climatic impact of aerosols. However, additional information from ground-based and/or in-situ measurements is necessary to distinguish between the real effects of aerosols from artifacts that may exist in satellite-based products. So multiple aerosol products derived from satellites, ground-based radiometers, and in-situ measurements are analyzed painstakingly on global and regional scales in this study. The focus is on the satellite-based aerosol products while ground-based and in-

situ measurements are used to investigate those aerosol properties that cannot be determined solely from satellites.

The ultimate goal of this study is to improve the global and regional characterization of aerosols from satellites and to help acquire long-term aerosol estimations for climatic applications. First, we try to identify the major problems of importance in satellite-based aerosol retrievals by comparing the global aerosol products derived from two historically prominent sensors: the AVHRR (Mishchenko et al., 1999; Geogdzhayev et al., 2002) and the TOMS (Torres et al., 2002). The AVHRR and the TOMS have the longest records among the existing satellite sensors although they were not originally designed for the remote sensing of aerosols. It is necessary to compare different products, to identify the problems of importance and to quantify the associated errors. An in-depth comparison of two decades of monthly products performed in this study reveals some common characteristics of aerosol distributions and regions of major problems in satellite-based aerosol remote sensing.

Aerosol retrievals from different sensors or algorithms have advantages and disadvantages according to the sensor's characteristics, the applied techniques, and the assumptions made in the algorithms. Satellite remote sensing is in general an ill-posed problem so that information derived from an observation is limited and a unique solution is not always guaranteed. Acquiring synergetic information by combining different aerosol products (or independent observing techniques) is useful to obtain better estimations concerning aerosols.

The majority of past satellite sensors such as the AVHRR and the TOMS were not designed for aerosol remote sensing. They are thus more erroneous than that from

the MODIS that was designed with aerosol retrievals in mind. Therefore, it is very important to compare the current and past aerosol products to assure that the retrievals made in the past are consistent with current ones, to identify the problems that cause inconsistencies, if any, and to quantify or correct for the errors. This study attempts to reveal the factors that cause the discrepancies between the aerosol products from the AVHRR (Mishchenko et al., 1999; Geogdzhayev et al., 2002) and the MODIS (Tanré et al., 1997) and to quantify the contributions of different factors to the observed discrepancies. This effort will ultimately help bridge current and past estimations concerning aerosols so that long-term records for climate studies can be acquired.

To understand the role of aerosol in cloud formation, it is important to know the properties and quantities of aerosols near clouds. However, aerosol remote sensing based on radiometric measurements are subject to errors due to cloud contamination and enhanced scattered radiation by inhomogeneous clouds that cannot be easily estimated from theoretical calculations (referred to as the 3D cloud effect). It was not recommended to use aerosol retrievals near clouds. On the other hand, aerosol particles can become swollen at high relative humidity, thereby resulting in a substantial increase in the scattering coefficients. Therefore, it is debatable whether an enhanced aerosol quantity (i.e., AOT) retrieved near clouds is due to cloud contamination or due to the aerosol swelling effect. Neither effect can be estimated solely from satellites. This study attempts to parameterize the aerosol swelling effect (also referred to as the aerosol humidification effect) on the column AOT in response

to the changes in the column mean relative humidity (RH) based on aircraft measurements of aerosol profiles.

Finally, the parameterized aerosol humidification effect will be used to investigate the effects of clouds on aerosol retrievals. The effects and artifacts of clouds on aerosol distributions will be identified and quantified using numerous measurements from a suite of instruments available at the Atmospheric Radiation Measurement (ARM) Southern Great Plains (SGP) Cloud and Radiation Testbed (CART) site. The results of this study help better characterize the aerosols near clouds, thereby assisting the studies of the aerosols' effects on clouds and the climate.

In summary, analyzed in this study are several aerosol products based upon satellite measurements, sun-photometer and in-situ measurements by taking advantage of each measurement technique. Chapter 2 deals with global aerosol products derived from the AVHRR and the TOMS, which have the longest records. Consistency between the two aerosol products will be examined and synergic information will be extracted. Inter-comparisons between the AVHRR and the MODIS aerosol products will be performed in chapter 3. The causes for any discrepancies between the two aerosol datasets will be explored with a focus on the aerosol models employed by the respective retrieval algorithms. Both chapter 2 and 3 contain regional and global analyses on the aerosol distributions and deal with several important issues related to the uncertainties in the remote sensing of aerosol from satellites. Chapter 4 is concerned with the aerosol humidification effect on the AOT using in-situ airborne measurements over the ARM SGP CART site, which is important in understanding the real effect of aerosols from the artifacts due to cloud

contamination. The effects of clouds on the AOT will be examined in chapter 5. Factors that cause the correlation between the AOT and cloud cover (or cloud fraction) will be examined and the real effects and artifacts will be investigated, which will ultimately help us correct satellite-based aerosol products for the artifacts associated with clouds. The summary, concluding remarks and future work are provided in chapter 6.

Chapter 2: Compatibility and Synergy Analyses on Global Aerosol Products derived from AVHRR and TOMS

2.1. Introduction

The AVHRR has been most extensively employed for aerosol studies, from which many aerosol products have been generated using dual-channel algorithms (e.g., *Higurashi and Nakajima*, 1999; *Mishchenko et al.*, 1999; *Ignatov and Stowe*, 2002a), as well as single-channel algorithms (*Rao et al.*, 1989; *Stowe et al.*, 1997; *Ignatov et al.*, 2004). The dual-channel algorithms solve for two aerosol parameters (AOT and AE) simultaneously, whereas the 3rd generation single-channel algorithm first estimates AOTs in individual channels, and subsequently estimates AE from the AOTs (*Ignatov et al.*, 2004). Concerning the TOMS instrument, after its measurements were found to be sensitive to biomass burning smoke (*Hsu et al.*, 1996), two major aerosol products were developed: the Aerosol Index (AI) (*Herman et al.*, 1997) and the AOT at 0.38 μm (*Torres et al*., 1998 and 2002). The long-term record of aerosols based on AVHRR and TOMS measurements has been well documented with distinctive features on a global scale (e.g., *Herman et al.*, 1997; *Torres et al*., 2002; *Geogdzhayev et al.*, 2002; *Mishchenko et al.*, 2003; *Stowe et al.*, 2002).

Despite the generally reasonable agreements reported between AOTs from satellites and ground-based measurements (*Ignatov et al.*, 1995; *Stowe et al.*, 1997; *Torres et al.*, 2002), these aerosol data suffer from numerous inherent shortcomings

that have not been fully understood. Substantial differences were found among various satellite-based AOT estimates and in comparison with ground-based observations (*Myhre et al*., 2004; *Kinne et al.*, 2001). Part of the inconsistencies originate from the mismatch between the products, especially between satellite (areal mean) and surface point measurements due to spatial and temporal sampling differences (*Haywood et al.*, 2001; *Kinne et al.*, 2001). Causes for the remaining inherent differences have yet to be identified and quantified.

For global aerosol retrievals, various assumptions were made concerning the physical and/or optical characteristics of aerosols (e.g., spherical versus non-spherical particle shape, different refractive indices with wavelength dependencies, and various shapes and size distributions and vertical profiles) (*Mishchenko et al.*, 1995; *Tanré et al.*, 1997; *Kaufman et al.*, 1997; *Mishchenko et al.*, 2003). Selection of an appropriate aerosol model is a major challenge, especially for global aerosol retrieval algorithms (*Nakajima et al.*, 1989; *Zhao et al.*, 2003) and can incur substantial discrepancies in the retrieval of aerosol optical depth (see Chapter 3). It is contingent upon the knowledge of aerosol type, which may be better obtained from sensors with a suite of channels that span a proper range of the spectrum, or alternately from a combination of multiple satellite sensors.

The AVHRR and TOMS aerosol products have their own advantages and disadvantages over each other. For example, the AVHRR products are limited to oceans due to difficulties in separating the signal of the aerosols from that of bright land surfaces (*Mishchenko et al.*, 1999), while TOMS can detect aerosols both over land and ocean except over the regions covered by snow/ice (*Herman et al.*, 1997;

Torres et al., 1998). The TOMS aerosol products are affected by aerosol layer altitude and single-scattering albedo, and are more susceptible to sub-pixel cloud contamination due to its large footprint (about 40x40 km^2 at nadir) (*Herman et al.*, 1997; *Torres et al.*, 1998). The TOMS aerosol data are thus derived from fewer samples than the AVHRR aerosol data. One may gain synergetic aerosol information by combining the two aerosol products. Few attempts have been made to improve aerosol characterization from multiple satellite sensors. *Cakmur et al.* (2001) used the TOMS AI and AOT from one-channel AVHRR retrievals to study the seasonal and inter-annual variability of dust aerosols. No such effort has been reported on a global scale. Analyses are also lacking toward revealing and understanding the discrepancies among various global aerosol products.

In Chapter 2, it is attempted to 1) improve the understanding of aerosol characteristics regarding their spatial and temporal variations; 2) identify any common features and differences between the AVHRR and the TOMS aerosol products through comprehensive analyses of the products over some special regions of interest; and 3) explore and take advantage of any synergy existing between the two products for classifying aerosol types over global oceans and generate a global aerosol climatology over both ocean and land at a common wavelength (0.55 μm).

The data sets employed are introduced in Section 2.2. Regional characteristics and variations of the aerosol climatology are analyzed in Section 2.3. Section 2.4 introduces the classification of aerosol types and the generation of an integrated aerosol product. Concluding remarks are given in section 2.5.

2.2. AVHRR and TOMS Aerosol Products

An AVHRR-based aerosol product generated under the Global Aerosol Climatology Project (GACP) (*Mishchenko et al.*, 1999; Geogdzhayev *et al.*, 2002; updated at http://gacp.giss.nasa.gov/) is employed in this study (hereinafter the product will be referred to as GACP/AVHRR or simply AVHRR product). It contains monthly mean AOT at 0.55 μm and AE from July 1983 through September 2001 over oceans. The product resolution is 1x1 degree in latitude and longitude. It was derived from clear-sky calibrated radiances from AVHRR channel 1 (nominal wavelength, λ=0.63 μm) and channel 2 (λ=0.85 μm) contained in the International Satellite Cloud Climatology Project (ISCCP) DX dataset (*Rossow and Schiffer*, 1999). The spatial resolution of the product is 30 km aggregated from AVHRR Global Area Coverage (GAC) data with 4-km resolution sampled from the 1-km raw data. Aerosol particles are assumed to be homogeneous spheres with optical properties determined by the Lorenz-Mie theory. A modified power law size distribution was adopted with the aerosol refractive indices fixed as m=1.5-0.003i. The shaping constant (i.e., the power exponent in the size distribution function), which is the parameter that determines the shape of the modified power law size distribution, has a unique relationship with the AE and the effective radius of aerosols.

The performance of a dual-channel-based algorithm is expected to be superior to that of a single-channel algorithm in terms of information content (*Tanré et al.*, 1997; *Nakajima and Higurashi*, 1998; *Kahn et al.*, 1998; *Higurashi and Nakajima*, 1999) if the quality of both channels is similar. However, even in such cases, there are many sources of errors inhibiting accurate aerosol retrievals (*Ignatov et al.*, 1998;

Mishchenko et al., 1999). Radiance calibration is one of the major uncertain factors (e.g., *Higurashi and Nakajima*, 1999; *Ignatov*, 2002), which could change the AOT by more than 40% (*Geogdzhayev et al.*, 2002). Another major error source is cloud screening (*Ignatov and Nalli*, 2002; *Myhre et al.*, 2004). In addition to the ISCCP cloud detection algorithm (*Rossow and Garder*, 1993), more conservative cloud screening algorithms were applied by *Mishchenko et al.* (1999) and *Geogdzhayev et al.* (2002). The additional cloud screening aims to eliminate small cumulus clouds and optically thin cirrus clouds. On the other hand, strict cloud masking could have the adverse affect of discarding strong aerosol signals (*Husar et al.*, 1997; *Haywood et al.*, 2001). Other possible error sources include the assumptions about aerosols (i.e., spherical particle, size distribution function and refractive indices) and boundary conditions (i.e., fixed wind speed and water-leaving radiance), and water vapor absorption at channel 2.

In general, AE is known to be erroneous for small AOT (AOT<0.2) (*Ignatov et al*., 1998) and is related to the spectral separation between the channels (*Ignatov and Stowe*, 2002b). Yet the accuracy of satellite-based AE is vulnerable to various uncertainties (*Ignatov and Stowe*, 2000; *Myhre et al*., 2004). *Ignatov* (2002) showed that the calibration gain is one of the most important factors hampering the retrieval accuracy of the AE, while *Geogdzhayev et al.* (2002) argued that uncertainties in the calibration intercept introduced an error in AE less than 0.4. Use of a long-term climatology can suppress random-like errors especially those associated with radiometric noise and digitization (*Ignatov et al*., 1998; *Ignatov*, 2002).

The TOMS aerosol products used here include the monthly mean AOT at 0.38 μm (*Torres et al.*, 1998 and 2002) and the monthly AI (level 3, version 7) (*Herman et al.*, 1997). They were inferred from TOMS measurements made by Nimbus-7 and Earth Probe from 1979 to 2000 (the AI data are archived at http://toms.gsfc.nasa.gov/). The TOMS AOT data have the same spatial resolution (1x1 degree) as the AVHRR data, while the TOMS AI data have a resolution 1x1.25 degree, but are interpolated to 1x1 degree grids. A temporal gap of three years exists between May 1993 and July 1996, mainly because the data from the METEOR-3 satellite were not used in aerosol data processing due to its precessing orbit (*Herman et al.*, 1997).

The TOMS AI was calculated from the ratio of radiance measurements made at 340 and 380 nm. The index has the unique capability of differentiating between absorbing and non-absorbing aerosols in the UV wavelengths over both oceans and land (*Hsu et al.*, 1996; *Herman et al.*, 1997) and even over very bright surfaces like clouds and ice/snow (*Hsu et al.*, 1999a). Its sign is positive for absorbing aerosols such as mineral dust, biomass burning aerosols and volcanic ashes, and negative for non-absorbing aerosols. The monthly mean datasets, however, were computed using only positive AI values. Any negative values were set to zero.

A quantitative measure of aerosol load and AOT was also derived from TOMS (*Torres et al.*, 1998 and 2002). The TOMS AOT is most sensitive to aerosol absorption. The retrieval employed eight spherical aerosol models: one sulfate, three carbonaceous, and four dust models with a log-normal size distribution and slightly wavelength-dependent refractive indices (*Torres et al.*, 2002). The vertical

distribution of aerosols was assumed to be a Gaussian distribution centered at 3 km for carbonaceous aerosols. For mineral dust, the climatological altitudes based on a chemical transport model (*Ginoux et al.*, 2001) were used. Both TOMS AOT and AI are sensitive to the altitude of the aerosol layer (*Hsu et al.*, 1999b). An error of 2% in the AOT may result from an altitude error of 1 km for non-absorbing aerosols and 65% for strongly absorbing aerosols (*Torres et al.*, 2002). The TOMS AOT is relatively insensitive to the aerosol particle shapes (i.e., non-spheroid) due to the dominance of multiple molecular scattering in the near-ultraviolet (UV) region that weakens the effect of particle shape (*van de Hulst*, 1957).

Sub-pixel cloud contamination is another major source of error that leads to overestimation of the TOMS AOT and is due to the large field of view of TOMS (40x40 km^2 at nadir). This effect is more significant for light loading of non-absorbing aerosols. Fortunately, the bulk of absorbing aerosols are heavily loaded (e.g. dust storms and smoke plumes). The estimated overall uncertainty for the TOMS AOT is about 20% for non-absorbing aerosols and 30% for moderately absorbing aerosols. A wrong choice of aerosol type can increase an AOT error by a factor of two (*Torres et al.*, 2002).

Our analyses employed data that had all four aerosol parameters available. One year of data after the Mt. Pinatubo eruption (1991) were discarded in order to concentrate on tropospheric aerosols. So, the data periods of our study include July 1983 – June 1991, July 1992 – April 1993, and August 1996 – December 2000, with a total of approximately 13 years.

2.3. Regional Analyses

The long-term averaged (1983-2000) seasonal maps of the four variables (i.e., GACP/AVHRR AOT and AE, TOMS AOT and AI) are presented in Fig 2.1 (only June, July, August (JJA) are shown). In general, the four products are complimentary to each other. For example, off the west coast of North Africa (10~25ºN, 15~60ºW; NW Africa), all products detected enhanced aerosol features simultaneously to a varying degree. For the AVHRR though, the continental source areas cannot be seen except for a large aerosol plume with a decreasing AOT gradient along the downwind direction indicating the source of aerosols (i.e., North Africa) that are clearly marked by the TOMS AOT and AI. However, the locations of the highest aerosol loading over land indicated by the TOMS AI and AOT are somewhat different from each other. The differences may stem from different treatments of cloud contamination. Since the TOMS AOT is more affected by residual clouds than the TOMS AI (*Herman et al.*, 1997), the former algorithm uses more strict cloud screening based on both AI and reflectivity thresholds (*Torres et al.*, 2002). Consequently, their monthly products can originate from somewhat different samples.

The TOMS AI is sensitive to both dust and smoke aerosols, although the sensitivity is higher for dust than for smoke (*Hsu et al.*, 1999b). The combination of TOMS AI and AVHRR AE help differentiate the two types of aerosols. Optical properties of biomass burning aerosols are dominated by the accumulation mode (*Remer et al.*, 1998; *Eck et al.*, 1999) with the AE ranging from 1.0 to 2.3 (*Eck et al.*, 1999; *Dubovik et al.*, 2002), whereas those for dust are usually dictated by the coarse mode (*Eck et al.*, 1999; *Tanré et al.*, 2001) with a typical AE range of 0.1 to1.0 (*Eck*

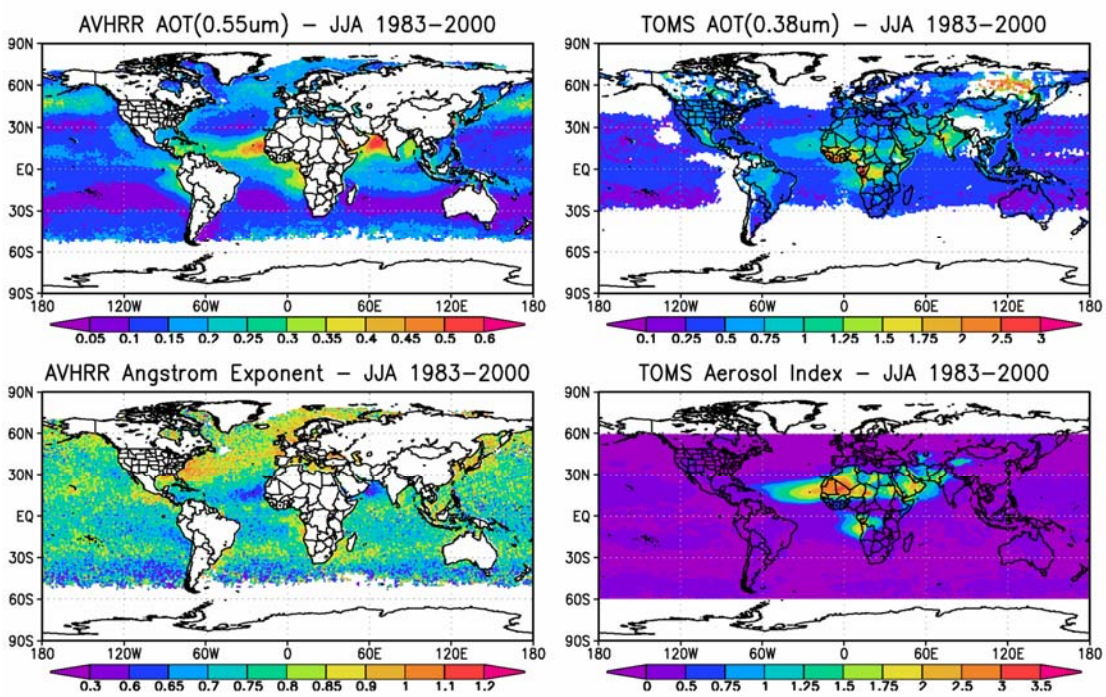

Fig 2.1. Long-term (1983-2000) seasonal mean global distributions of AVHRR AOT and AVHRR Ångström exponent (left panels) and TOMS AOT and TOMS AI (right panels).

et al., 1999; *Dubovik et al.*, 2002). The generally low AVHRR AE around NW and West-Central (5ºS~10ºN, 35ºW~10ºE; WC Africa) African regions (exact locations vary with season) coincides with the enhanced TOMS AI and AOT, signifying the dominant dust aerosols there. A region off the Southwest Africa (5~25ºS, 15ºW~15ºE; SW Africa) is abundant in biomass burning aerosols (*Husar et al.*, 1997) whose seasonal occurrence and transport are discernable from the four aerosol products. During the months of JJA (Fig 2.1) and September, October, November (SON, not shown), for instance, all four variables are significantly high. This feature is not seen in other seasons, consistent with the finding that savanna and grassland fires generally occur from July to October (*Andreae et al.*, 1994; *Husar et al.*, 1997). The Gulf of Guinea (i.e., WC Africa region) is affected by both biomass burning and

dust (Husar et al., 1997), which is echoed by relatively high AI and AOTs but intermediate AE.

Clouds pose the most serious problem in satellite aerosol retrievals. They may exert influence in three ways: cloud contamination, misclassification of aerosol as cloud, and bias in data sampling due to the presence of clouds (no retrieval for cloudy pixels). Especially, heavy aerosol in the North Pacific Ocean (40~60ºN, 150ºE~150ºW), the North Atlantic Ocean (30~60ºN, 0~60ºW), the Eastern Equatorial Pacific Ocean (0~20ºN, 80~180ºW; EC Pacific), and open oceans in the Southern Hemisphere mid-latitudes (40~60ºS) must be interpreted, or used, with caution, as they correspond to regions of extensive cloud cover. This is clearly seen from the JJA map of the ISCCP cloud fraction averaged from 1983-2000 (*Rossow and Schiffer*, 1999) (Fig 2.2). Almost all the regions of enhanced AOT coincide with high cloud

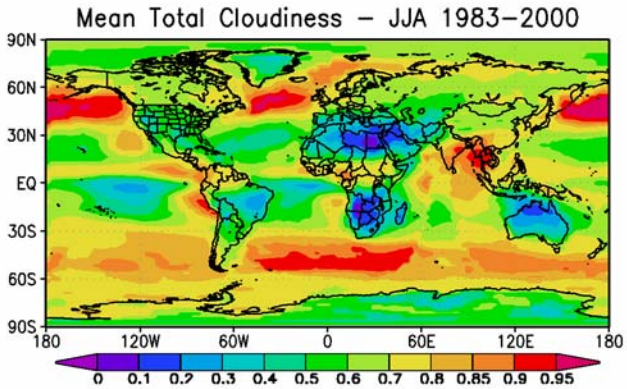

Fig 2.2. Seasonal mean cloud fraction from International Satellite Cloud Climatology Project (ISCCP) data for the same period as plots shown in Fig 2.1.

fractions (>0.7). The distribution patterns of AVHRR AOT and ISCCP cloud fraction are so similar that this leads to a strong suspicion of cloud contamination, although one cannot rule out the possibility that aerosols are coincident with clouds. To gain further insight into the problem, regional analyses are presented below.

2.3.1. Peru Region

Off the coast of Peru and Chile (10~30ºS, 70~90ºW) is a region of enhanced AOT (from the AVHRR) and cloud cover, small AE and zero AI. Adjacent to the South American continent, this region could be influenced by land sources of aerosol and the small AE might be a signal of dust aerosols transported westward from the Saharan desert. However, the AI value indicates little influence by any UV-absorbing aerosols (dust or biomass burning). Moreover, AERONET (*Holben et al.*, 1998 and 2001) data collected at a few sites located upwind from Peru (e.g., Arica, Rio Branco, and Santiago, etc.) do not show the small AE values as obtained from the AVHRR. Yet, the seasonal variation of AE from AERONET is quite different from AVHRR, as seen in Fig 2.3. It shows the annual variations of daily AE measured at Arica (18.5S, 70.3W) from 1999-2000 and long-term monthly means and standard deviations (STD) of AE from the AVHRR. Data from other nearby AERONET sites (not shown here) have even larger differences in terms of the seasonal variability. The incompatibility of AE attests to the possibility of cloud contamination of the AVHRR data, which is also supported by the correlations between the AVHRR AOT (and also the AE) and the spatial variability (STD) of the ISCCP cloud fraction (Fig 2.4). The

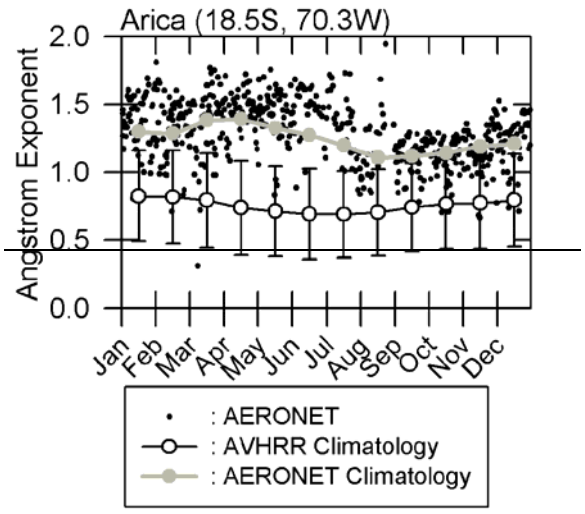

Fig 2.3. Annual variation of daily (small dots) and monthly (gray circles) Ångström exponents from an AERONET site (Arica, 1999-2000) and long-term (1983-2000) averaged AVHRR Ångström exponents (open circles) over the Peru region. Bars represent the standard deviation which contain the interannual variability.

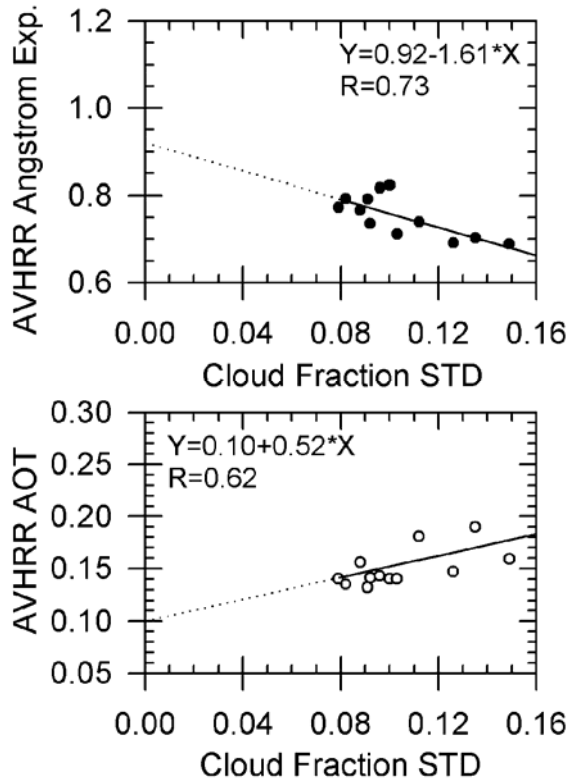

Fig 2.4. Ångström exponent and AOT as a function of standard deviation of the ISCCP cloud fraction.. R is the correlation coefficient.

STD was computed from cloud fractions within the Peru region and serve as a proxy of contamination by residual clouds. Cloud fraction itself may also serve as a proxy (Ignatov and Nalli, 2002). However, we prefer to use STD since it is less affected by any bias existing in the ISCCP cloud fraction estimation. The STD was found to be positively correlated with the AOT and negatively correlated with the AE with the correlation coefficients equal to 0.62 and 0.73, respectively.

Apart from cloud contamination, the region is likely to have a relatively high aerosol loading. Aerosol measurements during the East Pacific Investigation of Climate (EPIC) field experiment (September-October, 2001) (*Bretherton et al*., 2003) suggest that small particles from pollution sources along the Chilean coast and/or from local photochemical processes may be dominant in this region. *Kuang and Yung* (2000) reported the effects of anthropogenic sulfate aerosols in light of large SO_2 sources nearby and negative values of daily TOMS AI. Given various unusual features over this region, more detailed investigations are warranted to quantify the contributions of cloud contamination, local pollution and aerosol indirect effects, which may require *in situ* measurements.

2.3.2. Equatorial Regions

The long plume of enhanced AOT in the Equatorial Eastern Pacific (0~20ºN, 100~180ºW; EC Pacific) is a common feature in satellite aerosol products (*Husar et al.*, 1997; *Myhre et al.*, 2004), but not in the results of aerosol transport models (*Chin et al*., 2002) and model-satellite assimilations (*Yu et al.*, 2003). Questions are thus raised if the feature is an artifact of the satellite products, and, if not, what are the

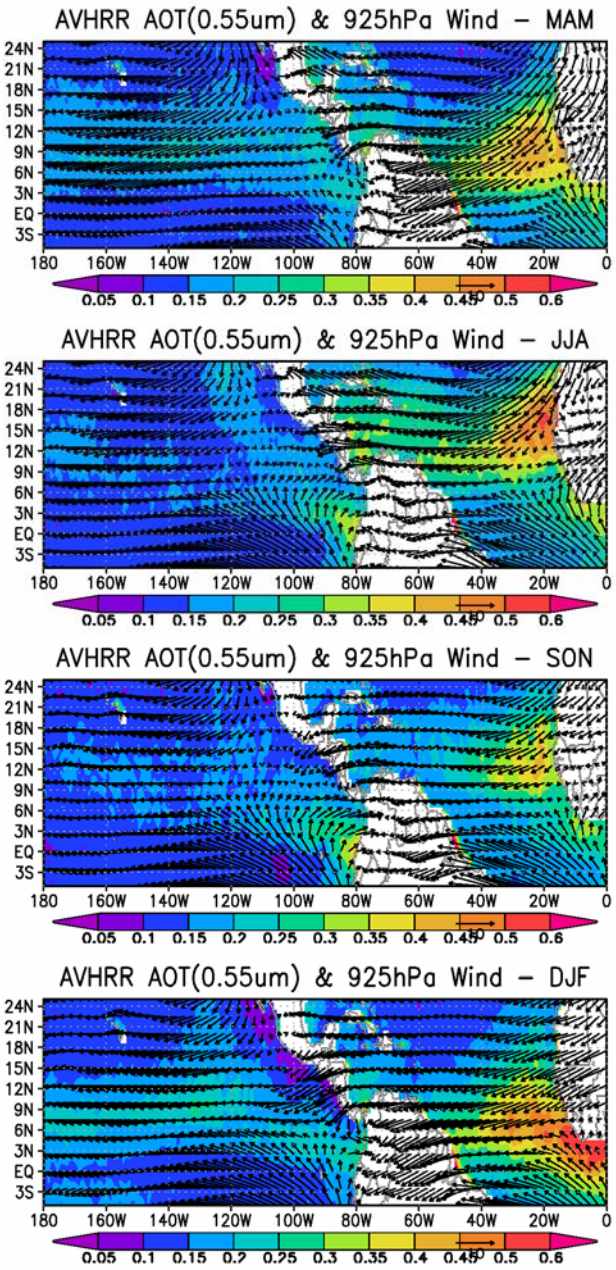

Fig 2.5. Seasonal mean AVHRR AOT around the Equator in the Pacific and the Atlantic Oceans. Wind vectors at 925hPa from NCEP/NCAR Reanalysis datasets are superimposed on the plots.

causes for the plume. To address these questions, the AVHRR AOT is plotted over a large tropical domain for four seasons (Fig 2.5). Superimposed on the AOT map are the wind vectors from the National Centers for Environmental Prediction (NCEP) Reanalysis by the National Oceanic and Atmospheric Administration-Cooperative Institute for Research in Environmental Sciences (NOAA-CIRES) Climate Diagnostics Center (http://www.cdc.noaa.gov/). The patterns of the aerosol distribution are well correlated with low-level (e.g., 925 hPa) wind vectors, but not correlated with wind speeds at 1000 hPa (not shown here), suggesting a weak contribution of locally generated sea-salt aerosol. A visual examination of all individual monthly AOT and wind vector maps for 1983-2000 suggests that the long aerosol plume across the equatorial Pacific does not come from a single dominant source. It originates from Central America (during March, April, May (MAM) and JJA), the northern part of South America and North Africa (all seasons), as well as oceanic sources along the prevailing trade wind. The plume is located between the North Pacific and the South Pacific Highs, but its strength and pattern seem to vary with wind direction. The convergence of the trade winds in the north and south corresponds to the Inter-tropical Convergence Zone (ITCZ), but the plume does not exactly coincide with the ITCZ.

The annual variations of the AVHRR AOT, AE, and the TOMS AOT are plotted for consecutive regions starting from the west coast of Africa through to the East Pacific oceans (Fig 2.6). The annual variations of AOT and AE are very similar in NW Africa, the Caribbean (10~25ºN, 60~80ºW), and Central America (10~25ºN, 80~110ºW; C America) except during MAM in C America. From NW Africa to C

America, the AOT decreases while the AE increases, indicating a decreasing influence of dust from Africa. The discordance during MAM for C America is

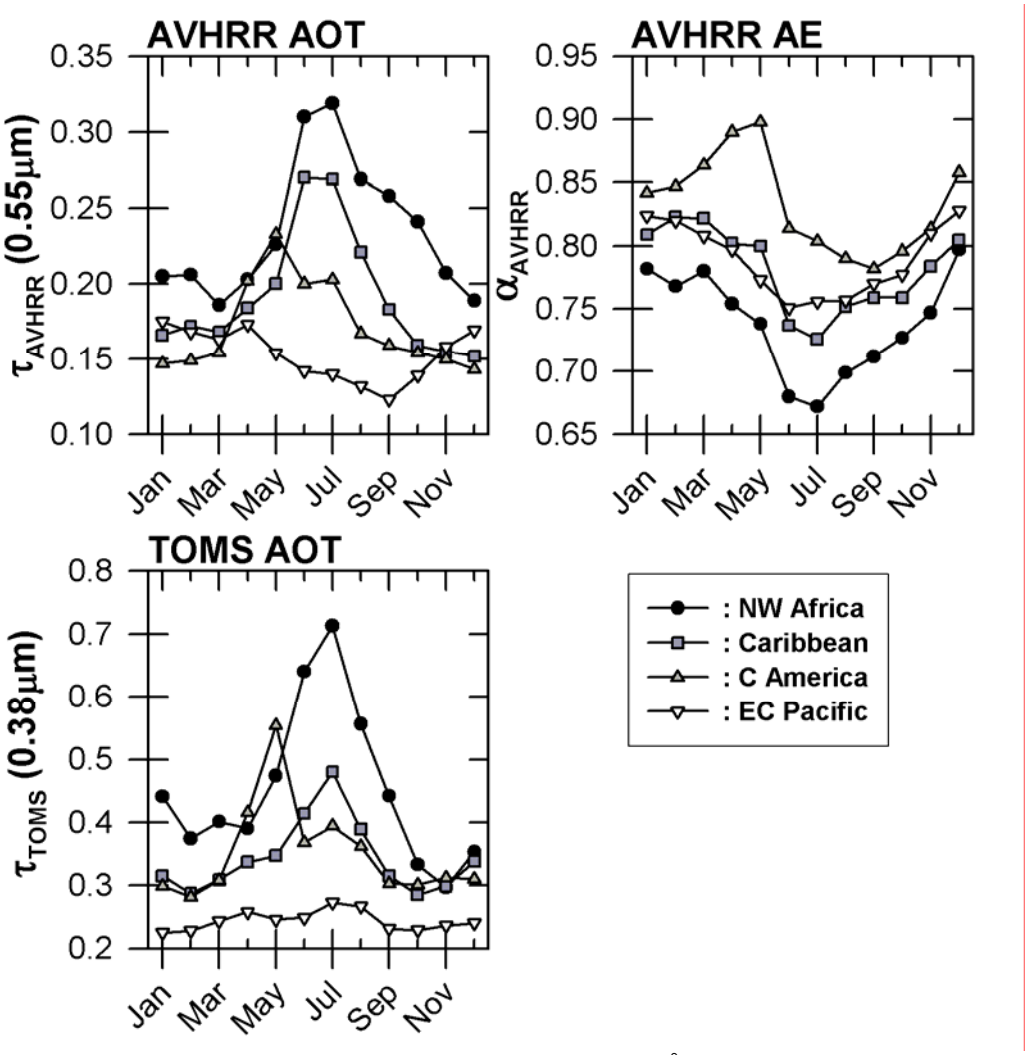

Fig 2.6. Long-term monthly mean AVHRR AOT, Ångström exponent, and TOMS AOT over NW Africa, Caribbean, C America, and EC Pacific. Regions are as defined in the text. These regions are located next to each other along a latitudinal band.

attributed in part to biomass burning which is active during this season and to local sources and transported pollutants (*Husar et al.*, 1997). There are mixed signals of aerosols influencing the EC Pacific: the AVHRR AOT for EC Pacific is about the same or even greater than that for C America in the upwind region; the pattern of the AE is similar to the Caribbean and NW Africa. There are two weak peaks in the TOMS AOT that are coincident with the biomass burning aerosol signal in C America and the dust signal in the upwind regions. All these lead to the conclusion that biomass burning and dust affect the aerosol characteristics in the EC Pacific. Using a different AVHRR-based aerosol product based on a single-channel algorithm (*Stowe et al.*, 1997), *Husar et al.* (1997) argued that the region is influenced by non-sea-salt (nss)-sulfates, Asian aerosols, and aerosols from volcanic activities, which is not obvious from this analysis.

We thus make a hypothesis that the EC Pacific is likely influenced by various types of aerosols including sea-salt, nss-sulfate, dust and biomass burning aerosols, all depending upon the wind fields. Since some observations reported a weak seasonality in oceanic aerosols (*Husar et al.*, 1997), the seasonal changes revealed in this study attest to the contributions of aerosols from land sources.

2.3.3. North Pacific and Far East Asia Regions

Many recent studies (e.g., *Husar et al.*, 2001; *Gong et al.*, 2003; *Zhang et al.*, 2003) dealt with the transport of Asian dust across the North Pacific. While the events were often detected from instantaneous AVHRR and TOMS data (*Herman et al.*, 1997; *Husar et al.*, 2001), the monthly data used here appear to indicate the

dominance of small-sized aerosols even during MAM when Asian dust outbreaks occur. Fig 2.7 shows the distribution of the seasonal mean AVHRR AOT and AE across the North Pacific for MAM and JJA. Enhanced AOT (>0.2) spreads through almost the entire region north of 30^{o}N during MAM; it shrinks to a much smaller area during JJA and SON (not shown). However, the seasonal variation of the AE is much less marked, with slightly larger values during MAM and December, January, February (DJF; not shown) than during JJA and SON. This is contradictory to the seasonal trend of dust activities. Most likely, the magnitude of the seasonal change in the AE is less than its uncertainty. The lack of seasonal variation in the AE may have a physical reason. Unlike Saharan dust, Asian dust outbreaks are sporadic. Therefore, on a monthly time scale and on a 1x1 degree grid scale, averaging may smear out the signal of Asian dust. There are other possibilities. The dust events could be misclassified as clouds and removed (*Husar et al.*, 1997; *Haywood et al.*, 2001) and it may be that AE and AOT are contaminated by ocean color.

To help reveal the sources (types) of aerosols that drive the seasonal and regional variations in the region, wind vectors at 925 hPa and 700 hPa from the NCEP/NCAR reanalysis are superimposed over the AVHRR AOT and AE maps, respectively, in Fig 2.7. A strong correlation is found between the AVHRR AOT and the wind direction, with all high (low) AOT corresponding to westerly (easterly) winds. During MAM and DJF, the westerly wind is dominant over the region such that aerosols from land sources (e.g., China, Korea and Japan) can be transported toward the east. The area of enhanced AOT also diminishes as the westerly wind retreats northward in JJA and SON. If this correlation is physically true, the enhanced

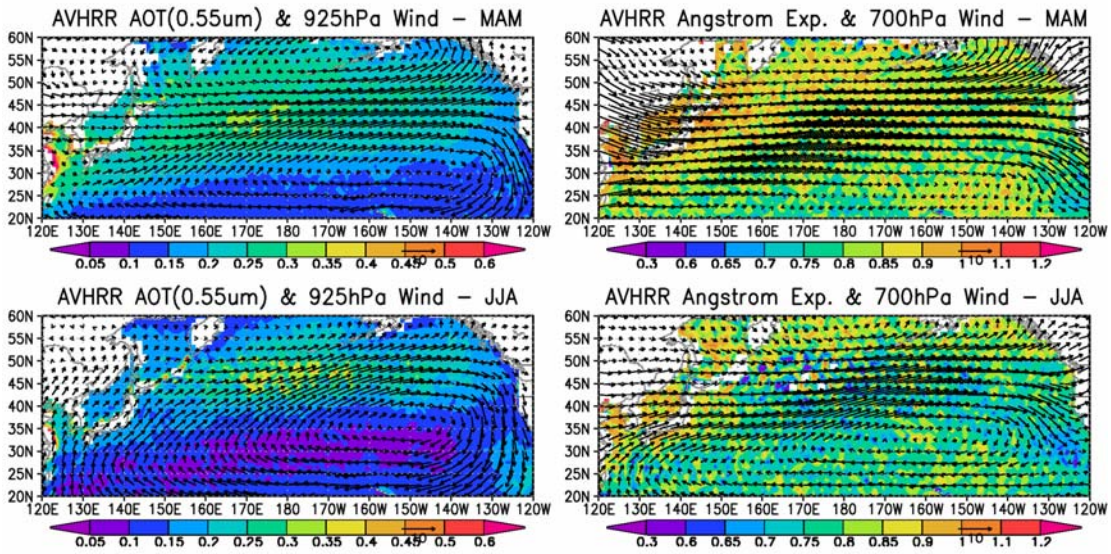

Fig 2.7. Seasonal mean (MAM and JJA) AVHRR AOT (left panels) and Ångström exponent (right panels) across the North Pacific Ocean. Wind vectors at 925hPa and 700hPa from NCEP/NCAR Reanalysis datasets are superimposed on the AVHRR AOT and Ångström exponent plots, respectively.

AOT may be explained by fine-mode pollution aerosols generated in Far East Asia, combined with background oceanic aerosols. In this case, the AOT is expected to decrease toward the Pacific, and the particle size (AE) is expected to increase (decrease) due to hygroscopic growth. This explanation seems to be corroborated with the regional variations of the AVHRR AOT and the AE plotted in Fig 2.8. It shows monthly AOT and AE at four regions located consecutively from west to east, namely, the Yellow Sea (25~45ºN, 120~130ºE), Japan (30~50ºN, 130~145ºE), NW (30~50ºN, 145~180ºE) and NE (30~50ºN, 140~180ºW) Pacific. Traces of Asian aerosols were observed over Midway Island and the Hawaii islands (*Prospero and Savoie*, 1989; *Prospero et al.*, 2003).

An exception is noted in the middle of the Pacific where the AOT is high, especially during JJA. This points to another plausible cause, namely cloud

contamination. The left two panels in Fig 2.9 shows the ISCCP cloud cover distribution during JJA and MAM; the spatial pattern and temporal variation also bear a close resemblance to those of the AOT. Broadly speaking, a cloud cover of 0.7 (in yellow) seems to distinguish between AOT greater than and less than 0.2. There is a large area with cloud cover greater than 0.9 in the middle of the Pacific corresponding to the maximum in AOT. It is worth noting, however, that a large cloud cover does not necessarily lead to cloud contamination, which is dictated more by cloud scale than cloud cover frequency. Given that the presence of cloud in the region is controlled chiefly by large-scale frontal systems, the degree of cloud contamination should be less than in low-latitude regions. The relative uniformity and widespread extent of high AOT is more likely to be true in a qualitative sense, but a real

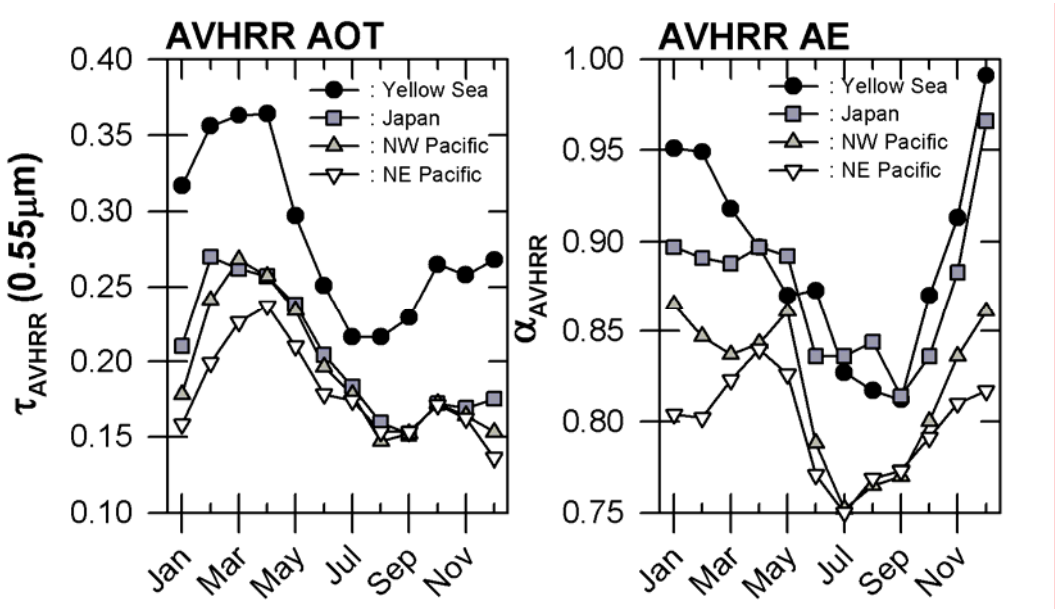

Fig 2.8. Long-term monthly mean AVHRR AOT and Ångström exponent over the Yellow Sea, Japan, NW Pacific, and NE Pacific.

challenge lies in quantifying the influence of cloud contamination on the satellite AOT retrievals.

Another factor is associated with phytoplankton, which could contribute to high AOT and/or induce an artifact to cause false high AOT. Normally, a high chlorophyll concentration is found along the coastal regions and mid- and high-latitudinal oceans, as is shown in the right two panels in Fig 2.9 (shown only for MAM and JJA; data generated by a NOAA-NASA's Coastal Zone Color Scanner (CZCS) reanalysis (NCR) effort (*Gregg et al.*, 2002)). All these regions have high AOT. Fig 2.10 presents the correlation between long-term monthly mean AOT and the chlorophyll concentration in July over both the regions under study (the Yellow Sea, Japan, and NE/NW Pacific), as well as other regions of high chlorophyll concentration (N Atlantic, 35~50ºN, 25~50ºW; W Europe, 35~60ºN, 0~25ºW). Positive correlations are found in all regions. The correlation coefficients are larger than 0.5, except for Japan where the correlation is lowered due to a few cases of exceptionally high AOT corresponding to low chlorophyll concentrations.

High phytoplankton concentrations can lead to formation of sulfate aerosols, which have important implications for climate (*Charlson et al.*, 1987). Planktonic algae produce dimethylsulphide (DMS) and then, through oxidization, the DMS transforms into sulfate aerosols that are a major source of cloud condensation nuclei (CCN). It is, however, difficult to link this effect to the monthly satellite data, since the portion of such sulfate aerosols would be small compared to the total aerosol loading in the atmosphere. Besides, it is likely that the high AOT may be an artifact. Very high chlorophyll concentrations ($\geq$2.0mg/m^3) and enhanced sedimentation can

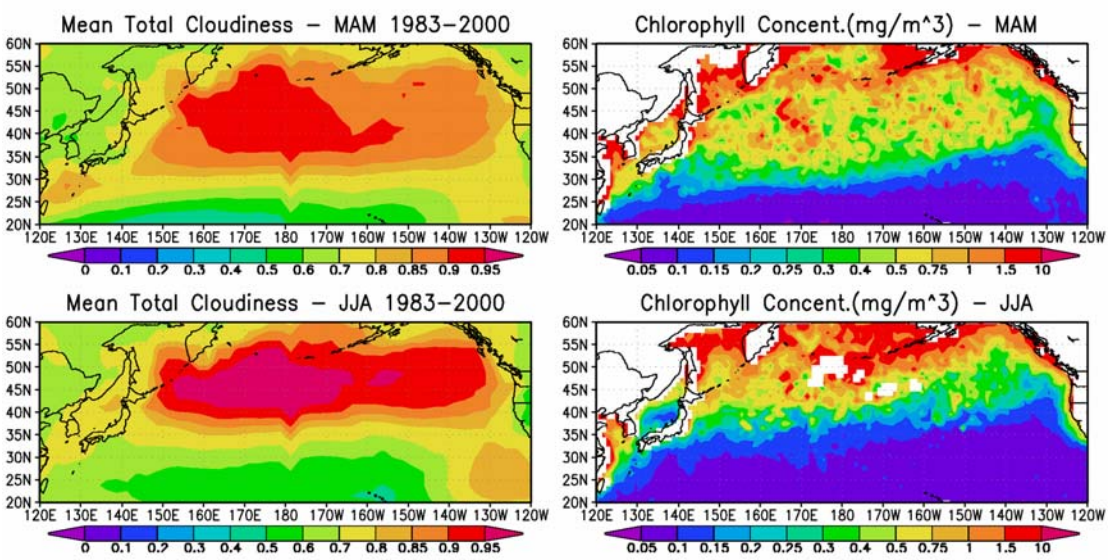

Fig 2.9. Seasonal mean cloud fraction (left panels; MAM and JJA, 1983-2000) from ISCCP datasets and seasonal mean chlorophyll concentration (right panels; MAM and JJA, 1978-1986) from NOAA-NASA's Costal Zone Color Scanner (CZCS) reanalysis (NCR) effort across the North Pacific Ocean.

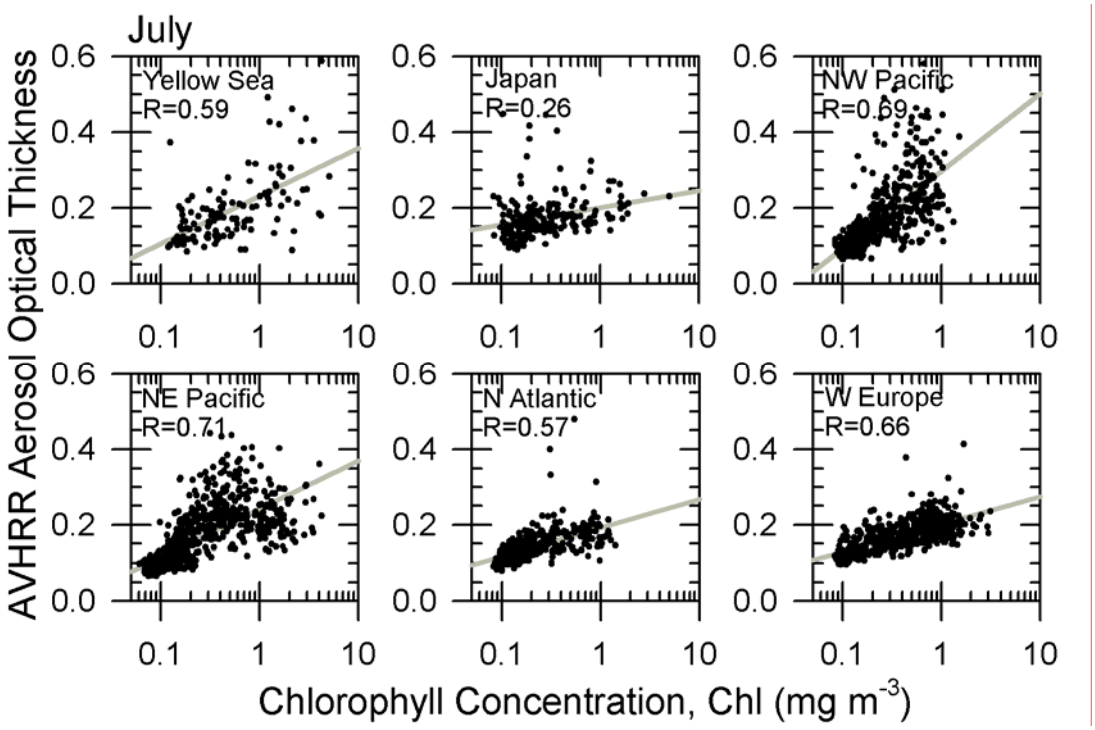

Fig 2.10. Long-term mean AVHRR AOT as a function of NCR chlorophyll concentration (Chl) over various regions in the North Pacific and North Atlantic Oceans. Solid gray lines represent the least-squared linear fit. R is the correlation coefficient.

increase the water-leaving radiance in the visible spectrum (*Siegel et al.*, 2000). Since the retrieval algorithm does not account for such changes, the AOT may be overestimated. This is apparently the case for the sharp increase in AOT over a narrow strip along the east coast of China where ocean color is exceptionally bright due to sedimentation of very turbid water from the Yangtze River. The retrieval of ocean color (or chlorophyll concentration) and aerosol is often a convolved problem and thus becomes an obstacle in the retrieval of each other (e.g., *Fukushima and Toratani*, 1997). Another challenge posed here is how to unravel their effects.

We may thus make another conjecture that the lack of consideration of changes in ocean color may contribute to the spatial variation in AOT, but is unlikely to be the primary cause for the general trend of the AOT variation. So, again, the real challenges are 1) to quantify this artificial effect, and 2) to establish a genuine physical relation between chlorophyll concentrations and oceanic aerosol loading. To this end, *in situ* measurements and modeling would be helpful. These issues will be addressed in future studies.

2.4. Synergetic Analyses

It follows from the above analyses that the AVHRR and the TOMS do a reasonable job in retrieving AOT. On the other hand, they suffer from numerous problems, due to instrumental limitations and inversion difficulties. Note that neither of the instruments was optimized for aerosol studies. As each of the datasets has different advantages and shortcomings, the two may be combined to enrich aerosol information and to derive a synergetic product.

One major difficulty in producing such synergy is that the TOMS and AVHRR retrievals typically have only a few days in common in each month and have different over-passing times, so that their individual monthly averages may have large uncertainties (*Cakmur et al.*, 2001). As the uncertainties are largely random, they are suppressed by averaging (*Mishchenko et al.*, 1999). As a measure of data compatibility, we first computed a test AE (α_{test}) from the TOMS and AVHRR AOTs:

$$\alpha_{test} = -\ln(\tau_{0.38\mu m}^{TOMS} / \tau_{0.55\mu m}^{AVHRR}) / \ln(0.38\mu m / 0.55\mu m) \quad (2.1)$$

Noting that the range of the AE due to the variability of aerosol properties is estimated to be 0-2 (*Kinne et al.*, 2001; *Dubovik et al.*, 2002), we can diagnose if the data sets are spectrally consistent by establishing whether α_{test} falls within a valid range of values. This has been proposed and used by *Ignatov and Nalli* (2002) for their AVHRR-based aerosol products. The estimates of α_{test} as computed by (1) contain both systematic and random errors. Systematic errors occur if the AOT from one sensor is systematically higher/lower than that of the other, out of a range expected for the channel difference. Random errors are primarily due to cloud contamination. *Myhre et al.* (2004) noted that the AOT from TOMS is systematically higher than that from AVHRR and further investigation into this discrepancy is presented later (Section 4.2). If values of α_{test} are less than 0 or greater than 4, we deem them inconsistent and discard them. The test AE was calculated on different time scales: individual monthly means and seasonal means, and monthly and seasonal means averaged over the entire data period. 10% to 30% of the α_{test} computed from

individual monthly AOTs fell within the range of abnormal values (i.e., $\alpha_{test} < 0$ or $\alpha_{test} > 4$). For the long-term averaged monthly and seasonal means, 2.6-3.8% and 2.1-2.6% of the α_{test}, respectively, also fell within the range of abnormal values. Fig 2.11 shows the distribution of α_{test} calculated from the long-term mean AOT in JJA. The magnitude of α_{test} is systematically greater than the AVHRR AE except over major cloud regimes, while the gross pattern of distribution is similar to that of the AVHRR (see Fig 2.1). In terms of spatial distribution, most of the unreasonable α_{test} values reside in areas of low AOT for which the AE is very sensitive to errors in AOTs (*Ignatov et al.*, 1998; *Geogdzhayev et al.*, 2002), as well as regions with cloud contamination.

These results suggest that AVHRR and TOMS AOTs do not have enough spectral consistency to be useful for extracting information concerning aerosol size due to differences in sampling and the magnitude/direction of their uncertainties. On the other hand, the distribution of α_{test} suggests that AVHRR and TOMS AOTs are correlated to each other geographicallyso are related to aerosol type. Any synergy existing between the two products should be exploited to help identify dominant aerosol types and to estimate AOT at one wavelength (AVHRR AOT) from the other (TOMS AOT).

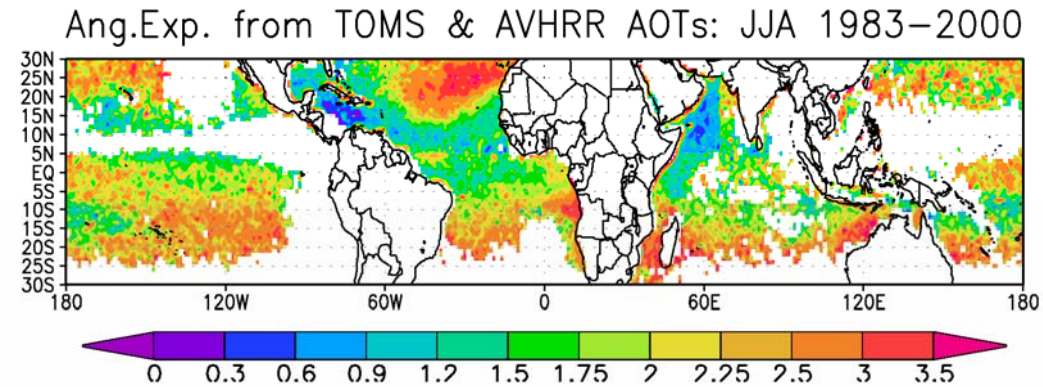

Fig 2.11. Ångström exponent derived from TOMS and AVHRR AOTs. (JJA)

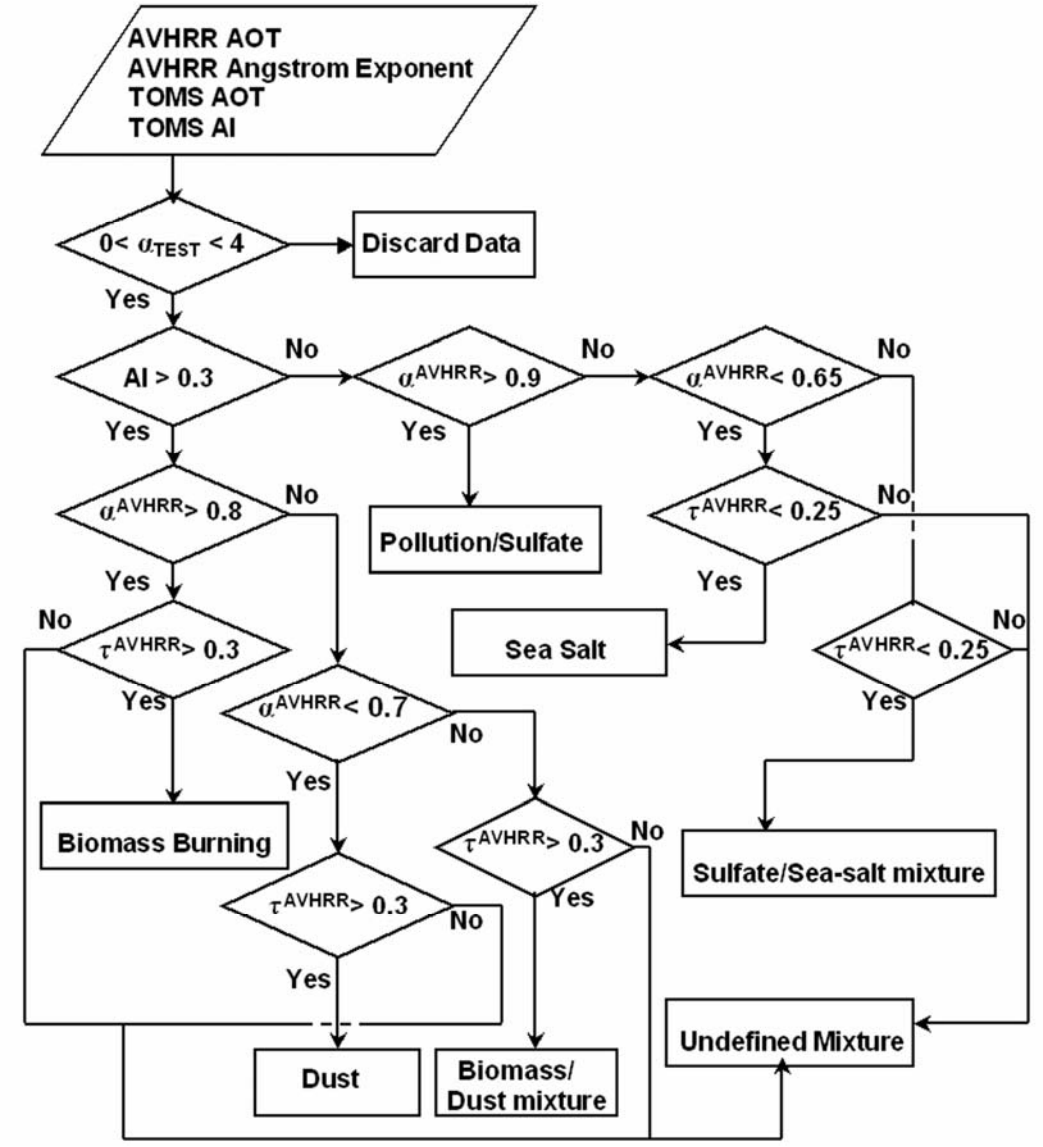

Fig 2.12. A classification algorithm for identification of dominant type(s) of aerosols.

2.4.1. Synergy I: Identification of Aerosol Types

Aerosol type information is crucial for many applications because different types of aerosols have distinct properties that may give rise to very different direct and indirect effects. Knowledge of aerosol type directly influences the quality of the AOT retrievals from satellite-measured radiances because the radiances are altered by both aerosol loading and aerosol optical properties. For global aerosol retrievals, several aerosol models are necessary to take into account highly variable aerosol characteristics (*Kaufman et al.*, 1997). These aerosol models may be differentiated in terms of absorbing strength, particle shape, vertical distribution, etc. Currently, global distributions of aerosol type have been primarily derived through modeling (e.g., *Tegen et al.*, 1997; *Chin et al.*, 2002; *Penner et al.*, 2002 and more references therein). A handful of recent efforts focused on using satellite data to classify aerosol type on a global scale (*Kaufman et al.*, 2002). By virtue of MISR multi-angle observations, aerosols can be retrieved as mixtures of several components (*Martonchik et al.*, 1998; *Kahn et al.*, 2001). *Bellouin et al.* (2003) attempted to separate dust, sea-salt, and smaller-particle aerosols by utilizing the AOT and the AE from POLDER together with pre-defined aerosol regimes based on geographical location.

While AVHRR data have been employed to extract aerosol size information and TOMS data have been used to measure aerosol absorption, the two data sets have not been combined to infer aerosol type. The analyses in section 3 demonstrated the utility of synchronizing the AVHRR AOT and AE and the TOMS AOT and AI to identify aerosol type. The algorithm is delineated in the flowchart shown in Fig 2.12.

First, α_{test} [see Eqn. (2.1)] is calculated from AVHRR and TOMS AOTs and only qualified data (i.e., $0<\alpha_{test}<4$) are employed. The TOMS AI can distinguish between UV-absorbing (biomass burning particles and dust) and non-UV-absorbing aerosols (sea-salt, sulfate, pollution, etc.). Small (biomass burning particles, pollution, sulfates) and large (dust, sea-salt) particles can be differentiated using the AVHRR AE. Intermediate values of the AE are assumed to represent mixtures of small and large particles. Numerous thresholds are applied to the AOT to refine the classification. For example, biomass burning, dust and some heavy pollution aerosols tend to have larger AOTs while the AOTs for light pollution (oceanic nss-sulfate and sea-salt) tend to be smaller. Some complicated mixtures of aerosols are designated as belonging to the "undefined" group, together with inconsistent data caused by data mismatch and cloud contamination. The threshold values are also given in the flowchart and were chosen based on aerosol climatologies derived from AVHRR and AERONET (*Dubovik et al.*, 2002).

Fig 2.13 shows global seasonal maps of the dominant aerosol types classified by this algorithm. It captures well the seasonal and regional characteristics of the aerosols, as discussed in many other studies (e.g., *Husar et al.*, 1997; *Herman et al.*, 1997, *Torres et al.*, 2002, etc.). As examples, one can find the pollution plumes over the mid-latitude North Atlantic Ocean, Far East Asia and the North Pacific, and dust and biomass burning aerosols from Africa. The colored areas over land indicates source areas for biomass burning and dust aerosols based on the values of the TOMS AOT (>1.0) and the AI (>1.25). The area with light pink over Russia during JJA

represents aerosols from boreal fires as indicated by TOMS AOTs over a period of 1983-2000.

The classification algorithm is flexible in that it can be adapted to any other dataset containing similar information, although the threshold values may need adjustment. For instance, the AE is not an absolute measure of aerosol size and can

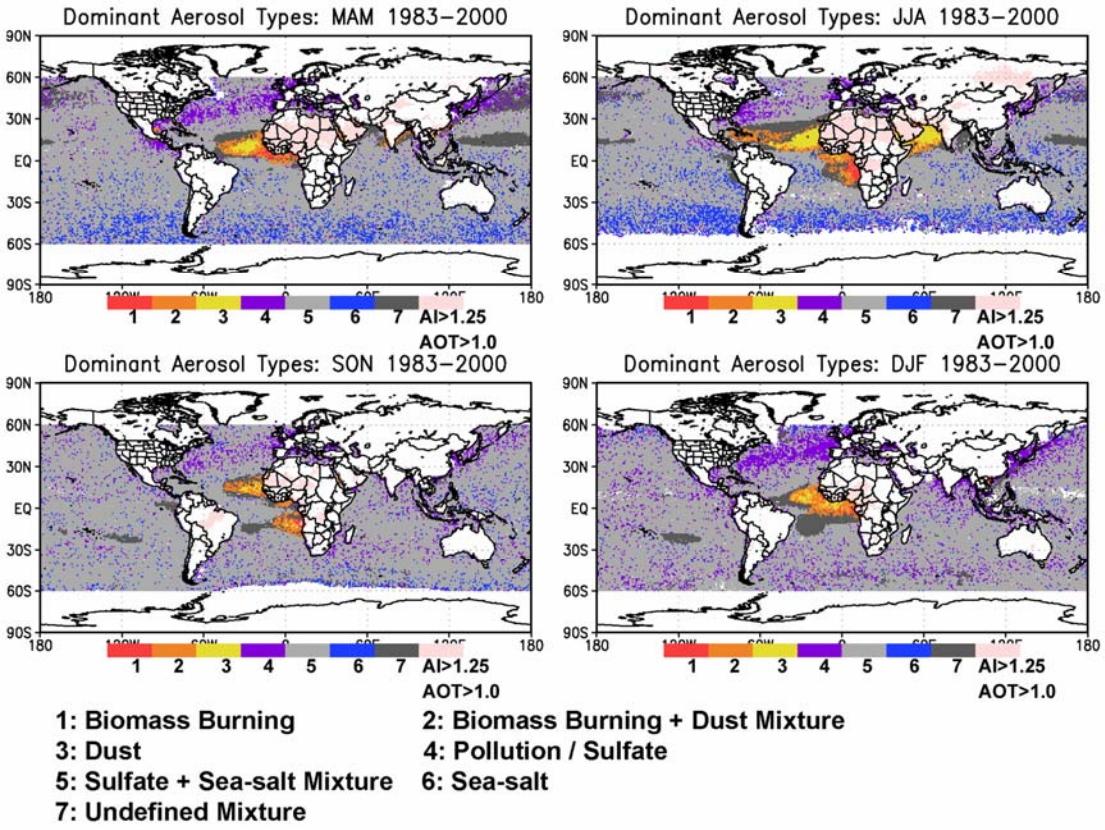

Fig 2.13. Global seasonal maps of dominant aerosol types based on the algorithm delineated in Fig 2.12. Land areas with TOMS AOT greater than 1 and AI greater than 1.25 are colored in light pink to indicate some major aerosol sources.

vary with the wavelengths of the channels from which it is computed, and with physical/optical properties of aerosols. Thus, its threshold may be tuned for different instruments and/or spatio-temporal resolutions. In addition, if a more robust physical parameter for aerosol size is available, such as the effective radius, better results may be acquired. For example, this algorithm could be applied to the MODIS and TOMS datasets. However, the Earth Probe/TOMS sensor's calibration problem since November 2000 (http://toms.gsfc.nasa.gov/aerosols/aerosols.html) may be a limiting factor. The algorithm would work better if data were from a single sensor or from sensors aboard a single satellite in order to avoid or lessen data mismatch problems.

The algorithm has some limitations related to the appropriateness of the following assumptions: the characteristic size for each aerosol type, the capability of TOMS AI to discriminate UV-absorbing aerosols from non-UV-absorbing aerosols, and the consistency of data from different satellites. The performance of this algorithm is affected by the accuracy of the aerosol size parameter. Some aerosol events may possess particles with different size characteristics from those generally known, such as large biomass burning aerosols due to coagulation processes in thick smoke plumes (e.g., *Hobbs et al.*, 2003) or due to hygroscopic growth (e.g., *Zhou et al.*, 2002) and small to intermediate-sized marine boundary layer aerosols containing sea-salt (*Murphy et al*., 1998), to name a few. When datasets from different satellites are used, they may be derived from different scenes, in spite of the data consistency test procedures.

2.4.2. Synergy II: Estimation of Global AOT at 0.55μm

It would be more useful to estimate the AOT at the same wavelength over both oceans and land so that one can identify more readily aerosol sources and their transportation. The AOT at 0.55 μm (or 0.5 μm) has been used as a common aerosol parameter in various studies (e.g., *Masuda et al.*, 1995; *Li and Moreau*, 1996). An attempt is thus made here to generate a global integrated AOT product at 0.55 μm from AVHRR and TOMS instruments. This is achieved by first developing regressional relationships between the AVHRR AOT and the TOMS AOT over oceans where both products are simultaneously available. To reduce random errors, the long-term (1983-2000) monthly averages are used. Fig 2.14a shows the relationship for biomass burning aerosols, dust aerosols and non-UV-absorbing aerosols. Overall, the TOMS AOT is systematically and significantly larger than the AVHRR AOT by a factor of approximately 2. Part of the difference is caused by the wavelength difference between the two channels (0.55 μm versus 0.38 μm), as is shown by three simulated relationships for dust, sulfate and carbonaceous model aerosols employed in the TOMS AOT retrieval (*Torres et al.*, 2002). As is expected, larger differences correspond to finer aerosol particles. While the three lines are located among the observed data points, they are also all above the regression lines, implying that the AOT differences exceed the spectral dependence. It can thus be concluded that one product is over(under)-estimated relative to the other. Such systematic differences are better accounted for by sorting the data according to aerosol type, as is shown in Fig 2.14b-d. After data sorting, the two types of AOT have linear relationships whose slopes vary with aerosol type. Note that the intercept

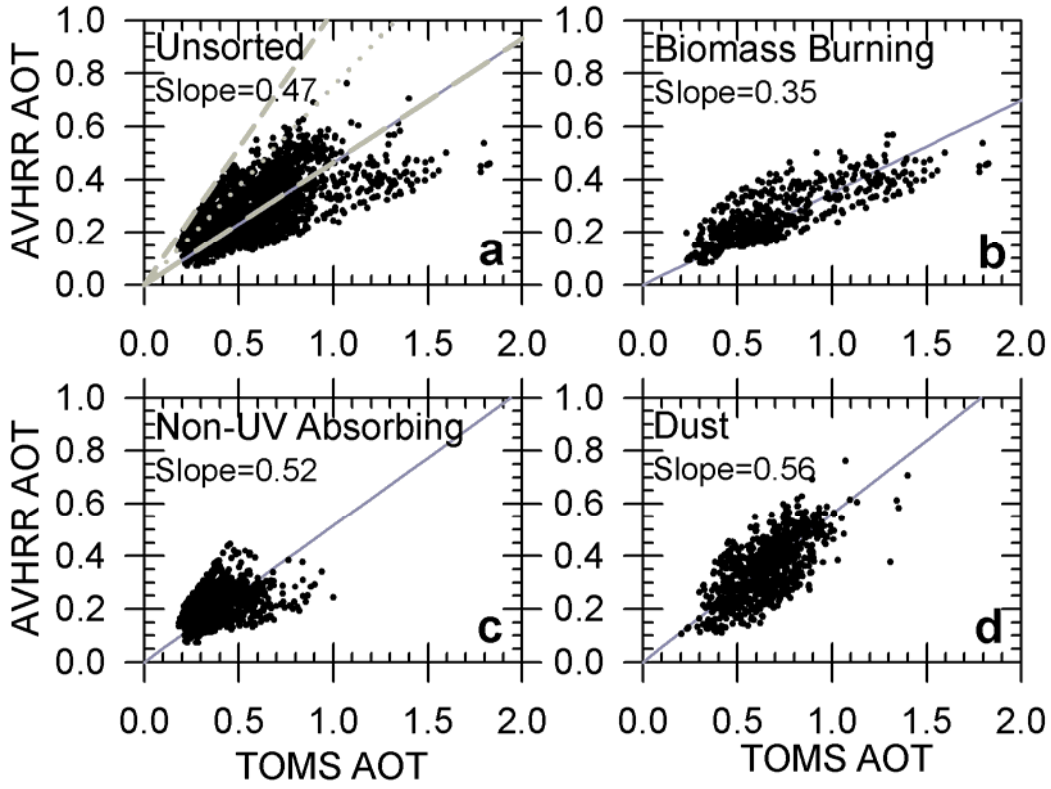

Fig 2.14. Scatter plots of TOMS AOT as a function of AVHRR AOT for various dominant types of aerosols. Their linear regression lines are marked in panels b-d. In panel a, modeled relationships are given for three dominant aerosol types as used in the TOMS aerosol algorithm: dust (medium-dash line), sulfate (short-dash line), and carbonaceous (long-dash line).

was set to zero in the regression. The difference diminishes to a factor of 1.7 for dust aerosols. We can use the relationship to estimate the AVHRR AOT from the TOMS AOT, or vice-versa. The overall error range of estimation is $\pm 0.08 \pm 0.20\tau$, within which more than 95% of the data points reside.

Without sorting the data according to aerosol type, *Myhre et al.* (2004) argued that the overall substantial scattering in the data results from differences in data sampling and cloud screening. We agree that part of this scattering is related to cloud and data sampling but this scatter can be reduced after sorting the data into different

aerosol types. Another contributing factor lies in the use of different aerosol models in the retrieval algorithms. In Chapter 3, it is demonstrated that considerable discrepancies between the AOT estimated from AVHRR and MODIS are attributed to differences in aerosol size distributions, namely, the power-law (AVHRR) and (bi-modal) log-normal (MODIS) functions. Since the TOMS AOT is based on the log-normal size distribution, similar discrepancies may also exist between TOMS and AVHRR. Large scattering is expected for non-UV-absorbing aerosols and low aerosol loading to which TOMS is rather insensitive.

The AOT at 0.55 μm over land was obtained by applying the derived regression equations to the TOMS AOT, together with the AI and land cover data from the International Satellite Land Surface Climatology Project (ISLSCP; *Meeson et al.*, 1995). Due to a lack of dynamic knowledge of aerosol types over land, the latter two datasets were used to grossly separate the data into smoke, dust and non-UV-absorbing aerosols. The AI was first used to group aerosols into UV-absorbing and non-absorbing aerosols. Absorbing aerosols are then classified as dust or biomass burning aerosols, depending if it is over vegetated or barren land. This simple assumption was made out of necessity. The maximum range of error due to this assumption is ±0.21*(TOMS AOT), when biomass burning was mistakenly selected instead of dust, or vice versa. However, this type of error is not a major factor according to comparisons against MODIS AOT as shown in the following discussions. The ensuing land AOTs are combined with the AVHRR AOTs over ocean to form a global climatology whose long-term average (1983-2000) is presented in Fig 2.15. It is seen that there is no artificial discontinuity between ocean

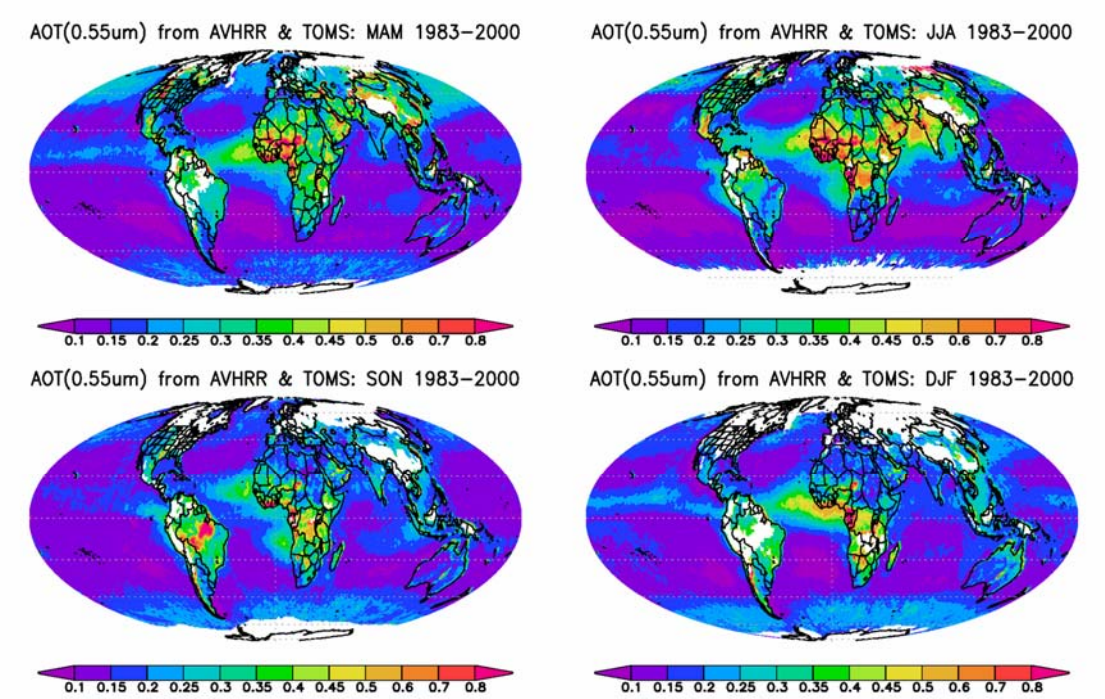

Fig 2.15. Global maps of seasonal mean AOT at 0.55μm. AOT over land was estimated from regression equations based on relationships among TOMS AOT and AI and AVHRR AOT. AOT over ocean is the AVHRR AOT as originally reported.

and land and the map provides certain information pertaining to aerosol sources and transport.

The estimated AOT over land are compared against monthly mean AERONET measurements (Fig 2.16). The best results are achieved in the Arabian region (Solar Village and Bahrain) followed by the South African region, with small random errors and little or no bias. Almost all data points fall within the range of estimated errors marked by the dashed lines. Larger scatterings exist for other locations, which is partially due to sampling errors in point specific measurements (*Kinne et al.*, 2001) and unexplained variability by the regression equations, as well

as errors in the TOMS AOT data. There is a slight underestimation of the AOT in North Africa and an overestimation of the AOT in South America, but the bias errors in general are very small. While aerosols in both South Africa and South America stem from biomass burning, one reason for the better agreement in the former region is because the data used for developing the regression for biomass burning came from the region off the west coast of South Africa. The use of geographic location to select a regression equation can introduce errors especially for mixtures of dust and biomass burning aerosols in the Sahel region. Despite the numerous errors, most (~70%) of the estimated AOT reside within the estimated error range, when compared against AERONET data.

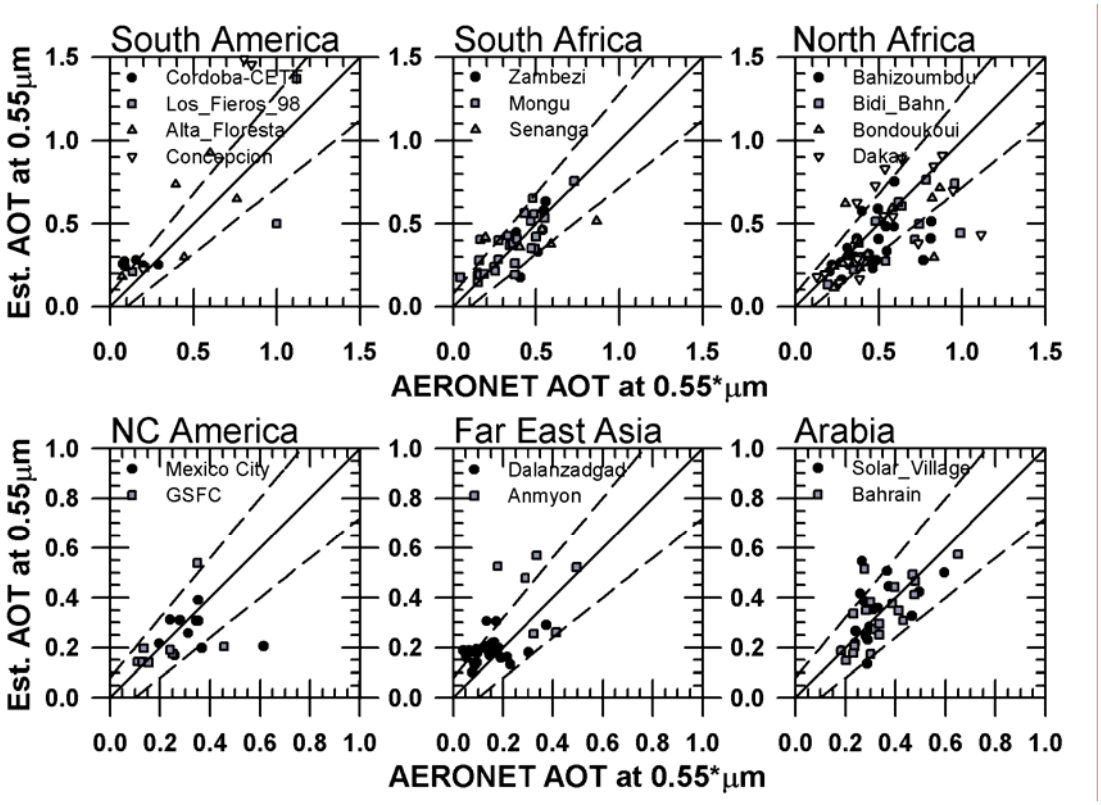

Fig 2.16. Comparison of estimated AOT over land against monthly AERONET AOT at 0.55μm. AERONET AOT was interpolated using the Ångström exponent. The solid line is the one-to-one line and dashed lines denotes the estimated error range.

The MODIS AOT data (April 2000 – March 2004) at 0.55μm over land are compared with our results. Since the overlapping period is short (less than a year), the comparison is performed for their respective long-term means. Fig 2.17 shows the maps of the seasonal mean differences between MODIS and the estimated AOTs over land. The two AOTs agree well with each other in general except for Asia. The primary reasons for the large disparity in Asia are likely to include 1) the fact that statistical relations between TOMS and AVHRR AOTs for heavy pollution and Asian dust were not established due to ubiquitous missing data in TOMS AOT at higher latitudes along major cloud regimes and 2) the dependence of TOMS AOT on aerosol altitude (i.e., lower altitude near the source regions).

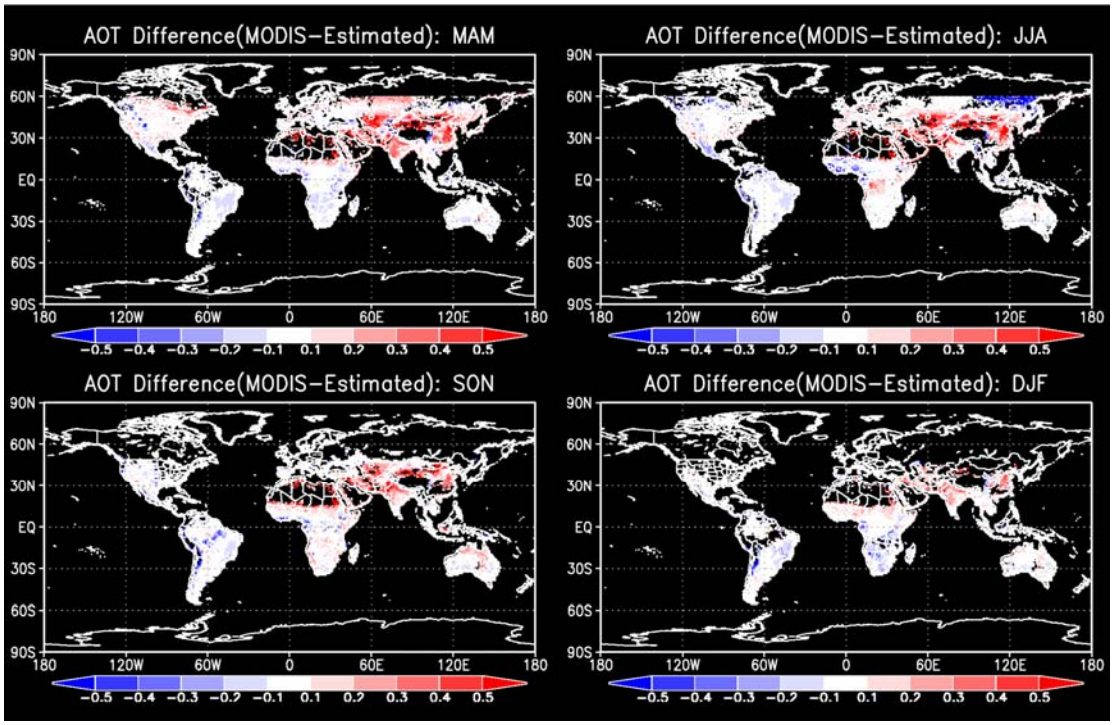

Fig 2.17. Seasonal mean difference maps between the estimated AOT over land at 0.55μm (1983-2000) from TOMS and AVHRR datasets (as shown in Fig 2.15) and MODIS AOT (April 2000 – March 2004).

Fig 2.18 shows multi-year monthly averages of the two AOTs over the respective continents. On a continental scale, our AOT estimation from TOMS data shows a similar seasonality to that from MODIS. Good agreement is found in North America and Australia. For South America and Asia, systematic differences are found, but their seasonal variations track each other quite well. It is interesting to note that the MODIS AOT and our AOT estimations over South Africa cross each other before and after the peak season of biomass burning. It is difficult to pinpoint the causes, but

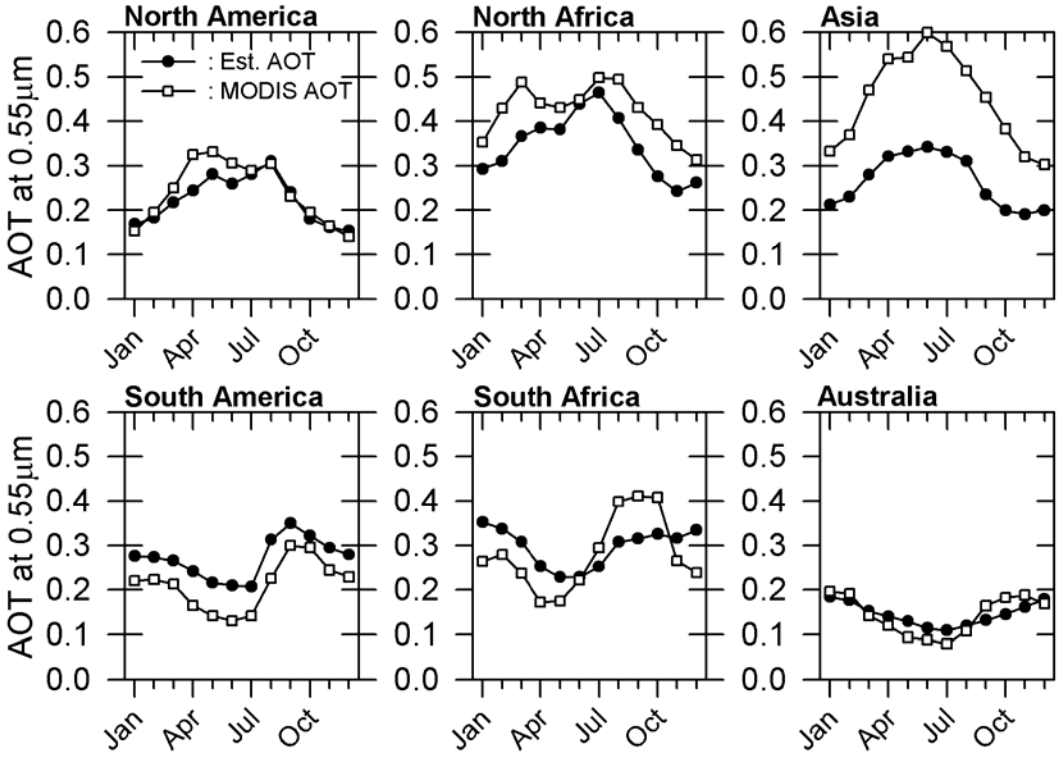

Fig 2.18. Comparison of multi-year monthly averages of the estimated AOT (1983-2000) and MODIS AOT (April 2000 – March 2004) over the continents. Note that Africa was separated at the equator into North and South regions. Each continental monthly average includes all available co-located data sets for respective continents.

major factors influencing the systematic differences may include: 1) systematic differences between regional mean MODIS and GACP/AVHRR AOTs as revealed in Chapter 3, noting that the estimated AOT over land is a GACP/AVHRR-like AOT); 2) the dependence of TOMS AOT on the altitude of the aerosol layer (and topography) and aerosol absorption (single-scattering albedo), especially in the dust and biomass burning regimes; 3) differences in sampling periods, which may explain the large blue area over Russia during JJA in Fig 2.17. The sound agreement between the two AOTs and their seasonality suggest that AOT estimations from the past can be linked to current state-of-art AOT estimations for development of continuous long-term records.

2.5. Summary

Global aerosol products play an important role in climate change studies due to their complex direct and indirect effects. While numerous global aerosol products have been generated from various satellite sensors, much more insight into these products is needed to understand them in terms of their strengths, weaknesses and synergies, in order to 1) make informative and creative use of the data, 2) to extract as much information as possible from the data, and 3) to filter out any inherent noise and uncertainties for future improvement in both data quality and quantity. Presented here is a preliminary study towards achieving this goal by examining the quality, compatibility and synergy between two prominent global aerosol products derived from AVHRR and TOMS (*Mishchenko et al.*, 1999; *Torres et al.*, 2002).

Cloud contamination has been a common inherent problem suffered by both products (*Ignatov and Nalli*, 2002; *Myhre et al.*, 2004). Nearly all aerosol-laden regions outside of the tropics correspond to high/frequent cloud cover. Regions of highly suspected cloud contamination include the Southern Hemispheric Oceans (30~60°S) in all the seasons and some parts of the North Pacific Oceans during JJA (and MAM but much weaker). Unfortunately, the monthly products used here convey little information to aid in comprehending the problem. On the other hand, regional analyses with aerosol physics in mind are instrumental in gaining further insight into the likely effects of cloud and other factors. In general, it seems safe to conclude that while cloud contamination contributes to AOT values to a varying degree, the general patterns of enhanced AOT appear to be true, rather than artifacts due to cloud contamination. Unraveling the various other effects remains a major challenge, which is crucial to furthering our understanding of many aerosol-related issues.

To this end, attempts are made here to conduct in-depth regional analyses using a variety of data sets. The following regions were selected based on certain unique features that have not been previously addressed: off the coast of Peru, a tropical zone between western Africa to Eastern Central Pacific, and North Pacific regions. First, the high AOT associated with small AE off the shores of Peru is due to cloud contamination. If this were not so, the presence of small AE would contradict other studies that reported small particles in this region and argued about the apparent evidence of an aerosol indirect effect. Second, the long plumes of enhanced AOT along the Equatorial Eastern Pacific (EC Pacific) have a complex and interesting seasonality that is driven by atmospheric circulation. The plume is a manifestation of

the convergence of various types of aerosols (dust, smoke, pollution aerosols, etc.) transported by prevailing winds that change with season. Third, the generally enhanced aerosol field over the North Pacific is found to consist primarily of fine-mode aerosols and the loading responds sharply to the changes in wind direction, signifying heavy influence by aerosols (especially pollution) transported from Asia. However, there is no discernible dust signal in terms of relative values of AE even during the dust-active season in spring. This could be due to the smearing out of sporadic dust episodes by averaging in a month or due to the misclassification of dust as cloud. On the other hand, significant correlations found between the AVHRR AOT and chlorophyll concentration around these regions suggest a possible influence of ocean color contamination and/or induced oceanic aerosols such as nss-sulfate, which can be linked to phytoplankton activity.

The AVHRR and TOMS aerosol products also exhibit a good synergy, which is exploited here. For example, TOMS data alone has difficulty in differentiating between dust and biomass burning aerosols, which can be compensated for by the AVHRR AE pertaining to aerosol size. Taking advantage of their respective strengths, we developed an algorithm to classify aerosol types into dust, biomass burning, a mixture of the two, sulfate/pollution, and sea-salt, etc. Using this algorithm, regions under the dominant influence of various types of aerosols are determined from the two satellite products alone. Prior to MODIS and MISR, it has been difficult to gain such information from a single satellite. The performance of this algorithm is influenced by the quality of each aerosol product (especially the AVHRR AE and the TOMS AI).

As an application of the classification and exploitation of the synergy, the two AOT products are integrated to generate an AOT product at a common wavelength (0.55 μm) of truly global coverage covering both ocean and land. To reduce the large scattering and biases exhibited when direct comparisons of the two products were made, different relationships were derived between the TOMS and AVHRR AOTs according to aerosol type. The range of uncertainty of the estimated AOT is $\pm 0.08 \pm 0.20\tau$. These inferred AOTs are compared to AERONET measurements, and most of the estimations fall within this range of uncertainty. In addition, comparisons of the inferred AOTs with MODIS AOTs show good agreement in terms of magnitude and seasonality, suggesting that bridging past and current AOT estimations is promising.

Chapter 3: Quality and Compatibility Analyses on Global Aerosol Product Derived from AVHRR and MODIS

3.1. Introduction

Satellite-based remote sensing plays a vital role in gaining a good knowledge and understanding of global aerosol variations and interaction with the Earth's climate (*Kaufman et al.* 2002). While satellite data have long been employed for aerosol studies, major challenges still confront us in almost every step of the retrieval process, namely, sensor calibration, cloud screening, corrections for surface reflectivity and variability of aerosol properties (size distribution, refractive index, etc.) (*King et al.*, 1999). Consequently, significant differences exist among various aerosol products generated from the AVHRR (*Stowe et al.*, 1997; *Higurashi and Nakajima*, 1999; *Mishchenko et al.*, 1999; *Ignatov and Stowe*, 2002a; *Ignatov et al.*, 2004), the MODIS (*Tanré et al.*, 1997; *Kaufman et al.*, 1997, *Remer et al.* 2005), the Total Ozone Mapping Spectrometer (TOMS) (*Herman et al.*, 1997; *Torres et al.*, 1998, 2002), the Polarization and Directionality of the Earth's Reflectances (POLDER) instrument (*Goloub et al.*, 1999; *Deuzé et al.*, 2000), and the Multi-angle Imaging Spectroradiometer (MISR) (*Kahn et al.*, 1998, 2001), etc. *Myhre et al.* (2004) compared a large number of global aerosol products and revealed the general features of agreement and discrepancies, but insights into the causes for the discrepancies were lacking and the state-of-the-art aerosol product from the MODIS was excluded from their work.

This study conducts a more detailed comparison of aerosol products over oceans from two prominent sensors: MODIS and AVHRR (*Tanré et al.*, 1997; *Mishchenko et al.*, 1999). Possessing the longest satellite record, AVHRR data have been employed in studying long-term variations of atmospheric aerosols (*Mishchenko et al.*, 2003). Using various retrieval algorithms, aerosol optical thickness (AOT) was inferred from reflectances measured at a single channel (*Rao et al.*, 1989; *Stowe et al.*, 1997; *Ignatov et al.*, 2004), and at multiple channels (*e.g., Higurashi and Nakajima*, 1999; *Mishchenko et al.*, 1999; *Ignatov and Stowe*, 2002a). In some algorithms, an additional parameter (often the Ångström exponent) was also estimated. So far, all global aerosol products generated from the AVHRR have been confined to oceans primarily due to difficulties in separating aerosol signals from those from land surfaces of high reflectivity (*King et al.*, 1999). Taking advantage of a unique relationship between reflectances at longer and shorter wavelengths available from the MODIS, *Kaufman et al.* (1997) proposed a method that extends the retrieval of the AOT over the majority of land areas except over bright desert or barren land. Note that a different algorithm was used to retrieve the AOT over oceans (*Tanré et al.*, 1997). Validations of the MODIS AOT retrievals against ground-based Aerosol Robotic Network (AERONET) (*Holben et al.*, 1998 and 2001) observations showed good accuracies over both oceans and land (*Remer et al.*, 2002; *Chu et al.*, 2002).

In addition to the AOT, the Ångström exponent (α) (*Ångström*, 1929 and 1964) has been widely used for various applications by virtue of its relationship to aerosol size. For instance, α is used for interpolation (or extrapolation) of aerosol optical thickness (AOT) at a certain wavelength (e.g., *Kinne et al.*, 2001; *Myhre et al.*,

2004) and is used as a proxy of particle size when direct measurements of aerosol particle size (effective, mean or mode radius, etc.) are not available (*Chou et al.*, 2002; *Sakerin and Kabanov*, 2002; *Moorthy et al.*, 2003). *Nakajima et al.* (2001) used α to study the aerosol indirect effect which is defined as the radiative forcing associated with the modification of cloud microphysics due to aerosols (*Twomey et al.*, 1984; *Coakley et al.*, 1987; *Charlson et al.*, 1992). Note that α depends on the wavelengths for which it is derived.

Retrievals of AOT and α are affected by aerosol size distributions and optical properties. Numerous studies reported diverse optical and physical properties of aerosols (e.g., *O'Neill et al.*, 2002; *Dubovik et al.*, 2002; *Eck et al.*, 2003). The treatment of aerosol size distributions and optical properties in aerosol retrieval algorithms is generally poor and varies from one algorithm to another. Inherent discrepancies are thus incurred between different aerosol products, which should be well understood and quantified before attributing the discrepancies to factors that are not readily verified such as cloud screening. The choice of aerosol models on retrieved AOT was deemed to be small (less than 10%) by *Geogdzhayev et al.* (2002) whose choice of aerosol models was not as diverse as those employed in the MODIS retrieval though. *Chylek et al.* (2003) found that the uncertainties in aerosol parameters such as refractive index and aerosol shape have large effects on the phase function at large scattering angles (greater than 100 degrees). As satellite aerosol retrievals are typically performed at such large scattering angles, the impact of aerosol model choice is expected to be significant.

The objective of this study is to understand and quantify the uncertainties and discrepancies in the AOT and the α derived from the MODIS (*Tanré et al.*, 1997) and the AVHRR (*Mishchenko et al.*, 1999; *Geogdzhayev et al.*, 2002) with more focus on the possible effects of aerosol model difference. In Chapter 2, other factors affecting the aerosol retrievals were also investigated. In section 3.2, the aerosol products used are briefly described. Section 3.3 presents the comparisons of the AOT derived from the MODIS and the AVHRR and investigations of their discrepancies. Similar studies but for α and its relation to aerosol effective radius are given in section 3.4. The summary and conclusive remarks are provided in section 3.5.

3.2. MODIS and AVHRR Aerosol Products

3.2.1. The GACP/AVHRR Aerosol Product

An AVHRR-based aerosol product generated under the Global Aerosol Climatology Project (GACP) (*Mishchenko et al.*, 1999; *Geogdzhayev et al.*, 2002; updated at http://gacp.giss.nasa.gov/) is employed in this study (hereinafter the product will be referred to as GACP/AVHRR or simply AVHRR product). It contains the monthly mean aerosol AOT at 0.55 μm and α from July 1983 through September 2001 over oceans. The product resolution is 1x1 degree on an equal-angle grid. It was derived from clear-sky radiances from AVHRR channel 1 (nominal wavelength, λ=0.63 μm) and channel 2 (λ=0.85 μm) contained in the ISCCP DX dataset (*Rossow and Schiffer*, 1999). Note that the ISCCP radiance data were obtained following post-launch calibration (*Brest et al.*, 1997). Aerosol particles are assumed as homogeneous spheres whose optical properties are determined by the Lorenz-Mie theory. A

modified power law size distribution was adopted with the aerosol refractive indices fixed as m=1.5-0.003i. The shaping factor, which is the parameter that determines the shape of the modified power law size distribution, has a unique relationship with α and the effective radius of aerosols.

There are many sources of errors inhibiting accurate aerosol retrievals (*Mishchenko et al.*, 1999). Radiance calibration is one of the major uncertain factors (*e.g., Higurashi and Nakajima*, 1999; *Ignatov and Stowe*, 2002b) and can change the AOT by more than 40% (*Geogdzhayev et al.*, 2002). Cloud screening could lead to very larger errors in AOT (*Ignatov and Nalli*, 2002; *Myhre et al.*, 2004). More conservative cloud screening algorithms were applied by *Mishchenko et al.* (1999) and *Geogdzhayev et al.* (2002), in addition to the ISCCP cloud detection algorithm (*Rossow and Garder*, 1993). The additional cloud screening aims to eliminate small cumulus clouds and optically thin cirrus clouds. On the other hand, the strict cloud masking may have an adverse impact of discarding useful aerosol signals by misclassifying them as clouds (*Husar et al.*, 1997; *Haywood et al.*, 2001). For instance, an AOT threshold of 1 is used for the GACP/AVHRR product as a part of cloud screening, which will discard some cases with heavy aerosol loading. Other important error sources are the assumptions about aerosols. *Mishchenko et al.* (1999) showed a use of fixed refractive index introduces systematic regional difference. *Geogdzhayev et al.* (2002) argued that the effect on the retrieved AOT of the choice of aerosol size distribution function would be less than 10%. *Mishchenko et al.* (2003) found that the spherical assumption can cause errors up to a factor of two for non-spherical particles like mineral dust. Other possible sources of error include

uncertainties in boundary conditions (i.e., fixed wind speed and water-leaving radiance) and water vapor absorption at channel 2.

In general, the accuracy of the α is known to be inversely proportional to the AOT (*Ignatov et al.*, 1998) and related to the spectral separation between the channels (*Ignatov and Stowe*, 2002b). Yet, the accuracy of the α is lower than that of the AOT (*Ignatov and Stowe*, 2000). *Geogdzhayev et al.* (2002) estimated that the retrieval accuracy in the α, when taking into account the calibration uncertainty, the choice of aerosol size distribution, and the selection of a fixed wind speed, was less than 0.4, 0.3 and 0.125, respectively. Use of a long-term climatology can suppress random-like errors especially those associated with radiometric noise and digitization (*Ignatov et al.*, 1998).

3.2.2. The MODIS Aerosol Product

The MODIS aerosol product was generated by different algorithms, depending on whether the surface was ocean (*Tanré et al.*, 1997) or land (*Kaufman et al.*, 1997). Since the AVHRR aerosol product is retrieved over oceans only, aerosol products were selected from March 2000 through April 2001 when both AVHRR and MODIS aerosol products over ocean were available. The MODIS product is version 4 of the MOD08 dataset with a spatial resolution of 1x1 degree. The product includes numerous parameters such as the AOT, α, the effective radius, the number of cloud condensation nuclei, the asymmetry factor, and the backscattering ratio. Employed in this study are AOT at 0.55 μm and α derived from the channels centered at 0.55 μm and 0.87 μm.

The retrieval algorithm was originally documented by *Tanré et al.* (1997) and updated by *Levy et al.* (2003). It utilizes radiances observed at six bands (nominal wavelengths of 0.55, 0.66, 0.87, 1.24, 1.64, and 2.13 μm) at a spatial resolution of 500m under clear-sky conditions determined by a dedicated cloud-masking algorithm (*Martins et al.*, 2002). Aerosol particles are also assumed to be spherical as in the AVHRR AOT retrieval. However, the aerosol models employed in the MODIS algorithm are much more sophisticated than any prior algorithms. It adopted bi-modal log-normal size distribution functions as suggested by measurements (*Whitby*, 1978; *Kaufman et al.*, 1994; *Kaufman and Holben*, 1996; *Dubovik et al.* 2002) with 20 combinations of nine basic modes including four "fine" and five "coarse" modes. Each mode has a wavelength dependent refractive index. Aerosol optical properties (single scattering albedo and phase function) were computed and stored as look-up-tables (LUTs) for the 9 basic modes at various AOT values (0-2.0), 9 solar zenith angles, 16 satellite zenith angles, and 16 relative azimuth angles. Reflected radiances from the two log-normal size distributions are approximated by the weighted average of those for each individual distribution (*Wang and Gordon*, 1994). A radiance measurement is matched to a weighted combination of computed radiances corresponding to the coarse and fine mode aerosols. The aerosol modes and weighting factors were selected based on the sum of square differences at six channels. Note that more than one aerosol model may be selected, depending if the radiance differences fall within the given margins of tolerance, rather than the minimum differences (*L. Remer,* private communication). The retrievals are averages of all the qualified values.

The MODIS products have been validated over land (*Chu et al.*, 2002) and ocean (*Remer et al.*, 2002 and *Levy et al.*, 2003) against AERONET data following a standardized procedure introduced by *Ichoku et al.* (2002). *Remer et al.* (2002) showed AOT errors over ocean for non-dust aerosols fall within the estimated accuracy of $\Delta\tau = \pm 0.03 \pm 0.05\tau$ (*Tanré et al.*, 1997) and the retrieved aerosol effective radius also agreed with that derived from AERONET to within ±0.1 μm. For dust aerosols, *Levy et al.* (2003) found similar agreements in the AOT estimates but with a slight wavelength dependence, underestimation at 0.87 μm and overestimation at 0.47 μm and 0.55 μm. However, they reported a larger underestimation (20-100%) in the dust particle size, which was conjectured to stem from the spherical particle assumption. *Chu et al.* (2002) showed that the root-mean-square of errors (RMSE) of the MODIS AOT varied from 0.07 to 0.11 for inland regions, but increased up to 0.3 for coastal regions due to water color contamination. For the α, the MODIS values are correlated with AERONET values at a correlation coefficient of 0.50 for MODIS AOT greater than 0.20 at 0.66 μm.

3.3. Aerosol Optical Thickness (AOT)

3.3.1. Comparison of GACP/AVHRR and MODIS AOT

Fig 3.1 shows the global distributions of the AOT from MODIS and AVHRR (upper panels) and their absolute and relative differences (lower panels). While the gross patterns of the AOT global distributions are similar to each other, their

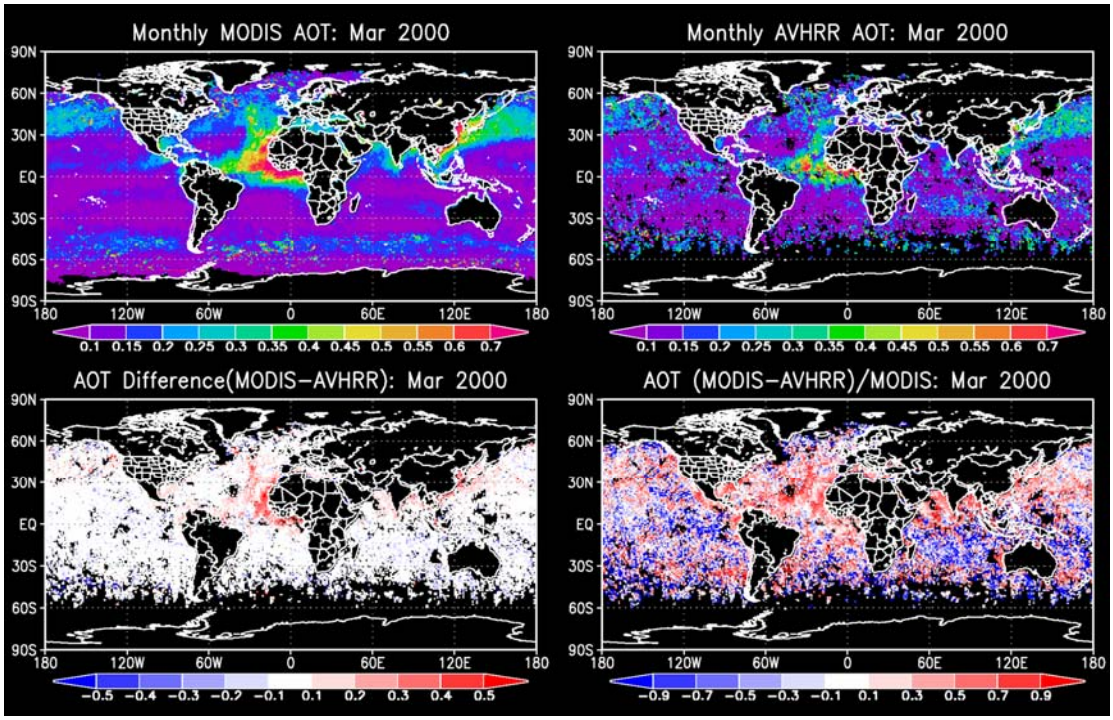

Fig 3.1. Monthly distribution of MODIS AOT (upper-left), AVHRR AOT (upper-right), their difference (MODIS minus AVHRR; lower-left), and relative difference (lower-right), respectively (March, 2000).

magnitudes are rather different, especially over regions affected by major aerosol regimes (e.g., off the west coast of Africa, the North Pacific Ocean, the North Atlantic Ocean, and spotty areas in the mid-latitude Southern Hemispheric Oceans). The maps of absolute and relative differences reveal that the two AOTs agree with each other to within ±0.2, with relative differences often exceeding 10% and sometimes reaching 100%. The largest discrepancies in AOT are found off the west coast of Africa by roughly up to 0.5. It is worth noting that larger discrepancies (> 0.3) are mostly positive (i.e. MODIS AOT > AVHRR AOT) except for some patchy areas in the Southern Hemispheric Oceans (30~60˚S).

To gain further insight into these discrepancies, regional means of MODIS and AVHRR AOTs were compared for all the available months over regions influenced by various aerosol regimes (see Fig 3.3). Fig 3.2 delineates all the rectangular regions under study together with the dominant aerosol types (c.f. Chapter 2). The two mean AOTs are much better correlated, thanks to the averaging which eliminates/suppresses the random component of the discrepancies. However, there are significant regional differences, indicated by the slope of the regression line between the two sets of AOT. The slope is less than 1.0 (underestimation by AVHRR) for most regions of elevated aerosol loading by mineral dust, biomass/coal burning, and heavy pollution. Over the open oceans (EC/WC Pacific regions, SE Pacific, etc.), the two AOTs match well with each other. The low correlation found over the Central America and Peru regions likely results from the varying aerosol influences as discussed in Chapter 2.

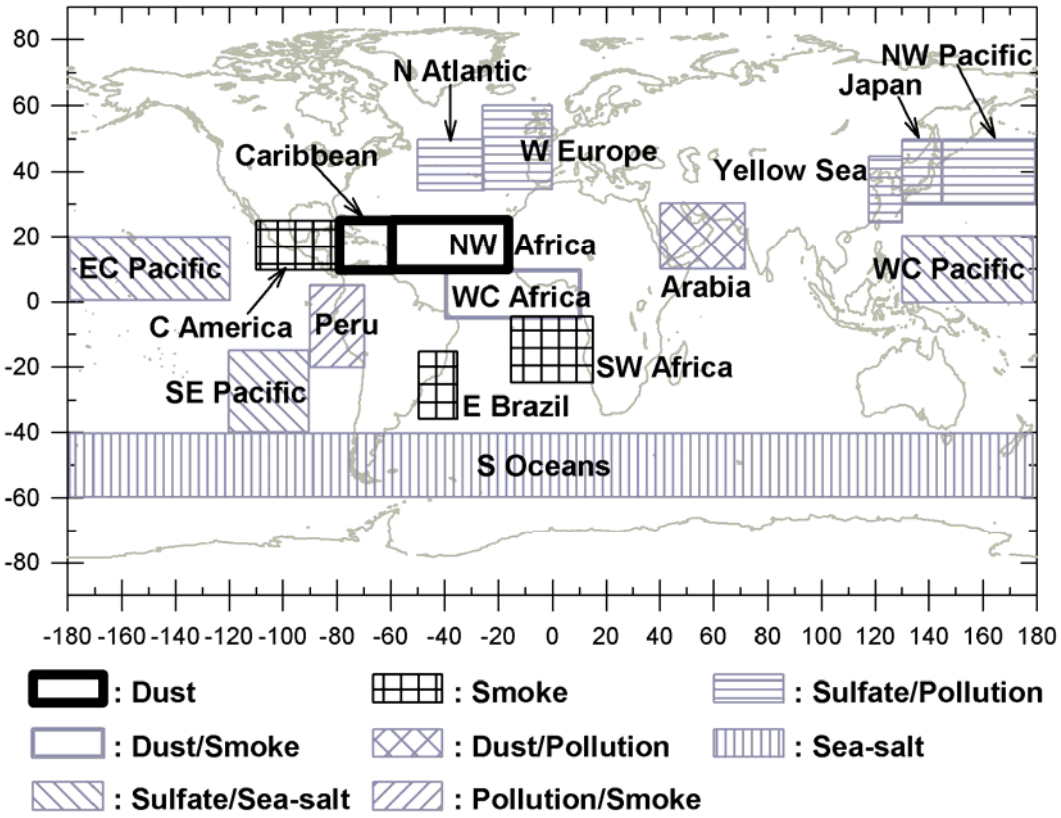

Fig 3.2. Aerosol regions over the oceans. Regions are defined as rectangles for which regional averages of AOT and Ångström exponent are calculated (see Fig 3.3 and Fig 3.9). For some regions containing land masses, averages were obtained only over water.

3.3.2. Factors Contributing to the AOT Discrepancies

It is very important and challenging to unravel the physical causes for the systematic discrepancies. While errors in AOT retrievals are incurred by numerous factors, cloud screening was often blamed for any large discrepancies (*Myhre et al.*, 2004). We agree that cloud screening contributes significantly to the discrepancies as shown in Fig 3.1. Clouds affect the performance of aerosol retrievals in three ways (*e.g., Husar et al.*, 1997; *Haywood et al.*, 2001; see also Chapter 2): 1) through cloud contamination, 2) misclassification of aerosols as clouds, and 3) bias in aerosol sampling due to presence of clouds (i.e., no retrieval for cloudy pixels). The first effect leads to overestimation of the AOT, the second to underestimation of the AOT, and the third to either over- or underestimation of the AOT (thus produces random-like errors). It is more likely that misclassification of aerosols as clouds underestimates the AOT for instances of high aerosol loading, while cloud contamination results in AOT overestimation under any instance of aerosol loading. One may thus conjecture that the discrepancies shown in Fig 3.3 are caused by misclassification of clouds and aerosols in the AVHRR product or by cloud contamination in the MODIS product. Unfortunately, this inference cannot be tested with the data available for this investigation, which would require analysis of individual scenes for better discrimination between cloud and heavy aerosol episodes.

One must also bear in mind that other factors may be as important as cloud in causing the discrepancies. Use of different types of aerosol models can be a major source of discrepancy. The aerosol models are differentiated by aerosol particle size distribution and refractive index. The following model simulations offer insights into

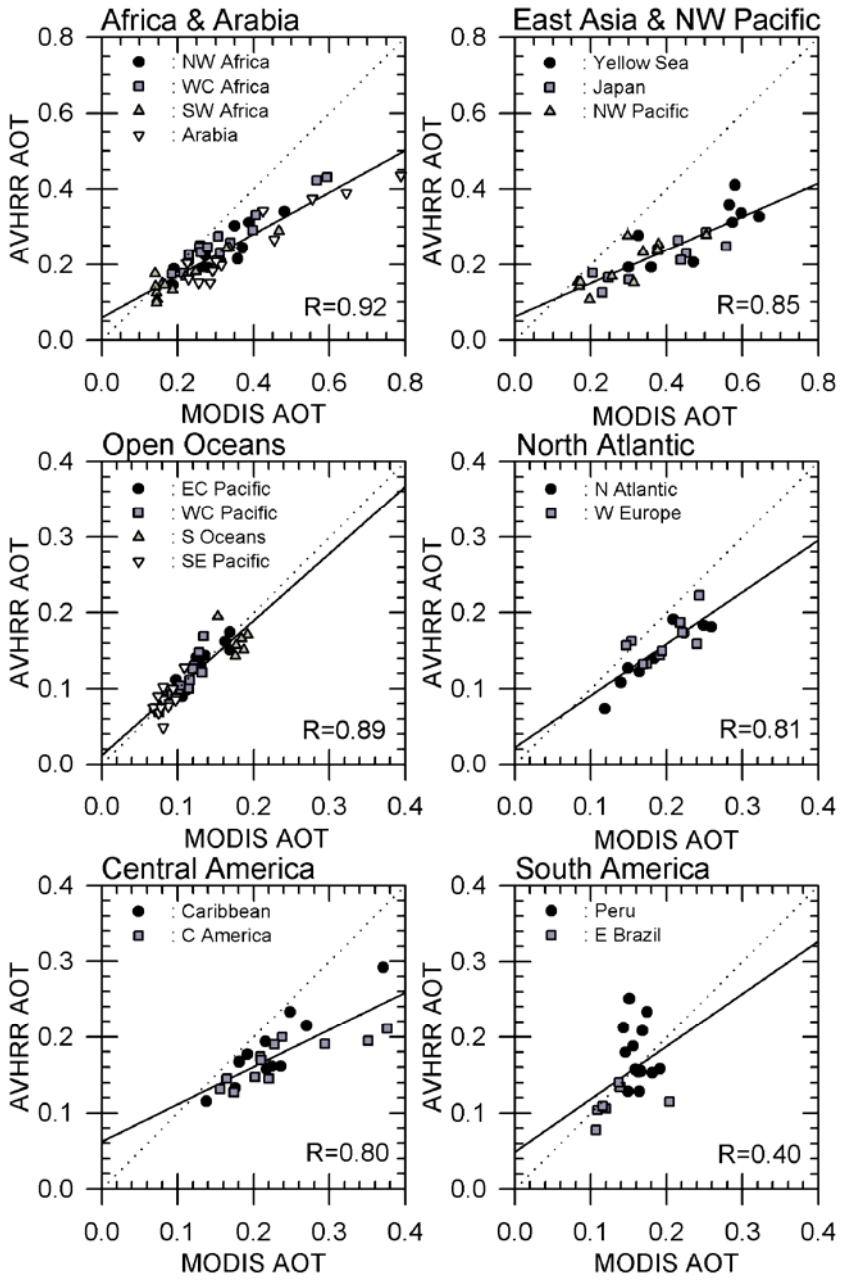

Fig 3.3. Comparison of co-located AVHRR and MODIS AOTs averaged over each region. Each symbol stands for areal average over the regions defined in Fig 3.2 for individual month. Black solid and dotted lines stand for linear fit curve and one-to-one line, respectively. Note some regions are named referring to the nearby continental locations, but they are all over oceans.

the impact of the aerosol size distribution and refractive indices defining the different aerosol models used by the MODIS and the AVHRR retrievals. The AVHRR retrieval algorithm adopts a modified power law size distribution (hereinafter referred to as the MP model) and a fixed refractive index. The MODIS algorithm employs a bi-modal log-normal size distribution (hereinafter, BL models). The two functions of aerosol size distribution have often been employed in aerosol retrievals from space (*Stowe et al.*, 1997; *Mishchenko et al.*, 1999; *Higurashi and Nakajima*, 1999; *Tanré et al.*, 1997). They are given as follows:

Modified power law:

$$n(r) = \begin{cases} C, & r \le r_1 \\ C \cdot (r / r_1)^{-\nu}, & r_1 < r \le r_2 \\ 0, & r > r_2 \end{cases} \tag{3.1}$$

where r_1=0.1 μm, r_2=10.0 μm, and the shaping factor, $\nu \in (2.5,5.0)$. C is a normalization constant chosen to satisfy the condition that

$$\int_0^\infty n(r)dr = 1.$$

Bi-modal log-normal:

$$n(r) = \frac{dN(r)}{dr} = \sum_{j=1}^{2} \frac{dN_j(r)}{dr} \tag{3.2}$$

$$\frac{dN_j(r)}{dr} = \frac{N_j}{(2\pi)^{1/2}\sigma 2.3r} \exp\{-\frac{(\log r - \log r_{m,j})^2}{2\sigma^2}\}$$

where N is the density number, r_m is median radius, and $\sigma^2 = \left\langle (\log r - \log r_m)^2 \right\rangle$.

The MODIS BL models are combinations of two individual log-normal size distributions with one of four small modes (denoted as S1-S4 in Table 3.1) and

Table 3.1. Aerosol models used in the experiment for testing the impacts of aerosol model selection. As for the MP models, 26 shaping factor (ν) values ranged from 2.5 through 5.0 with an interval of 0.1 were used in this study, but only six cases are shown in the table. Detailed description for BL models that are used by the MODIS aerosol retrieval algorithm can be found in Table 1a, b in Levy et al. (2003)'s paper.

MP model		Small (Sx) and Large (Bx) modes for BL model				
ν	r_{eff} (μm)	ID	m* (λ=0.47~086)	r_g (μm)	σ_g	r_{eff} (μm)
2.5	3.63	S1	1.45-0.0035i	0.07	0.40	0.10
3.0	2.01	S2	1.45-0.0035i	0.06	0.60	0.15
3.5	0.86	S3	1.40-0.0020i	0.08	0.60	0.20
4.0	0.37	S4	1.40-0.0020i	0.10	0.60	0.25
4.5	0.21	B5	1.45-0.0035i	0.40	0.60	0.98
5.0	0.15	B6	1.45-0.0035i	0.60	0.60	1.48
		B7	1.45-0.0035i	0.80	0.60	1.98
		B8	1.53-0.0030i (0.47μm) 1.53-0.0010i (0.55μm) 1.53-0.0000i (0.66μm) 1.53-0.0000i (0.86μm)	0.60	0.60	1.48
		B9	1.53-0.0030i (0.47μm) 1.53-0.0010i (0.55μm) 1.53-0.0000i (0.66μm) 1.53-0.0000i (0.86μm)	0.50	0.80	2.50

*m: refractive indices.
Note: Refractive indices for MP models are fixed as m=1.5-0.003i.

another out of five large modes (B5-B9). The refractive index for each model is also listed in the table. In addition to the choice of 20 combinations of small and large modes, the MODIS aerosol model also varies with a weighting factor between the small and large modes. In this study, 220 (= 20x11) cases are used by changing the weighting factor from 0 to 1 with an interval of 0.1. Likewise, simulations with the MP model assumed 26 values for the exponent of the size distribution (i.e., the shaping factor) ranging from 2.5 through 5.0 with an interval of 0.1. Mie calculations

were first conducted to generate the optical properties of each model aerosol and these were then fed into the SBDART radiative transfer model (*Ricchiazzi et al.*, 1998) to compute reflectance at the top of the atmosphere. The computational burden was lowered considerably by adopting an approximation proposed by *Wang and Gordon* (1994) that was also employed in the MODIS algorithm (*Tanré et al.*, 1997). The approximation treats radiance due to multiple scattering from two log-normal modes as a weighted average of radiances from each individual mode for the same optical thickness.

The ocean surface boundary condition was based on *Cox and Munk* (1954) with the wind speed set to 7 m/s, as was employed by both MODIS and AVHRR algorithms (*Geogdzhayev et al.*, 2002; *Levy et al.*, 2003). The standard mid-latitude summer atmosphere (*McClatchey et al.*, 1972) was assumed, together with exponentially decreasing aerosol number density with increasing altitude as was provided by 5S (*Tanré et al.*, 1990). Note that atmospheric profiles have little influence on the retrievals (*Mishchenko et al.*, 1999). Radiances were simulated for all possible satellite-sun geometries with the scattering angle varying from 90 to 180 degrees. To avoid sun glint, calculations for which the zenith angle of the reflected light is within a cone of 40 degrees from the direction of specular reflection for a flat surface were excluded as was done in both MODIS and AVHRR retrievals (*Mishchenko et al.*, 1999; *Tanré et al.*, 1997; *Levy et al.*, 2003). The AOT at 0.55 μm was allowed to change from 0.01 to 1.0. The AOTs associated with the MP models were matched with those from the BL models according to reflectances computed by the two models at the two nominal AVHRR wavelengths (0.63 μm and 0.83 μm). The

margin of match in reflectance was set to $1x10^{-4}$ which is a very high accuracy compared to the uncertainties in ISCCP channel 1 reflectance data (±0.01~0.02) (*Brest et al.*, 1997).

The overall comparison of matched AOTs simulated by the models is shown in Fig 3.4a. They exhibit very large discrepancies by up to a factor of two. This suggests that the selection of a particular aerosol model is an important factor influencing the retrieval of the AOT. However, its range of effect is still smaller than that of the observed differences between the MODIS and the AVHRR as is shown in Fig 3.4b. Since the two types of aerosol models differ in both size distribution and refractive index, a further attempt is made to separate the impact of the two factors by setting the refractive index of the BL models to the same value as the MP models (i.e., m=1.5-0.003i) but retaining the original size parameters. They are referred to as BL' models. Fig 3.4c presents the same scatter plot as in Fig 3.4a but compares the AOTs retrieved with the MP and BL' models. The scattering is almost as large as in Fig 3.4a but shows more systematic differences with the AOT from the MP model larger than that from the BL' model. This implies that the difference in size distribution functions contributes to the substantial discrepancies between the MODIS and the AVHRR AOTs. This finding underlines the importance of selecting the most appropriate aerosol size distribution function in the retrieval of the AOT. The biased distribution in Fig 3.4c and the more symmetric distribution in Fig 3.4a suggest that the refractive index has an opposite effect, which is reinforced by a comparison of the AOTs retrieved from the BL versus BL' models (Fig 3.4d). Since the two models have the same size distribution but different refractive indices, the resulting

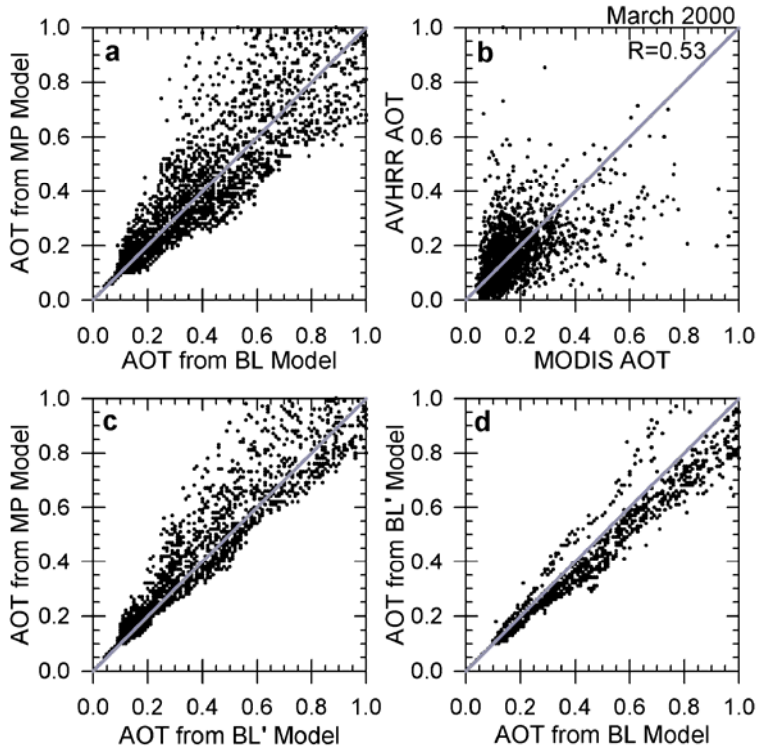

Fig 3.4. (a) Scatter plot of AOT from MP models versus that from BL models. (b) Scatter plot of observed AOT from MODIS and AVHRR (global, March 2000) (c) The same as Fig 3.4a but refractive index for BL models were replaced by a single fixed value (i.e., m=1.5-0.003i) as used in the MP models, which are referred to as BL' models. (d) Analogous to Fig 3.4a and Fig 3.4c except for BL' versus BL models. Gray solid line is one-to-one line.

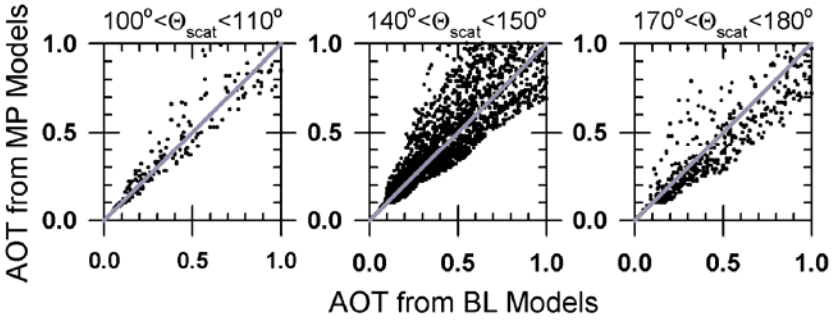

Fig 3.5. The same as Fig 3.4a, but scatter plots are presented separately for the scattering angles, 100-110°, 140-150°, and 170-180°.

differences reflect the sole effect of refractive index. The absolute difference is less than 0.2 for almost all the cases, but increases with increasing AOT within a difference range of $\pm 0.2\tau$. It should be noted that our simulation result indicates the bulk range of potential errors incurred by differences between the two aerosol models, implying that for fixed radiances, retrieval of AOT is very sensitive to the selection of aerosol models.

The comparisons shown in Fig 3.4 suggest that the aerosol size distribution is one of key factors responsible for the large random discrepancies in the AOT retrievals from the MODIS and the AVHRR, while both the size distribution and refractive index contribute to the systematic differences. Another hidden factor that is linked to the aerosol model difference is the scattering angle. Different aerosol models have different phase functions and the differences in phase function vary with the scattering angle. Fig 3.5 shows the comparisons of the AOT retrieved from the BL and MP models for three ranges of potential scattering angles: 100-110, 140-150, and 170-180 degrees. There are large differences of about the same sign and magnitude as seen in Fig 3.4a for both low and high angles. Note that the dominant scattering angle for both the AVHRR and the MODIS is centered around 140-150 degrees.

In Fig 3.6, all the data used in Fig 3.4a were grouped according to the exponent (i.e., the shaping factor; ν) of the MP model. The discrepancies in AOT between the MODIS and AVHRR products show a clear dependence on the shaping factor in the AVHRR algorithm. For example, for a small shaping factor (e.g, ν =2.5; large particles), the AVHRR AOT could to be larger than the MODIS AOT by up to a

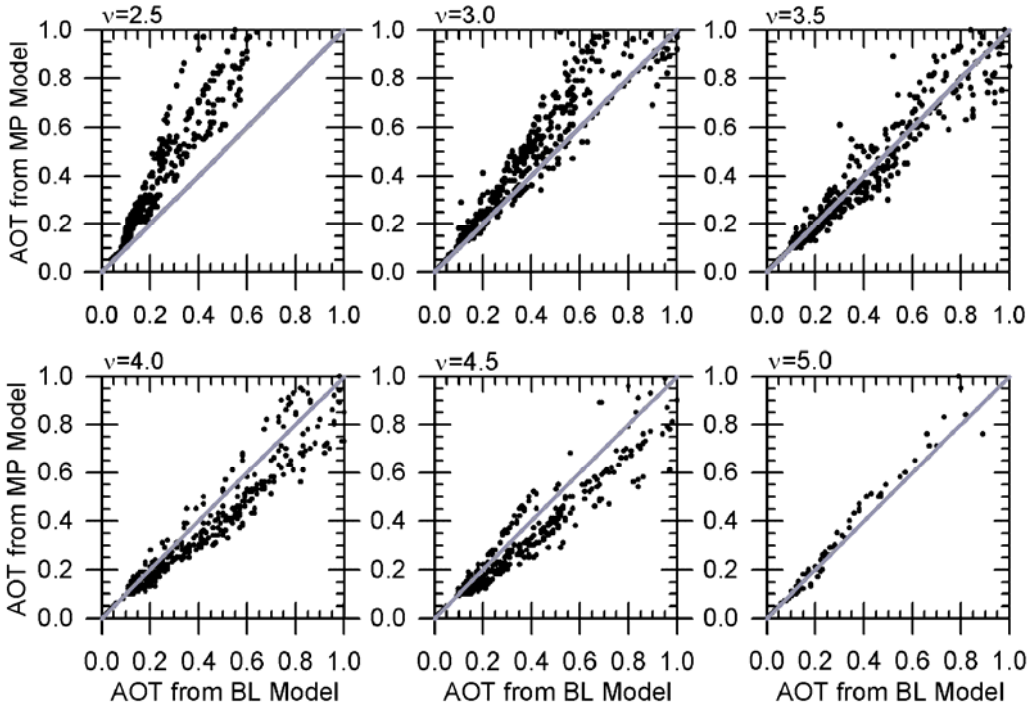

Fig 3.6. Same as Fig 3.4a, but the scatter diagrams are plotted according to the exponent (i.e., the shaping factor) of the MP models.

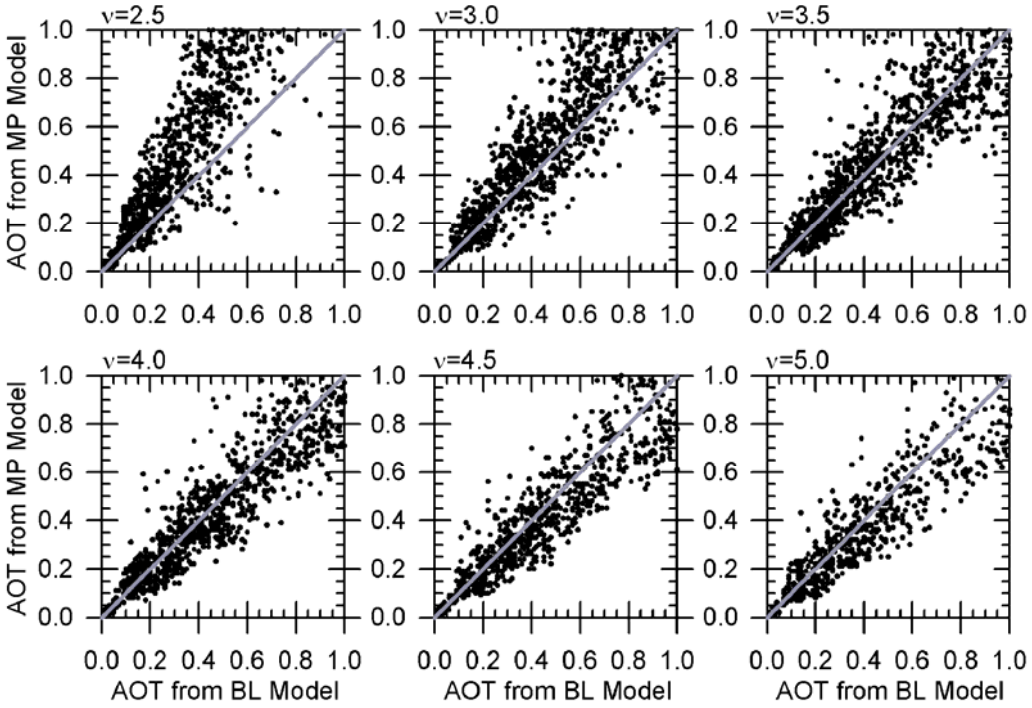

Fig 3.7. The same as Fig 3.6, but with a permitted reflectance error of 10^{-2}.

factor of two. On the other hand, for a larger shaping factor (e.g., ν=5.0; small particles), the two agree well with each other. Assuming ν ranged from 2.5 to 3.0 for sea-salt, 3.0~3.5 for dust, 4.0~4.5 for biomass burning, and 4.5~5.0 for sulfate/pollution (cf. Fig 7 of *Mishchenko et al.*, 1999), we may make some interesting inferences with reference to Fig 3.3. First, for the dust regimes such as NW Africa and Arabia, the AVHRR AOT (i.e., AOT from MP model) is expected to be higher than the MODIS AOT (AOT from BL model) according to our simulation, while the observations show an opposite result. Second, for East Asia and NW Pacific regions where pollution is known to be dominant, our simulation suggests the MODIS AOT should be slightly higher or about the same as the AVHRR AOT. There is a weak agreement with the observations. Third, for open ocean regions such as EC Pacific and S Oceans where sea-salt is presumably dominant, the observations reveal good agreements between the two AOTs, contrary to the simulation result suggesting higher AVHRR AOT than the MODIS AOT. We may thus infer that the difference in cloud screening might be a more significant factor than the aerosol model difference. It is almost certain that the lower AVHRR AOT values over heavy dust regions result from the ceiling of the AVHRR AOT product, which most likely exceeds the effects of aerosol model difference. For East Asia and NW Pacific, both effects render higher MODIS AOT than the AVHRR AOT. Good agreements in the open oceans may be explained by the compensation of the two offsetting effects.

Another important factor is the radiometric uncertainty in AVHRR measurements. To evaluate this effect, we performed the same simulation but permitting larger reflectance errors of 10^{-2}, which corresponds to the level of the

radiometric uncertainties of ISCCP data (*Brest et al.*, 1997). The results are presented in Fig 3.7. For each shaping factor group, the ranges of discrepancies are larger than those found in Fig 3.6, as one would expect. However, the overall ranges of the AOT discrepancies remain virtually the same, if the points from all the panels were put together. We may, therefore, conclude that the radiometric uncertainties in the AVHRR affect more significantly the selection of aerosol models (i.e., size or α) than the retrieval of AOT. It is thus unlikely to explain the systematic differences between the MODIS and GACP/AVHRR AOTs, unless there were biases due to radiometric calibration that are much larger than those reported by *Brest et al.* (1997).

3.4. Ångström Exponent (α)

3.4.1. Evaluation and Comparison of GACP/AVHRR and MODIS α

The global distributions of the Ångström exponent (α) derived from MODIS and AVHRR shows more substantially different features than those of the AOT (Fig 3.8). First, individual monthly α from AVHRR (α_{AVHRR}) is much more noisier than that from MODIS (α_{MODIS}). The α_{MODIS} is large near the coasts, and decreases toward the ocean interior. This trend of variation is far less clear for α_{AVHRR} due to its noisy distribution pattern. In a similar manner for the regional characteristics, α_{MODIS} is smaller (0.4-0.6) in NW Africa and larger (~1.2) in SW Africa. For α_{AVHRR}, the general trend is somewhat similar but much less obvious. As such, the difference ($\Delta\alpha_{MA} = \alpha_{MODIS} - \alpha_{AVHRR}$) map (bottom panel in Fig 3.8) shows structured patterns:

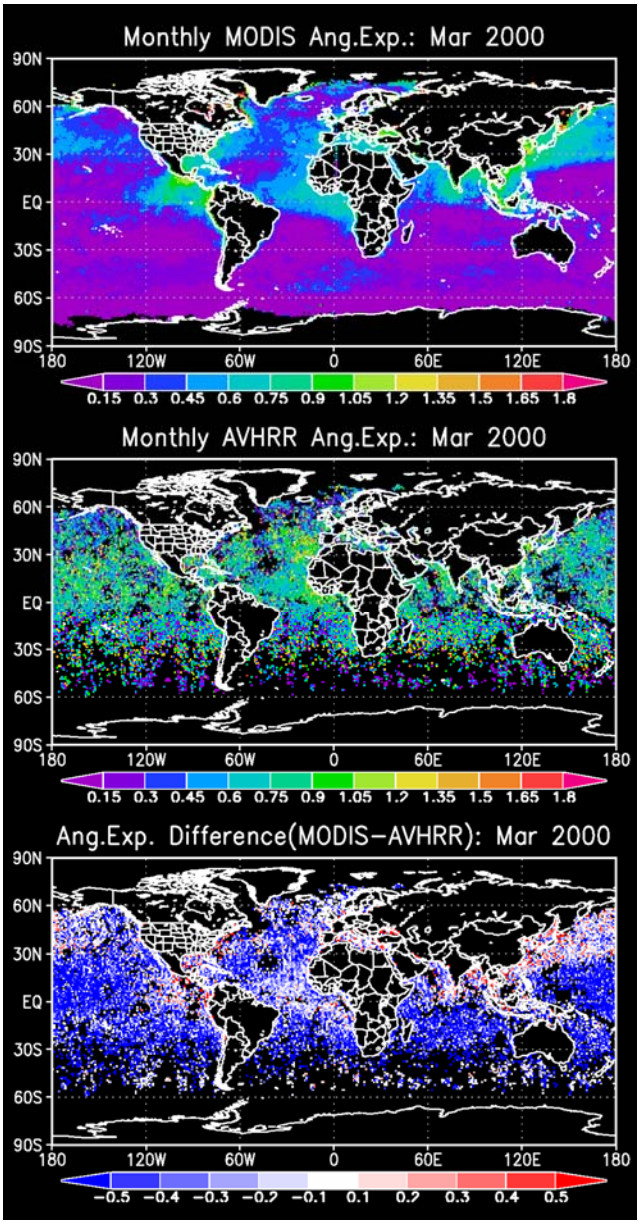

Fig 3.8. Monthly distributions (March 2000) of MODIS (upper panel) and AVHRR (middle) Ångström exponent, and their difference (MODIS minus AVHRR; bottom).

large positive $\Delta\alpha_{MA}$ along the coastlines and regions dominated by smaller particles (e.g., NW Pacific, and C America), large negative $\Delta\alpha_{MA}$ over the open oceans where the AOT is small (<0.2), and small $|\Delta\alpha_{MA}|$ over NW/WC Africa, where the AOT is large. A large uncertainty exists in the estimates of α for small AOT (<0.2) (*Ignatov et al.*, 1998; *Higurashi and Nakajima*, 1999), which may explain the large discrepancies found over open oceans.

After averaging over a long period (about 13 years), the distribution of α_{AVHRR} (c.f. Fig 2.1 in Chapter 2) are much more similar to α_{MODIS}, but the magnitudes and dynamic ranges of the two still differ significantly. Likewise, the regional averages of α_{AVHRR} are better correlated with those of α_{MODIS}, although the correlation coefficients are not high, as is shown in Fig 3.9 for the 17 regions defined in Fig 3.2. This is in contrast to the generally high correlations between AOTs derived from MODIS and AVHRR over the same regions as is shown in Fig 3.3. In general, α_{AVHRR} shows a considerably narrower dynamic range of variation than that of α_{MODIS}. Regions of low correlation in α correspond to low AOT.

The quality of the satellite-based estimates of α can be evaluated by plotting it as a function of the AOT for the four aerosol regions. As is shown by *Eck et al.* (1999) using AERONET measurements, this kind of plot shows unique relationships for different types of aerosols. For instance, for biomass burning aerosols, α should increase with AOT. As the AOT increases, the proportion of smoke aerosols grows larger. Since smoke aerosol particle size is small, it leads to larger α. The expected positive correlation between the AOT and α, or negative correlation between the AOT

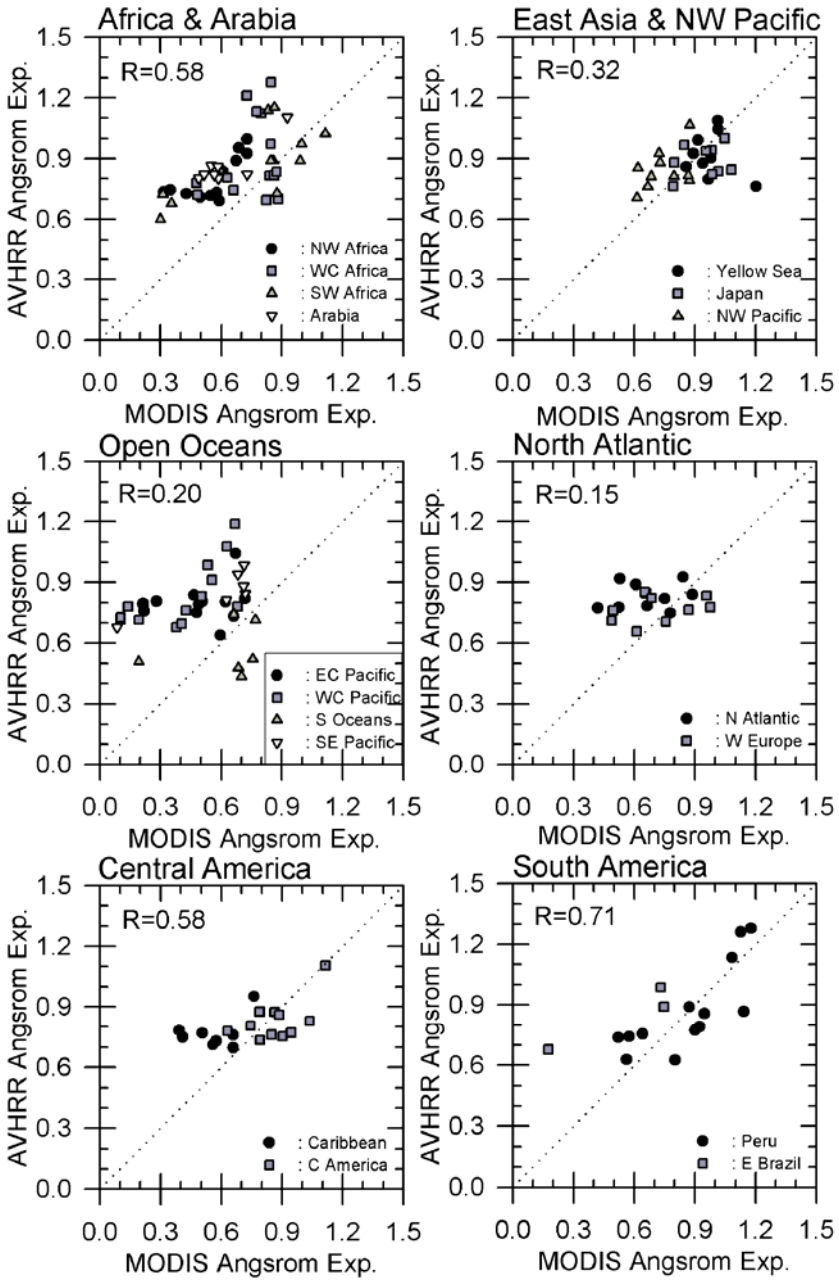

Fig 3.9. Comparison of co-located AVHRR and MODIS Ångström exponent averaged over each region. Dotted lines stand for one-to-one line.

and the particle size, is clearly seen in Fig 3.10 over the West Central and South African regions. Similar results were obtained by *Reid et al.* (1999) from *in situ* airborne measurements during the Smoke/Sulfates, Clouds and Radiation – Brazil campaign (*Kaufman et al.*, 1998). By the same token, one would expect to see a good correlation, but of opposite sign, between α and the AOT for dust aerosols since dust particles are larger in size than the background aerosols. Such a trend is not observed over the ocean off NW Africa and the Arabian Sea, where dust plays a dominant role; α tends to be constant around 0.4-0.6, although the data points are tightly clustered together. This may be explained by the fact that given the distance of these bodies of water from the source of dust generation, the gigantic dust particles lifted by strong dust storms have time to wash out of the atmosphere due to gravitational settling. As a result, the size of transported dusts is rather constant so that α is invariant with the AOT. This invariance in dust particle size has been reported by *Maring et al.* (2003) in their aircraft measurements of dust particles over the Canary Islands and Puerto Rico. It is interesting to note that the signals of biomass burning, dust and their mixture from MODIS data co-exist over the WC African region. In contrast, similar plots for AVHRR-retrieved AOT and α are all widely scattered without showing any of the above features.

The large uncertainties in the estimates of α_{AVHRR} warrants much caution when using it to address climate issues such as aerosol indirect effects. It is our belief that the monthly values of α_{AVHRR} contain so much uncertainty that it is of limited utility for climate studies, while the long-term and/or regional means contain certain useful information. The uncertainty may originate from calibration errors at the two

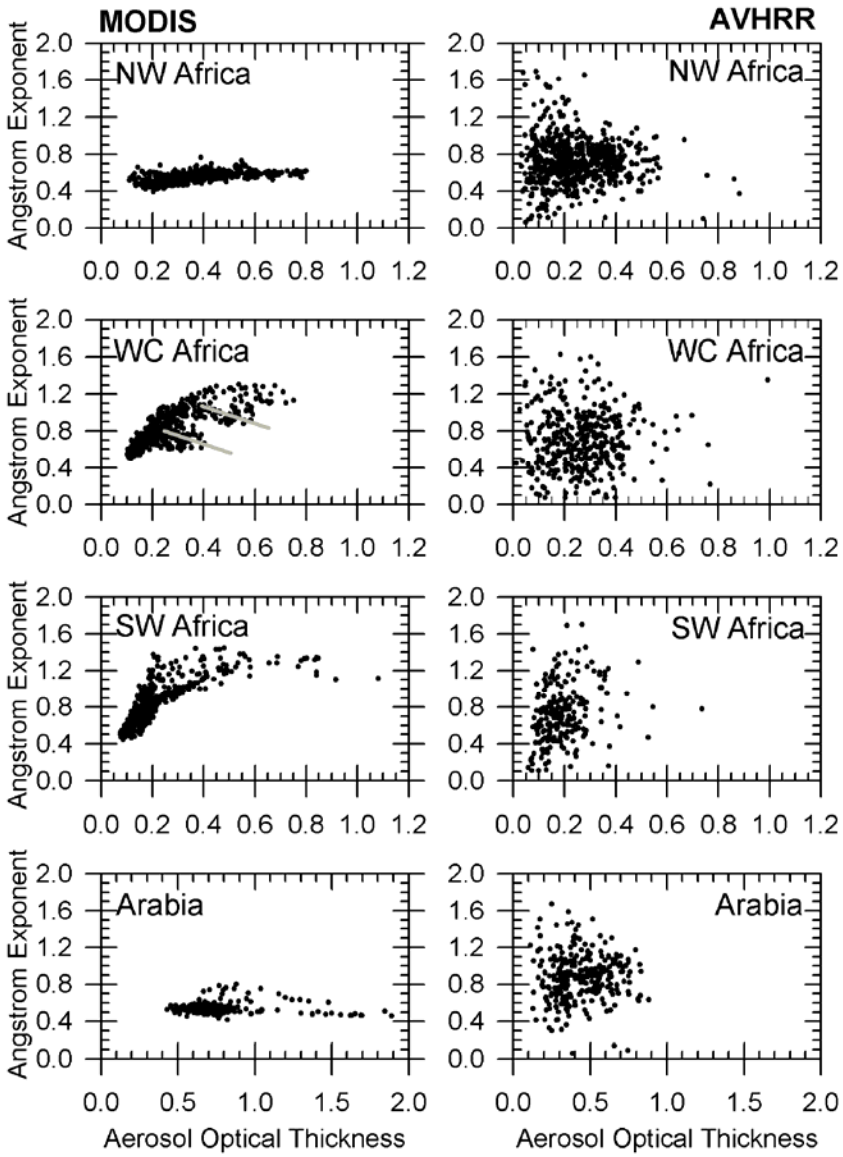

Fig 3.10. Scatter plots of Ångström exponent versus AOT. Left panels are based on MODIS data while the right panels are from AVHRR data for the same period (July, 2000). Gray lines provided in the WC Africa region for MODIS indicate possible signals from dusts co-existing with biomass burning aerosols in this region.

channels of AVHRR and/or errors related to the retrieval algorithm. As pointed out in other studies (*Ignatov et al.*, 1998; *Higurashi and Nakajima*, 1999), α is very sensitive to errors in the spectral AOTs, especially for small AOT values. Relative to α_{MODIS}, α_{AVHRR} is noisy even for higher AOT (>0.4). In the following discussions, we investigate the impact of various factors on estimates of α, especially the aerosol size distribution, optical properties, and selection of wavelength pairs from which α is derived.

3.4.2. Factors Influencing α and its Discrepancies between MODIS and GACP/AVHRR

To investigate the impact of aerosol model differences between MODIS and AVHRR aerosol retrieval algorithms, α is calculated based on the BL and MP models, respectively, following the work described in section 3.2. Differences in the pair of channels used to derive α are taken into account so that α from the MP models (α_{MP}) is derived from the AOTs at 0.63 μm and 0.83 μm while α from the BL models (α_{BL}) is derived from the AOTs at 0.55 μm and 0.87 μm. A comparison of α_{BL} as a function of α_{MP} is plotted in Fig 3.11. The discrepancies between α_{MP} and α_{BL} are fairly large (~0.5), almost comparable to the observed differences, suggesting that the impact of the aerosol model differences could potentially explain a good portion of the observed discrepancies in magnitude but not necessarily in its spatial distribution pattern.

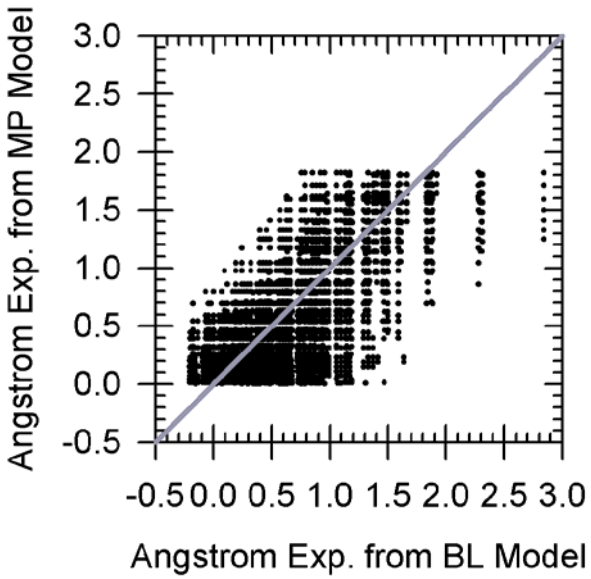

Fig 3.11. Same as Fig 3.4a except for Ångström exponent.

Since the observed discrepancies stem partially from the use of different wavelength pairs, the effect of wavelength selection is studied first. Typically, α is computed by

$$\alpha = -\ln(\tau^a_{\lambda 1} / \tau^a_{\lambda 2}) / \ln(\lambda_1 / \lambda_2) \tag{3.3}$$

or more generally,

$$\alpha = -\frac{d \ln C_{ext,\lambda}}{d \ln \lambda} \tag{3.4}$$

where $C_{ext,\lambda}$ is the spectral extinction cross-section. The α can be computed from the AOT (τ^a_λ) measured at two wavelengths or by means of regression of the AOTs measured at several wavelengths. The wavelengths chosen do not include the absorption bands due to ozone, water vapor and other absorbing gases. Also, whether the selected wavelengths can resolve the particle size of interest is taken into

consideration. Measurements at different spectral regions have been employed including the visible (0.4-0.7 μm), near-infrared (around 0.87 μm, excluding water vapor absorption bands), and/or UV-A (0.34-0.38 μm) (*Iqbal*, 1983; *Holben et al.*, 1998; *Kinne et al.*, 2001). Here, four pairs of wavelengths are considered: 0.66-0.87 μm, 0.55-0.87 μm, 0.47-0.66 μm, and 0.47-0.55 μm, which comprise the nominal wavelengths of the MODIS and AVHRR channels. The following pairs are actually used to derive α: 0.55-0.87 μm for MODIS ocean, 0.47-0.66 μm for MODIS land, and 0.66-0.87 μm for AVHRR. In addition, α is also derived from regression of the AOTs at all four wavelengths (i.e., 0.47, 0.55, 0.66, and 0.87 μm). Since α derived from the MP model is not sensitive to the selection of wavelength, the study is limited to BL models.

Fig 3.12 shows the comparisons of the Ångström exponents computed from the four wavelength pairs. The Ångström exponents simulated for the MODIS ocean algorithm is plotted as X-axis, and the remainders are shown in Y-axis, one of which is for AVHRR simulation. It is seen that the discrepancies resulting solely from the wavelength differences between MODIS and AVHRR are rather insignificant (<0.1). However, possible errors in spectral radiance measurements and an inconsistent estimation of the spectral AOT can cause much larger differences, especially when the signs of the errors for different wavelengths are opposite to each other (*Ignatov et al.*, 1998; *Ignatov and Stowe*, 2000). The best accuracy in current satellite-based AOT estimations is expected to be $\pm 0.05\,\tau \pm 0.03$ (for MODIS, *Remer et al.* (2002)). As shown in Fig 3.12, such AOT errors can cause very large errors in α (up to ±0.5). In this sense, a regression solution of α using several wavelengths, if available, is an

effective means of suppressing this kind of error. As is also shown in the Fig 3.12, α from the regression is less vulnerable to errors in individual channels.

A major utility of the Ångström exponent is to infer basic information about aerosol particle size (*Holben et al.*, 1991; *O'Neill and Royer*, 1993; *Nakajima and Higurashi*, 1998; *Eck et al.*, 1999). While qualitative information pertaining to aerosol particle size may be readily gained from α, quantitative estimation of the aerosol effective radius (r_{eff}) from α would be much more cumbersome due in part to the strong dependence of the relationship between r_{eff} and α on the selection of aerosol size distribution, as is shown in Fig 3.13. The relationships were obtained for various BL and MP models with fixed complex refractive index (m=1.5-0.003i). The BL models are from 20 different combinations of small and large modes, and one MP model with varying shaping factor. α is calculated for the wavelength pair of 0.55-0.87 μm. It is seen that corresponding to a fixed value of α is a wide range of r_{eff} that depends on the aerosol size distribution. The family of BL curves differs considerably among themselves, and even more from the MP curve, especially for low values of α (say, α <0.5). This implies that for large particles α can be related to drastically different values of r_{eff} simply by assuming different size distribution models, posing a major difficulty in obtaining aerosol particle size.

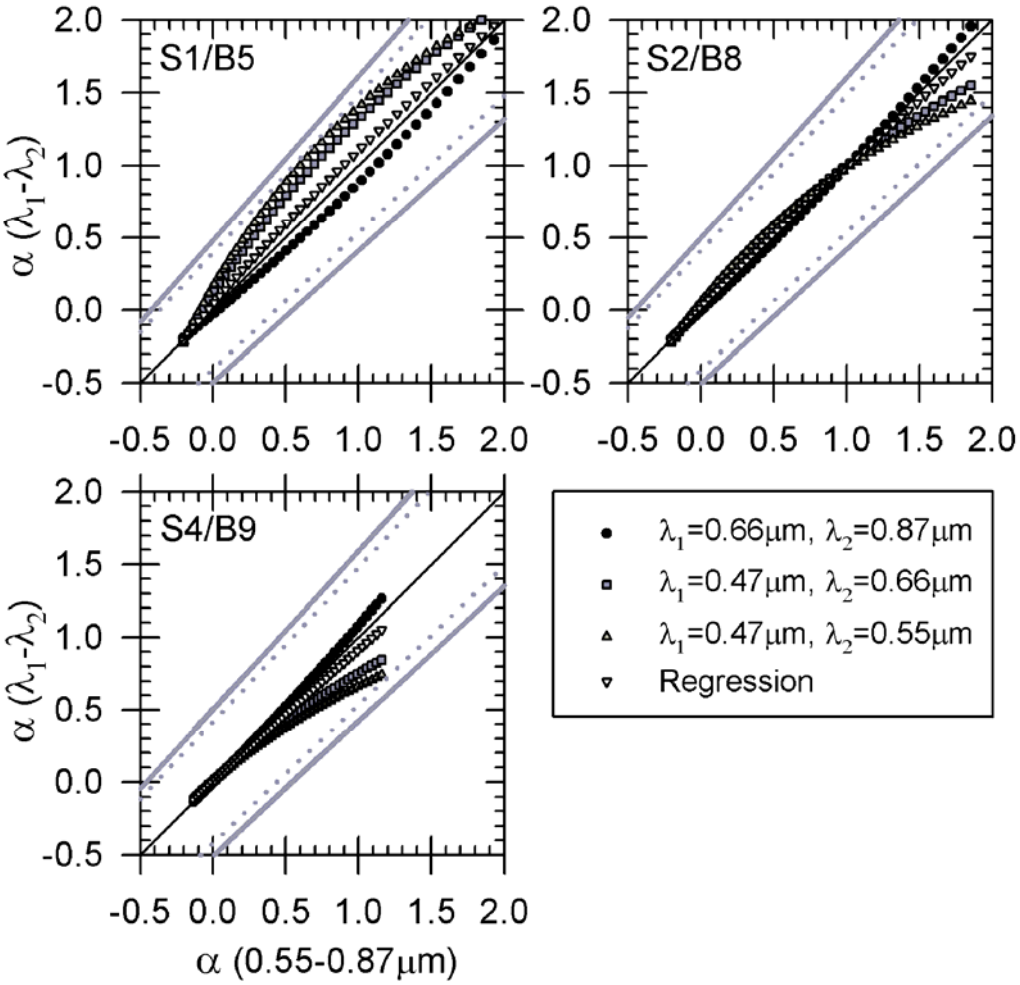

Fig 3.12. Influence of wavelength selection on Ångström exponent for three different BL models (S2/B8, S1/B5, and S4/B9; counter-clock-wise from the upper-right panel). Ångström exponent was calculated for several combinations of two wavelengths from Eq. (3.3). Regression solution is calculated via linear regression for the four wavelengths (0.47, 0.55, 0.66, and 0.87μm) in logτ-logλ space. Thick gray solid lines represent marginal errors of Ångström exponent due to spectral AOT errors of $\pm 0.05\,\tau \pm 0.03$ for the wavelength pair of 0.55 and 0.87μm while gray dotted lines are those for regression solution from AOTs at the four wavelengths. Thin solid line is one-to-one line.

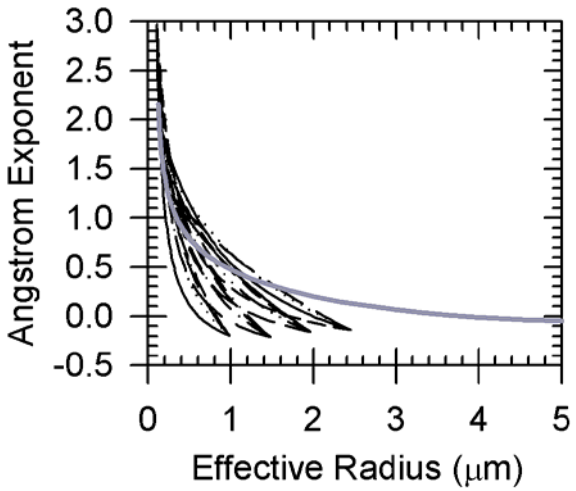

Fig 3.13. Ångström exponent versus effective radius for modified power size distributions (thick gray line) and for various combinations of bi-modal size distributions (thin lines with various types). Each line stands for different combinations of small and large modes that compose bi-modal log-normal size distributions.

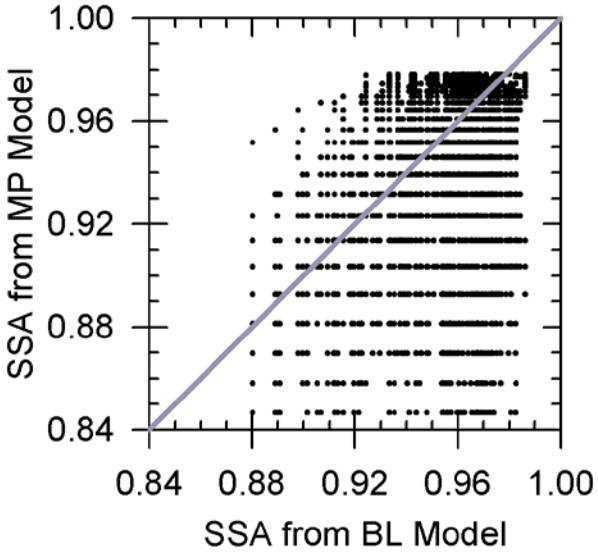

Fig 3.14. Same as Fig 3.4a except for single scattering albedo (SSA).

In addition to aerosol size distributions, aerosol absorption is another major factor influencing the retrieval of the AOT. Since the two types of aerosol models employed in MODIS and AVHRR retrievals differ in refractive index as well as in the size distribution, the resulting differences in single-scattering albedo (SSA) also contribute to discrepancies in AOT retrievals. Fig 3.14 shows a comparison of the SSA computed from the two aerosol models that generate the same reflectances. The SSA from the MP model is dependent only on aerosol size (shaping factor or α) when the refractive index is fixed so that significant errors are expected for large non-absorbing (at visible and near-infrared) aerosols (e.g., dust), and for small absorbing aerosols (e.g., smoke) (*Mishchenko et al.*, 2003). The contradicting finding that the AVHRR AOT is significantly lower than that from MODIS for the Saharan region implies that the AOT for dust is severely underestimated by the AVHRR (*Haywood et al.*, 2001). This is most likely caused by misclassification of aerosol scenes as clouds. While, in general, good AOT retrieval accuracies were reported for non-dust aerosols retrieved from MODIS (Remer et al., 2002), the AOT underestimation for some smoke events was attributed to slightly higher SSA for smoke assumed in MODIS algorithm (*Ichoku et al.*, 2003).

3.5. Summary

In light of large discrepancies among various satellite-based global aerosol products, two prominent monthly global aerosol products retrieved from GACP/AVHRR (*Mishchenko et al.*, 1999) and MODIS (*Tanré et al.*, 1997) measurements are compared and factors leading to their discrepancies are explored.

Comparisons of the monthly aerosol optical thickness (AOT) at 1x1 degree resolution showed substantial scattering and moderate systematic differences. However, their regional means (also long-term means) are much better correlated with the general tendency that the AVHRR values are smaller than the MODIS values, especially for heavy aerosol loadings. Difference in the cloud screening is likely a factor (*Myhre et al.*, 2004), but other factors can also come into play, for example, use of different aerosol models differentiated in size distribution function and refractive index.

The MODIS retrieval algorithm employs 20 combinations of aerosol size distributions given by bi-log-normal (BL) functions with variable refractive index. The GACP/AVHRR algorithm used a modified power (MP) law size distribution with a fixed refractive index. Extensive model simulations were conducted to investigate the impact of the differences in the size distribution function and the refractive index on the AOT discrepancies. It is found that the difference in the size distribution function can bring about substantial AOT discrepancies of up to a factor of 2, while different refractive indices cause a moderate systematic difference. The discrepancies depend on the similarity in aerosol size modes selected by the two algorithms. More drastic underestimations of AOT by the GACP/AVHRR relative to the MODIS is more likely induced by the differences in cloud screening including misclassification of heavy aerosols as clouds in the GACP/AVHRR product. Thus, more attention should be paid to aerosol size distributions in addition to refractive index and cloud screening. The noisiness of the GACP/AVHRR aerosol retrievals is partially affected by the radiometric uncertainty of the AVHRR radiances, but it is

unlikely to explain the large systematic discrepancies between the MODIS and GACP/AVHRR AOTs.

Larger discrepancies exist in the Ångström exponent (α) derived from the MODIS and the GACP/AVHRR. The GACP/AVHRR retrievals seem to suffer from random-like errors with low signal-to-noise ratio. In comparison, the MODIS α product is of better quality in terms of spatial variation and its correlation with the AOT. We attempted to understand the discrepancies between α derived from the MODIS and the AVHRR by modeling the effects of aerosol size distribution function, wavelength selection, and refractive indices on α retrieval. While errors in the α retrieval originate from numerous sources (e.g., selection of different wavelength pairs can cause a difference in α of up to 0.5), our model simulations also point to a big contribution by different aerosol models used in the AVHRR and MODIS retrieval algorithms. The influence of aerosol size distribution on the estimation of aerosol effective radius from α is also evaluated. For a given α, the corresponding aerosol effective radii may differ by more than 1 μm among the various size distribution functions.

Chapter 4: Effect of Relative Humidity on Aerosol Optical Thickness

4.1. Introduction

Aerosol optical thickness (AOT) is a vertically integrated (column) quantity whose magnitude depends on aerosol mass loading, scattering and absorption efficiencies, that are further linked with aerosol size distribution and composition. In addition to these inherent properties, AOT also varies with ambient humidity. There have been numerous investigations concerning the relationship between relative humidity (RH) and aerosol light scattering. These include theoretical investigations (e.g., Kasten, 1969; Hänel, 1976; Hegg et al., 1993; Tang, 1996; Li et al., 2001) and field experiments conducted using instruments on the aircrafts as well as on the surface (e.g., Charlson et al., 1984; Rood et al., 1987; Kotchenruther and Hobbs, 1998; Li-Jones et al., 1998; Kotchenruther et al., 1999; Gasso et al., 2000).

The hygroscopic property of aerosols is represented by the aerosol humidification factor (AHF), which is defined as the ratio of the aerosol scattering coefficient at a high humidity (RH; ~85%) or an ambient RH to the aerosol scattering coefficient at a low RH (~40%) (Covert et al., 1972; Rood et al., 1987; Hegg et al., 1996). The AHF is normally measured using an integrating nephelometer (e.g., Charlson et al., 1991; Li-Jones et al., 1998; Kotchenruther et al., 1999; Gasso et al., 2000) and was also estimated from a lidar-derived aerosol scattering profile together with a RH profile under the special condition of a well-mixed boundary layer capped by stratiform clouds (Feingold and Morley, 2003).

To date, some studies investigated the influence of humidity on the AOT (e.g., Hegg et al., 1997; Öström and Noone, 2000) by apportioning the observed AOT among various contributing factors. However, those studies are based on the measurements made for short time periods, reporting the range of contribution of humidity effects. It is necessary to study the behavior of AOT in response to changes in humidity variables throughout the atmospheric column using data sets incorporating the simultaneous vertical distributions of humidity and aerosols together.

Quantifying the humidification effects of aerosols has important implications. For example, the correlation between AOT and cloud fraction has been reported (Ignatov and Nalli, 2002; Kaufman et al, 2005; Jeong and Li, 2005), and there have been arguments as to whether it is cloud contamination or the aerosol humidification effect (AHE). It is important to know the contribution of the AHE to the AOT and to quantify and eliminate any artifact due to cloud contamination (including enhanced scattering by clouds) in order to obtain true aerosol information.

An observational study of the aerosol indirect effect (AIE) requires information about the AHE. AOT or aerosol extinction coefficients have been used as a proxy for cloud condensation nuclei (CCN) in AIE studies (Kaufman and Nakajima, 1993; Nakajima et al., 2001; Bréon et al., 2002; Feingold et al., 2003). However, AOT might not be a good proxy for CCN (e.g., Feingold, 2003), since AOT is a vertically integrated quantity and depends not only on the number of particles, but also on humidity, size distribution, etc. Some efforts were made (Nakajima et al., 2001; Bréon et al., 2002) to reduce the uncertainty of using AOT as a proxy for CCN

by considering the effects of aerosol size. However, little consideration has been given to account for the AHE, which has the potential to influence the AOT.

This study attempts to quantify the effect of aerosol humidification on the AOT derived from the in-situ airborne aerosol profile measurements taken over the Central Facility (CF) site in the Southern Great Plains (SGP). In section 4.2, the data and the methodology used in this study are described. The column AHF for AOT is defined in section 4.2 and its relationship with humidity variables is presented in section 4.3. Several methods to estimate the column AHF are introduced and compared in section 4.4. Then, the sensitivity of the AHF to a very humid atmospheric layer is tested in section 4.5. Summary and concluding remarks are provided in section 4.6.

4.2. Data and Methodology

The primary source of data came from measurements taken during In-situ Aerosol Profiling (IAP) flights made under the aegis of the Department of Energy's Atmospheric Radiation Measurement (ARM) Program. A light aircraft (Cessna C-172N) flew at nine level legs between 0.5 km and 4 km above the ground level over the SGP site, collecting aerosol data every second and flying (Table 4.1).

Table 4.1. Typical altitudes of observations made during the In-situ Aerosol Profiling flights.

Level-leg ID	Altitude	Level-leg ID	Altitude
1	3.6km	6	1.2km
2	3.1km	7	0.9km
3	2.4km	8	0.6km
4	1.8km	9	0.5km
5	1.5km	10*	5m

*: The data are actually taken from the Aerosol Observation System at the surface.

The measurements include scattering and absorption due to aerosols. The aerosol scattering is measured using nephelometers (Model TSI 3563; TSI Inc., Minneapolis, Minnesota), and aerosol absorption is obtained using a particle soot absorption photometer (PSAP; Radiance Research, Seattle, Washington). Measurements of the scattering coefficients at blue (450 nm), green (550 nm) and red (700 nm) channels under low (RH~40%) and high (RH~80%) humidity conditions were taken, as well as measurements of the absorption coefficients at a green channel with RH~40%, the ambient RH, and temperature/pressure profiles. Detailed information about the measurement uncertainty and experiment is documented by Anderson and Ogren (1998) and Andrews et al. (2004), respectively.

It is well known that aerosol scattering depends on the relative humidity (RH) (e.g., Hänel, 1976; Hegg et al., 1993). The humidity dependence may be expressed as (e.g., Hänel, 1976; Remer et al., 1997):

$$\frac{k_{sca}^{a}(RH_1)}{k_{sca}^{a}(RH_2)} = \left(\frac{1-RH_1}{1-RH_2}\right)^{-\gamma} \tag{4.1}$$

where $k_{sca}^{a}(RH)$ represents the aerosol scattering coefficient at a certain RH and γ is a constant that can be determined empirically. If measurements are available at different humidity levels, the dependence of aerosol scattering on RH can be fitted to an analytic function with 2-3 or more parameters determined from the measured aerosol scattering coefficients and RH (e.g., Hänel, 1976; Kotchenruther and Hobbs, 1998; Kotchenruther et al., 1999). This study uses a two-parameter fitting since the measurements are only available at two different humidity levels (low and high). The aerosol humidification factor, f(RH), can be defined as follows:

$$f(RH) \equiv \frac{k_{sca}^{a}(RH)}{k_{sca}^{a}(40\%)} \tag{4.2}$$

A two-parameter function has been widely used to describe the RH-dependence of aerosol scattering coefficient (e.g., Kasten, 1969; Hänel, 1976; Kotchenruther et al., 1999; Andrews et al., 2004):

$$f(RH) = a \cdot \left(1 - \frac{RH(\%)}{100}\right)^{-b} \tag{4.3}$$

where a and b are the parameters to be determined from the scattering coefficients measured at low and high RHs. One may then estimate the scattering coefficients of aerosols under any humidity using Eq. (4.3). f(RH) is dependent not only on RH but also on the chemical and optical properties of aerosols. The latter dependence can be determined using measurements at fixed two specific humidity levels (generally, 40% and 85%), i.e.,

$$f(85\%) \equiv \frac{k_{sca}^{a}(85\%)}{k_{sca}^{a}(40\%)}. \tag{4.4}$$

f(85%) is dictated by the chemical and optical properties of the aerosols.

f(RH) may also be given in terms of aerosol total extinction which is the sum of scattering and absorption coefficients:

$$k_{ext}^{a}(RH) = k_{sca}^{a}(RH) + k_{abs}^{a}. \quad (4.5)$$

Since the humidity dependence of aerosol absorption is mostly unknown (Andrews et al., 2004), no attempt to correct for the humidity effect on the absorption is made in this study. The nephelometers aboard the IAP aircraft measure only sub-micron-sized (i.e., particle diameter, Dp<1.0 μm) aerosols. However, super-micron-sized aerosols sometimes become important so that a correction for super-micron aerosols is necessary in order to have the AHE applicable to general measurements of AERONET and MODIS that are sensitive to all sizes of aerosol particles. This study follows the method proposed by Andrews et al. (2004) for this correction. Surface measurements made by the Aerosol Observing System (AOS) are employed, which have similar instrumentation (Sheridan et al., 2001) as the IAP aircraft on-board instruments. In brief, the IAP scattering (and absorption) coefficients for Dp<1 μm was adjusted to represent those for Dp<10 μm by taking the ratios between scattering (and absorption) coefficients for Dp<1 μm and Dp<10 μm from the AOS operating at the surface.

Since we are interested in a column quantity, the profiles of aerosol extinction coefficients are integrated using a simple trapezoidal scheme. One of the important problems in calculating AOT by integrating aircraft measurements is that aerosols tend to populate at low levels, mostly below the lowest flight level. In such cases, they are not real representation of the atmospheric column. Therefore, we combined

measurements from the AOS at the surface with the IAP measurements for the AOT calculation.

Scattering coefficients at three different humidity conditions (RH=40%, 85%, and ambient RH, RH) were computed before and after the super-micron aerosol correction, separately. We define scattering AOT at different RH levels – $\tau_{sca}^{IAP}(40\%)$, $\tau_{sca}^{IAP}(85\%)$, and $\tau_{sca}^{IAP}(RH)$ - as follows:

$$\tau_{sca}^{IAP}(40\%) = \int_{z1}^{z2} k_{sca}^{a}(40\%, z)dz \tag{4.6}$$

$$\tau_{sca}^{IAP}(85\%) = \int_{z1}^{z2} k_{sca}^{a}(85\%, z)dz \tag{4.7}$$

$$\tau_{sca}^{IAP}(RH) = \int_{z1}^{z2} k_{sca}^{a}(RH, z)dz \tag{4.8}$$

where z_1 is the altitude of the AOS measurement and z_2 is the highest altitude at which the IAP measurements were made. Likewise, the absorption and extinction AOTs (i.e., τ_{abs}^{IAP}, $\tau_{ext}^{IAP}(40\%)$, $\tau_{ext}^{IAP}(85\%)$, and $\tau_{ext}^{IAP}(RH)$) at different RH levels can be calculated following similar integration. RH values representing the column of interest are necessary in order to relate RH to the derived AOT, so we define a column-mean RH as:

$$< wRH >\equiv \int_{z1}^{z2} k_{ext}^{a}(RH, z) \cdot RH(z)dz / \int_{z1}^{z2} k_{ext}^{a}(RH, z)dz \tag{4.9}$$

which is an aerosol extinction weighted column mean RH (<wRH>). In case an aerosol extinction profile is unavailable, an arithmetic column mean RH (<RH>) might be used instead:

$$< RH >\equiv \int_{z1}^{z2} RH(z)dz / \int_{z1}^{z2} dz \quad . \tag{4.10}$$

to see if there is any statistical relationship with AHE. Or, an average profile of aerosol extinction coefficients ($k_{ext}^{avg}(RH)$) may be used in computing <wRH> instead of $k_{ext}^{IAP}(RH)$ in Eq. (4.9). Using the AOTs and column RH defined above, we define a column aerosol humidification factor (AHF) as the ratio of two AOTs due to scattering at different RH levels:

$$R(RH) \equiv \tau_{sca}^{IAP}(RH) / \tau_{sca}^{IAP}(40\%) \tag{4.11}$$

Similar to f(85%), the column aerosol humidification factor can be defined at two fixed RH levels:

$$R(85\%) \equiv \tau_{sca}^{IAP}(85\%) / \tau_{sca}^{IAP}(40\%) \tag{4.12}$$

Finally, the relative AHE is defined as:

$$AHE \equiv \frac{\tau_{sca}^{IAP}(RH) - \tau_{sca}^{IAP}(40\%)}{\tau_{ext}^{IAP}(RH)} \tag{4.13}$$

4.3. Effects of Aerosol Humidification on Aerosol Optical Thickness

To gain a general idea of the AHE, Fig. 4.1 presents the profiles of mean aerosol scattering and extinction profiles and average f(RH) and f(85%) profiles derived from 70 IAP measurements over the ARM SGP region from April 2003 to June 2004. The aerosol scattering coefficients profiles are provided under three different RH levels (i.e., 40%, 85% and ambient RH) and aerosol extinction profile at ambient RH is shown together. AHE is moderate and decreases with altitude. Two different averaging methods were taken to derive f(RH) and f(85%) profiles: simple arithmetic averaging and aerosol extinction (at RH=40%) weighted averaging. It is

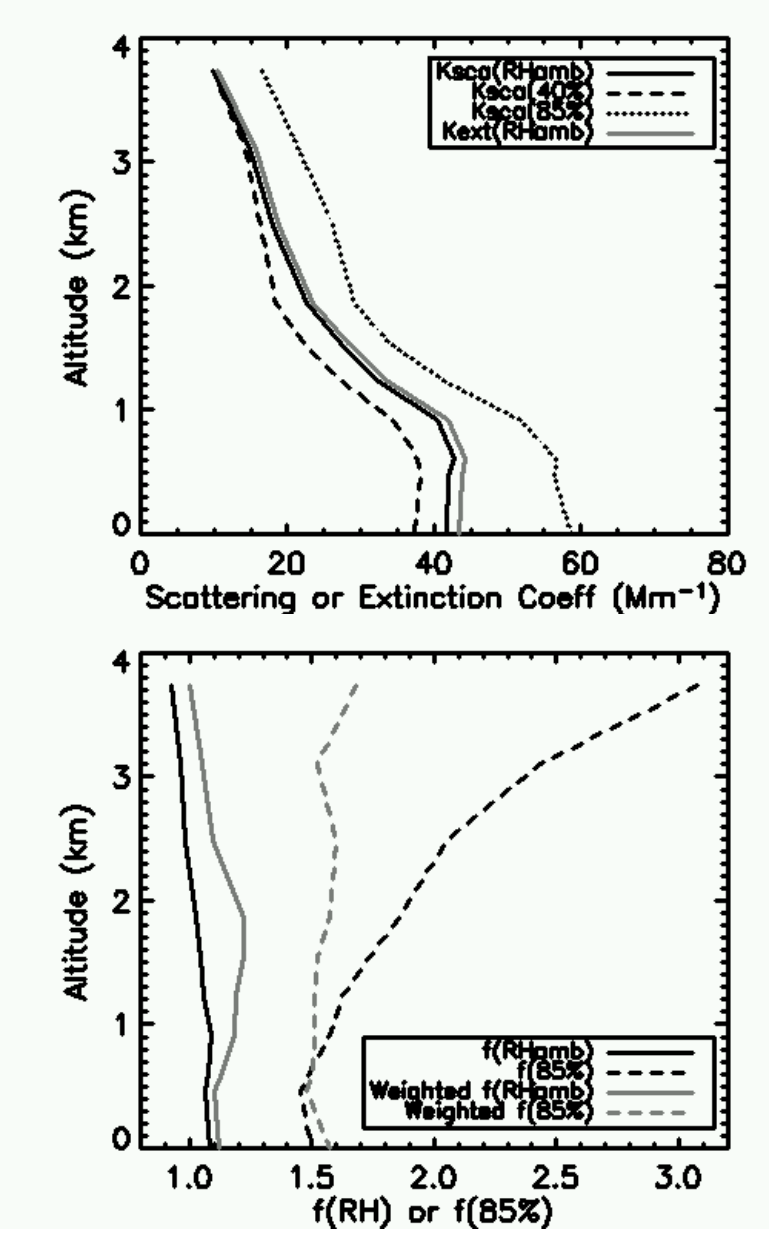

Fig 4.1 The profiles of aerosol scattering and extinction coefficients (denoted as Ksca and Kext) averaged from the IAP measurements (April 2003- June 2004) at ambient and fixed RH values (upper panel). The profiles of mean f(RH) and f(85%) derived from the IAP measurements. Both the arithmetic and aerosol extinction weighted means are provided (lower panel).

interesting to note that weighted mean f(RH) is larger than arithmetic mean f(RH) in all altitudes especially around 1.5~2km. RH and aerosol extinction for dry particles (RH=40%) are positively correlated with stronger correlation around 1.5~2km. Arithmetic mean f(85%) increases with altitude and larger than weighted f(85%) above 0.5km, while weighted f(85%) remained relatively constant around 1.55. An increase in aerosol extinction for dry particles at higher altitudes may be caused by a decrease in aerosol hygroscopicity or f(85%) due to smoke or dust.

Before dealing with column-mean AHE, it is necessary to compare column total AOT data from different sources. Here, we compare the AOT derived from the IAP measurements (hereinafter referred to as IAP AOT) with AERONET AOT at the time of the IAP measurements. Since IAP observations take 20 ~ 60 minutes (Andrews et al., 2004) and AERONET measurements would have maximum 4-5 measurements an hour depending on sky conditions, we allow a 60-minute window to match up IAP AOT with AERONET AOT. Although we fill the gap below the lowest flight level-leg with the AOS measurements, aerosols above the highest flight level-leg were missed. However, roughly 90% of the aerosols over the SGP site tend to reside below 4 km (Turner et al., 2001). In addition, since the bulk of the water vapor is concentrated within the altitude range where the IAP observations were made (Turner et al., 2001), the aerosol humidification effect, which is our main concern, may be negligible above 4 km. Nevertheless, we attempted to correct for the missing aerosols above 4 km using Raman Lidar (RL) measurements of aerosol extinction profiles, proposed by Andrews et al. (2004), in order to make the data comparable with AERONET AOT. Given the ubiquitous small values of AOTs, an attempt to

incorporate stratospheric AOT was made using the monthly mean stratospheric AOT from Stratospheric Aerosol and Gas Experiment (SAGE) II data (version 6.2 available at http://www-sage2.larc.nasa.gov/data/v6_data/) for a latitude band of 25~45 degrees North. The IAP-based AOT after all corrections are applied is calculated by

$$\tau_{corr}^{IAP}(RH) = (\tau_{sca}^{IAP}(RH) / r_{sca}(RH) + \tau_{abs}^{IAP} / r_{abs}) / (1 - r_{miss}) + \tau_{strato}^{SAGE} \qquad (4.14)$$

where r_{sca} and r_{abs} are correction factors for super-micron aerosols derived from the AOS observations as described in the previous subsection, r_{miss} is the ratio of RL AOT above the highest IAP level-leg to total RL AOT (used as a proxy for the missing aerosols from the IAP flights).

Fig 4.2 shows the comparison of $\tau_{corr}^{IAP}(RH)$ with the AERONET AOT. AERONET AOT at 500 nm was adjusted to the value at 550 nm by interpolating AERONET AOTs at 500 nm and 670 nm. $\tau_{corr}^{IAP}(RH)$ is reasonably correlated with AERONET AOT (R=0.86) with an intercept of 0.02 and a slope of 0.978. This result shows a slight improvement over a comparison made by Andrews et al. (2004) (intercept=0.04, slope=1.04) although the analysis periods are different. Also, their analyses do not include aerosol scattering measurements at high RH levels. Therefore, a humidity correction factor had to be estimated indirectly in their study while the humidity correction is directly determined from the measured data in our study. In addition, the inclusion of the AOS data together with some minor corrections (e.g., stratospheric AOT) contributed to this comparison result.

The column aerosol humidification factor, R(RH) and R(85%) as defined in Eqs. (4.11) and (4.12), respectively, were plotted as a function of time in Fig 4.3. It

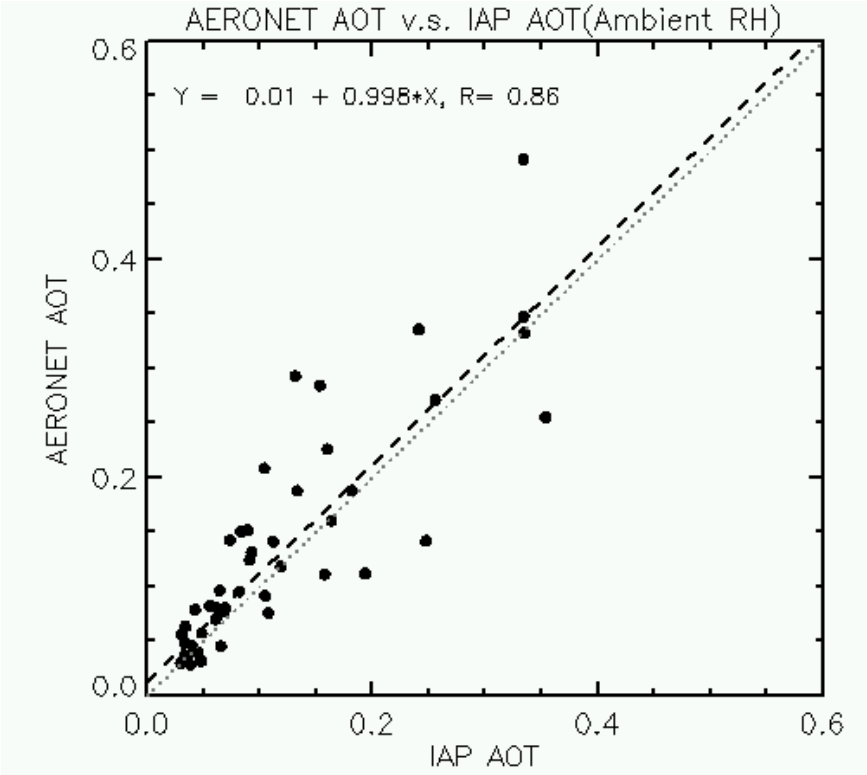

Fig 4.2. Comparison of aerosol optical depth (AOT) derived from IAP flights against AOT measurements from the AERONET. Gray dotted and black dashed lines represent one-to-one and linear fit lines, respectively.

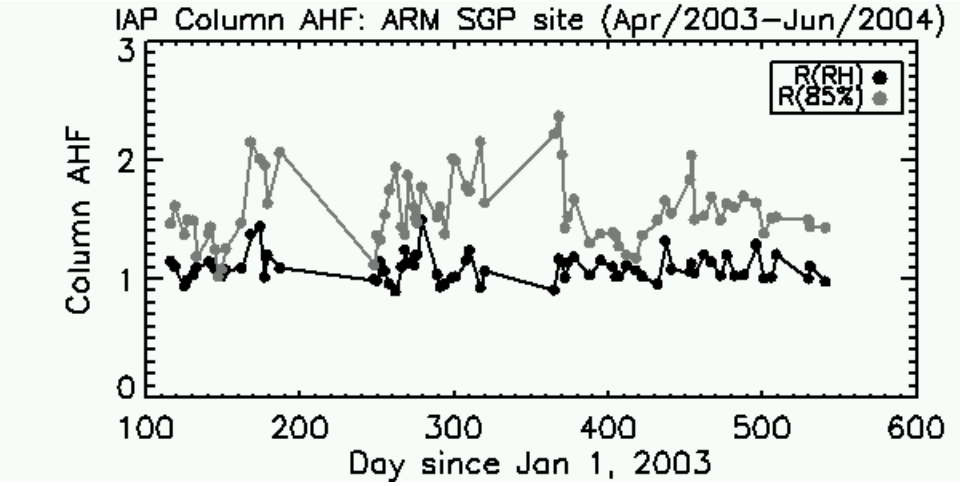

Fig 4.3. Time series of the column aerosol humidification factor (AHF) derived from IAP observations. Black line stands for column AHF for the ambient RH profiles, or R(RH), while gray line corresponding to a fixed RH=85%, or R(85%).

reveals that R(RH) values during the observation period were very small (mean=1.09) with little variability (STD=0.12), indicating that the contribution of the AHE to the total AOT is small on average. On the other hand, R(85%) is significantly larger (1.55±0.30) than R(RH), implying that there were significant potentials of AHE, but the atmospheric column observed by IAP aircraft over the SGP have been rather dry. When the data shown in Fig 4.3 are plotted as a function of <wRH>, AHE can be viewed clearly (Fig 4.4). The column AHF, R(RH), shown in the upper panel, illustrates a clear dependence on <wRH> and is reasonably fitted to both linear and non-linear curves. The non-linear curve provides a better fit but it produces a larger uncertainty for higher RH values, especially when <wRH> is greater than 80%. However, since <wRH> is a column quantity, such high <wRH> is very rare in the real atmosphere. Contrary to R(RH), column AHF at a fixed RH level, R(85%), shows no dependence on <wRH>. Since R(85%) pertains information about aerosol chemical/optical properties and correlation between aerosol extinction and RH, this result is expected.

Based on the above discussions, the AHE on the total (i.e., scattering + absorption) AOT is plotted as a function of the column mean RH, <wRH>, in Fig 4.5. Since there is no information available yet concerning the aerosol absorption dependence on RH, the assumption that the AHE influences aerosol scattering only is made. The AHE is defined as the ratio of the difference between the scattering AOT derived for the ambient RH profiles and the scattering AOT at RH=40% to the extinction AOT with ambient RH profiles. Data points with different AOT ranges are presented in different colors to see if any dependence of the AHE on the magnitude of

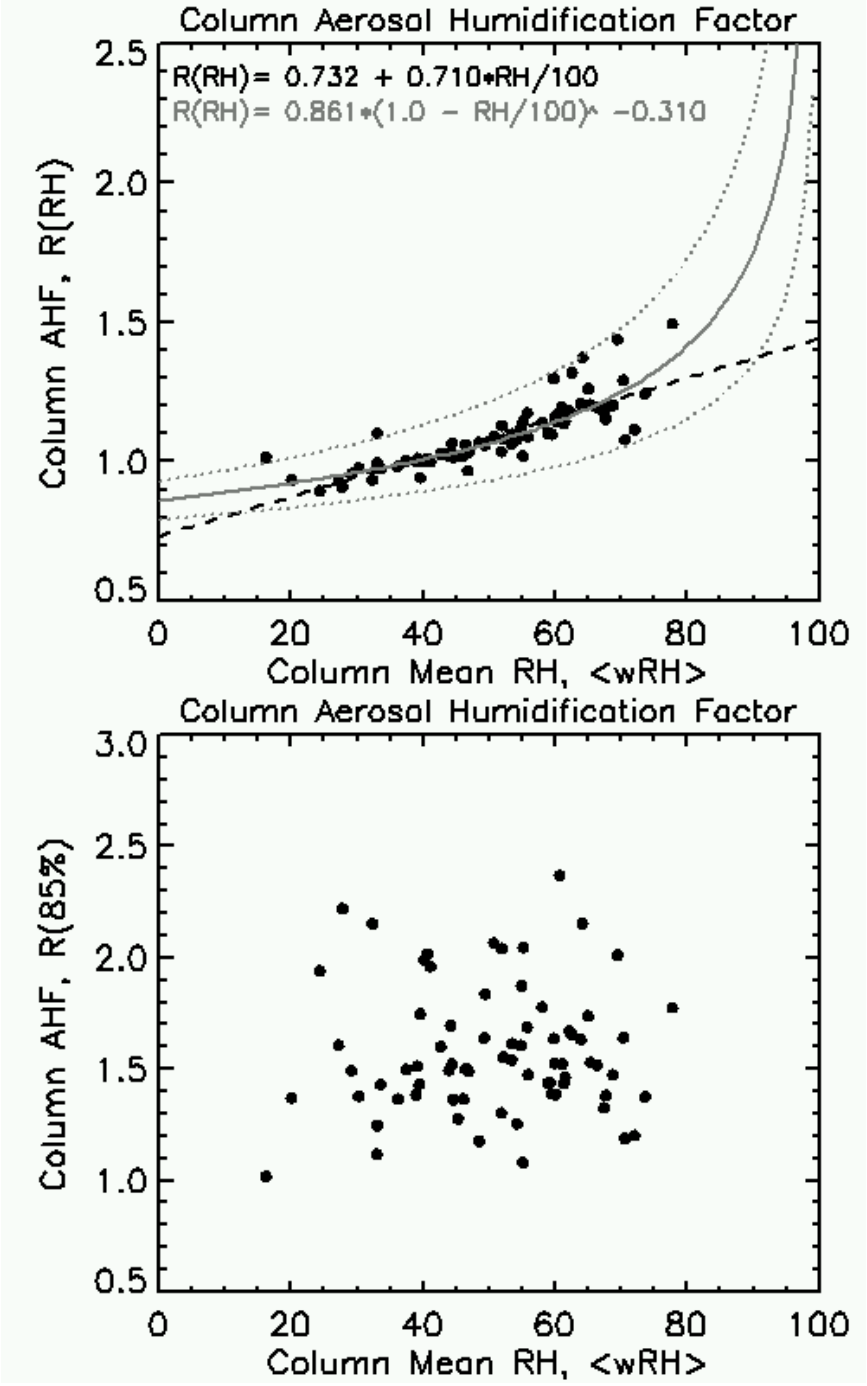

Fig 4.4. Column-mean aerosol humidification factor, R(RH) as a function of column mean RH weighted by aerosol extinction (upper panel). Linear (black dashed line) and two-parameter fitting (gray solid line) lines are provided. Gray dotted lines corresponds to ±2σ of fitted parameters, providing range of uncertainty. Column mean R(85%) is plotted against column mean RH in the lower panel.

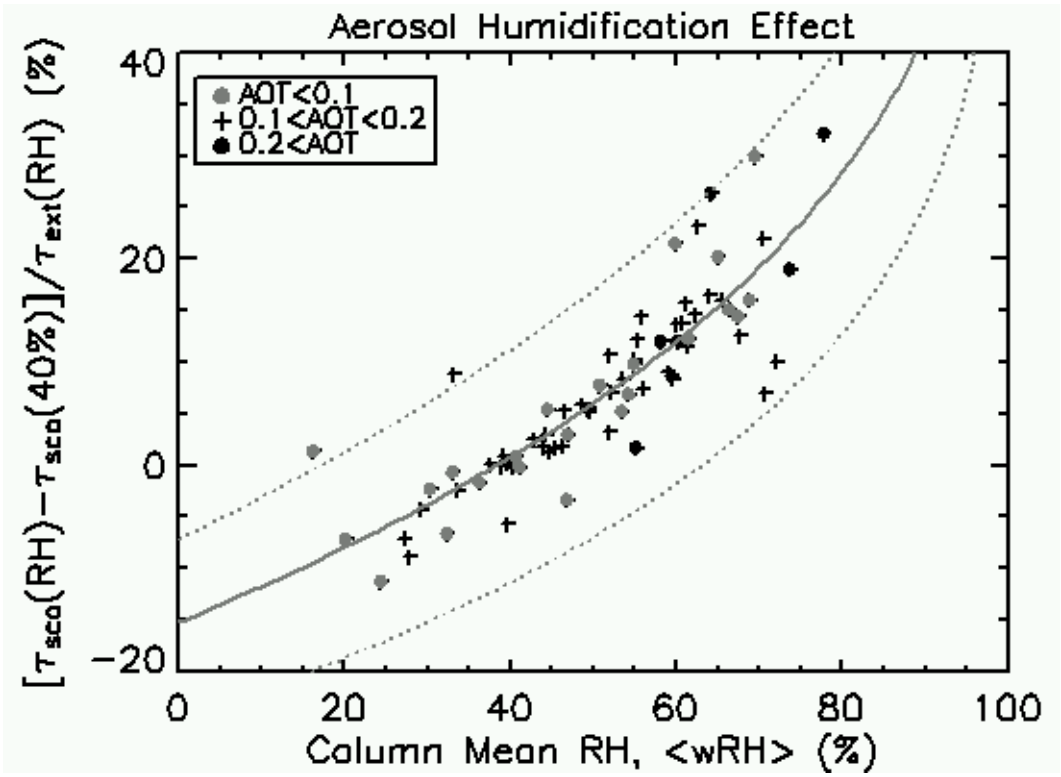

Fig 4.5. Relative aerosol humidification effect (percentage to the total AOT) as a function of the column-mean RH. Data points of different ranges of AOT values are shown in different symbols. The solid line is the regrssional fitting and dotted line is the estimated range of uncertainty (i.e., ±2σ of fitted parameters).

AOT is evident. The AHE shows an exponential dependence on the column mean RH, which ranges from –6% to 25%. Öström and Noon (2000) reported that humidity-induced growth of aerosols over oceans could contribute about more than half of the measured AOT. The humidity effect over oceans is higher than over land in general, and oceanic aerosols like sea-salt are more hygroscopic than those over the SGP, which are likely to contain more hydrophobic aerosols like smoke or dust.

4.4. Estimating the Column Aerosol Humidification Effect

If aerosol profiles are not available - often the case - column AHF might be determined by column-mean RH or precipitable water (PW) alone as RH profiles or PW are more readily available than aerosol profiles. Fig 4.6 shows their relationships. Albeit being weaker than using <wRH>, linear relationships do exist. There are less number of data points for the AHF versus PW plot due to less match-ups for PW which is obtained from the AERONET measurements. The linear relationships may be used to estimate R(RH) for a limited range of column mean RH (e.g., 20~70%). However, given the non-linear response of aerosol humidification effect to RH, R(RH) tends to be underestimated for higher RH. It is thus necessary to extend the relation to higher RH.

When only RH measurements are available, two different approaches may be adopted to estimate the AHE: 1) using <RH> in lieu of <wRH> and 2) using an average aerosol extinction coefficient profile. <RH> is correlated with <wRH> reasonably well (R=0.73), as shown in the upper panel of Fig 4.7. In general, <wRH> is higher than <RH> indicating that aerosol extinction profiles are positively

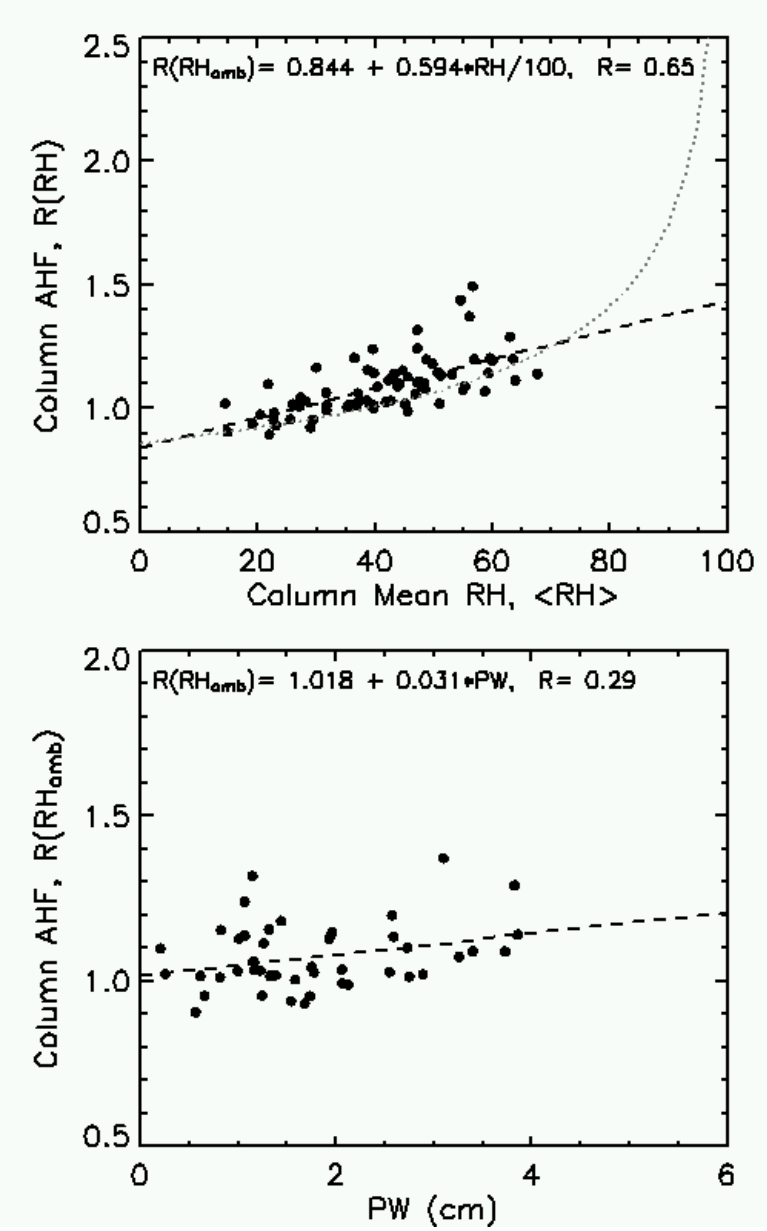

Fig 4.6. Similar to Fig. 4.5 but as functions of simple arithmetic means of RH (<RH>; upper panel) and precipitable water (PW; lower panel). The dashed lines are least-squared linear regressions. A gray dotted line in the upper panels is the same as the gray solid line shown in Fig 4.4 and provided here for a reference.

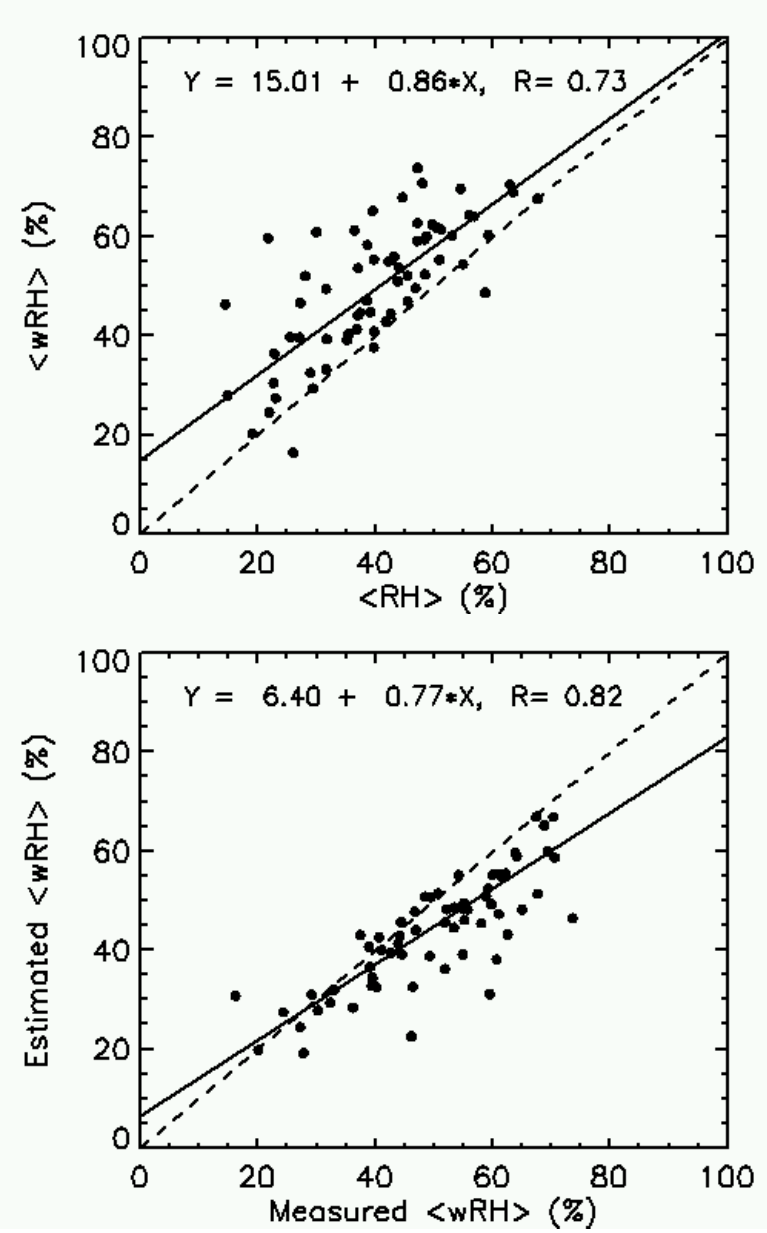

Fig 4.7. Correlation between two column-mean RH obtained by simple arithmetic averaging of RH (<RH>.) and weighted by the aerosol extinction coefficient (<wRH>) (upper panel). Comparison of measured <wRH> with estimated <wRH> using measured RH profiles and an average aerosol extinction profile (lower panel).

correlated with RH profiles. The two column-integrated amounts of RH get closer to each other as RH increases. The lower panel of Fig 4.7 shows a comparison of <wRH> estimated using the average aerosol extinction profile of the data as presented in Fig 4.1 against measured <wRH>. The estimated <wRH> has a better correlation with the measured <wRH> than <RH>, but tends to be underestimated. Since the systematic bias may be corrected, it is better to use an average aerosol extinction profile to estimate <wRH>.

Six methods (hereinafter, denoted as M1~M6) to estimate the AHE are introduced in Table 4.2 based on the two approaches but with different details. In brief, M1~M3 utilize the relationship between <wRH> and R(RH) as shown in Fig. 4.4. That is the column-mean AHE can be derived using the column-mean RH of aerosol extinction (i.e., <wRH>) similar to Eq. (4.3):

$$R(RH) = a \cdot \left(1 - \frac{< wRH >}{100}\right)^{-b} \tag{4.15}$$

where a=0.861 and b=0.310 that were derived in Fig 4.4. M1~M3 differ in ways deriving <wRH>. M1 can be applied when both aerosol extinction and RH profiles are available. M2 uses known a priori relationship between <RH> and <wRH> so that <wRH> may be estimated without aerosol profiles. In M3, <wRH> is estimated from an average profile of aerosol extinction. The second approach includes M4~M6, which compute the AHE by directly integrating the assumed profiles concerning aerosols. M4 and M5 uses

$$R(RH) = \frac{\int k_{sca}^{avg}(40\%, z)\, f^{est}(RH)dz}{\int k_{sca}^{avg}(40\%, z)dz}\ , \tag{4.16}$$

Table. 4.2. Different methods of estimating aerosol relative humidity effect in case direct measurements are not available.

Methodology	Method ID	Descriptions on Methods
Relationship between R(RH) and <wRH>	M1	Using Eq. (4.15) and measured <wRH>
	M2	Using Eq. (4.15), but <wRH> is estimated following a linear regression, <wRH> = c + d <RH>, where c=15, d=0.86
	M3	Using Eq. (4.15), but <wRH> is estimated from an average profile of aerosol extinction at ambient RH, $k_{ext}^{avg}(RH)$ *, and measured RH profiles, i.e., $< wRH >= \frac{\int k_{ext}^{avg}(RH,z)RH(z)dz}{\int k_{ext}^{avg}(RH,z)dz}$
Assumptions on the vertical distribution of aerosol scattering, extinction, or hygroscopic property	M4	Using Eq. (4.16) from average profiles* of aerosol scattering coefficient at RH=40% [$k_{sca}^{avg}(40\%)$] and f(85%) [$f^{avg}(85\%)$] and measured RH profiles
	M5	Using $k_{sca}^{avg}(40\%)$ and measured RH profiles; assume the profiles of $f(85\%)$ is a constant whose value is the same as the one observed at a surface station (i.e., $f_{sfc}^{AOS}(85\%)$ &)
	M6	Using measured profiles of $k_{sca}(40\%)$ and RH, but assume $f(85\%) = f_{sfc}^{AOS}(85\%)$

* Average profiles of aerosol scattering, extinction, and hygroscopicity are provided in Fig 4.1.

& $f_{sfc}^{AOS}(85\%)$ denotes f(85%) measured from the Aerosol Observing System (Sheridan et al., 2001) at the surface of the ARM SGP CART site.

where $k_{sca}^{avg}(40\%)$ is the average aerosol scattering profile at RH=40%, and $f^{est}(RH)$ is a profile of the aerosol scattering humidification factor estimated from a measured

RH profile with an assumed f(85%) profile. When f(85%) can be estimated, f(RH) may be calculated by combining Eq. (4.2) and Eq. (4.3). M4 uses an average profile of f(85%) while M5 uses a measurment of f(85%) at the surface assuming the same f(85%) value aloft. For M6, R(RH) can be derived by replacing k_{sca}^{avg} with an observed $k_{sca}(\sim 40\%)$ in Eq. (4.16). M6 has been suggested to use if f(85%) or γ in Eq. (4.1) can be assumed when the profiles of aerosol scattering coefficients at a dry condition (RH~40%) are measured (e.g., Remer et al., 1997; Andrews et al., 2004).

The estimated R(RH) using the proposed methods (M1~M6) are compared with the measured R(RH) in Fig 4.8. Among the four methods, M1 shows the best agreement, which is not a surprise since Eq. (4.15) is derived by fitting to measured R(RH), followed by M6. M6 has been used in the literature (e.g., Remer et al., 1997; Andrews et al., 2004). Two methods are applicable to different situations. For example, M1 can be to Raman Lidar measurements from which profiles of aerosol extinction coefficients at ambient RH are available together with RH (e.g., Turner et al., 2001; also see Chapter 5). On the other hand, M6 can be used when airborne measurements of aerosol scattering coefficients are obtained only at a dry RH condition (e.g., Andrews et al., 2004). The overall results in Fig 4.8 can be summarized as follows: 1) when both aerosol extinction and RH profiles are available, best estimation of R(RH) is achieved using M1, followed by M6, 2) when aerosol profiles are unavailable, use of representative profiles of aerosol scattering coefficients and f(85%) (i.e., M4) would be a next choice, followed by M5, which uses f(85%) measured at the surface. It, however, should be noted that all the methods tend to underestimate R(RH). Such R(RH) underestimation for M2~M5 originates

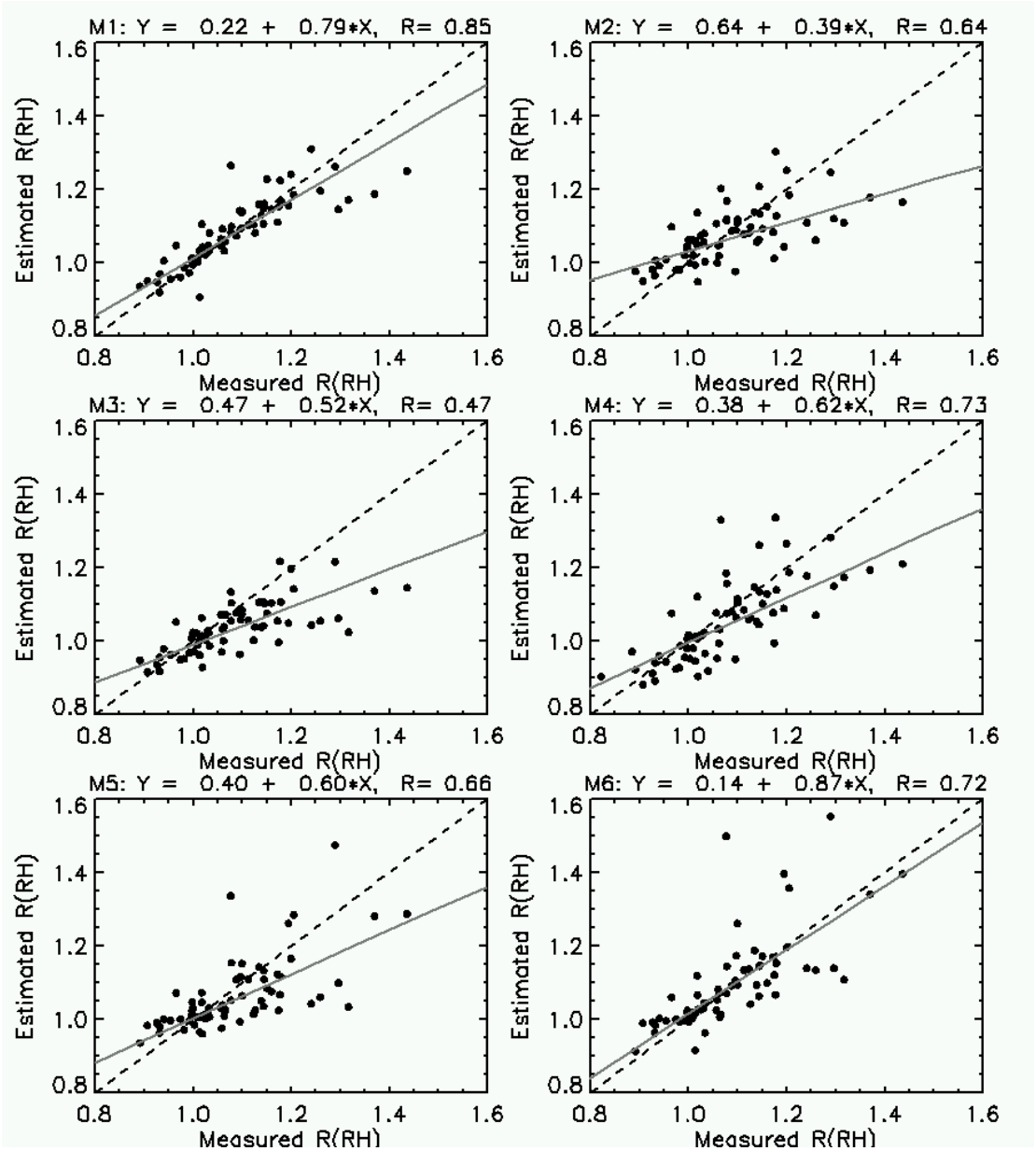

Fig 4.8. Comparison of estimated column aerosol humidification factor, R(RH) following six different methods (M1~M6). Gray solid lines and black dashed lines are linear fit and one-to-one lines, respectively.

from the fact the aerosol profiles tend to be correlated to RH in natural conditions, which was not the case when an average aerosol profile was used. Also, for M1~M3, the limited range of <wRH> used for deriving Eq. (4.15) degrades R(RH) estimation at higher RH – i.e., <wRH> greater than 80%.

The methods proposed above are useful to assess the AOT derived from satellite-based and/or ground-based radiometric measurements. For instance, it has been reported in the literature that the AOT derived from satellites is correlated with cloud fraction or its variability (e.g., Ignatov and Nalli, 2002; Kaufman et al., 2005; see also Chapter 2), and such apparent correlation was speculated as either AHE or cloud contamination. Separating and quantifying such effects are very important to improve satellite-based aerosol retrievals. In addition, knowledge about AHE on a given AOT helps characterize aerosols in terms of their number concentration, thereby valuable for some observational studies (e.g., Feingold et al., 2003 and 2005) on the aerosol indirect effect.

4.5. Sensitivity of the Aerosol Humidification Effect to a Very Humid Layer

The sensitivity of the column AHF (i.e., R(RH) as defined in Eq. (4.11)) to the presence of a very humid layer, which could be missed by the IAP observations, was tested. This scenario may happen when there is a layer of scattered clouds or a locally very humid layer, which is distant from where an IAP observation was made. Fig 4.9 shows such an example. The figure shows a RH profile obtained from an IAP flight at discrete levels and a ground RH from the AOS. Besides, two continuous RH profiles were acquired from the Twin Otter aircraft during the aerosol intensive observation

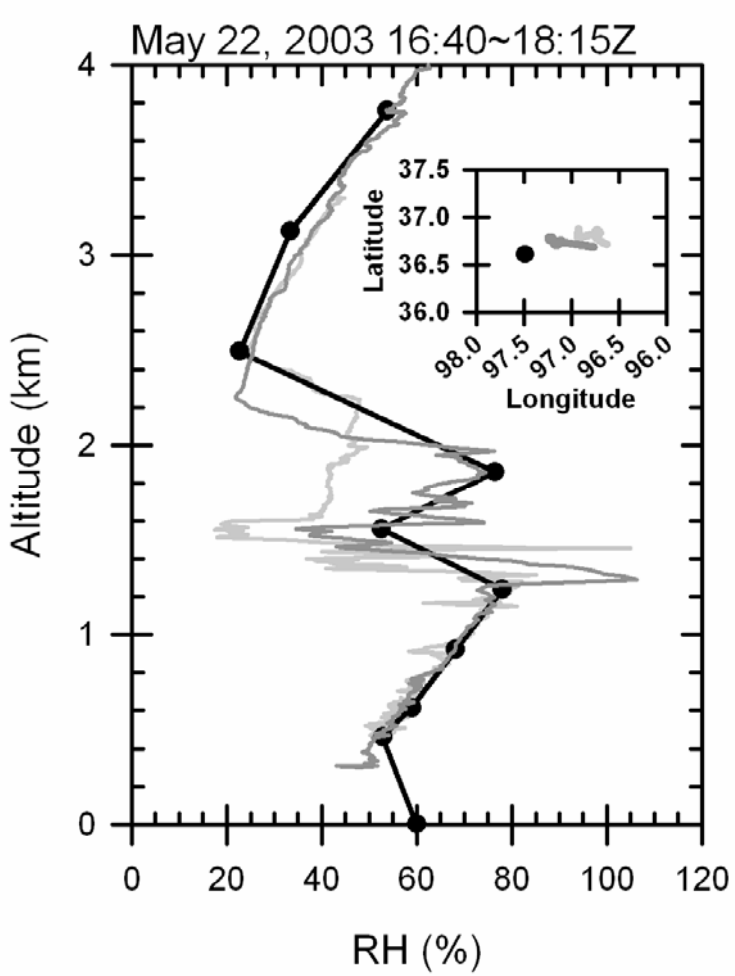

Fig 4.9. A profile of RH obtained from an IAP flight and a coincident AOS measurement at the surface (solid black line) and two profiles of ambient RH from Twin Otter flights during the Aerosol Intensive Operation Periods over the SGP site in 2003 (dark and bright gray lines). The locations of measurements are also indicated in the sub-panel.

period (IOP) led by Dr. Richard Ferrare (relevant proposal available at http://www.db.arm.gov/cgi-bin/IOP2/selectPreProposal.pl?proposalNo=1524) over the SGP site in 2003. The IAP RH profile agrees very well with the other two RH profiles taken from Twin Otter at slightly different locations and times, except for sharp peaks (RH>100%) with a depth of 0.1~0.2 km, illustrating the presence of very humid layer missed by the IAP data. Thus, it is assumed there is a humid layer with RH=99% that the IAP measurements missed among the nine-level legs plus a layer between the surface and the lowest level-leg per flight. The altitudes of the respective level-legs are provided in Table 4.1. In each test, the observed ambient RH for a selected level-leg was replaced by RH=99%. This test was repeated for the ten levels, respectively. The scattering coefficient for the selected layer (i.e. the layer where RH was forced to be 99%) was recalculated to derive the AOT. A series of such sensitivity tests were performed for cases when a very humid layer exists in the different altitudes. Fig 4.10 shows the column AHF (i.e., R(RH)) as a function of <wRH>, derived from the sensitivity test with very humid layer depths equal to the depths of the IAP level-legs. The observed column AHF without consideration of the humid layer was also provided for reference. For example, R(RH) for an atmospheric column containing a very humid layer with a depth of the IAP level-leg centered at 3.1 km can be as high as 5 while the maximum of the observed R(RH) was 1.3. The larger sensitivities of R(RH) happen when a humid layer is present at higher altitudes. This may result from the fact that the depths of IAP level-legs are larger for higher altitudes. Or, if higher altitudes (>3km) are normally drier than lower altitudes, it can cause higher sensitivity at higher altitudes. However, if aerosol extinction is too low,

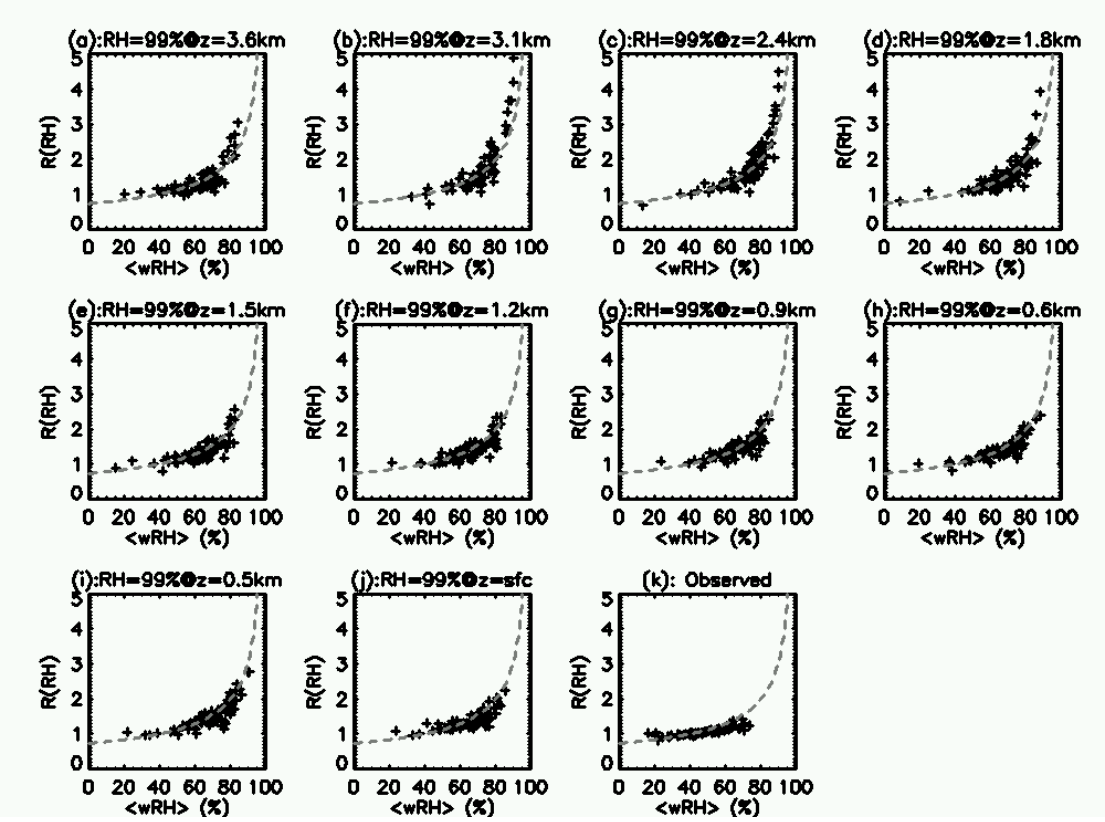

Fig 4.10 (a)-(j) Column-mean aerosol humidification factor as functions of the weighted column mean RH, <wRH>. The ambient RH at one of the ten level-legs of the IAP measurements is replaced with RH=99%. The bottom of the replaced layer is indicated in each panel (a – j) in which the aerosol scattering coefficients and AOT were recalculated accordingly. (k) The same as (a)-(j) but using the original ambient RH profile. The gray dashed line is the fitting line of Eq. (4.14) to the all the data shown in this figure.

the effect is small, just as shown for the highest level-leg (3.6km). The dashed line in Fig 4.10 was derived by fitting all the data shown in the figure to Eq. (4.15). The coefficients a, b for this the curve are 0.728 and 0.621, respectively.

It is necessary to normalize R(RH) to those values found when there are equal depths of the humid layer at different levels in order to see if there is any dependence of R(RH) on the altitudes of the humid layer. Thus, similar sensitivity tests as the ones made above were performed, but with the depths (Δz) of the very humid layers fixed to 0.2 km. It was found that high R(RH) values (>3.0) shown in the previous tests disappear (Fig 4.11), suggesting that the larger very humid layer depths are the primary reason why the higher R(RH) sensitivities appeared at higher altitudes in the previous tests. Fig 4.11 shows that R(RH) is normally less than 2 and does not depend on the altitude of the humid layer when Δz is fixed. These results show that a "missing" humid layer could introduce slight discrepancies of R(RH) from what was observed from the IAP flights, when a reasonable depth of such layer is considered. The scattering AOT within a very humid layer was compared with the scattering AOT with the observed ambient RH profiles in Fig 4.12. The scattering AOT within the humid layer is systematically higher than the observed. Such systematic differences vary with the altitude of the humid layer (0~20%) with a tendency of larger systematic differences for the cases when the humid layers exist at low levels in the atmosphere. This result seems reasonable because the aerosol population is normally larger at low levels (e.g., <2 km).

It is also interesting to know the sensitivity of R(RH) to the depth of the assumed humid layer. The same tests were conducted in addition to the previous tests,

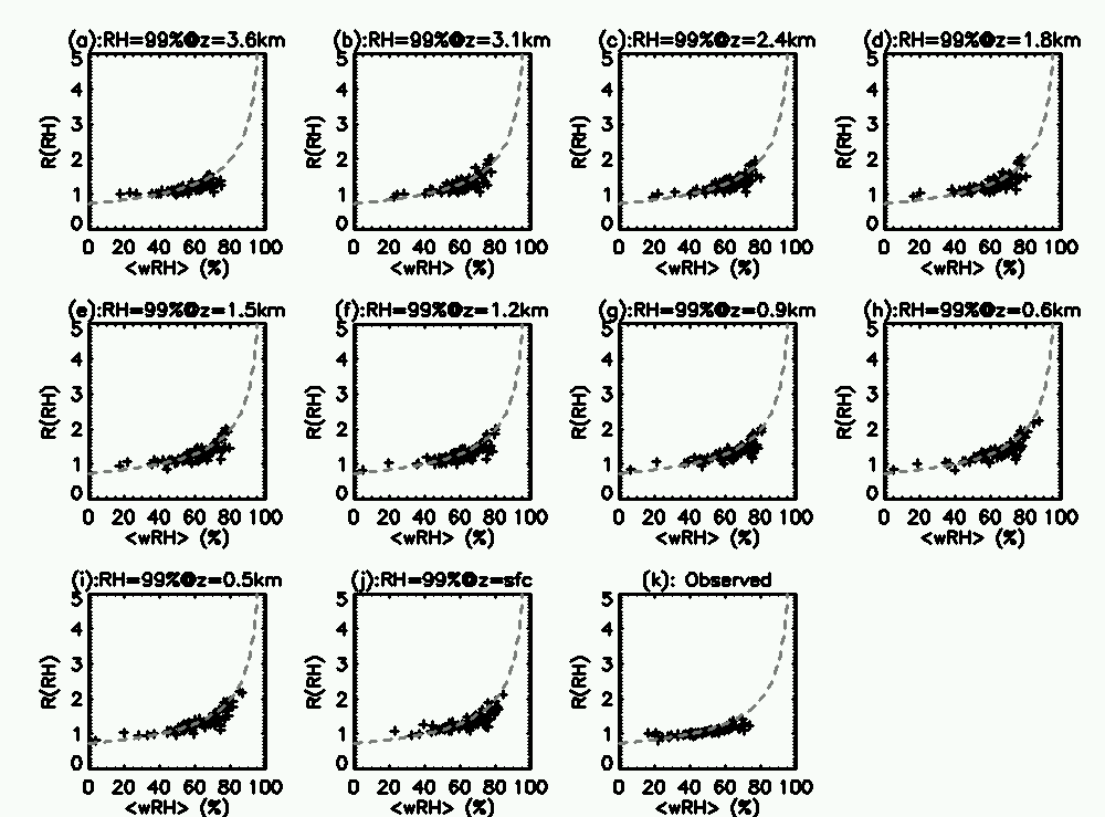

Fig 4.11. The same as Fig 4.10, but the depth of very humid layer (RH=99%) was set to 0.2km for respective levels shown in panel (a)-(j). The dashed gray line is the same line as shown in Fig 4.10.

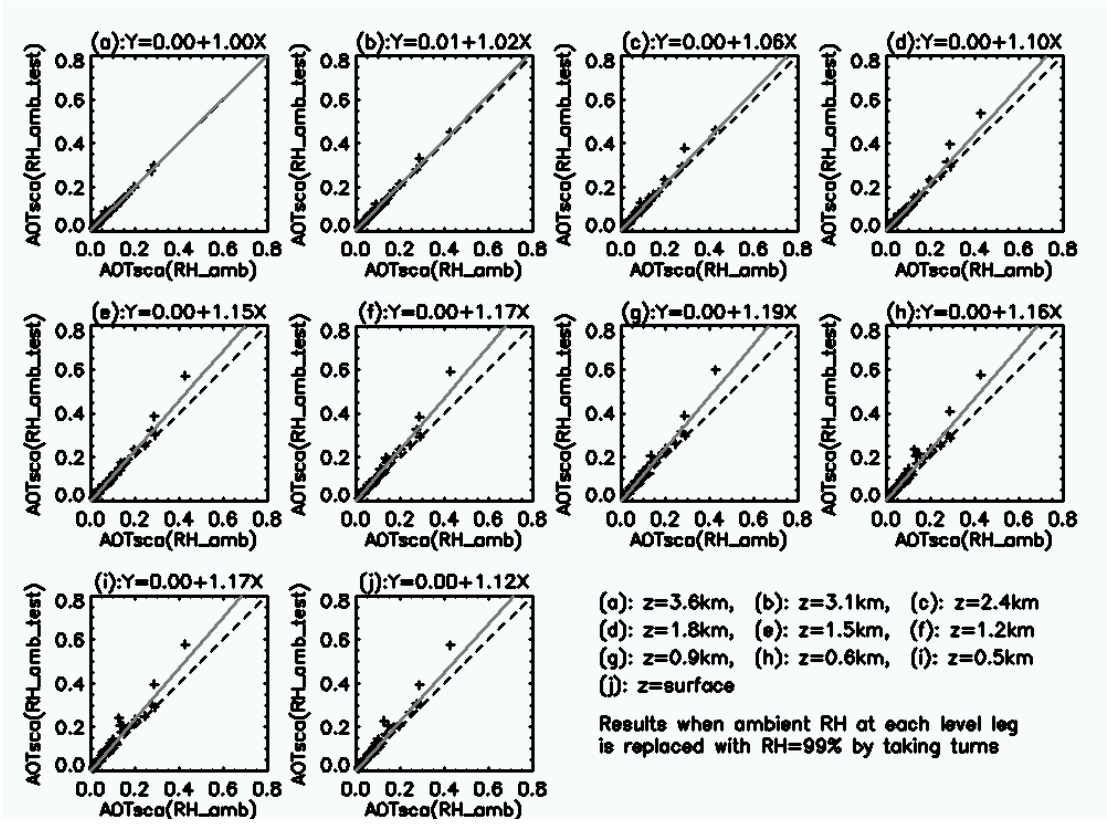

Fig 4.12. Comparisons between observed AOT and those derived assuming a humid layer of 0.2km. Dashed black and solid gray line stand for one-to-one and linear fit lines, respectively. Panel (a)-(j) correspond to the tests as described in Fig 4.11.

but with different depths (Δz) for the humid layer. The results are summarized in Table 4.3 and Table 4.4 for cases with Δz=0.1 km, Δz =0.2 km, Δz=0.3 km, and Δz equal to the depth between the IAP flight level-legs. No significant dependence on the altitude of the very humid layer was found except for the highest level (3.6 km), which showed a smaller sensitivity than the other levels. It is mainly due to small population of aerosols at that (and above) altitude. The average R(RH) for all the IAP data available in this study (i.e., 70 profiles) was 1.09±0.12. In Table 4.2, R(RH) changes 4~13% from the observed R(RH) when Δz=0.1 km, and varies 9~27% and 15~42% when Δz=0.2 km and Δz=0.3 km, respectively. These R(RH) changes result in AOT changes from the observed by up to 9%, 19%, and 28% for the respective Δz. These values, in turn, correspond to the AHE on AOT by 15~25%, 15~41%, and 15~55% for the respective Δz, as given in Table 4.3.

Table 4.3. Averages of the column aerosol humidification factor derived from the sensitivity test for the given depth (Δz) of a very humid (RH=99%) layer. The numbers in the parentheses are standard deviation. ($N^{\&}$=70)

Test ID*	Mean R(RH)			
	Δz= level-leg depth#	Δz=0.1km	Δz=0.2km	Δz=0.3km
1	1.420 (±0.415)	1.117 (±0.112)	1.174 (±0.139)	1.235 (±0.194)
2	1.772 (±0.774)	1.174 (±0.139)	1.288 (±0.241)	1.407 (±0.367)
3	1.838 (±0.724)	1.185 (±0.143)	1.308 (±0.235)	1.439 (±0.347)
4	1.573 (±0.527)	1.169 (±0.140)	1.277 (±0.229)	1.392 (±0.339)
5	1.387 (±0.331)	1.163 (±0.149)	1.268 (±0.225)	1.375 (±0.324)
6	1.415 (±0.322)	1.173 (±0.152)	1.288 (±0.225)	1.405 (±0.320)
7	1.495 (±0.330)	1.200 (±0.158)	1.341 (±0.234)	1.486 (±0.330)
8	1.416 (±0.318)	1.216 (±0.182)	1.372 (±0.288)	1.534 (±0.412)
9	1.520 (±0.410)	1.212 (±0.180)	1.363 (±0.286)	1.520 (±0.409)
10	1.364 (±0.239)	1.193 (±0.156)	1.327 (±0.219)	1.466 (±0.300)
Observed	1.090 (±0.116)			

*: Set to equal to the level-leg ID at which observed RH was replaced with RH=99% assuming a hypothetical humid layer that could have missed by the IAP measurements in the sensitivity test.
&: N is total number of the IAP profiles.
#: level-leg depths are approximately 0.5, 0.6, 0.65, 0.45, 0.3, 0.3, 0.3, 0.2, 0.3, and 0.25km for level IDs from 1 through 10, respectively.

Table 4.4. The slope between the scattering AOT including very humid layer (depth, Δz) and scattering AOT at RH=40%.

Test ID	Slope			
	Δz= level-leg depth[#]	Δz=0.1km	Δz=0.2km	Δz=0.3km
1	1.17	1.15	1.15	1.15
2	1.25	1.17	1.18	1.23
3	1.38	1.18	1.22	1.25
4	1.35	1.20	1.24	1.30
5	1.36	1.22	1.33	1.37
6	1.52	1.27	1.38	1.49
7	1.52	1.25	1.40	1.51
8	1.47	1.25	1.41	1.55
9	1.40	1.25	1.32	1.43
10	1.32	1.23	1.31	1.41
Observed	1.15			

Note: Intercepts for all cases were 0.

4.6. Summary

The aerosol humidification effect (AHE) on the aerosol optical thickness (AOT) measured over the Southern Great Plains (SGP) site was investigated. AOTs at different relative humidity (RH) levels (e.g., RH=40% and 85% throughout the column, and ambient RH profiles) were computed by integrating aerosol extinction profiles measured from a light aircraft (Cessna C-172N) under the In-situ Aerosol

Profiles (IAP) project, which is a joint effort between the Atmospheric Radiation Measurement (ARM) program of Department of Energy and the Climate Monitoring and Diagnostics Laboratory (CMDL) of the National Oceanic and Atmospheric Administration (NOAA). The AOT derived from the IAP agreed reasonably well with coincident AOT from the AErosol RObotic NETwork (AERONET).

Conventional two-parameter fitting (Hänel, 1976) was used to estimate AHE at ambient relative humidity and at 85% from the scattering coefficients from the IAP measurements. The column aerosol humidification factor, R(RH), was defined as the ratio of the AOT with an ambient (or desired) RH profile to the AOT at a 40% RH level throughout the column. R(RH) for ambient RH profiles for all available IAP data barely exceeds 1.3, which suggests that the AHE under the normal conditions of the IAP observations is small (mean equal to 1.09±0.12). An AOT increase due to the AHE is less than 30% compared to an AOT increase in dry conditions (RH=40%). On the other hand, the column AHF at RH=85%, R(85%), was greater than 1.5 for the majority of cases (mean equal to 1.57±0.28), implying that the AHE could have been larger than the observed if the column mean RH were higher or profiles of aerosols and RH were correlated better. It was shown that the column AHF can be represented as increasing functions of humidity variables such as the arithmetic column mean RH (<RH>), precipitable water, and aerosol extinction weighted column mean RH (<wRH>). R(RH) varies with <wRH> just as the AHF for the aerosol scattering coefficient, f(RH), changes in response to RH changes.

Six methods to estimate R(RH) are introduced and compared with measured R(RH). These alternative methods may be useful when direct measurements of

R(RH) are not available. The results suggest that the relationship between <wRH> and R(RH) work best if the profiles of humidity and aerosol extinction are available. If the data are not available, use of other relationships pending on available measurements may be resorted to with a varying accuracy.

The sensitivity of R(RH) to a very humid layer (RH=99%) was tested. Since the IAP data used in this study has a coarse vertical resolution (0.2~0.65 km), it is possible for the IAP observations to miss a layer of very high RH at or near the location of the measurements, especially when clouds exist nearby. R(RH) changed approximately 8%, 19%, and 31% from the observed R(RH) with changes in the depth of the very humid layer, Δz, (0.1 km, 0.2 km, and 0.3 km, respectively). R(RH) is insensitive to the altitude of the humid layer. The variability of R(RH) with different locations of the humid layer was about 2~6%, depending upon the Δz (0.1~0.3 km). Finally, it was estimated that AOT changes up to 9%, 19%, and 28% from the observed (ambient) AOT as Δz changes by 0.1 km, 0.2 km, and 0.3 km, respectively. These AOT changes correspond to an AHE on the AOT (i.e., AOT changes from AOT at RH=40%) of 27%, 41%, and 55%, respectively. Therefore, the AHE on the AOT over the SGP site is not likely to exceed 50% on average compared to the AOT at dry conditions (RH=40%).

Chapter 5: Real Effect or Artifact of Cloud Cover on Aerosol Optical Thickness?

5.1. Introduction

The current state-of-the-art satellite-based estimates over land– e.g., MODerate resolution Imaging Scanner (MODIS) aerosol optical thickness (AOT) (Kaufman et al., 1997)– still suffer from large uncertainties (±0.05±0.2*AOT) (Chu et al., 2002; Remer et al., 2005). Contamination due to sub-pixel and/or thin cirrus clouds is believed to be one of the major sources of uncertainties. Retrievals near clouds are not reliable, which reduces a considerable amount of useful data. In this regard, clouds are regarded as an artifact. However, clouds could have a real impact on AOT by changing humidity, which affects aerosols through the aerosol swelling effect. As a preliminary study, we first investigate the effects of cloud cover and humidity on the retrievals of AOT from ground-based Cimel sunphotometer measurements, in order to help us sort out the real influence and the artifact.

In general, it is very difficult to verify and quantify the effects of cloud on the satellite retrieval of aerosol quantities. Speculation and warning of cloud contamination have been made whenever there is a correlation between the retrieved AOT and cloud fraction or their spatial variabilities (e.g., Ignatov and Nalli, 2002; also see Chapter 2). It has also been argued that the aerosol humidification effect (AHE) might be at play (Ignatov and Nalli, 2002; Kaufman et al., 2005). The ample measurements available from ARM over the SGP region may allow us to unravel this

complex issue. In this study, we report that the AOTs from various measurements are correlated with cloud cover (or fraction) for small and moderate aerosol loading (i.e., AOT<1.0). Possible causes - including real effects and artifacts - are discussed and the most likely scenarios are proposed. This study help 1) evaluate various effects on the retrievals of AOT from both satellite and ground sensors; 2) quantitatively separate the artifact from the real effect; and 3) create "clean" aerosol products for the study of their direct and indirect effects.

5.2. Data

Aerosol measurements taken over the Southern Great Plains (SGP) Cloud And Radiation Testbed (CART) site under the aegis of the Department of Energy's (DOE) Atmospheric Radiation Measurement (ARM) program characterize the temporal variability, vertical distribution, and optical properties of aerosols in the region using a large array of state-of-the-art instruments. They include the Cimel sunphotometer, Multifilter Rotating Shadow-band Radiometer (MFRSR), Raman Lidar, In situ Aerosol Profiling (IAP) flights, and the Aerosol Observing System (AOS). The spatial variability of aerosols relies on a network of MFRSRs at the Central Facility (CF) and Extended Facilities (EF), together with satellite remote sensing.

The Cimel sunphotometer data employed are the AErosol RObotic NETwork (AERONET; level 2.0, cloud-screened & quality assured). Only the AERONET AOT data at 550 nm that were linearly interpolated from AOT at 500 nm and 675 nm are used. The profiles for aerosol extinction and relative humidity (RH) from the Raman Lidar (Goldsmith et al., 1998; Turner and Goldsmith, 1999) are used to compute the

aerosol extinction weighted column mean RH. Sky condition was recorded by the Total Sky Imager (TSI) continuously at the ARM SGP site (Central Facility) from 2003 to 2004 from which cloud mask data were generated. We also used the MODIS AOT and the cloud fraction from the Level 2 MODIS aerosol product over land (MOD02) and MODIS cloud mask product (MOD35). Details of the data are described in the following subsections.

5.2.1. AERONET Sun photometer Measurements of AOT

The aerosol optical thickness (AOT) measured from the AERONET Cimel sunphotometer (Holben et al., 1998) has been used in numerous studies concerning aerosols and their radiative and climatic effects. The Cimel sunphotometer has eight channels spanning the ultra violet, visible and near infrared (340, 380, 440, 500, 675, 870, 940, and 1020 nm). It is composed of two collimators: one for direct sun measurements and the other for sky radiance measurements. Both collimators have an equal field of view (1.2^{o}), but the aperture for the sky-photometers is 10 times larger than that for the sunphotometer so that the necessary dynamic range to observe the sky is provided. One set of direct normal measurements is made every 15 minutes and one set of sky radiance measurements is made per hour. Sky radiance measurements include scanning the sky along the principal plane and different azimuth angles at a fixed zenith angle to obtain the angular variation of skylight (i.e., the almucantar scan). Through inversion techniques, the sky radiance measurements are combined with the direct normal measurements to estimate the aerosol size distribution and the single scattering albedo (Dubovik and King, 2000; Dubovik et al., 2000). The AOT is

calculated from the transmission obtained from direct normal measurements using the Beer-Bouguer-Lambert's law after taking into account the attenuation due to molecular scattering and trace gas absorption. The AOT is derived to an accuracy of ±0.02~0.04 at an optical airmass of 2 (Rainwater and Gregory, 2005).

The primary issue regarding the uncertainty of the AERONET AOT is cloud screening. Therefore, a strict cloud-screening algorithm based on examining the temporal variability of measured AOT (Smirnov et al., 2000) is applied. Each set of measurements consists of three measurements (a triplet), each made 30 seconds apart during the course of a minute. In order to discriminate clouds, first, the variability of the triplet AOT is examined and when the variability is either smaller than 0.02 or 0.03*AOT (whichever is higher), the data are accepted for the next test. All the data that fail this triplet stability test are classified as cloudy. If the stability test is passed, a diurnal stability test is applied and if the standard deviation of the AOT at 500 nm is less than 0.015, the measurement is classified as cloud-free. If the data fails this test, smoothness of the data temporal variability is checked by limiting the second derivative of the AOT with respect to time within certain values. Besides, AOT at 500 nm and the Angstrom exponent are required to fall within three standard deviations for each day. While the method works effectively to get rid of most, if not all, cloud-contaminated data, it can be too strict to discard some variable aerosols like smoke plumes (Kaufman et al. 2005). Also, it may fail to detect very thin stable cirrus (Kinne et al., 1997; Kaufman et al., 2005). However, less than half of the cirrus optical thickness is expected to contribute to the observed AOT due to strong forward scattering by ice crystals (Kinne et al., 1997).

For the SGP CART site, AERONET AOT measurements have been collected since 1994. We used two years worth (2003-2004) of level 2.0 (cloud screened and quality assured) AOT data for this study.

5.2.2. Cloud Cover from the Total Sky Imager

The Total Sky Imager (TSI; Model 880) captures images of the sky during daylight hours using a charged-coupled device (CCD) imager looking down a mirror that reflects the hemispheric sky. A shadowband on the mirror blocks the direct sunlight in order to protect the optics of the imager and to provide a good sensitivity to both dark (blue sky) and bright (cloud) targets. The images are recorded as 24-bit color JPEG files at 352x288 pixel resolution. Fractional cloud cover is determined by examining the relationships between the colors of the acquired image pixels within the field of view of 160^{o} (zenith angle less than 80^{o}) to infer if a pixel represents clear sky, thin or opaque cloud (Long et al., 2001). The color relationship is based on the fact that molecular scattering is much stronger in the blue spectral range than in the red spectral range while clouds more or less equally scatter in both blue and red spectral ranges. Although the solar disk is blocked, it is difficult to discriminate clear sky from clouds in the vicinity of the Sun and for the angular area centered on the solar azimuth angle (outlined by gray lines in Fig 5.1). This is because the intensity range of the CCD camera is limited compared to the very large intensity changes near the Sun's position. Therefore, whenever the intensity becomes larger than the maximum that the CCD camera can handle, bright circum-solar areas appear as white, resulting in a color relationship in that area that is similar to that for clouds (Long et

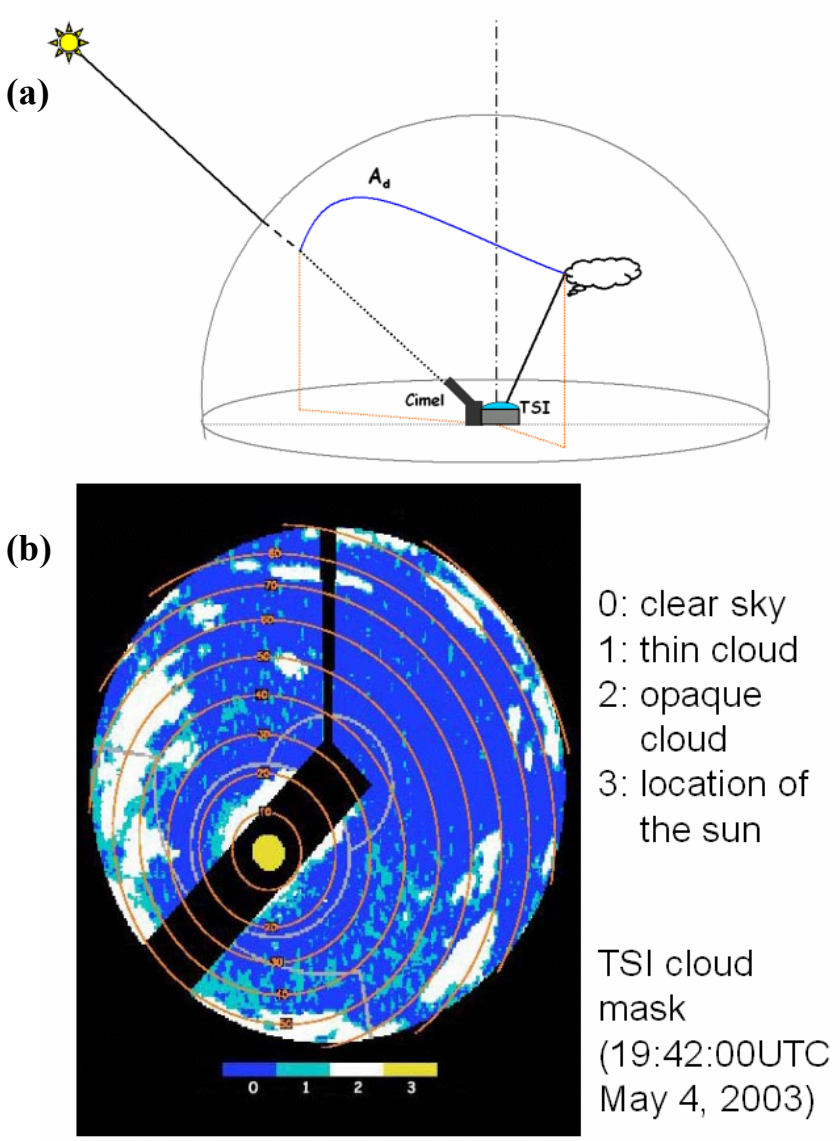

Fig 5.1. (a) Geometry of observation for the Cimel sun-photometer and for the Total Sky Imager (TSI). A_d stands for an angle between the pixel of the sun's position and any other pixels in a whole sky image taken by the TSI. (b) A sample image of cloud mask from TSI. Index 0, 1, 2, and 3 stand for "clear sky", "thin cloud", "opaque cloud", and "location of the sun", respectively. Circum-solar areas for which cloud cover is acquired are presented together with the cloud mask image.

al., 2001). The cloud cover estimated from the TSI agrees within 5% (10%) with more accurate estimates from a more advanced instrument named the Whole Sky Imager (WSI) (Long et al., 2001) for 87% (94%) of the data under comparison. We assume that the cloud cover from the TSI has an uncertainty level of 5-10% according to the statistics. However, since aerosols can cause errors in the cloud cover estimation by enhancing the aureole radiation due to strong forward scattering, it is necessary to examine the performance of the TSI cloud mask in association with our study.

To this end, we computed the cloud cover for the circum-solar areas with varying angular distances (A_d) from the Sun's position. As shown in Fig 5.1, A_d was computed for both all pixels composing the TSI image and for the circum-solar area within an angular distance of 10-20^o (area A1; see Fig 5.2b), 10-30^o (area A1+A2), 10-40^o (A1+A2+A3), and so on. In addition to cloud covers for the different circum-solar areas, we also computed cloud covers for circular areas of the same zenith angles but different azimuth angles at 90-degree intervals (0, 90, 180, and 270 degrees from the Sun's azimuth angle; see Fig 5.2a). Much less problem is expected for circular areas in domain 1-3.

Assuming that the cloud cover has statistically equal chances of occurrence for the four regions defined in Fig 5.2a, more cloud cover in the circum-solar area (azimuth ID #0) can be considered an artifact in the cloud cover estimation due to the uncertainty in cloud discrimination near the Sun's position. This seems to be the case as revealed in Fig 5.3 showing a comparison of the innermost circum-solar area (10-20^o; A1) with its counterparts at different azimuth angles (but with equal zenith

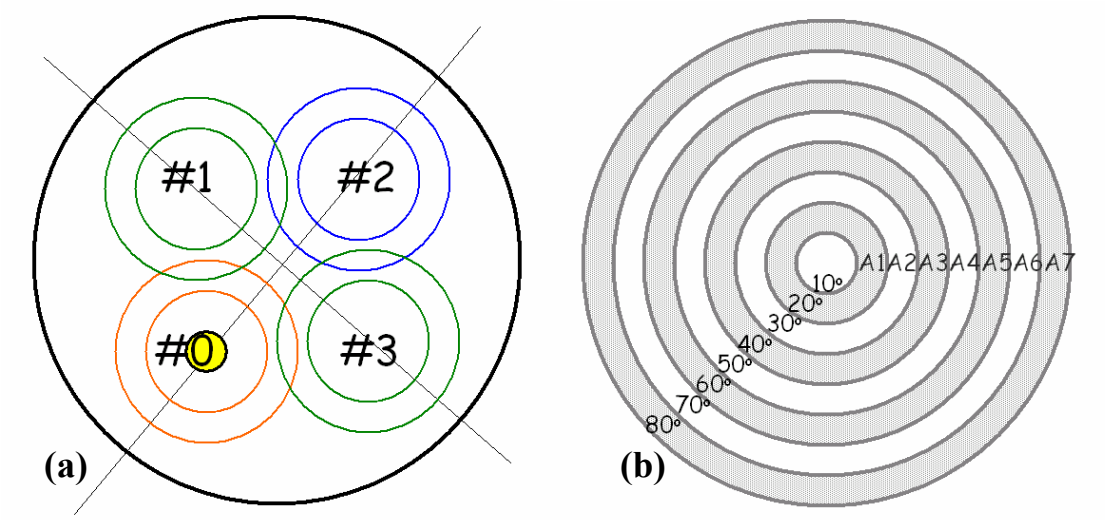

Fig 5.2. (a) Definition of azimuth ID for computing cloud cover from a TSI cloud mask image. The position of the sun of the image is marked by a yellow circle. (b) Definition of circular area (a doughnut shape) over which cloud cover is computed.

angle) for all sky conditions (upper four panels in Fig 5.3). A high frequency of cloud cover around the Sun is seen, in contrast to the other cases. Azimuth ID #1~#3 shows ~40% occurrence of cloud-free conditions while less than 10% occurrence of clear condition is observed around the Sun (azimuth ID #0). Note that the assumption of equal chances of cloud occurrence seems to be valid since all the azimuth domains except for ID #0 showed virtually equal cloud cover frequency distributions. The lower four panels of Fig. 5.3 present similar statistical results derived when the AERONET AOT was acquired. Azimuth ID #1~#3 shows an 80% occurrence of cloud-free skies, while only about 15% occurrence of clear condition is observed around the Sun (azimuth ID #0). 30% occurrence of very high cloud cover (>0.95)

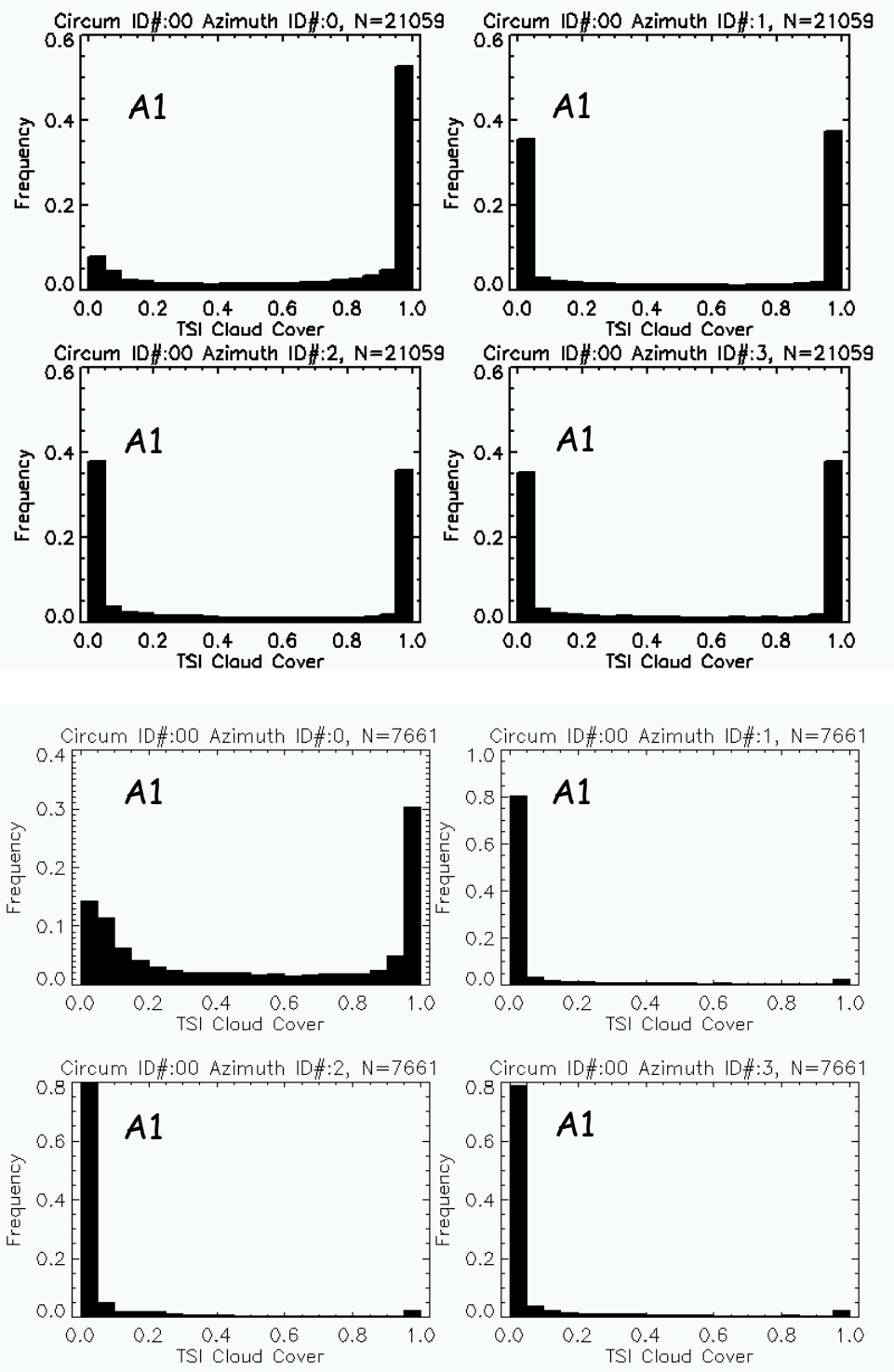

Fig 5.3. Histograms of TSI cloud cover for inner circular area with angular distance between 10-20 degree (A1 in Fig 5.2) from the center of respective azimuth ID. The upper four panels are statistics for all sky conditions while the lower four panels for conditions coincident with the AERONET AOT measurements.

around the Sun indicates that the problems with the TSI cloud cover are very serious in this area. However, this area constitutes a small portion of the whole sky, so the effect on the whole sky cover may be much smaller than shown in Fig 5.3. Thus, we performed a similar test for larger circular areas with different inner-circular areas removed. That is, we computed cloud cover for the areas with a radius between 10-80º, 20-80º, 30-80º, and 40-80º. Figure 5.4 shows the comparisons of cloud cover computed for the four areas in two azimuth IDs, #0 and #2. It clearly shows that a significant bias exist if the innermost circum-solar areas (10-30º; A1 and A2) are included in cloud cover calculations. Nearly identical histograms between the two azimuth IDs are obtained when areas A1, A2, A3 (10-40º) are excluded.

The results of the tests above suggest that removal of the circum-solar area within a 40º angular radius helps remove the overestimation of TSI cloud cover for the whole sky. However, since such an area occupies a significant portion of the sky and the problem of the TSI cloud mask does not happen all the time, discarding such a large area may result in the loss of much useful data. So, we recommend removing 30º of the circum-solar area instead of 40º as a compromise based on Fig 5.4.

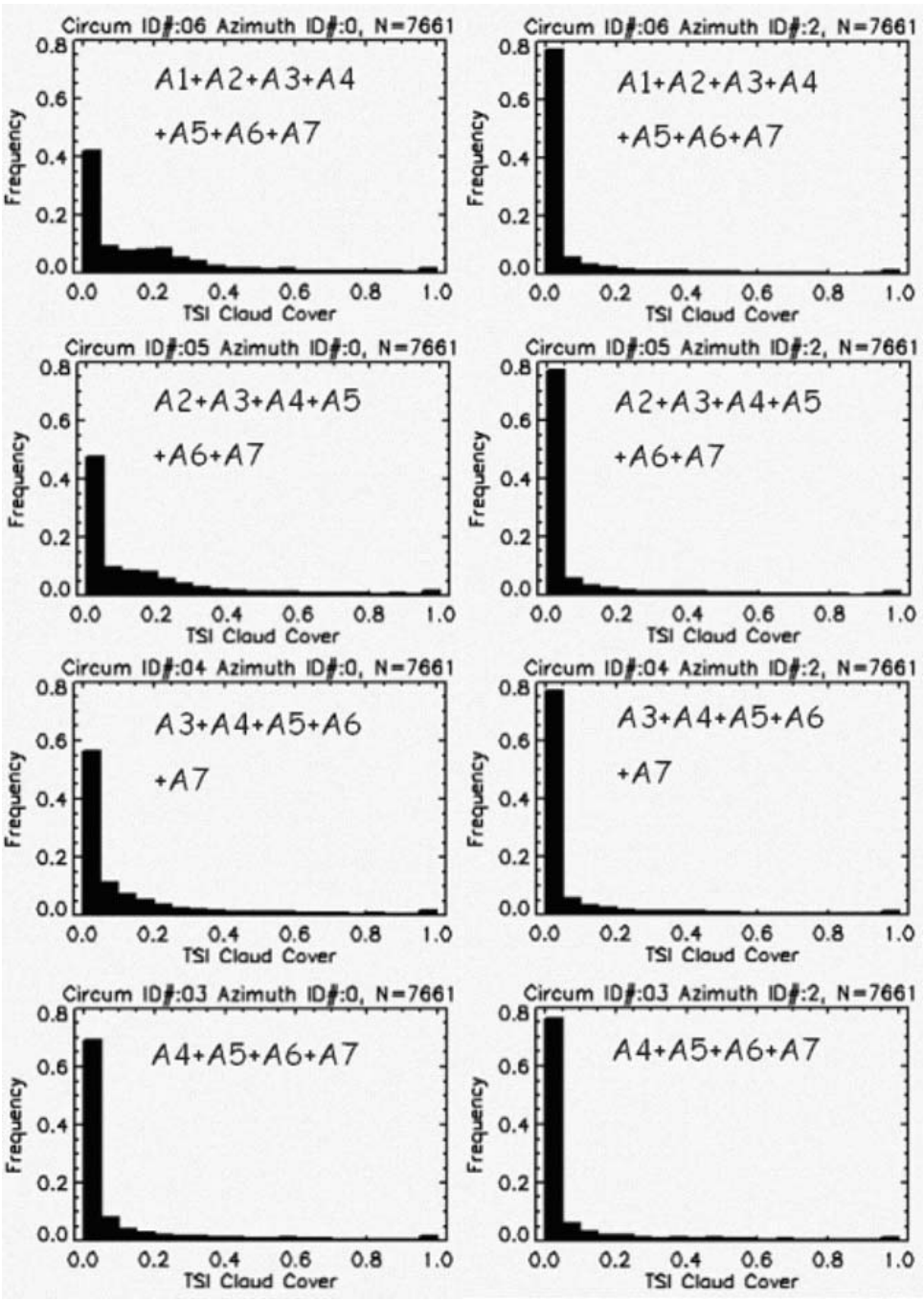

Fig 5.4. Histograms of TSI cloud cover computed for different inner circular areas and different azimuth domains.

5.2.3. CART Raman Lidar

The CART Raman Lidar (CARL) is a custom-designed instrument developed for the ARM program by the Sandia National Laboratories. CARL is an active, ground-based laser remote sensing instrument that measures the profiles of water vapor, aerosols, and clouds in the troposphere (Goldsmith et al., 1998). It is composed of a Nd:YAG (Yttrium Aluminum Garnet; $Y_3Al_5O_{12}$) laser that transmits light pulses at 355 nm with 400 mJ at 30 Hz and a receiving telescope of 61 cm diameter. It collects the light backscattered by molecules and aerosols at the laser wavelength and the Raman scattered light from water vapor (408 nm) and nitrogen (387 nm) molecules. The profiles of aerosol backscattering and extinction coefficients, water vapor mixing ratio and relative humidity are derived on a routine basis using a set of automated algorithms (Turner et al., 2002). Aerosol scattering ratio profiles can be computed using the Raman scattered light (387 nm) from nitrogen molecules and the backscattered light at 355 nm. Then, the profiles of aerosol backscattering cross-sections are computed using the aerosol scattering ratio profile and a molecular scattering cross-section profile derived from a density profile of the atmosphere. Aerosol extinction profiles are then computed by taking the derivative of the logarithm of the Raman scattering signal from nitrogen with respect to the lidar range. Water vapor mixing ratio can be computed by taking the ratio of the Raman scattered signal from water vapor to that from nitrogen molecules. Then, temperature profiles from the Atmospheric Emitted Radiance Interferometer (AERI) are used together with the water vapor mixing ratio profiles to compute the profiles of relative humidity. Further details are documented by Ferrare et al. (2004) and Turner (2004).

5.2.4. MODIS Aerosol Product over Land

The MODIS aerosol products are generated by two independent retrieval algorithms, one for aerosols over ocean (Tanré et al., 1997) and the other for aerosols over land (Kaufman et al., 1997). Since the area of interest in this study is Central Facility (CF) of the ARM SGP site, which is located inland (36.6°N, 97.5°W; Oklahoma, United States), the MODIS aerosol land product and algorithm are dealt with here. Details of the MODIS ocean aerosol algorithm and ocean aerosol products are described in Chapter 3. The MODIS product is Collection 004 of Level 2 (named as MOD04) data set with spatial resolution of 10x10km at the nadir. The MODIS land aerosol product includes AOT, Angstrom exponent, AOT ratio of small mode aerosols, aerosol mass concentration, and so on and also provides cloud fraction, transmitted and reflected fluxes. The parameters used in this study are AOT and cloud fraction.

The aerosol retrieval algorithm for over-land aerosols was documented by Kaufman et al. (1997) and updated by Remer et al. (2005) for the Collection 004 data. The aerosol products are retrieved reflectances measurements made at three MODIS bands (0.47, 0.66, and 2.13μm) with 500m-resolution pixels. For the initial retrievals of 20x20 adjacent pixels over a 10x10km box (at nadir) cloud screening is applied to discard contaminated pixels. The cloud screening procedures follow first the standard MODIS cloud masking (MOD35; Platnick et al., 2003) and additional tests. These tests are based on spatial variability to identify low-level clouds (Martins et al., 2002)

and the 1.38μm-reflectance to identify high-level clouds (Gao et al., 2002). Snow/Ice pixels and pixels with large water body such as rivers and lakes are discarded using the MOD35 snow/ice mask and the Normalized Difference Vegetation Index (NDVI). Then, only the retrievals with surface reflectance less than 0.25 are retained for which the underlying surface is considered as dark enough to enable valid retrieval. . The brightest 50% and the darkest 20% of pixels of 0.66μm-reflectance are discarded for being potentially contaminated by clouds, or bright surfaces or cloud shadows. When the number of remaining pixels is greater than 12 (3% of the original 400 pixels) the reflectances at the three MODIS bands are averaged to denote the apparent reflectances of cloud-free pixels in the box. These averaged reflectances are then used for the surface reflectance inference and the aerosol retrievals. Surface reflectance at 0.47 and 0.66μm is determined from 2.13μm-reflectance using the empirical relationships proposed by Kaufman et al. (1997). Initial retrievals are performed based on a generic continental aerosol model to estimate AOT and path radiance at 0.47 and 0.66μm. A more appropriate aerosol model is then selected among the prescribed dynamic aerosol models (Kaufman et al., 1997; Remer and Kaufman, 1998; Remer et al., 2005) according to the spectral path radiance and geographical location from which the retrievals are revised to produce the final MODIS aerosol product over land.

The MODIS aerosol product over land has been evaluated using the AERONET data (e.g., Chu et al., 2002; Ichoku et al., 2005; Levy et al., 2005; Remer et al., 2005). The overall AOT errors ($\Delta\tau$) of $\Delta\tau = \pm 0.05 \pm 0.2\tau$, which was predicted by Kaufman et al. (1997), turned out to be reasonable estimation (Chu et al., 2002;

Ichoku et al., 2005). Remer et al. (2005) showed that the one-standard deviation of MODIS AOT falls within an uncertainty range of $\Delta\tau = \pm 0.05 \pm 0.15\tau$. In general, AOT was overestimated over land for low aerosol loading but underestimated for high aerosol loading in comparison with AERONET AOT (Levy et al., 2005; Ichoku et al., 2005). The errors were attributed to incorrect surface reflectance and/or use of inadequate aerosol models (Ichoku et al., 2003; Ichoku et al., 2005; Remer et al., 2005; Levy et al., 2005). Cloud contamination is another major source of uncertainty. Kaufman et al. (2005) argued that residual cirrus results in an overestimation of AOT by 0.015±0.003 and the errors caused by cloud contamination are close to 0.02 over the global oceans. Little effort has been reported for evaluating the cloud contamination over land, except for indirect inference of Kaufman et al. (2005) based on the correlation between the discrepancies of MODIS and AERONET AOT and cloud fraction. Thus, more direct approach is necessary to quantify the problem.

5.3. Correlation of AERONET AOT and Cloud Cover Measured from the Ground

5.3.1. Observed Correlation and Possible Causes

Cloud cover data from the TSI were first matched with AERONET AOT data, which were only retrieved for clear skies in the direction of the sun. The AERONET AOT was plotted as a function of the cloud cover in Fig 5.5. It is clear that the AERONET AOT increases with increasing cloud cover. In addition, the slope is higher than that reported from satellite-retrieved quantities (e.g., Ignatov and Nalli, 2002; see also Section 5.4). What causes this correlation between AOT and cloud cover? In theory,

several factors may bring about such the correlation: 1) aerosol humidification or aerosol swelling effects associated with increasing RH coincident with increasing cloud cover, 2) increasing aerosol concentration due to air convergence, 3) increasing number of cloud-processed particles, 4) new particle genesis, 5) cloud contamination in the AERONET AOT, and 6) an artifact due to the problem of cloud detection using the TSI. In the following subsections, the effects of the above factors are examined in detail.

5.3.2. Effect of the Uncertainty in the Cloud Cover Estimations

Given the difficulties to discriminate clear and cloudy skies around the Sun's position as discussed in Section 5.2, it is necessary to make sure whether the correlation shown in Fig 5.5 is an artifact or not. In addition, it is important to check the effects of our exclusion of data within innermost circum-solar area (<30°) for TSI cloud cover derivation. To this end, we correlated the cloud cover derived for the circum-solar areas with various angular distances (A_d) from the Sun's position (see Fig 5.1) with the AERONET AOT (Fig 5.6). The results show that the correlations between AERONET AOT and TSI cloud cover exist for all the circum-solar areas. The correlation coefficient R for the different circum-solar areas is rather similar (0.58~0.67) while the slopes increase as the circum-solar area increases (from 0.18 to 0.38). It is evident that the AERONET AOT has a stronger relationship with cloud cover - in terms of both slope and correlation coefficients- as the circum-solar area increases. These results indicate that the correlation between AERONET AOT and TSI cloud cover is not an artifact due to the problem of the TSI cloud mask.

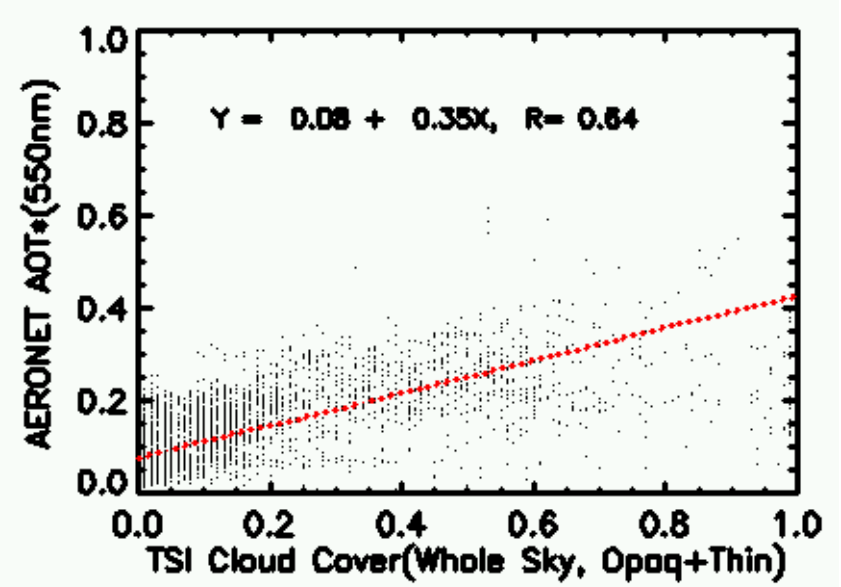

Fig 5.5. AERONET AOT as a function of cloud cover from the TSI. Red dotted line is the least squared fit, and R stands for correlation coefficient.

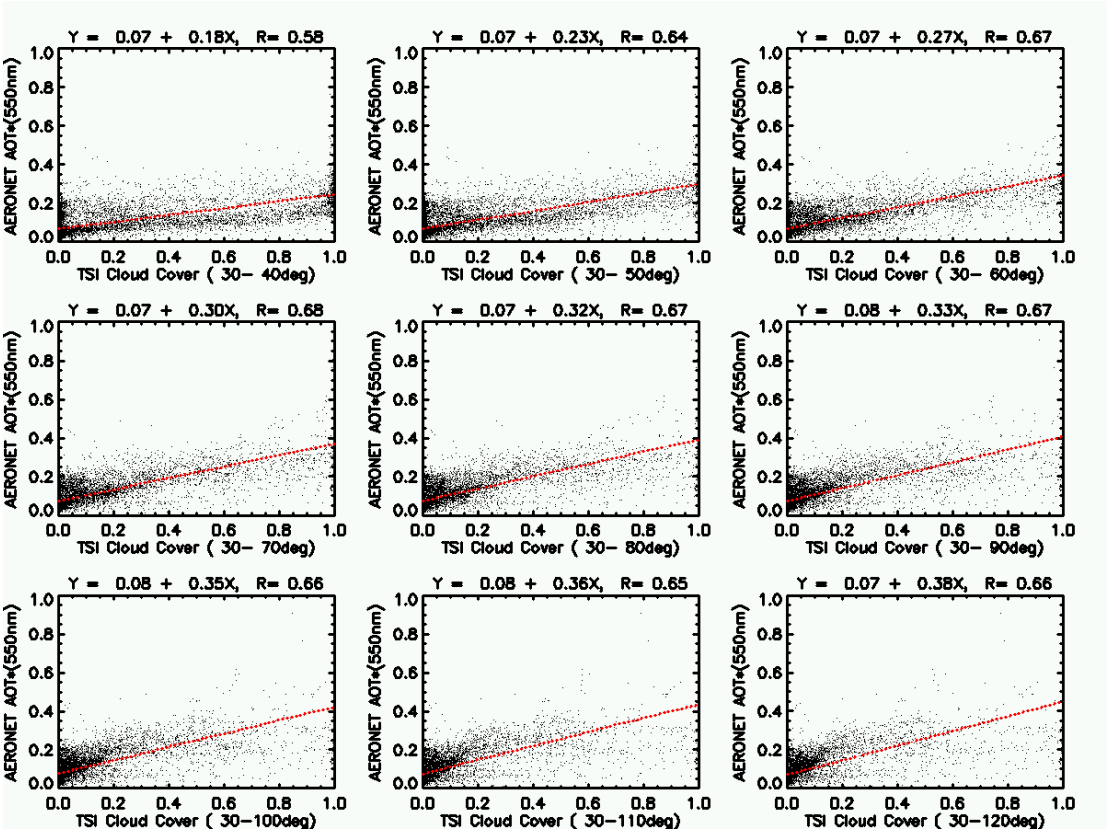

Fig 5.6. Scatter plots of AERONET AOT as a function of TSI cloud cover for the circum-solar areas within different angular distances from the line of sight to the sun.

Otherwise, steeper slopes would have been found for the inner circum-solar areas because the enhanced aureole radiation by aerosol scattering would cause more difficulty in discriminating cloud from the clear sky. On the other hand, the increasing slopes with increasing circum-solar areas may imply that the effects of cloud cover are related to increasing AHE, convergence, or processed/new particles. These effects would not significantly depend on the local clouds around the Sun.

Given the compromise we made regarding the cutoff angle for computing cloud cover, there is still a possibility of a remaining artifact in the TSI cloud cover even after the correction. So, we checked further if there is any dependence of the AOT-cloud cover correlation on the area of the inner circum-solar region discarded for the TSI cloud cover correction. In Fig 5.7, the cloud cover for panel (a) was computed for a circum-solar area within 10-50^{o}, panel (b) within 20-50^{o}, panel (c) within 30-50^{o}, and panel (d) within 40-50^{o}. Note that both the slopes and R showed little change after the data within innermost circum-solar area were excluded for the TSI cloud cover derivation. According to Fig 5.4 and from visual examination, the TSI cloud masking is rarely affected by intense aureole radiation for angular distances greater than 40^{o} except for large solar zenith angles (e.g., >70^{o}). Therefore, we do not expect a significant correlation due to the erroneous TSI cloud mask in panel (d). Thus, the rather invariant slopes, intercepts, and R in Fig 5.7 indicate that the correlation between AERONET AOT and TSI cloud cover is not affected by the problem of the TSI cloud masking near the Sun's position.

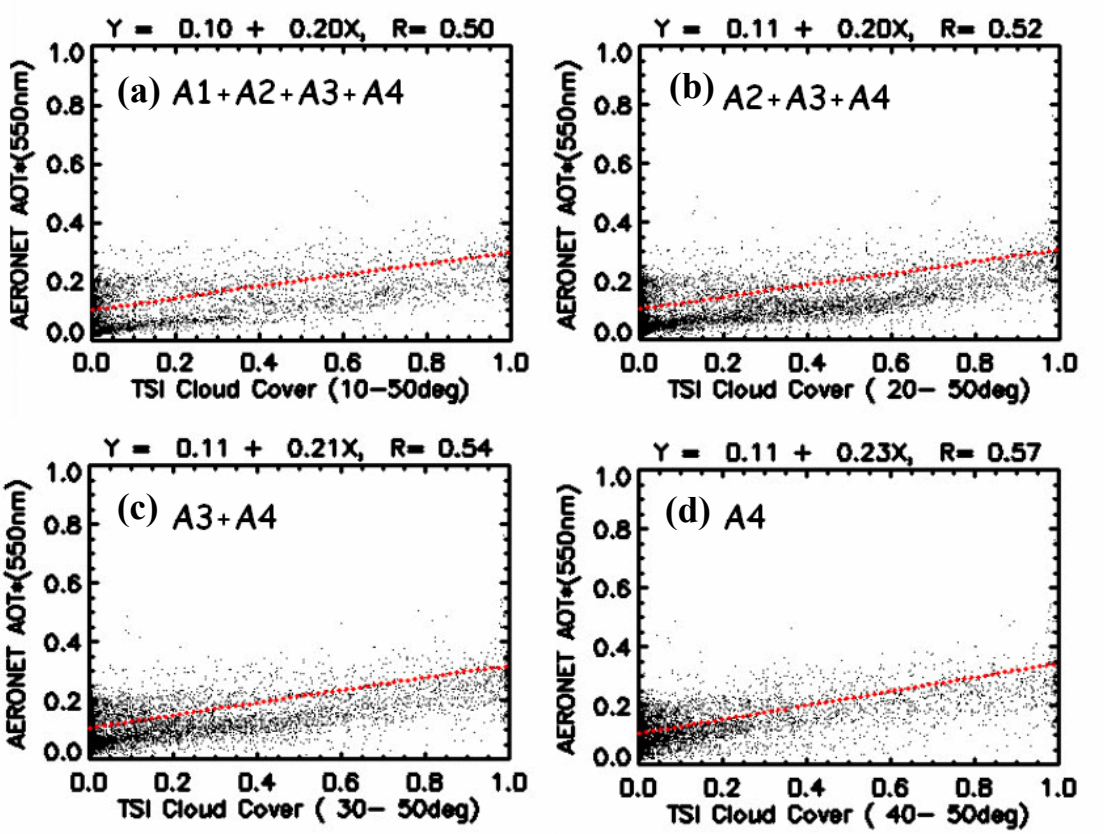

Fig 5.7. AERONET AOT as a function of the TSI cloud cover for circum-solar areas with angular distance from the sun's position between 10 and 50 degree (a), 20-50 degree (b), 20-40 degree (c), and 40-50 degree (d).

5.3.3. The Effect of Relative Humidity

Having shown that the AOT-cloud cover correlation does not originate from an artifact in the TSI cloud cover estimation, the remaining possibilities are the AHE, convergence, cloud-processed particles and new particle genesis. First, we try to examine the relationship between cloud cover, RH, and AOT. Fig 5.8 shows AERONET AOT as a function of 1) TSI cloud cover (top), 2) aerosol extinction weighted column mean RH, <wRH> (middle), <wRH> as a function of TSI cloud cover is also shown (bottom). Variables in the Y-axis are averages over the bins of the X-axis with intervals of 0.05. <wRH> is defined in Eq. (4.9). It was calculated using the profiles of RH and aerosol extinction from the Raman Lidar. Fig 5.8 shows that the AERONET AOT is well correlated to <wRH>, as well as the cloud cover. The slopes are nearly equal (0.24 and 0.23) and the correlation coefficients, R, are similar to each other (0.88 and 0.92). However, the intercepts are somewhat different (0.12 and 0.05). Interestingly, however, the slope and correlation between <wRH> and cloud cover are very low (slope=0.13, R=0.64). It should be noted that the dynamic range of the binned average of <wRH> against TSI cloud cover is confined between 0.4 and 0.7 throughout the cloud cover range (0 to 1). This result indicates that a cloud cover increase is not necessarily accompanied by an increase in column RH or vice versa. <wRH> and cloud cover appear independent from each other. Thus, the comparable correlations of the two variables with AOT are likely to be associated

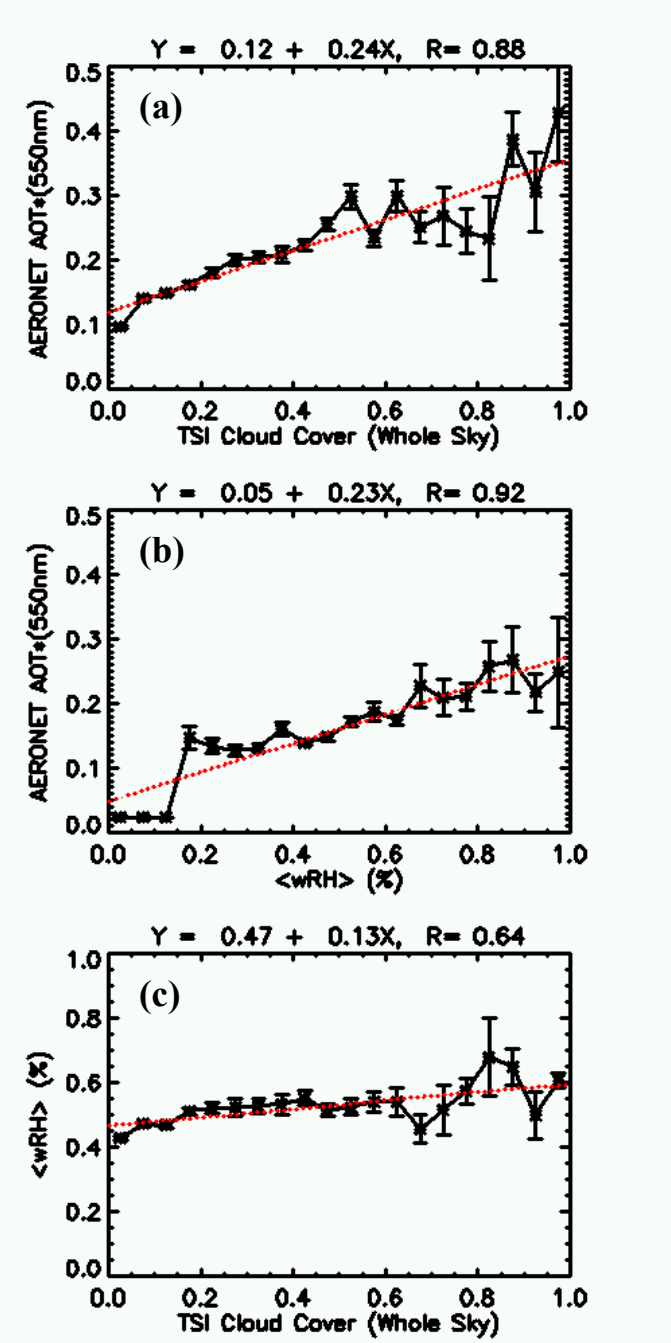

Fig 5.8. (a) Binned average of AERONET AOT as a function of TSI cloud cover, (b) binned average of AERONET AOT as a function of aerosol extinction weighted column mean RH, <wRH>, (c) and binned average of <wRH> as a function of TSI cloud cover.

with different factors. At this point, we may speculate that cloud-processed particles (and new particles) may be related to the correlation between AOT and cloud cover, while the AHE is linked to the correlation between AOT and <wRH>. Both correlations may be associated with a third variable such as air convergence that can cause increases in cloud cover, aerosol and water vapor.

It is very difficult to determine the contribution of the AHE to the AERONET AOT since it requires vertical profiles of RH and aerosol properties (e.g., profiles of aerosol scattering and absorption coefficients at an ambient, low RH). In Chapter 4, we showed that the AHE over the ARM SGP site is a function of a column mean RH. We use aerosol extinction weighted column mean RH, <wRH>, the column aerosol humidification factor (AHF), R(RH), and the AHE as defined in Eq. (4.9), (4.11) and (4.13). By combining Eq. (4.11) and (4.13), the AHE can be rewritten as:

$$AHE = \frac{R(RH) - 1}{R(RH) - 1 + 1/\omega_0}, \tag{5.1}$$

where ω_0 is the column mean single scattering albedo at a dry condition (RH~40%). We use the aerosol extinction at 355 nm, RH profiles derived from the Raman Lidar (Turner et al., 2002) and the parameterized relationship between <wRH> and AHE, which was proposed in Chapter 4. In presence of clouds or very humid layer it was shown that the column AHF over the SGP site can be represented by Eq. (4.15).

Thus, the AHE can be inferred by combining Eq. (4.15) and (5.1). The single scattering albedo is 0.95, which is the average observed from the AOS at the SGP site (Sheridan et al., 2002). The AHE is not sensitive to the single scattering albedo for R(RH)<3. Estimations of the AHE using this method may be subject to errors due to the variability of the aerosol hygroscopicity since the methodology is based on the

connectivity between aerosols and RH (i.e., <wRH>). However, since a large amount of data are available from the Raman Lidar, a statistically significant number of match-ups with AERONET and TSI measurements can be obtained, enabling the examination of the statistical relationship between AOT and cloud cover. The contributions of the AHE to the AERONET AOT and the AERONET AOT without the AHE are shown in Fig 5.9. The AOT due to the AHE is nearly zero for <wRH> less than 40% and sharply increases for <wRH> greater than 80%. From Fig 5.8 (b) and Fig 5.9 (a), it can be seen that the AHE contributes up to 30% of the AOT on average. Fig 5.9 (b) shows estimations of the AERONET AOT with the AHE contribution removed. It is obvious that the AOT dependence on <wRH> disappears when the AHE is removed from the AERONET AOT. Note that the parameterization of the AHE as function of <wRH> was derived solely from the IAP observations and is independent from the AERONET and Raman Lidar measurements.

Having successfully removed the AHE from the AERONET AOT, the AOT due to the AHE and without the AHE are correlated with the TSI cloud cover in Fig 5.10. Interestingly, both AOT show a significant correlation with the cloud cover. However, the slope for the AOT due to the AHE (0.07) is roughly half of that for the AERONET AOT without the AHE (0.16), while the correlation coefficient is similar (0.79 and 0.83). This result shows that the AHE contributes about one third of the slope for the AERONET AOT and TSI cloud cover relationship. Other factors affecting the AOT-cloud cover correlation must be at play. As discussed in section 5.2.1, any cloud contamination that may exist in the AERONET AOT would be due to thin, steady clouds (cirrus and some low clouds according to our visual

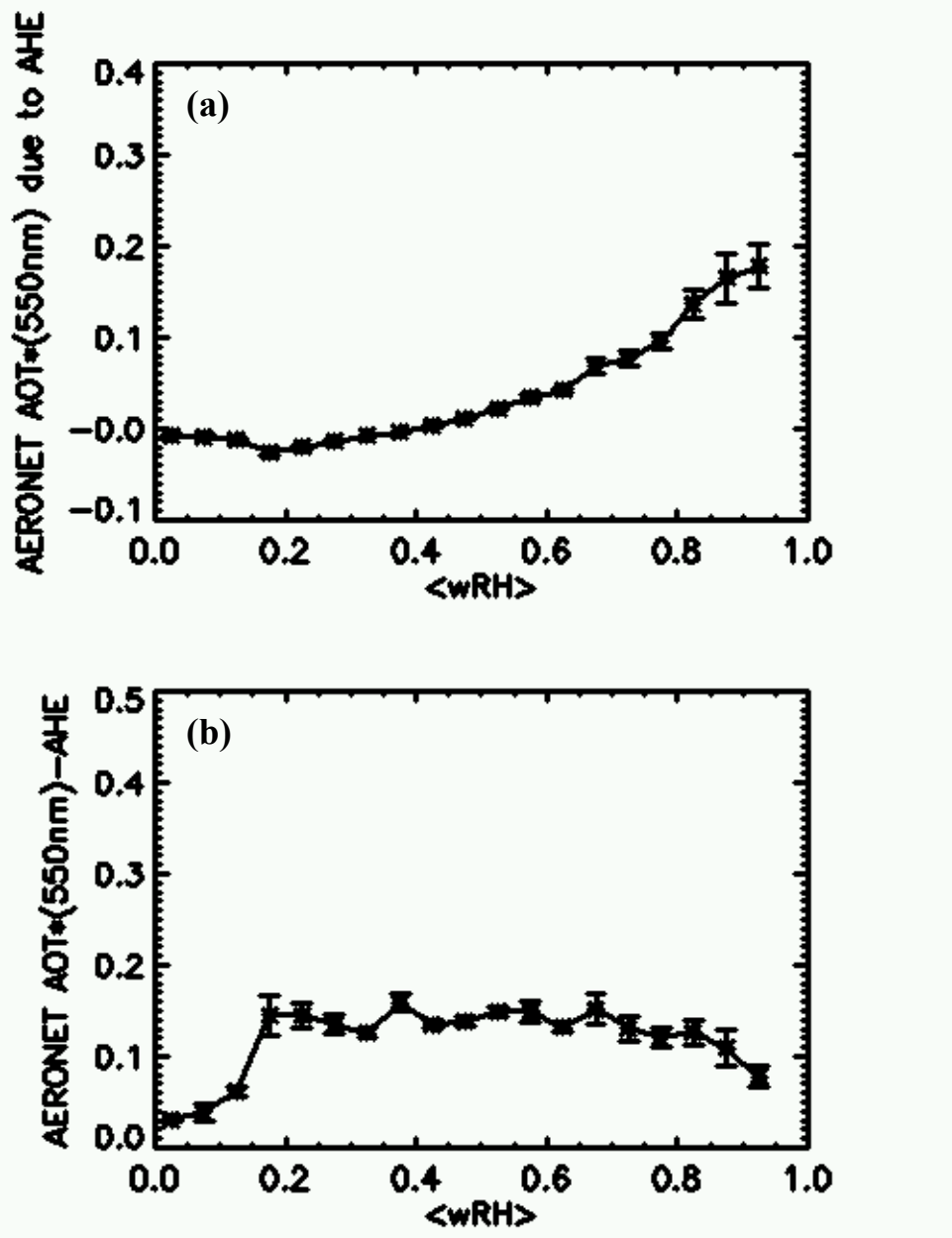

Fig 5.9. (a) Binned average of AERONET AOT due to the aerosol humidification effect (AHE) as a function of <wRH>. (b) Same as (a) but for AERONET AOT without the AHE.

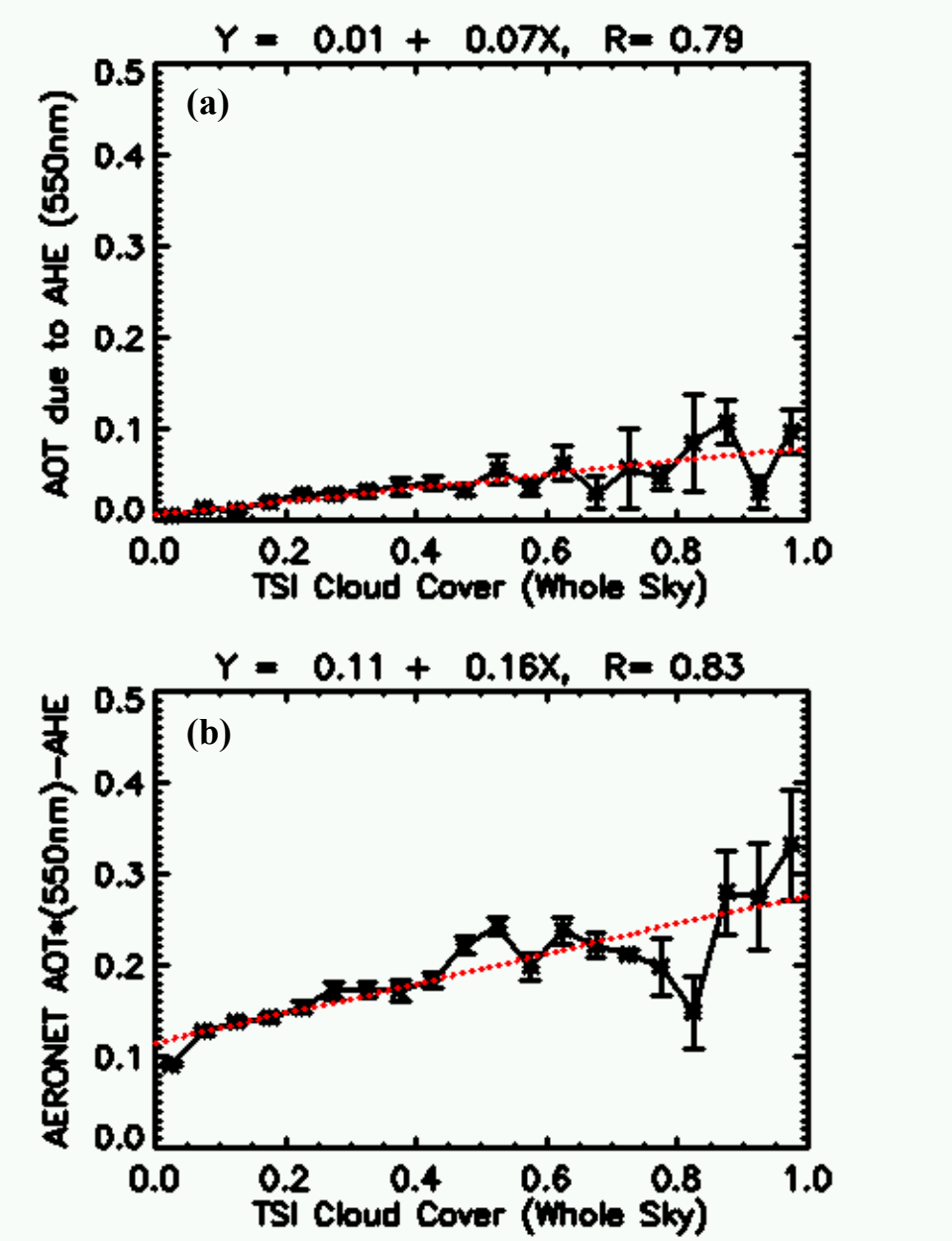

Fig 5.10. (a) Binned average of AERONET AOT due to the AHE as a function of TSI cloud cover. (b) Same as (a) but AERONET AOT without the AHE.

examination) while, the TSI cloud mask also often fails to detect such thin clouds. Therefore, cloud contamination is not likely the major contributor to the observed correlation between the AERONET AOT and TSI cloud cover. Otherwise, an increase in the TSI cloud cover should be linked to an increase in cloud optical thickness (COT) for the persistent, thin clouds that were not detected by the AERONET cloud-screening algorithm. Thus, we conclude that cloud contamination does not significantly affect the correlation between the TSI cloud cover and the AERONET AOT although we acknowledge that the AERONET AOT is not free from cloud contamination. So, only the effects of convergence, cloud-processed particles, and new particle genesis on the AERONET AOT are discussed in the following subsections as candidates to explain the remaining AOT-cloud cover correlation.

5.3.4. The Effects of Convergence and Cloud-Processed /New Particles

It is necessary to use three-dimensional information concerning aerosols and winds to quantify the effects of convergence. This may be done by simulations of an aerosol chemistry and transport model. However, since such model or simulation results with a mesoscale resolution are not available to us, we use wind and water vapor fields from a mesoscale model output, the Rapid Update Cycle (RUC; Benjamin et al., 2004; http://maps.fsl.noaa.gov/), which runs operationally at the National Centers for Environmental Prediction (NCEP). The RUC is an operational atmospheric prediction system comprised of a numerical forecast model and an analysis system to initialize the model. It has a high temporal resolution (one hour)

and assimilates data from numerous measurements by commercial aircraft, wind profilers, rawinsondes, satellites, etc. The resolution of the RUC has been improved from 60 km to 40 km to 20 km. The RUC data we use in this study has a 20-km resolution (hereinafter referred to as RUC20).

We begin with an assumption that the convergence of wind and/or water vapor (specific humidity) can be used as a proxy of the convergence of aerosols. Convergence of wind, water vapor and aerosol may be written as follows:

$$-\nabla \cdot \vec{U} \ , \tag{5.2}$$

$$-\nabla \cdot \left(q\vec{U} \right) = -\vec{U} \cdot \nabla q - q\nabla \cdot \vec{U} \ , \tag{5.3}$$

$$-\nabla \cdot \left(N^a \vec{U} \right) = -\vec{U} \cdot \nabla N^a - N^a \nabla \cdot \vec{U} \ , \tag{5.4}$$

where $\vec{U}$, q, and N^a are the three-dimensional (3-D) wind vector, specific humidity, and aerosol number concentration, respectively. One can expect that the assumption would be valid when wind convergence is dominant or when water vapor advection is dominant and proportional to aerosol advection. On the other hand, it becomes invalid when aerosol advection (the first term on the right hand of Eq. 5.4) is dominant and is not correlated with water vapor advection.

Six sets of aerosol extinction profiles obtained from the IAP and the AOS, as well as the 3-D convergence of water vapor and wind are shown in Fig 5.11. In each set of measurements, three aerosol extinction profiles (for Dp<1μm, Dp<10μm at ambient RH, and for Dp<1 at RH=40%) are shown in the figure. Since the IAP system has a size cut-off for Dp<1 μm, a simple correction was done to account for

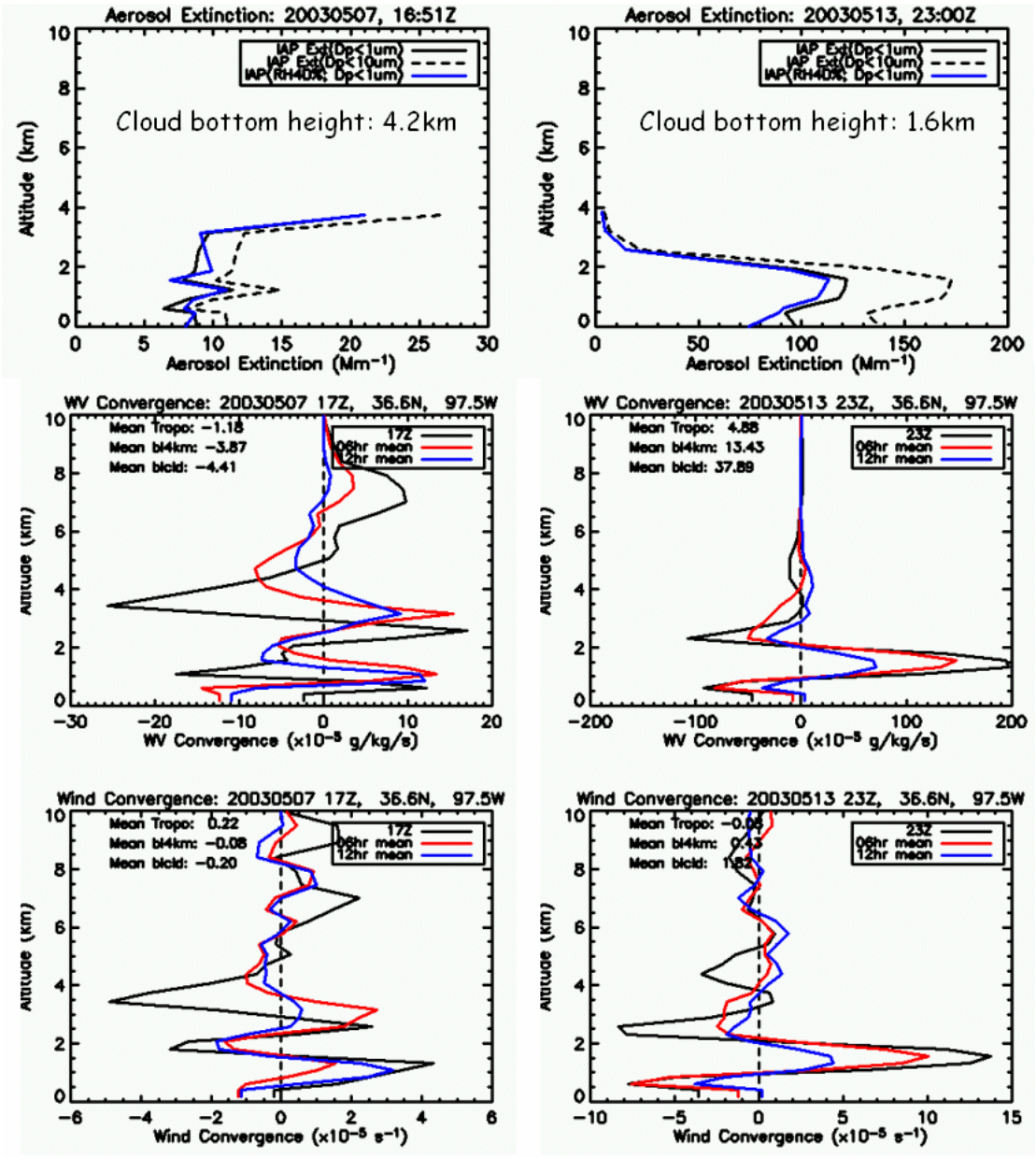

Fig 5.11. (a) Upper panels: aerosol extinction profiles from the IAP on May 7, 2004 (left) and May 13, 2003 (right). Aerosol extinction profile for submicron particles (Dp<1μm) at ambient RH and R=40% are shown in black and blue solid lines, respectively. Aerosol extinction profiles for particles with Dp<10μm at ambient RH is given in black dashed line. Middle panels: Corresponding profiles of water vapor over the SGP CF computed from the Rapid Update Cycle data at a 20km horizontal resolution (RUC20). Three profiles are plotted for the time of the IAP observation (black), and 6 hour- and 12 hour-averages ending at the IAP observation time (red and blue solid lines, respectively). Lower panels: same as middle panels but for wind convergence.

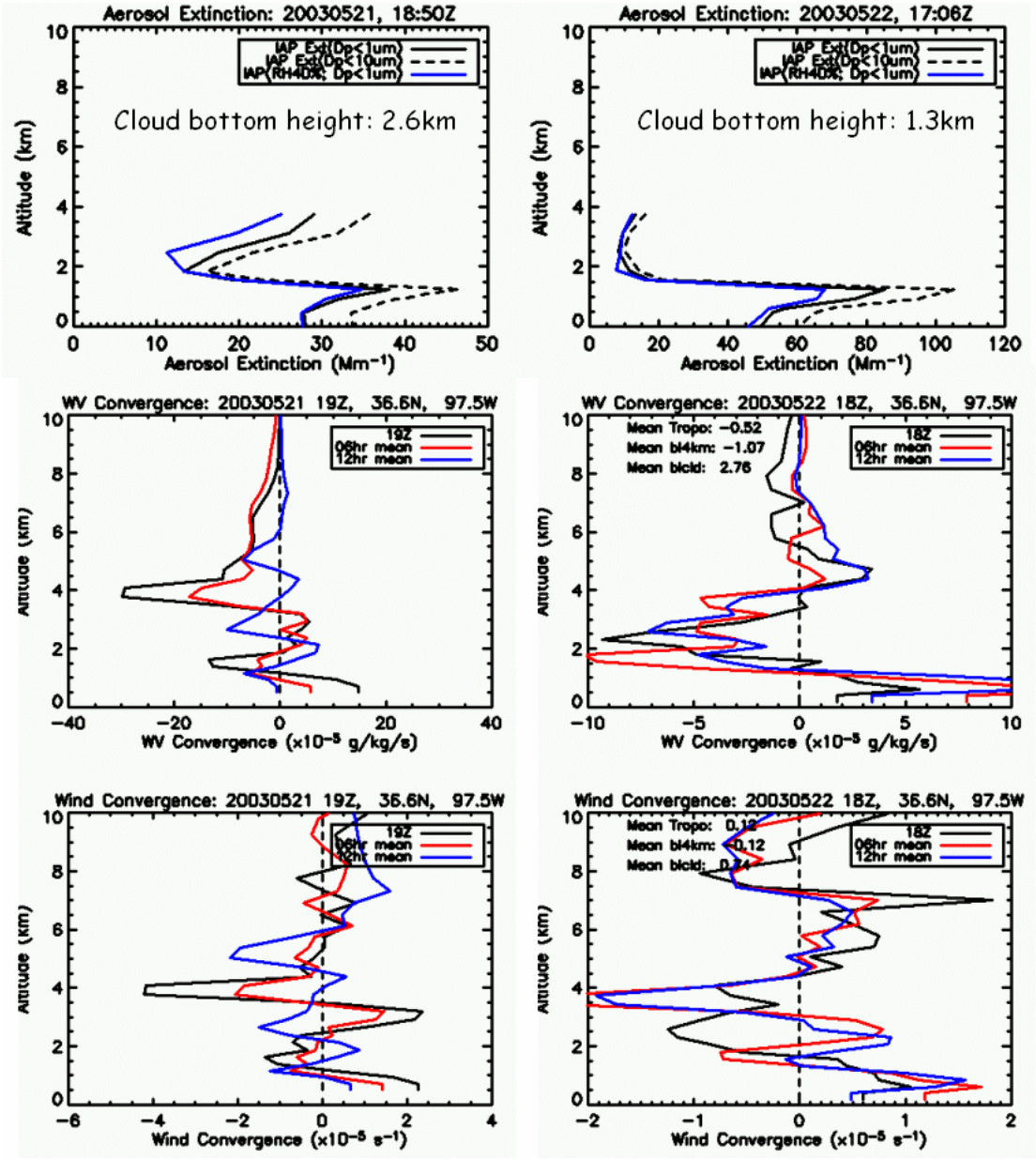

Fig 5.11. (b) The same as Fig 5.11 (a), but data for May 21, 2003 (left panels) and for May 22, 2003 (right panels).

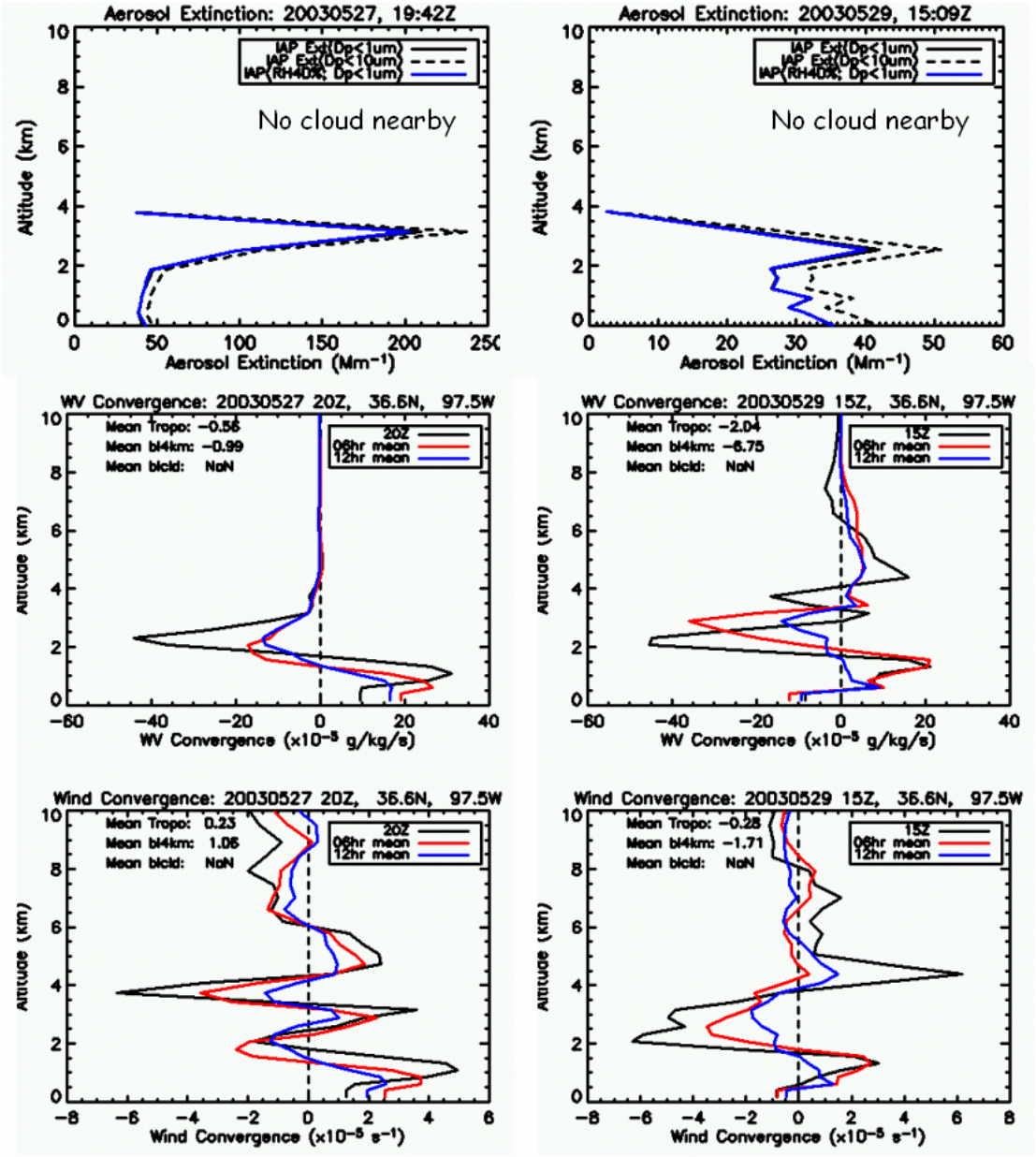

Fig 5.11. (c) The same as Fig 5.11 (a), but data for May 27, 2003 (left panels) and for May 29, 2003 (right panels).

super-micron particles, as previously described in Chapter 4. Again, the estimated aerosol extinction profiles at ambient RH for Dp<10 μm will guide represent the upper limits of the real extinction profiles. Also, aerosol extinction profiles at a fixed RH (40%) are presented to limit the aerosol humidification effects. As for the convergence, instantaneous, 6-hour averaged, and 12-hour averaged profiles are shown. Fig 5.11 demonstrates that the aerosol extinction profiles are well correlated with the 3-D convergence profiles of water vapor and/or wind, especially on May 7, 13, 21 and 22 when both water vapor and wind convergence profiles track well with the aerosol extinction profiles. While on May 27, the water vapor convergence does not agree with the aerosol extinction profile in general; but a peak in the wind convergence at 3 km coincides with the peak of the aerosol extinction profile at the same altitude, indicating wind convergence plays a certain role in this case. It is worth noting that the strongest peak in the wind convergence is located at 1 km and there is no corresponding peak in the aerosol extinction profile. Negligible aerosol humidification (virtually no difference between ambient and dry aerosol extinction coefficients and a humidification factor close to unity – not shown in the figure) and relatively larger aerosol extinction values on this day seem to indicate the presence of transported hydrophobic aerosols like smoke, rather than particles originating from local sources. As for the May 29 case, the locations of the water vapor convergence peaks correspond to those for aerosol extinction although the strength of the peaks are not proportional to each other. It is not clear whether the aerosol extinction peak is a residue from the transported aerosols on May 27, which is likely as the hygroscopic factor is close to unity (not shown in the figure). It should also be noted that the

altitudes of the aerosol extinction peaks are coincident with those of clouds (May 7, 13, 21, and 22; no clouds for the other two days). Sky conditions including cloud cover and cloud-bottom height for the six cases shown in Fig 5.11 are presented in Table 5.1.

Table 5.1. Sky conditions for the cases shown in Fig 5.11.

Date	Cloud Cover*	Cloud Bottom Height&	Remark
May 7, 2003	0.4	4.2km (Cu) 7.2km (Ac)	Sparse low cloud (Cu), Ac dominant
May 13, 2003	0.1	1.6km (Cu) 11.3km (Ci)	Dissipating small clouds
May 21, 2003	0.9	2.6km (Sc)	Nearly overcast
May 22, 2003	0.1	1.3km (fair weather Cu)	Repetitive generation /dissipation of clouds
May 27, 2003	0.0	No clouds nearby	-
May 29, 2003	0.1	No clouds nearby 11km (Ci)	Very thin Ci

*Cloud cover in fraction unit (i.e., overcast is 1.0) obtained from ARM SGP Meta Data System (MDS; available at http://www.db.arm.gov/cgi-bin/MDS/Search.pl).
&Cloud bottom height from ARSCL based on Micro-Pulse Lidar (MPL)
Note: Ac, Cu, Ci, and Sc stand for altocumulus, cumulus, cirrus, and stratocumulus, respectively.

The coincident occurrence of cloud and aerosol extinction peaks may both result from the atmospheric convergence, implying that the atmospheric dynamics plays a role in shaping the vertical distribution of aerosols. . We attempted to correlate the model computed convergence (horizontal/2-D and 3-D) and the AERONET AOT (result not shown here); However, no significant correlation was found except for a very weak tendency of the AOT to increase with increasing

convergence. This may be caused either by little influence of convergence or by inadequacy of water vapor or wind convergence as a proxy of aerosol convergence. In fact, it is very difficult to link the model computed convergence to the AERONET AOT since we have no information about the 3-D aerosol distribution at the time of the AERONET observations and convergence that is not weighted by the aerosol distribution can cancel out if averaged over the column. Thus, a complete 3-D aerosol transport/chemistry model with mesoscale simulation capability is necessary to quantify the effect of convergence and separate it from the effects of clouds (e.g., cloud-processed particles).

Another possibility is that the aerosol peaks near cloud layers are caused by cloud-processed particles (Hoppel et al., 1990) or newly generated particles under a humid environment. In order to see the effects of these factors, AOT derived from the IAP measurements is correlated to the cloud cover estimated from the TSI. The scattering and absorption coefficients at 550 nm and at a low RH (~40%) from the IAP were vertically integrated using a simple trapezoidal scheme as done in Chapter 4. Comparisons between the IAP AOT at low RH for aerosol particles less than 1 μm in diameter and the AERONET AOT are shown in Fig 5.12. The two AOTs are well correlated each other but, obviously, there is systematic differences between them, which originates from the missing contributions of the AHE, super micron sized particles and aerosols above the highest level leg in the IAP measurements. We adjusted the IAP AOTs for Dp<1 μm to that for Dp<10 μm in order to make the IAP AOT comparable with the AERONET AOT. This was done following the correction procedures described in Chapter 4. The resulting AOT may be overestimated because

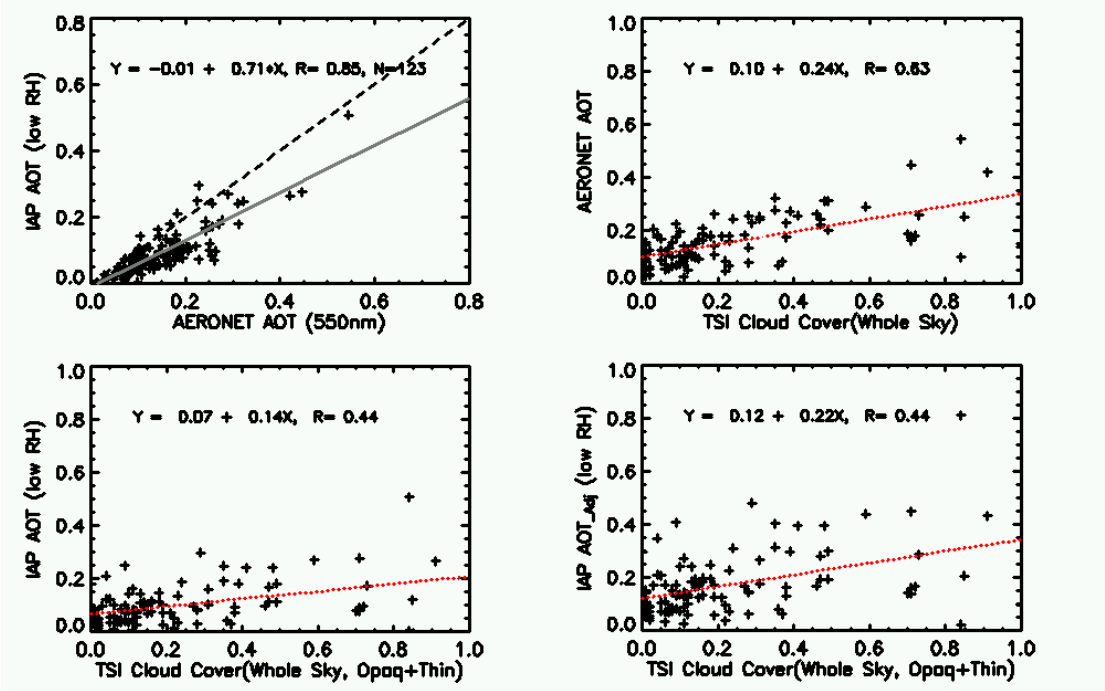

Fig 5.12. Comparison of the IAP AOT at low RH (~40%) with Dp<1μm and AERONET AOT (top-left). AERONET AOT coincident with IAP observations as a function of the TSI cloud cover (top-right). IAP AOT with Dp<1μm (bottom-left) and IAP AOT after aerosol size adjustment to be compatible with Dp<10μm (bottom-right) as functions of the TSI cloud cover, respectively.

large particles tend to reside in the lower portion of the atmosphere unless there are large dust particles aloft (Andrews et al., 2004). Thus, we believe that the true IAP AOT values lie somewhere between the IAP AOTs for Dp<1 μm and for Dp<10 μm. The coincident AERONET AOT and IAP AOTs for Dp<1 μm and for Dp<10 μm are plotted as functions of the TSI cloud cover in Fig 5.12. The three AOTs are correlated with the cloud cover but showing slightly different slopes, intercepts, and correlation coefficients, R. The AERONET AOT has the highest slopes (0.24) and R (0.63), which is expected since the AERONET AOT may be additionally affected by the AHE and cloud contamination that do not affect the IAP AOTs. As mentioned above,

the true IAP AOT values without the AHE would be somewhere between the IAP AOTs before and after the size adjustment, considering super-micron particles.

The correlations between IAP AOTs and TSI cloud cover reflect the effects of convergence, cloud-processed particles, or new particles. As the AHE contributes to about 1/3 (in slope) of the correlation between AERONET AOT and cloud cover (Fig 5.8a and Fig 5.10), the true slope for dry conditions would be around 0.16 if there is no effect of cloud contamination on the AERONET AOT. Thus, we infer that the effects of convergence, processed/new particles contribute more than half (0.14~0.22 compared to the AERONET AOT's 0.24; possibly two thirds) of the slope of the AERONET AOT/TSI cloud cover relationship. By the same token, the contributions of aerosol humidification and cloud contamination are expected to be smaller than half of the slope, and cloud contamination, if any, should be less than 0.03 (<13%). Unfortunately, we are unable to separate the effects of convergence, processed/new particles, and new particle genesis, which requires rigorous measurements of aerosol sizes and chemical substances together with modeling of aerosols' evolutions with time under cloudy conditions. Given the large contributions of the three factors combined together, observation and modeling efforts are very important to further our understanding of the links between clouds and aerosols.

5.4. Correlation of MODIS AOT and Cloud Fraction

In the previous section, ground-based (AERONET) and in-situ (IAP) measurements showed that the correlation between the AOT and the cloud cover is mostly real, rather than artifacts due to cloud contamination. However, it does not

necessarily mean that a similar real correlation exists in satellite retrievals (Ignatov and Nalli, 2002; see Chapter 2 and Fig 5.13). As for the factors that may cause the AOT-cloud cover correlation, 3-D cloud effects and a greater chance of cloud contamination should be considered in addition to the factors affecting the AOT-cloud cover correlation found in ground-based/in-situ observations. Fig 5.13 shows the MODIS AOT and cloud fraction over the ARM SGP site. It is evident that the spatial distributions of the two are positively correlated for the given case. The aerosol humidification effect was estimated using the aerosol extinction and aerosol hygroscopic factor (AHF) profiles measured from the IAP, the 3-D distribution of RH from the RUC20 model, and Eq. (4.15). The horizontal distribution of the aerosol hygroscopicity is assumed homogeneous and the 3-D aerosol distributions are estimated by scaling the IAP aerosol profiles using the MODIS AOT. The original MODIS AOT and AOT without the aerosol humidification effect (AHE) are correlated with the MODIS cloud fraction in Fig 5.14. Similar to the results derived from the AERONET AOT, the AHE is not a major contributor to the dependence of AOT on cloud fraction.

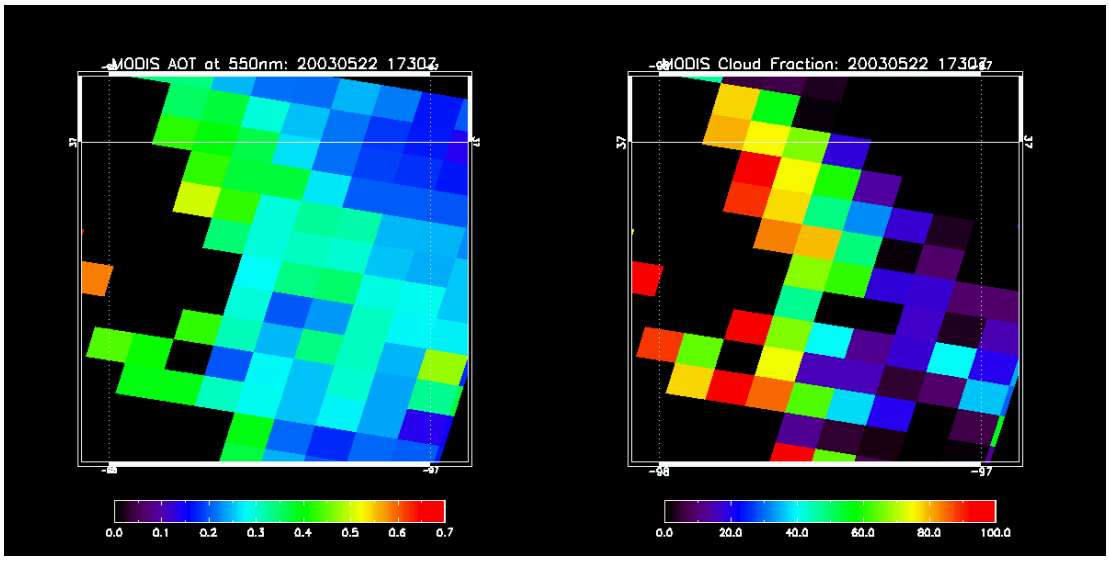

Fig 5.13. MODIS AOT at 550nm over the ARM SGP CART site (left) and cloud fraction (right; May 22, 2003).

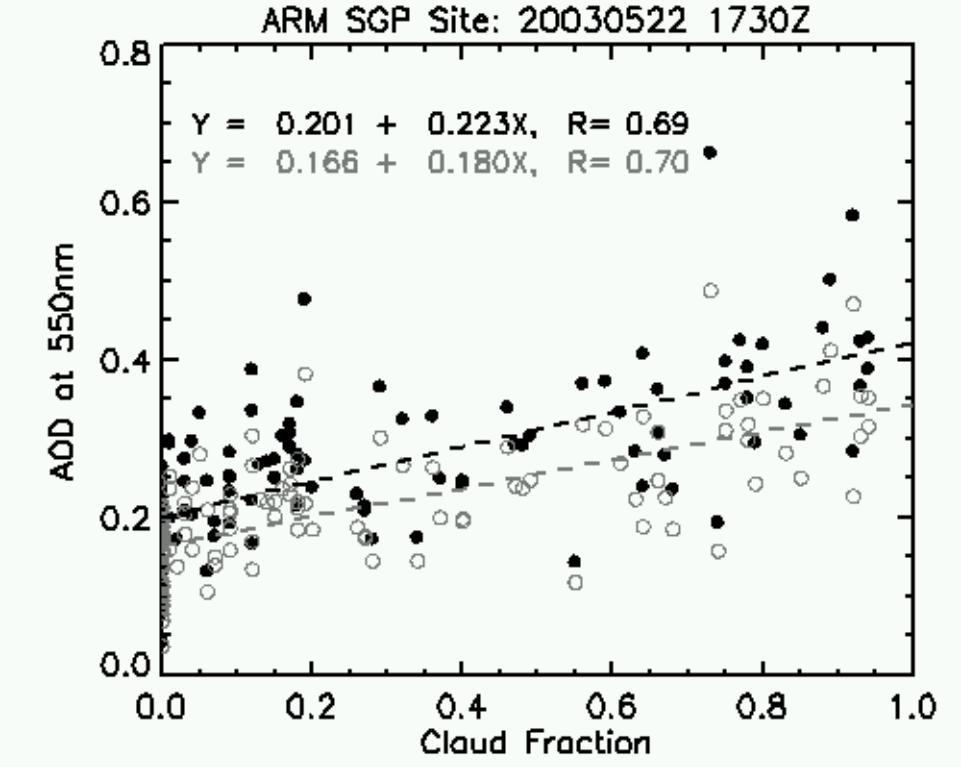

Fig 5.14. Correlation between MODIS cloud fraction and AOT. Black dots and gray open circles represent the original MODIS AOT and the AOT after aerosol humidification effect removed, respectively. Dashed lines are linear fit of respective AOTs.

5.4.1. The Effect of Air Convergence/Divergence

The effect of convergence on the spatial distribution of aerosol is assessed with a few assumptions to roughly estimate the magnitude of aerosol convergence. As discussed in section 5.3.5, water vapor and wind convergences are assumed as proxies of aerosol convergence. Fig 5.15 shows the column (between the surface and 2km) mean water vapor and wind convergences derived from the RUC20 data, noting that aerosols for this case are concentrated below 2km (Fig. 5.11). The convergence distribution pattern is somewhat similar to those of MODIS AOT and cloud fraction shown in Fig 5.13. It is necessary to examine how much air convergence explains the observed spatial variability of MODIS AOT. The continuity equation for aerosols may be written as:

$$\frac{\partial N^a}{\partial t} = -\nabla \cdot \left(N^a \vec{U} \right) + P - L , \tag{5.5}$$

where P and L denote the source and sink of aerosols respectively. Assuming their magnitudes are very small, they cancel out each other the distribution is dominantly affected by aerosol convergence. Then, Eq. (5.5) becomes:

$$\frac{\partial N^a}{\partial t} \sim -\left(N^a \nabla \cdot \vec{U} \right) - \left(\vec{U} \cdot \nabla N^a \right), \tag{5.6}$$

where the first term of the right-hand side (RHS) of Eq (5.6) is the product of wind convergence and aerosol number concentration, and the second term is the aerosol advection by wind. The total number of aerosols in an atmospheric column per unit area, N^a_{column}, can be defined as $N^a_{column} = \int_0^\infty N^a(z)dz$. Since AOT is proportional to

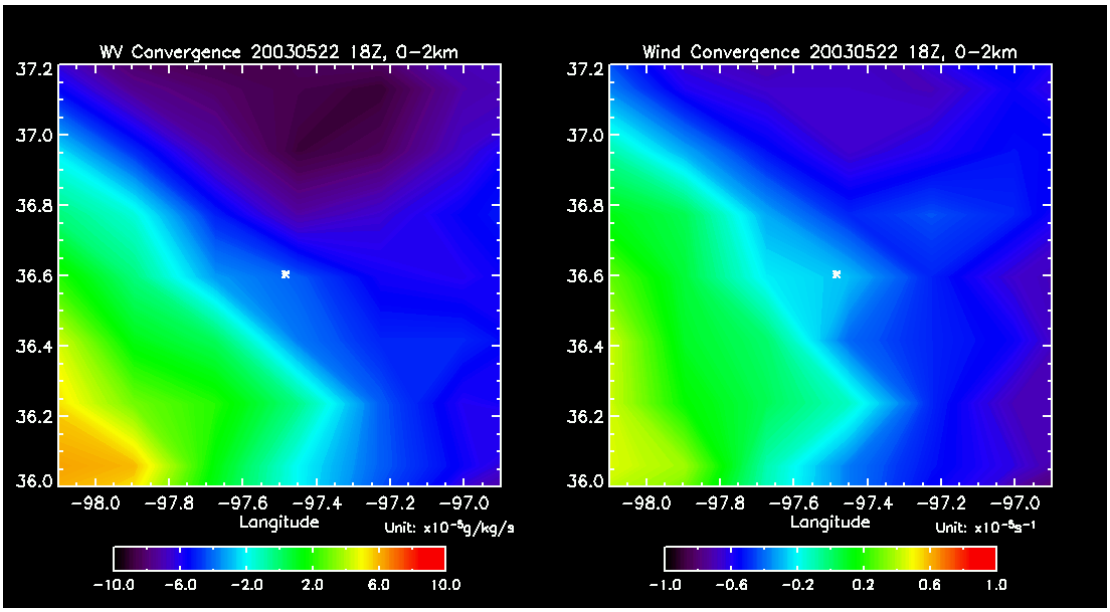

Fig 5.15. Horizontal convergence of water vapor (left panel) and wind (right panel). The Central Facility of the Southern Great Plains site is located by an asterisk (*).

aerosol number density unless other aerosol optical properties change, the magnitude of aerosol convergence can be estimated using the rate of change of total number of aerosols integrated throughout an atmospheric column ($\frac{\partial N^{a}_{column}}{\partial t}$).

In order to compute the RHS of Eq. (5.6), a generic shape of aerosol number density vertical distribution, which decreases exponentially with altitude, is assumed (see Fig 5.16a). Note that this vertical distribution is similar to the average aerosol extinction coefficient profile over the ARM SGP site as shown in Fig 4.1. To define an aerosol model to be used for linking aerosol number density to AOT, the aerosol size distributions retrieved from the AERONET (Dubovik et al., 2000) in May 2003 were fitted to a tri-modal log-normal size distribution (Fig 5.16b). The refractive index (=1.45-i0.0035 at 0.55μm) for the aerosol model was determined by matching a

typical single scattering albedo (i.e., 0.95 at 0.55μm) measured from the AOS and the IAP flights over the SGP site (Sheridan et al., 2002). Since the aerosol 3-D distributions are not available, the two terms in Eq. (5.6) are computed under different assumptions to infer their magnitudes.

The first term on the RHS of Eq. (5.6) was computed using RUC20 data by assuming a horizontally homogeneous aerosol field (i.e., AOT at 0.55μm, $\tau^{a}_{0.55\mu m}$=0.2 that is roughly the average AOT over the region) A variable aerosol field was assumed in computing the second term with a constant horizontal AOT gradient (i.e., $\tau^{a}_{0.55\mu m}$ changes at a rate of 0.2 per 40km toward the north-east direction according to the MODIS AOT distributions around the Central Facility (CF) of the ARM SGP site in Fig. 5.13). Table 5.2 summarizes the results corresponding to the MODIS overpass time on May 22, 2003. It is seen that the contributions of the two terms to columnar aerosols (i.e., AOT) have the same order of magnitude in terms of their maxima over the domain of interest (as shown in Fig 5.13 and Fig 5.15), and the two terms can influence up to 4% (=0.0071 hr^{-1}/0.2) and 10% (=0.0207 hr^{-1}/0.2) of AOT changes per hour, respectively (i.e., up to 14% AOT change per hour by aerosol convergence). The two terms computed for the columnar aerosols over the ARM SGP CF site indicate there was aerosol divergence, while the advection term (i.e., second term) is larger than the product of wind convergence and aerosol number density by a two-order of magnitude. The sum of the both terms demonstrates –6% AOT change per hour (= -[0.0002 hr^{-1}+0.0120 hr^{-1}]/0.2) could be introduced by aerosol convergence

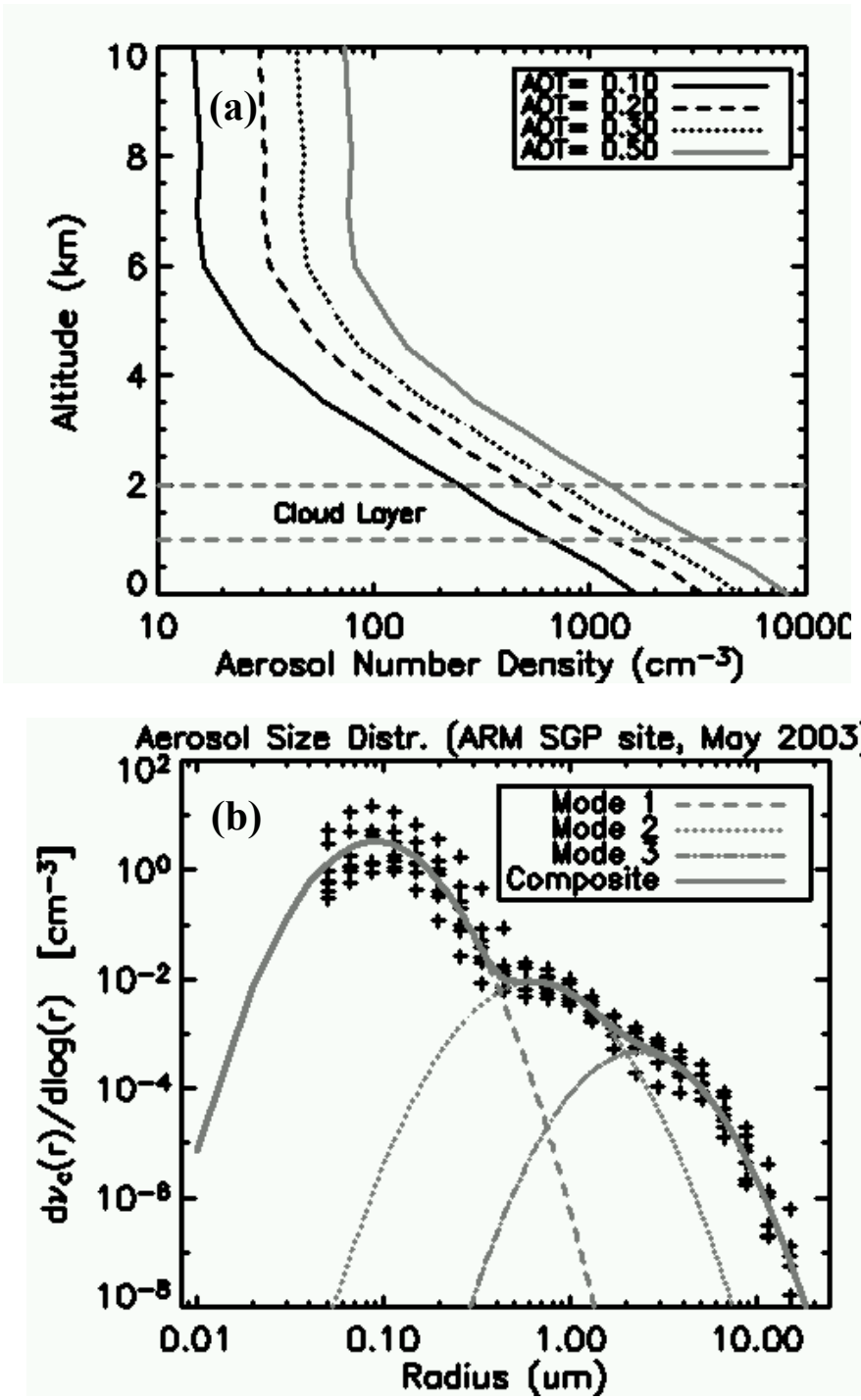

Fig 5.16. (a) Assumed vertical profiles of aerosol number density and location of a cloud layer. (b) The aerosol size distribution inferred from the AERONET (shown as crosses; May 2003) and log-normal size distributions (gray lines) fitted to the AERONET data.

Table 5.2. Aerosol number density, its rate of change, and associated AOT over the SGP CART site (May 22, 2003).

Data Sources	Aerosol-related Quantities			
Calculation based on RUC20 data and aerosol model introduced in Fig 5.16.	N^a_{column} [*] = 4.03x10^8 cm^{-2} at $\tau^a_{0.55\mu m}$=0.2			
			$-\left(N^a \nabla \cdot \vec{U}\right)$ [&]	$-\left(\vec{U} \cdot \nabla N^a\right)$ [#]
	Column Integrated $(\frac{\partial N^a_{column}}{\partial t})$	SGP CF	-4.40x10^5 cm^{-2} hr^{-1} (-0.0002 hr^{-1}) [%]	-2.41x10^7 cm^{-2} hr^{-1} (-0.0120 hr^{-1})
		Max.	1.42 x10^7 cm^{-2} hr^{-1} (0.0071 hr^{-1})	4.18x10^7 cm^{-2} hr^{-1} (0.0207 hr^{-1})
		Min.	-3.23 x10^7 cm^{-2} hr^{-1} (-0.0160 hr^{-1})	-1.60x10^8 cm^{-2} hr^{-1} (-0.0794 hr^{-1})
	Surface $(\frac{\partial N^a(sfc)}{\partial t})$ [@]	SGP CF	47 cm^{-3} hr^{-1}	128 cm^{-3} hr^{-1}
Aerosol Observing System	$N^a_{AOS}(sfc)$ [&] at 17UTC = 9556 cm^{-3} $N^a_{AOS}(sfc)$ at 18UTC = 11878 cm^{-3} $\Delta N^a_{AOS}(sfc)/\Delta t$ [$] = 192 cm^{-3} hr^{-1}			
AERONET AOT at 0.5μm	0.213 at 17:11UTC 0.190 at 17:26UTC 0.202 at 17:41UTC } mean: 0.202±0.011			

[*] N^a_{column} : Total number of aerosol in the column of the atmosphere per unit area

[&] $-\left(N^a \nabla \cdot \vec{U}\right)$ was calculated when $\tau^a_{0.55\mu m}$=0.2.

[#] $-\left(\vec{U} \cdot \nabla N^a\right)$ was calculated assuming AOT changes from 0.4 to 0.2 toward the north-east for a distance of 40km. (i.e., $\Delta\tau^a_{0.55\mu m}$/40km = 0.2).

[%] $\frac{\partial N^a_{column}}{\partial t}$ was converted into the rate of AOT change by multiplying "0.2/ N^a_{column}" and provided in the parentheses.

[@] $\frac{\partial N^a(sfc)}{\partial t}$: The rate of change of aerosol number density at the surface calculated from the RUC20 and assumed aerosol model

[&] $N^a_{AOS}(sfc)$: Aerosol number density measured from the AOS at the surface

[$] $\Delta N^a_{AOS}(sfc)/\Delta t$: The rate of change of aerosol number density measured from the AOS

over the SGP CF site. The AERONET AOT during this time (i.e., 1hour, 17~18UTC) showed an average of 0.202 with ±0.011 variability (Table 5.2). Since the –6%~14% of AOT changes per hour for mean AOT of 0.2 correspond to the AOT changes per hour by –0.012~0.028, the calculated contributions of aerosol convergence seem to reasonably explain the AERONET AOT variability.

To further examine the validity of our crude estimation about aerosol convergence, $\frac{\partial N^a}{\partial t}$ at the surface was calculated and compared with the observation from the AOS at the ARM SGP site. As also shown in Table 5.2, the calculated and the observed $\frac{\partial N^a}{\partial t}$ are similar to each other (47+128=175 cm^{-3} hr^{-1} versus 192 cm^{-3} hr^{-1}), indicating the calculated quantities reasonably estimate the magnitude of the aerosol convergence effect for the given case. The effects of aerosol convergence on the spatial distribution of AOT for the domain of our interest are shown in Fig 5.17. Upper panel shows the effect of wind convergence (i.e., the first RHS term of Eq. (5.6)). The effect of aerosol advection is shown via histogram. Note that our aerosol advection calculation is just for inferring the magnitude of the effect based on a crude assumption due to unavailability of 3D aerosol distribution. From these figures, the effect of wind convergence on AOT changes ranges from -0.005 to 0.003 (when background AOT is 0.2), while that of aerosol advection ranges –0.08~0.03 (when AOT gradient is 0.2/40km). Such magnitudes contribute to only small portion (less than 10%) of the MODIS AOT distribution. Therefore, other factors such as cloud contamination or 3-D cloud effect may play more significant roles in explaining the MODIS AOT distribution.

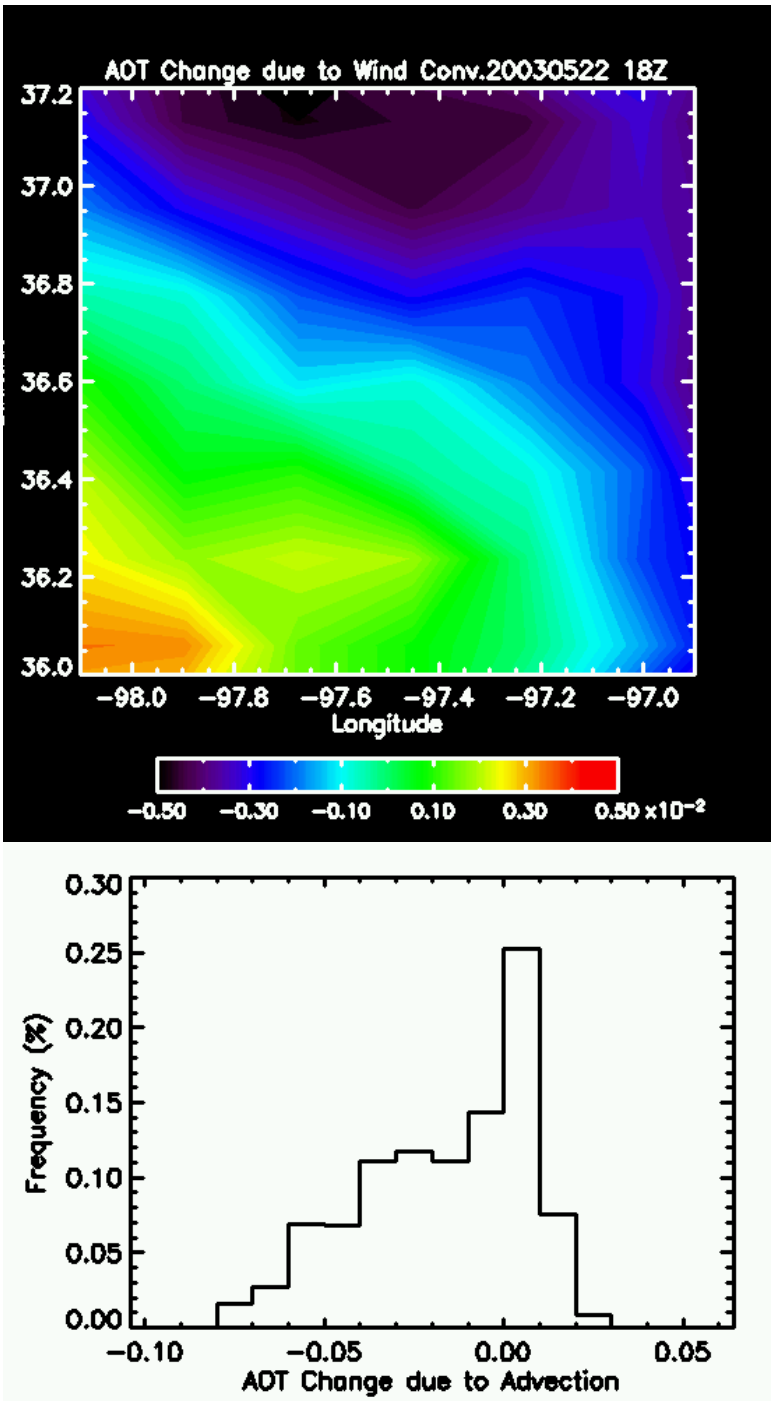

Fig 5.17. AOT variation caused by to wind convergence (upper panel) and the histogram of AOT change due to aerosol advection (lower panel).

5.4.2. The Effect of Sub-pixel Cloud Contamination

To investigate the effect of sub-pixel cloud contamination, the amount of sub-pixel cloud fraction not detected by the MODIS cloud mask is determined using TSI and Active Remote Sensing of Clouds (ARSCL) data over the ARM SGP site. Fig 5.18 shows the geometries of the MODIS and the TSI observations and the definitions of angles and distances, which are necessary to determine the areas to be matched up. First, the altitudes of the clouds are obtained from the ARSCL product, which is based on the Micro-Pulse Lidar (MPL). Then, the diameter of the footprint of the MODIS pixel at the altitude of the cloud, arc DE, is calculated using the spherical geometry as follows:

$$R_c = -(a_e + h_c)\cos\theta_{VZA} + \sqrt{\{(a_e + h_c)\cos\theta_{VZA}\}^2 + (a_e + h_s)^2 - (a_e + h_c)^2} \quad (5.7)$$

$$\theta_{Scan} = \cos^{-1}\left[0.5\left\{R_c^2 + (a_e + h_s)^2 - (a_e + h_c)^2\right\}/\{R_c(a_e + h_s)\}\right] \quad (5.8)$$

$$\theta_{Scan,1} = \theta_{Scan} - 0.5\psi_{FOV};\ \theta_{Scan,2} = \theta_{Scan} + 0.5\psi_{FOV} \quad (5.9)$$

$$\theta_{VZA,1} = \sin^{-1}\left\{(a_e + h_s)\sin\theta_{Scan,1}/a_e\right\};\ \theta_{VZA,2} = \sin^{-1}\left\{(a_e + h_s)\sin\theta_{Scan,2}/a_e\right\} \quad (5.10)$$

$$d_{c,1} = (a_e + h_c)(\theta_{VZA,1} - \theta_{Scan,1});\ d_{c,2} = (a_e + h_c)(\theta_{VZA,2} - \theta_{Scan,2}) \quad (5.11)$$

$$arcDE = (d_{c,2} - d_{c,1}) \quad (5.12)$$

where R_c, a_e, h_c, θ_{VZA}, h_s, and θ_{Scan} denote the distance between the satellite and the center of a pixel at cloud's altitude (h_c), the radius of the earth, the altitude of clouds, viewing zenth angle (VZA) of MODIS, the altitude of satellite, and the MODIS scan angle. ψ_{FOV} is the angle between the longest and the shortest sides'

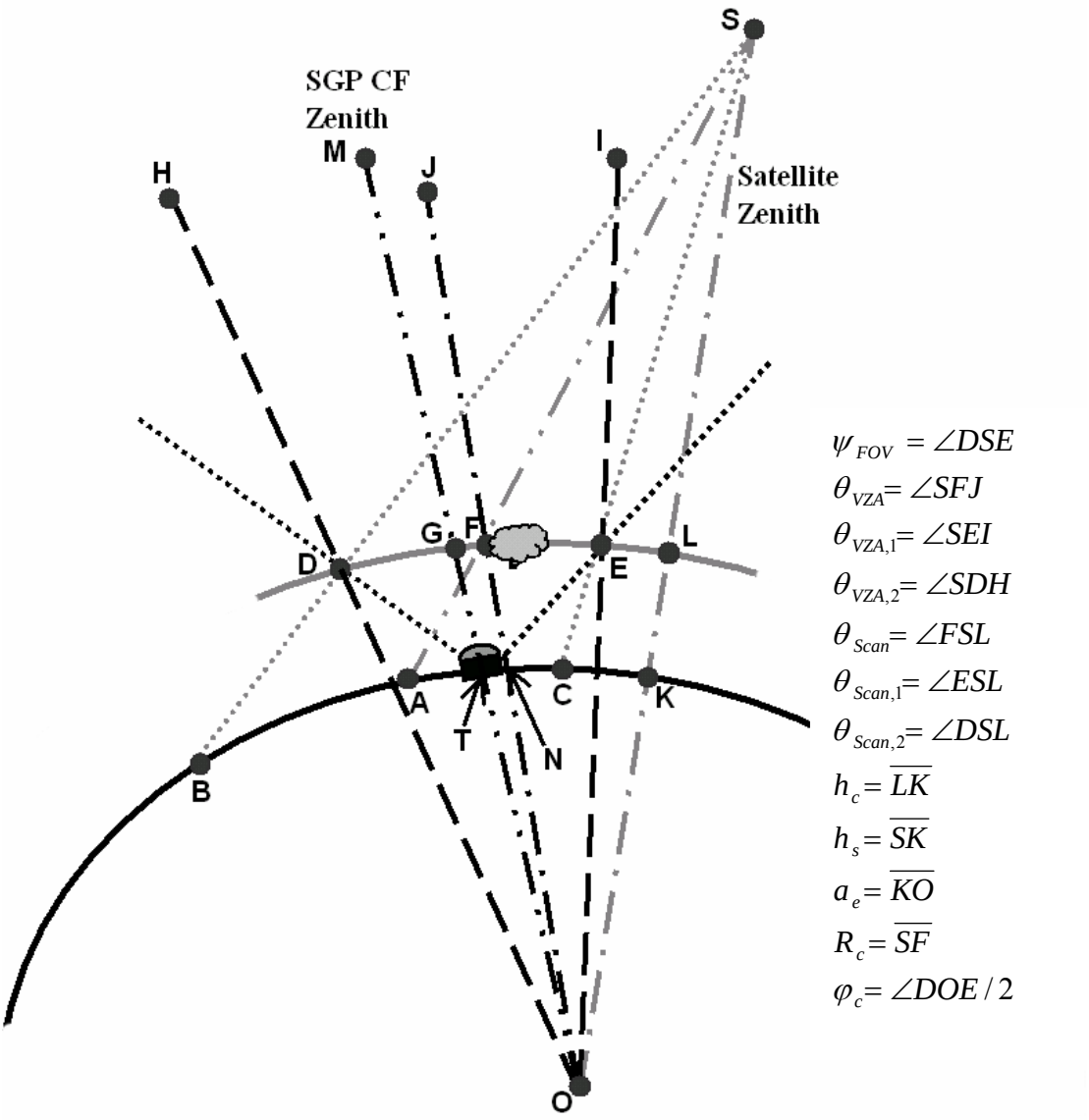

Fig 5.18. Viewing geometry of MODIS from space and TSI from the surface. The definitions of angles and lengths of lines or arcs are provided together. Arc DE stands for a diameter of a MODIS footprint (=1km at the surface in the nadir direction) at the altitude of a cloud (h_c) to be matched up with a TSI image. ψ_{FOV} is an angle corresponding to the field of view (FOV) of MODIS, θ_{VZA}, θ_{Scan}, h_c, h_s, a_e and R_c are viewing zenith angle (VZA) and scan angle of MODIS, cloud altitude, satellite altitude, the earth's radius and the distance between the satellite and the center of a pixel at h_c (i.e., point F). Note the point F was given to satisfy $\angle DSF = 0.5\psi_{FOV}$. $\overline{SD}$ and $\overline{SE}$ are the longest and the shortest sides' lengths of the tilted cone of MODIS FOV projected onto the spherical surface at h_c (i.e. the surface of the sphere with radius of $a_e + h_c$, which is guide by arc DL).

lengths of the tilted cone of MODIS FOV projected onto the spherical surface at h_c, which corresponds to the MODIS FOV. Two VZAs ($\theta_{VZA,1}$ and $\theta_{VZA,2}$) and two scan angles ($\theta_{Scan,1}$ and $\theta_{Scan,2}$) are defined at two local points (D and E in Fig 5.18) to compute the length of arc DL (i.e., $d_{c,2}$) and arc EL ($d_{c,1}$) using Eq. (5.11). Then, arc DE, the longest diameter of MODIS footprint at h_c can be determined using Eq. (5.12). Note that a MODIS footprint is an oval shape at a slant-viewing angle, while getting close to a circle as VZA goes to zero (i.e., a nadir view). It is assumed that a MODIS footprint is a circle with diameter of arc DE (or with radius of d_c) on the surface of the sphere with radius of ($a_e + h_c$) for convenience. Normally, the lengths of arc DG and arc GE are not equal except for VZA=0, but approximated to be equal here, which is valid when the length of arc AT is relatively small. The errors regarding these assumptions converge to zero as VZA decreases. When such approximations are valid, the range of the TSI viewing angle matched up with the radius of the MODIS footprint can be estimated as follows:

$$\varphi_c \approx \frac{d_c}{(a_e + h_c)} \tag{5.13}$$

The geo-location of a cloud from the MODIS can be erroneous as the viewing angle becomes larger. Such an error is a function of cloud altitude and satellite viewing zenith angle. It is estimated with an assumption that the Earth is a sphere with a radius of 6370.997 km. The error is presented in Fig 5.19a, which is defined as the arc AN on the surface of the earth in Fig 5.18. For example, the geo-location error for a cloud located 2 km above the surface and viewed at a 30^o zenith angle from the satellite is slightly larger than 1 km, which is comparable to the size of one MODIS

pixel. Therefore, this geo-location error should be considered when comparing ground-based observations with satellite-based ones. Also, the distance between the TSI location and sub-cloud point (i.e., arc TN in Fig 5.18) is provided in Fig 5.19b as a function of the viewing angle of the TSI and altitude of clouds to show the range of the TSI observations. For instance, when cloud altitude is 1.5km and MODIS views the nadir over the TSI, a MODIS pixel (0.5km radius) correspond to a circular area within 20° zenith angle of a TSI image.

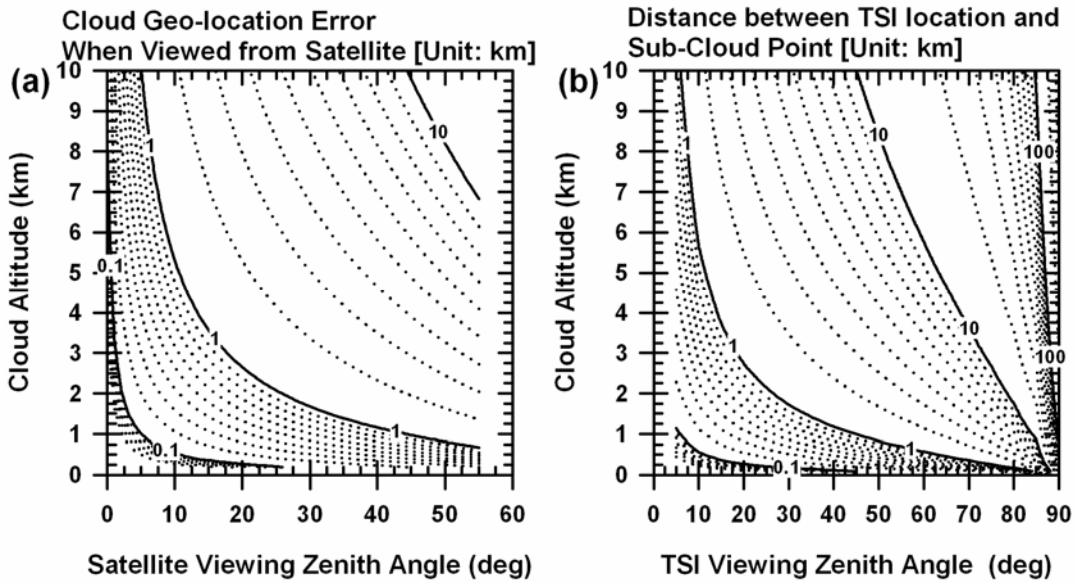

Fig 5.19. Cloud geo-location error as a function of satellite viewing zenith angle and cloud altitude (left). Distance between the location of TSI and sub-cloud point as a function of TSI viewing zenith angle and cloud altitude (right).

Two years (2002-2003) of MODIS cloud mask data were matched up with TSI data using the methods described above. Cloud fraction is then computed for the area on a TSI image (Fig 5.20). It shows the histogram of the TSI cloud cover computed for the MODIS footprint only when the MODIS cloud mask reported "confident clear" (see Platnick et al., 2003). For the two years, total 322 match-ups were acquired. The upper panel of Fig 5.20 shows the histogram of the TSI cloud cover for the MODIS footprint regardless of viewing zenith angle (VZA), while the lower panel shows the data with the VZA less than 15^{o}, which reduces the geo-location error. The two histograms show similar distributions, indicating that about 20% of the MODIS clear pixels may include 1-5% of sub-pixel clouds and another 10-20% of a MODIS clear pixel may be covered with more than 5% of clouds.

However, the MODIS aerosol retrieval algorithm adopted additional cloud-screening methods, including an internal cloud mask based on the spatial variability of the radiance at 0.5 km resolution to identify low-level clouds and the reflectance in the 1.38-μm band to identify high-level clouds (Remer et al., 2005). In addition, pixels of the brightest 50% of reflectance in the red (0.66 μm) spectrum are discarded. Therefore, it is reasonable to assume that sub-pixel clouds with a high cloud fraction are removed in the MODIS aerosol retrieval process. A visual examination of TSI images showed some false detection of cloud. The TSI cloud cover for the most of these cases, however, were high (>0.5) rather than small clouds (<0.2).

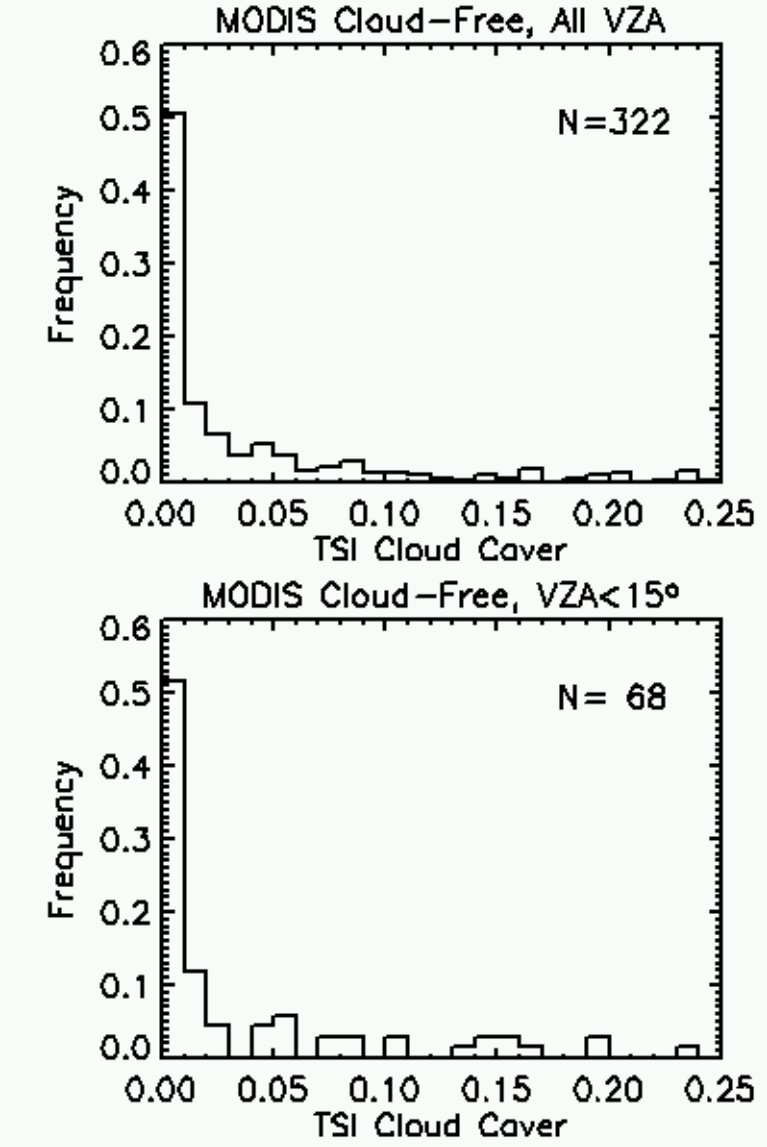

Fig 5.20. Histogram of TSI cloud cover collected only when MODIS cloud mask reported "confident clear". Data for all the available viewing zenith angles (VZA) are shown in the upper panel, and data with VZA<15°, in the lower panel.

A numerical experiment was performed to examine how much AOT error would be produced due to sub-pixel cloud contamination. The same aerosol model and its vertical distribution as those employed for the effect of aerosol convergence (see Fig 5.16 and corresponding description) are used. Clouds with different values of cloud optical thickness (COT; COT=1, 2, 4, and 8) are placed 1-2 km above the surface. As for COT values, we referred to AERONET level 1.0 and 2.0 data, which correspond to "unscreened" and "cloud-screened and quality assured" data. The "unscreened" AERONET AOT (level 1.0) may include optical thickness of clouds since cloud-screening is not applied at this level, while "cloud-screened and quality assured" AOT (level 2.0) contains only the data passed the complete cloud screening test. It is often seen that level 1.0 optical thickness shows sharp peaks with values ranging from 1 to 6, which disappear in level 2.0 data. So we assumed that the COT of transient small-scale clouds would span a similar range. As shown in the Fig5.16a, most of aerosol population resides below the clouds, which is the normal situation found over the ARM SGP site (see section 5.3).

Reflectance is simulated using the Santa Barbara DISORT Atmospheric Radiative Transfer (SBDART; Ricchiazzi et al., 1998) for cloud-free conditions with AOT=0.1 for various viewing geometries and similar simulations were made including clouds with various COT. The solar zenith angle (SZA) was fixed at 30°. The reflectance (ρ^{comp}) for a partial cloud fraction, f_c, is estimated using a linear composition of clear and cloudy reflectance (ρ^{clear} and ρ^{cloud}), that is,

$$\rho^{comp} = \rho^{clear}(1 - f_c) + \rho^{cloud} f_c \ . \tag{5.14}$$

The resultant cloud contamination on AOT is presented as functions of sub-pixel cloud contamination, COT, and viewing geometry in Fig 5.21. The upper panel shows a case with a fixed viewing angle (VZA=30°, Relative Azimuth Angle, RAA=60°) but with varying COT while the lower panel presents a case with a fixed COT (equal to 4), but with varying viewing geometries. The effect of the COT is linearly proportional to its value for the given range of sub-pixel cloud fraction. The effect of simulated cloud contamination varies with viewing angle, which is primarily due to the difference in the detailed structure of the phase functions of the clouds and the aerosols, while the geometry of 3-D clouds can play a significant role in a real situation. It is extremely difficult to consider such 3-D geometry of clouds; however, a possible range of such geometry effect may be guided by various ranges of viewing geometries for 1-D clouds, as illustrated in Fig 5.21b. The simulation result suggests that sub-pixel cloud with a 5% cloud fraction results in an overestimation of AOT ranging from 0.05 to 0.3 (50%~300% of the true AOT) depending on COT and viewing geometry. It is worth noting that the MODIS AOT shown in Fig 5.13 varies roughly from 0.2 to 0.6 in response to increasing cloud fraction. If we assume that the lowest value of AOT is free from cloud contamination and that the AOT spatial variation is solely due to cloud contamination, the corresponding cloud contamination would reach up to 200% (=[0.6-0.2]/0.2), similar to our simulation result. However, the major problem in this assumption lies in whether the MODIS cloud fraction can be linked to sub-pixel cloud contamination. If not, the correlation between the MODIS AOT and cloud fraction would not be due to sub-pixel cloud contamination.

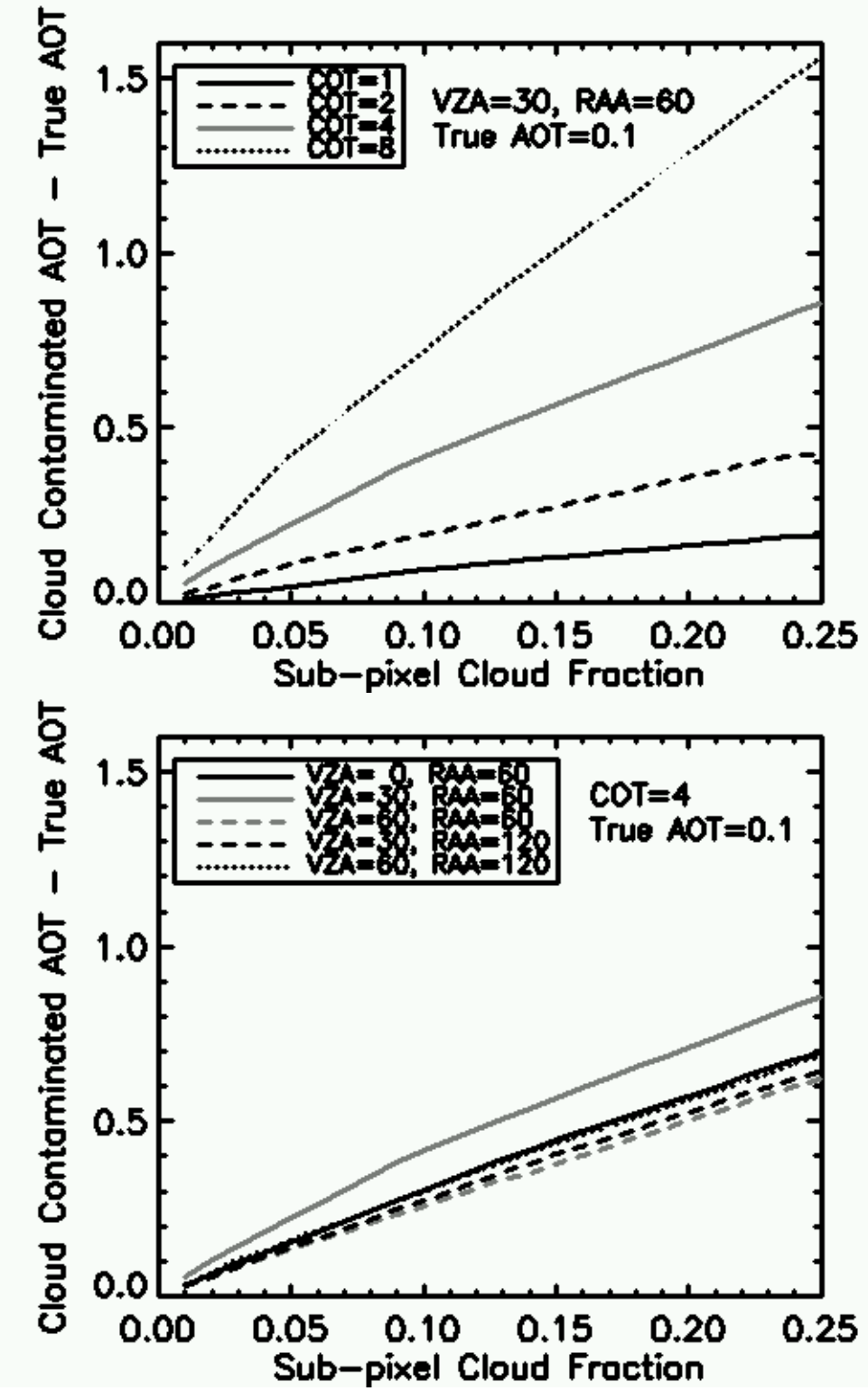

Fig 5.21. Cloud contamination in AOT as a function of sub-pixel cloud fraction for various cloud optical thickness (COT; upper panel). Lower panel is the same as upper panel but for various satellite-viewing geometries.

Moreover, since not all the original MODIS pixels (0.5x0.5km at nadir) selected as "cloud-free" pixels within an aerosol pixel (i.e., 10x10km box) are contaminated by sub-pixel clouds, if the radiances from contaminated and uncontaminated pixels averaged, the effect of sub-pixel cloud contamination will be less than the result of the above simulation. However, if one can relate the MODIS cloud fraction within an aerosol pixel with probability of sub-pixel contamination, chance of sub-pixel contamination and its range of magnitude may be estimated. In Fig 5.22a, probabilities of sub-pixel cloud contamination are provided as a function of the MODIS cloud fraction. The probabilities were calculated by dividing the number of false "clear" pixels by the total number of pixels declared as "clear" by the MODIS cloud mask. False "clear" pixels was defined as those pixels declared as "clear" by the MODIS cloud mask but the TSI cloud cover within the areas matched up with MODIS footprints indicates cloud cover greater than 2%. As show in Fig 5.22a, there is increasing trend of the probabilities of sub-pixel cloud contamination as the MODIS cloud fraction increases. Note that the probability greater than 20% exists even when the MODIS cloud fraction is low (<20%). Fig. 5.22b shows correlation between the TSI cloud cover and the MODIS cloud cover. An increasing trend of the TSI cloud cover is shown with increasing the MODIS cloud fraction, which is expected. Fig 5.22c is the same as Fig 5.22b but the data were conditionally sampled limiting to the cases when false "clear" pixels were declared by the MODIS cloud mask. Interestingly, no obvious trend was found contrast to Fig 5.22b. A sharp peak around 80% MODIS cloud fraction seems due to small number of samples. Considering the information from Fig 22a-c together, one can conclude that sub-pixel

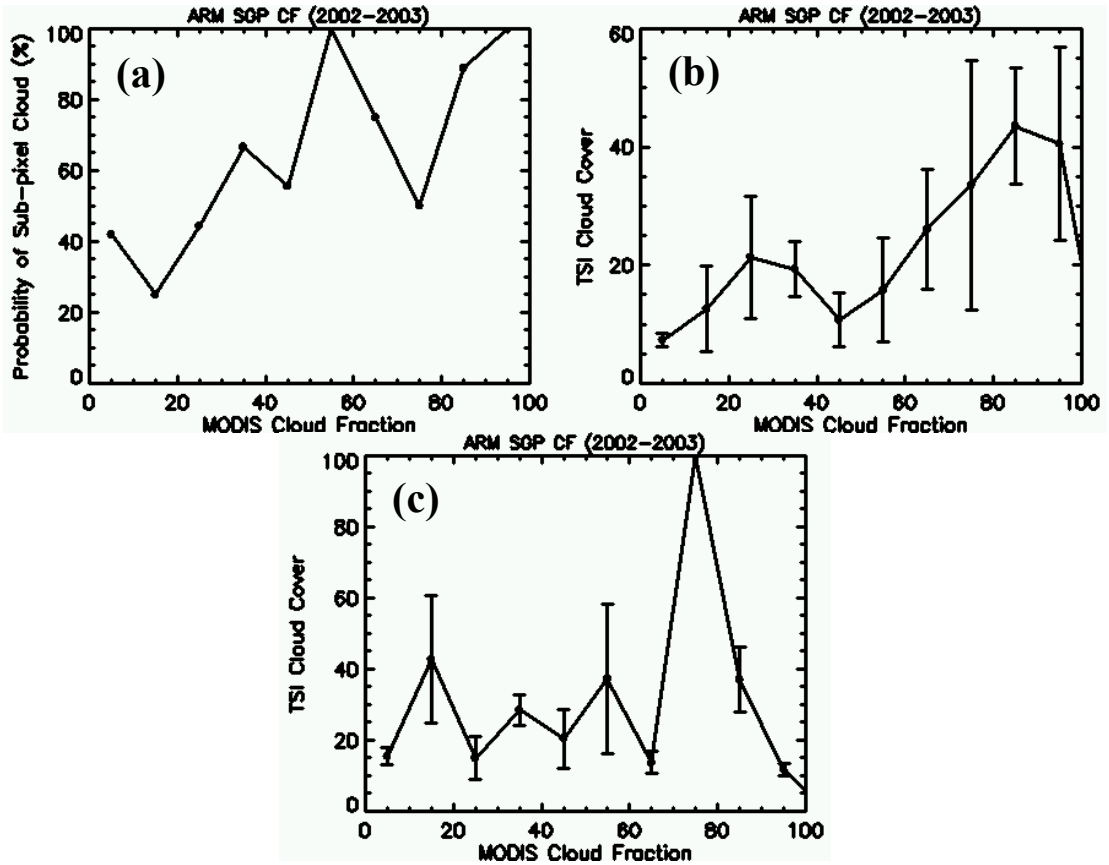

Fig 5.22. (a) Probability of sub-pixel cloud (i.e., # of false 'clear' pixels divided by total # of pixels declared as 'clear' by the MODIS cloud mask) as a function of MODIS cloud fraction. (b) The TSI cloud cover versus MODIS cloud fraction for an aerosol pixel (a 10x10km box at nadir) over the ARM SGP CF site. (c) The same as (b) but data were sampled only when false 'clear' pixels were declared by the MODIS cloud mask.

cloud contamination may affect the magnitude of contaminated AOT not by increased cloud amount but by increased chance of sub-pixel cloud contamination as the MODIS cloud fraction increases.

Although the magnitude of sub-pixel cloud contamination's effect shown to be as large as to explain the observed feature, one cannot rule out other factors such as enhanced scattering due to inhomogeneous clouds (the 3-D cloud effect) and cloud processed particles/new particle genesis under presence of clouds. Note that the

enhance scattering can play a significant role in the relationship between the MODIS AOT and cloud fraction for it is intuitively reasonable to assume that the scattered radiation due to clouds increases with increasing cloud fraction, which, in turns, would result in a proportional AOT overestimation. Therefore, further work will be warranted to resolve this issue more completely.

5.5. Summary

We report that AOTs are correlated with cloud cover (or fraction) from ground-based observations (AERONET AOT and TSI cloud cover) as well as from satellite-based observations (MODIS AOT and cloud fraction). The causes of the apparent correlation between AOT and cloud cover is investigated using a suite of instruments available at the ARM SGP CART site. We find that the correlation is not simply due to cloud contamination or humidified aerosols but also due to other factors such as air convergence, cloud-processed or new particles in the presence of clouds.

Analyses of AERONET AOT, TSI cloud cover, CART Raman Lidar, and IAP data show that the aerosol humidification effect (AHE) contributes about one third to the observed correlation between AERONET AOT and TSI cloud cover. The influence of cloud contamination is small. Air convergence plays a significant role in determining the vertical distribution of aerosols, while its contribution to the AOT-cloud cover correlation is not obvious. The AOT derived from the IAP measurements, which is not affected by cloud contamination and aerosol humidification, is also correlated with cloud cover, suggesting contributions from cloud-processed particles

and new particles near clouds and/or under humid environment. Contributions of these factors seem to reach as large as the two-thirds of the slope between cloud cover and AOT. However, we cannot separate the effects of convergence and cloud-processed particles and new particles. A 3-D aerosol transport/chemistry model with a built-in cloud microphysics is required to tackle with the issue.

The correlation of MODIS AOT with cloud fraction over the SGP site seems to be mainly associated with artifacts due to cloud contamination and the 3-D cloud effect. The contribution of the AHE is estimated to be small. Wind and water vapor convergence distributions are also somewhat correlated with those of the MODIS AOT, implying a possible effect of aerosol convergence. However, our rough estimation on the effect of aerosol convergence indicates a rather weak contribution (<10%). On the other hand, sub-pixel cloud contamination may have a much more significant effect on the MODIS AOT. The TSI cloud masks matched up with the MODIS footprints suggest that a significant number of MODIS "clear" pixels may include sub-pixel clouds with a 1~5% cloud fraction within a pixel. Model simulations show that the presence of 5% of sub-pixel cloud may result in an AOT overestimation of 0.05~0.3. On the other hand, sub-pixel cloud contamination seems to affect the magnitude of contaminated AOT not by increased cloud amount but by increased chance of sub-pixel cloud contamination as the MODIS cloud fraction increases. When such factor is considered, the magnitude of sub-pixel cloud contamination would be less than the simulation. Enhanced scattering due to 3-D cloud effects that cannot be simulated by a 1-D radiative transfer model and the

effects of cloud-processed particles/new particle genesis play a significant role, both effects are expected be proportional to cloud amount.

In conclusion, the correlation between AOT and cloud cover from AERONET and the TSI is mainly due to real effects: the AHE, cloud-processed/new particles and convergence. However, the correlation between MODIS AOT and cloud fraction is likely more severely influenced by cloud contamination and enhanced 3-D scattering due to clouds. Therefore, it is necessary to correct for these artifacts so that MODIS AOT (and other satellite-based AOT) near clouds can be used.

Chapter 6: Summary, Conclusions, and Future Work

6.1. Summary and Conclusions

A number of global aerosol products of varying quality, strengths and weaknesses have been generated. Synthetic analyses with regard to the quality, compatibility and synergy of two long-term global (1983-2000) aerosol products derived from the Advanced Very High Resolution Radiometer (AVHRR) and the Total Ozone Mapping Spectrometer (TOMS) were presented in this study. Four essential aerosol parameters, namely, aerosol optical thickness (AOT) from AVHRR under the Global Aerosol Climatology Project (GACP), TOMS AOT, Ångström exponent (AE) from AVHRR, and TOMS aerosol index (AI) are analyzed together with various ancillary data sets such as cloud data from the International Satellite Cloud Climatology Project (ISCCP), wind vectors from the National Centers for Environmental Prediction (NCEP)/National Center for Atmospheric Research (NCAR) reanalysis, ocean color from the Coastal Zone Color Scanner (CZCS), AOT from the Aerosol Robotic Network (AERONET), Moderate Resolution Imaging Spectroradiometer (MODIS) AOT, etc. While the two products reveal some common features, significant discrepancies exist. Reflectances measured at ultraviolet and visible wavelengths from the two sensors are incompatible in that the AE computed from the combination of the two TOMS channels differs considerably from that derived from the two AVHRR channels. The spatial distributions of the aerosol products from GACP/AVHRR and TOMS are complimentary in revealing different aspects of aerosol characteristics. The AOT from both sensors suffers from cloud

contamination in many regions. In-depth analyses were carried out over several regions under the influence of different types of aerosols such as biomass burning, dust, sea-salt, air pollution and their mixtures. A classification algorithm was developed to identify dominant types of aerosols around the globe using aerosol products from the two instruments. Aerosol type information is used to develop and apply relationships between the AVHRR AOT and the TOMS AOT. The latter was used to extend the AOT at 0.55 μm over land around the globe. Comparisons of monthly mean AOTs with AERONET monthly mean AOTs showed a general agreement to within an estimated error range of $\pm 0.08 \pm 0.20\tau$. Finally, a comparison between the estimated AOT with MODIS AOT over land showed good agreement in terms of magnitude and seasonality, suggesting a means of bridging past and current AOT estimations.

There currently exist numerous global aerosol products derived from various satellite sensors, but little insight has been gained about their compatibility and quality. This study presented a comparison of two prominent global aerosol products derived over oceans from the Moderate Resolution Imaging Spectroradiometer (MODIS) (*Tanré et al.*, 1997) and from the AVHRR (*Mishchenko et al.*, 1999). The comparisons are for monthly mean AOT and AE at a spatial resolution of 1x1 degree. The two monthly AOT products showed substantial discrepancies, with a tendency of higher values from MODIS than from GACP/AVHRR especially near the coasts of major aerosol outbreak regions. Individual monthly AOT values have poor correlation, but their regional means are moderately correlated (correlation coefficient

0.5<R<1.0). While cloud screening has often been argued to be a major factor explaining any large discrepancies, this study shows that differences in aerosol models selected by the two retrieval algorithms can lead to discrepancies as larger as the observed discrepancies. Contributions due to the size distribution are more significant than due to the refractive index. The former results in substantial random and systematic differences, while the latter gives rise to moderate systematic differences of opposite direction to that of the former. The noisiness of the GACP/AVHRR aerosol retrievals seem to be partially influenced by radiometric uncertainties in the AVHRR system, but it is unlikely a major factor to explain the observed systematic discrepancies between the MODIS and GACP/AVHRR AOTs. For AE, correlations between MODIS and GACP/AVHRR are much lower (0.2<R<0.7 for regional averages) than those for AOT. The MODIS AE shows a well-behaved dependence on the AOT contingent upon the type of aerosol, while the GACP/AVHRR AE has little correlation with the AOT. The high sensitivity in the selection of aerosol models (i.e., size parameter) to radiometric errors may be a primary reason for the worse comparison of AE, while AOT is affected more by the magnitude of measured reflectance than by aerosol models. Part of the discrepancies in AE is attributed to the selection of different aerosol particle size distributions. The variability of AE with aerosol size distribution, aerosol optical properties as well as wavelength selection is explored, together with ensuing difficulties in inferring aerosol particle effective radius from AE.

The aerosol humidification effect (AHE) on the aerosol optical thickness (AOT) measured over the Southern Great Plains (SGP) site was investigated. AOTs at different relative humidity (RH) levels (e.g., RH=40% and 85% throughout the column, and ambient RH profiles) were computed by integrating the aerosol extinction profiles measured from a light aircraft (Cessna C-172N) under the In-situ Aerosol Profiles (IAP) project, which is a joint effort between the Atmospheric Radiation Measurement (ARM) program of the Department of Energy and the Climate Monitoring and Diagnostics Laboratory (CMDL) of the National Oceanic and Atmospheric Administration (NOAA). The AOT derived from the IAP agreed reasonably well with coincident AOT from the AErosol RObotic NETwork (AERONET). The column aerosol humidification factor (AHF), R(RH), was defined as the ratio of the AOT with an ambient (or desired) RH profile to the AOT at an RH of 40% throughout the column. The R(RH) for ambient RH profiles for all available IAP data barely exceeds 1.3, which suggests that the AHE under the normal conditions of the IAP observations is small (mean 1.09±0.12) and that an AOT increase due to aerosol humidification is less than 30% when compares to the AOT increase at dry conditions (RH=40%). It was, then, shown that the column AHF may be represented as increasing functions of humidity variables such as the arithmetic column mean RH (<RH>), precipitable water, and the aerosol extinction weighted column mean RH (<wRH>). R(RH) varies with <wRH> just as the AHF for the aerosol scattering coefficient, f(RH), changes in response to RH changes. The AHE on the AOT was shown to be an increasing function of <wRH>, but its observed maximum was less than 25%.

Six methods to estimate R(RH) are introduced and compared with measured R(RH). These alternative methods may be useful when direct measurements of R(RH) are not available. The results suggest that the relationship between <wRH> and R(RH) work best if the profiles of humidity and aerosol extinction are available. If the data are not available, use of other relationships pending on available measurements may be resorted to with a varying accuracy.

The sensitivity of R(RH) to a hypothetically very humid layer (RH=99%) was examined. Since the IAP data used in this study have a coarse vertical resolution (0.2~0.65 km), it is possible for the IAP observations to miss instances of very high RH that may have been located somewhere at or near the location of the measurements, especially if clouds were present nearby. R(RH) changed approximately 8%, 19%, and 31% from the observed R(RH) with changes in the depth of the hypothetical humid layer, Δz (0.1 km, 0.2 km, and 0.3 km, respectively). R(RH) is insensitive to the altitude of the humid layer. The AOT with a hypothetical humid layer changes up to 9%, 19%, and 28% from the observed (ambient) AOT as Δz changes by 0.1 km, 0.2 km, and 0.3km, respectively. These AOT changes correspond to an AHE on the AOT (i.e., AOT changes from AOT at RH=40%) of 27%, 41%, and 55%, respectively. Therefore, the AHE on the AOT over the SGP site is not likely to exceed 50% on average when compared to the AOT at dry conditions (RH=40%) even when a locally very humid layer near clouds is considered.

We report that AOTs are correlated with cloud cover (or fraction) from ground-based observations (AERONET AOT and the cloud cover from the Total Sky

Imager, TSI) as well as from satellite-based observations (MODIS AOT and cloud fraction). The causes of the apparent correlation between AOT and cloud cover is investigated using a suite of instruments available at the ARM SGP Cloud And Radiation Testbed (CART) site. We find that the correlation is not simply due to cloud contamination or humidified aerosols but also due to other contributors such as convergence, cloud-processed or new particles in the presence of clouds.

Analyses of the AERONET AOT, the TSI cloud cover, the CART Raman Lidar (CARL), and IAP data show that the AHE contributes about one third to the observed correlation between the AERONET AOT and the TSI cloud cover. The contribution of cloud contamination is small. The effect of convergence plays a significant role in determining the vertical distribution of aerosols, while its contribution to the AOT-cloud cover correlation is not obvious. The AOT derived from the IAP measurements, which are not affected by cloud contamination and aerosol humidification, are also correlated with cloud cover, suggesting contributions from cloud-processed particles and new particles near clouds and/or under humid environment. Contributions of these factors seem to reach as large as the two-thirds of the slope between cloud cover and AOT. However, the uncertain contribution of convergence suggests the need of a 3-D aerosol transport/chemistry model with a meso-scale resolution to separate it from the contributions of cloud-processed and new particles.

The correlation of MODIS AOT with cloud fraction over the SGP site seems to be mainly associated with artifacts due to cloud contamination and the 3-D cloud effect. The contribution of the AHE is estimated to be small. Wind and water vapor

convergence distributions are also somewhat correlated with those of the MODIS AOT, implying a possible effect of aerosol convergence; however, our rough estimation about the effect of aerosol convergence indicates a rather weak contribution (<10%). On the other hand, sub-pixel cloud contamination may have a significant effect on the MODIS AOT. The TSI cloud masks matched up with the MODIS footprints suggest that a significant number of MODIS "clear" pixels may include sub-pixel clouds with a 1~5% cloud fraction within a pixel. Model simulations show that the presence of 5% of sub-pixel cloud may result in an AOT overestimation of 0.05~0.3. In addition, enhanced scattering due to clouds that cannot be simulated by 1-D radiative transfer should also play a significant role for its magnitude will be proportional to cloud fraction.

In conclusion, the correlation between AOT and cloud cover from AERONET and the TSI is mainly due to real effects: the AHE, cloud-processed/new particles and convergence. However, the correlation between MODIS AOT and cloud fraction is more significantly influenced by cloud contamination and enhanced 3-D scattering due to clouds. Therefore, it is necessary to correct for these artifacts so that MODIS AOT (and other satellite-based AOT) near clouds can be used.

6.2. Suggestions for Future Work

This study made the first step toward a complete assessment on the aerosol retrievals from satellites to improve global aerosol estimations for climate studies. As inter-comparison among different aerosol products revealed, large uncertainties exist

so that spatial characterization from satellites is not merely reflecting the reality but also mixed up with artifacts originated from clouds and surface. In addition, different assumptions on aerosol properties made by different aerosol retrieval algorithms result in inconsistency among various aerosol products and hinder from bridging current and past aerosol estimations to acquire long-term records. With such facts in mind, some suggestions for future work can be made.

Many efforts have been made to evaluate satellite-based aerosol retrievals, but most efforts provided simple comparisons between AOT from satellites and sun photometers at the ground (e.g., the AERONET) as ground truths. It should be noted that a good agreement in AOT does not guarantee that the derived aerosol quantities are based on the correct aerosol microphysical properties, since a good AOT estimation might be acquired by cancellations of errors. In this regard, future evaluation efforts should be made in consideration of aerosol microphysics and interferences among various errors. For example, our inter-comparison between the two long-term global aerosol products from the AVHRR and TOMS showed, discrepancies between different aerosol products depend on regions and aerosol types. Such dependencies may originate from different aerosol microphysics and many other details assumed by the respective aerosol retrieval algorithms, and limiting factors of respective sensors. So, a consideration of such factors in an evaluation effort will eventually help to improve aerosol retrievals from the satellites.

As for climatological effects of aerosols, building a long-term climatology on aerosols (e.g., AOT) will be necessary by bridging the past and current (and future) aerosol records. To this end, standardized methods that can be applied to different

satellite platforms and sensors (e.g., AVHRR and MODIS) need to be developed, especially in terms of cloud screening and aerosol models. No such attempt has been made yet, but it would be a crucial factor to maintain a consistency to account for the effects of aerosols, which are highly variable with space and time in contrast to the greenhouse gases, on the climate system.

Fusing different measurement techniques by taking advantage of respective data may give us an additional dimension to understand the effects of aerosols. Any single measurement technique has its own limitation and cannot reveal the whole feature of aerosols. Although simple examples of such effort are provided in this study, a lot more efforts of fusing multiple aerosol products or techniques including measurements of aerosol size, vertical distribution, absorption/scattering and hygroscopic properties will be necessary to acquire synthetic information. If such measurements can be combined together with satellite retrievals, it will significantly contribute to the understanding of the effects of aerosols on a global scale as well as reducing the uncertainties in satellite-based retrievals of aerosols.

Bibliography

Ackerman, S.A., K.I. Strabala, W.P. Menzel, R.A. Frey, C.C. Moeller, and L.E. Gumley (1998), Discriminating clear-sky from clouds with MODIS, J. Geophys. Res., **103**, 32141-32158.

Ackerman, A.S., O.B. Toon, D.E. Stevens, A.J. Heymsfield, V. Ramanathan, E.J. Welton (2000), Reduction of tropical cloudiness by soot, *Science*, **288**, 1042-1047.

Albrecht, B. (1989), Aerosols, cloud microphysics, and fractional cloudiness, *Science*, **245**, 1227-1230.

Anderson, T.L., and J.A. Ogren (1998), Determining aerosol radiative properties using the TSI 3563 integrating nephelometer, *Aerosol Sci. Technol.*, 29, 57-69.

Anderson, T.L., R.J. Charlson, S.E. Schwartz, R. Knutti, O. Boucher, H. Rodhe, J. Heintzenberg (2003), Climate forcing by aerosols – a hazy picture, *Science*, **300**, 1103-1104.

Andreae, M.O., J. Fishman, M. Garstang, J.G. Goldammer, C.O. Justice, J.S. Levine, R.J. Scholes, B.J. Stocks, A.M. Thompson, B.W. van Wilgen, and the STARE/TRACE-A/SAFARI Science Team (1994), Biomass burning in the global environment: First results from the IGAC/BIBEX field campaign STARE/TRACE-A/SAFARI 92, in *Global Atmospheric-Biospheric Chemistry*, R.G. Prinn (ed.), pp. 83-101, Plenum, New York.

Andrews, E., P.J. Sheridan, J.A. Ogren, and R. Ferrare (2004), In situ aerosol profiles over the Southern Great Plains cloud and radiation test bed site: 1. Aerosol optical properties, *J. Geophys. Res.*, 109, D06208, doi:10.1029/2003JD004025.

Ångström, A. (1929), On the atmospheric transmission of sun radiation and on dust in the air, *Geogr. Ann.*, **12**, 130-159.

Ångström, A. (1964), The parameters of atmospheric turbidity, *Tellus*, **16**, 64-75.

Baron, P.A. and K. Willeke (ed) (2001), *Aerosol measurement: Principles, techniques, and applications*, 2nd ed., Wiley Interscience, A John Wiley & Sons, Inc., Publication, 1131pp.

Bellouin, N, O. Boucher, D. Tanré, and O. Dubovik (2003), Aerosol absorption over the clear-sky oceans deduced from POLDER-1 and AERONET observations, *Geophys. Res. Lett*., *30*(14), 1748, doi:10.1029/2003GL017121.

Benjamin, S.G., D. Dévényi, S.S. Weygandt, K.J. Brundage, J.M. Brown, G.A. Grell, D. Kim, B.E. Schwartz, T.G. Smirnova, T.L. Smith and G.S. Manikin (2004), An Hourly Assimilation–Forecast Cycle: The RUC, *Monthly Weather Review*, **132**(2), 495–518.

Brest, C.L., W.B. Rossow, and M.D. Roiter (1997), Update of radiance calibrations for ISCCP, *J. Atmos. Oceanic Tech*., **14**, 1091-1109.

Bréon, F.-M., D. Tanré, and S. Generoso (2002), Aerosol effect on cloud droplet size monitored from satellite, *Science*, **295**, 834-838.

Bretherton, C.S., T. Uttal, C.W. Fairall, S.E. Yuter, R.A. Weller, D. Baumgardner, K. Comstock, R. Wood (2003), The EPIC 2001 stratocumulus study, *submitted to Bull. Amer. Meteorol. Soc.*.

Cakmur, R.V., R.L. Miller, I. Tegen (2001), A comparison of seasonal and interannual variability of soil dust aerosols over the Atlantic Ocean as inferred by the TOMS AI and AVHRR AOT retrievals, *J. Geophys. Res.*, *106*(D16), 18287-18303.

Charlson, R.J., J.E. Lovelock, M.O. Andreae, and S.G. Warren (1987), Oceanic phytoplankton, atmospheric sulphur, cloud albedo and climate, *Nature*, *326*, 655-661.

Charlson, R.J., J. Langner, H. Rodhe, C.B. Leovy, and S.G. Warren (1991), Perturbation of the northern hemisphere radiative balance by back scattering from anthropogenic sulfate aerosols, *Tellus*, Ser. B, **43**, 152-163.

Charlson, R.J., S.E. Schwartz, J.M. Hales, R.D. Cess, J.A. Coakley Jr., J.E. Hansen, and P.J. Hoffman (1992), Climate forcing of anthropogenic aerosols, *Science*, **255**, 423-430.

Chin, M., P. Ginoux, S. Kinne, O. Torres, B.N. Holben, B.N. Duncan, R.V. Martin, J.A. Logan, A. Higurashi, and T. Nakajima (2002), Tropospheric aerosol optical thickness from the GOCART model and comparisons with satellite and Sun photometer measurements, *J. Atmos. Sci.*, *59*, 461-483.

Chou, M.-D., P.-K. Chan, M. Wang (2002), Aerosol radiative forcing derived from SeaWiFS-retrieved aerosol optical properties, *J. Atmos. Sci.*, **59**(3), 748-757.

Chu, D.A., Y.K. Kaufman, C. Ichoku, L.A. Remer, D. Tanré, and B.N. Holben (2002), Validation of MODIS aerosol optical depth retrieval over land, *Geophys. Res. Lett*., **29**(12), doi:10.1029/2001GL013205.

Chylek, P., B. Henderson, M.I. Mishchenko (2003), Aerosol radiative forcing and the accuracy of satellite aerosol optical depth retrieval, *J. Geophys. Res.*, **108**, (D24), doi:10.1029/2003JD004044.

Coakley, J.A. Jr., R.D. Cess and F.B. Yurevich (1983), The effect of tropospheric aerosol on the earth's radiation budget: a parameterization for climate models. *J. Atmos. Sci.*, **40**, 116-138.

Coakley, J.A. Jr., R.L. Bernstein and P.A. Durkee (1987), Effects of ship stack effluents on cloud reflectance. *Science*, **237**, 953-1084.

Covert, D.S., R.J. Charlson, and N.C. Ahlquist (1972), A study of the relationship of chemical composition and humidity to light scattering by aerosols, *J. Appl. Meteorol.*, **11**, 968-976.

Cox, C. and W. Munk (1954), Statistics of the sea surface derived from sun glitter, *J. Mar. Res*., **13**, 198-227.

Crowley, T.J. (2000), Causes of climate change over the past 1000 years, *Science*, **289**, 270-277.

Deuzé, J.L., P. Goloub, M. Herman, A. Marchand, G. Perry, S. Susana, and D. Tanré (2000), Estimate of the aerosol properties over the ocean with POLDER, *J. Geophys. Res.*, *105*, 15329-15346.

Deuzé, J.L., F.M. Bréon, C. Devaux, P. Goloub, M. Herman, B. Lafrance, F. Maignan, A. Marchand, F. Nadal, G. Perry, and D. Tanré (2001), Remote

sensing of aerosols over land surfaces from POLDER-ADEOS-1 polarized measurements, *J. Geophys. Res.*, **106**, 4913-4926.

Diner, D.J., and Coauthors (1989), MISR: A Multiangle Imaging Spectro-Radiometer for geophysical and climatological research from EOS, *IEEE Trans. Geosci. Remote Sens.*, **27**, 200-214.

Diner, D.J., J. Beckert, T. Reilly, C. Bruegge, J. Conel, R. Kahn, J. Martonchik, T. Ackerman, R. Davies, S. Gerstl, H. Gordon, J-P. Muller, R. Myneni, P. Sellers, B. Pinty, and M. Verstraete (1998), Multi-angle Imaging SpectroRadiometer (MISR) instrument description and experiment overview, *IEEE Trans. Geosci. Remote Sens.*, **36**, 1072-1087.

Diner, D.J., W.A. Abdou, C.J. Bruegge, J.E. Conel, K.A. Crean, B.J. Gaitley, M.C. Helmlinger, R.A. Kahn, J.V. Martonchik, and S.H. Pilorz (2001), MISR aerosol optical depth retrievals over southern Africa during the SAFARI-2000 dry season campaign, *Geophys. Res. Lett.*, **28**, 3127-3130.

Dubovik, O., A. Smirnov, B.N. Holben, M.D. King, Y.J. Kaufman, T.F. Eck, and I. Slutsker (2000), Accuracy assessments of aerosol optical properties retrieved from Aerosol Robotic Network (AERONET) Sun and sky radiance measurements, *J. Geophys. Res.*, *105*(D8), 9791-9806.

Dubovik, O. and M.D. King (2000), A flexible inversion algorithm for retrieval of aerosol optical properties from Sun and sky radiance measurements, *J. Geophys. Res.*, **105**(D16), 20673-20696.

Dubovik, O., B. Holben, T.F. Eck, A. Smirnov, Y.J. Kaufman, M.D. King, D. Tanré, and I. Slutsker (2002), Variability of absorption and optical properties of key aerosol types observed in worldwide locations, *J. Atmos. Sci*., **59**, 590-608.

Eck, T.F., B.N. Holben, J.S. Reid, O. Dubovik, A. Smirnov, N.T. O'Neill, I. Slutsker, and S. Kinne (1999), Wavelength dependence of the optical depth of biomass burning, urban, and desert dust aerosols, *J. Geophys. Res.*, **104**(D24), 31333-31349.

Eck, T.F., B.N. Holben, D.E. Ward, M.M. Mukelabai, O. Dubovik, A. Smirnov, J.S. Schafer, N.C. Hsu, S.J. Piketh, A. Queface, J. Le Roux, R.J. Swap, and I. Slutsker (2003), Variability of biomass burning aerosol optical characteristics in southern Africa during the SAFARI 2000 dry season campaign and a comparison of single scattering albedo estimates from radiometric measurements, *J. Geophys. Res.*, **108**(D13), 8477, doi:10.1029/2002JD002321.

Feingold, G. (2003), Modeling of the first indirect effect: Analysis of measurement requirements, *Geophys. Res. Lett.*, **30**(19), 1997, doi:10.1029/2003GL017967.

Feingold, G. and B. Morley (2003), Aerosol hygroscopic properties as measured by lidar and comparison with in situ measurements, *J. Geophys. Res.*, **108**(11), 4327, doi:10.1029/2002JD002842.

Feingold, G., W.L. Eberhard, D.E. Veron, and M. Previdi (2003), First measurements of the Twomey aerosol indirect effect using ground-based remote sensors, *Geophys. Res. Lett.*, **30**(6), 1287, doi:10.1029/2002GL016633.

Feingold, G., R. Furrer, P. Pilewskie, L.A. Remer, Q. Min, and H. Jonsson (2005), Aerosol indirect effect studies at Southern Great Plains during the May 2003 Intensive Operations Period: Optimal estimation of drop-size from multiple instruments, Submitted to *J. Geophys. Res.*

Ferrare, R.A., D. Covert, R. Elleman, D.D. Turner, J.A. Ogren, E. Andrews, M. Clayton, J.E.M. Goldsmith, H.H. Jonsson, B.S. Schmid, and J. Redemann (2004), Raman Lidar measurements of aerosols and water vapor during the May 2003 Aerosol IOP, Fourteenth ARM Science Team Meeting Proceedings, Albuquerque, New Mexico, March 22-26, 2004 (available at http://www.arm.gov/publications/ proceedings/conf14/author.stm), 7pp.

Fukushima, H. and M. Toratani (1997), Asian dust aerosol: Optical effect on satellite ocean color signal and a scheme of its correction, *J. Geophys. Res.*, *102*(D14), 17119-17130.

Gao, B.-C., Y.J. Kaufman, D. Tanré, and R.-R. Li (2002), Distinguishing tropospheric aerosols from thin cirrus clouds for improved aerosol retrievals using the ratio of 1.38-µm and 1.24-µm channels, *Geophys. Res. Lett.*, **29**, 1890, doi:10.1029/2002GL015475.

Gasso, S., D.A. Hegg, D.S. Covert, D. Collins, K.J. Noon, E. Ostrom, B. Schmid, P.B. Russell, J.M. Livingston, P.A. Durkee, and H. Jonsson (2000), Influence of humidity on the aerosol scattering coefficient and its effect on the upwelling radiance during ACE-2, *Tellus*, **52B**, 546-567.

Geogdzhayev, I.V., M.I. Mishchenko, W.B. Rossow, B. Cairns, and A.A. Lacis (2002), Global two-channel AVHRR retrievals of aerosol properties over the

ocean for the period of NOAA-9 observations and preliminary retrievals using NOAA-7 and NOAA-11 data, *J. Atmos. Sci.*, **59**(3), 262-278.

Ginoux, P., M. Chin, I. Tegen, J. Prospero, B. Holben, D. Dubovik, and S.J. Lin, 2001 (2001), Sources and distributions of dust aerosols simulated with the GOCART model, *J. Geophys. Res.*, *106*, 20255-20273.

Goldsmith, J.E.M., F.H. Blair, S.E. Bisson, and D.D. Turner (1998), Turnkey Raman lidar for profiling atmospheric water vapor, clouds, and aerosols, *Appl. Opt.*, **37**, 4979-4990.

Goloub, P, D. Tanré, J.L. Deuzé, M. Herman, A. Marchand, and F-M Breon (1999), Validation of the first algorithm applied for deriving the aerosol properties over the ocean using the POLDER/ADEOS measurements, *IEEE Trans. Geosci. Remote Sensing*, **37**, 1586-1596.

Gong, S.L., X.Y. Zhang, T.L. Zhao, I.G. McKendry, D.A. Jaffe, and N.M. Lu (2003), Characterization of soil dust aerosol in China and its transport and distribution during 2001 ACE-Asia: 2. Model simulation and validation, *J. Geophys. Res.*, *108*(D9), 4262, doi:10.1029/2002JD002633.

Gregg, W.W., M.E. Conkright, J.E. O'Reilly, F.S. Patt, M.H. Wang, J.A. Yoder, and N.W. Casey (2002), NOAA-NASA Coastal Zone Color Scanner reanalysis effort, *Appl. Optics*, *41*(9), 1615-1628.

Hänel, G. (1976), The properties of atmospheric aerosol particles as functions of the relative humidity at thermodynamic equilibrium with the surrounding moist air, *Adv. Geophys.*, **19**, 73-188.

Hansen, J., M. Sato, and R. Ruedy (1997), Radiative forcing and climate response, *J. Geophys. Res*. **102**(D6), 6831-6864.

Haywood, J.M., P.N. Francis, I. Geogdzhayev, M. Mishchenko, and R. Frey (2001), Comparison of Saharan dust aerosol optical depths retrieved using aircraft mounted pyranometers and 2-channel AVHRR algorithms, *Geophys. Res. Lett*., **28**(12), 2393-2396.

Hegg, D.A., T. Larson, and P. Yuen (1993), A theoretical study of the effects of relative humidity on light scattering by tropospheric aerosols, *J. Geophys. Res.*, **98**, 18435-118439.

Hegg, D.A., D.S. Covert, M.J. Rood, and P.V. Hobbs (1996), Measurements of aerosol optical properties in marine air, *J. Geophys. Res.*, **101**, 12893-12903.

Hegg, D.A., J. Livingston, P.V. Hobbs, T. Novakov, and P. Russell (1997), Chemical apportionment of aerosol column optical depth off the mid-Atlantic coast of the United States, *J. Geophys. Res*., **102**(D21), 25293-25303.

Herman, J.R., P.K. Bhartia, O. Torres, C. Hsu, C. Seftor, and E. Celarier (1997), Global distribution of UV-absorbing aerosols from Nimbus 7/TOMS data, *J. Geophys. Res.*, **102**(D14), 16911-16922.

Higurashi, A. and T. Nakajima (1999), Development of a two-channel aerosol retrieval algorithm on a global scale using NOAA AVHRR, *J. Atmos. Sci.*, **56**, 924-941.

Hobbs, P.V., P. Sinha, R.J. Yokelson, T.J. Christian, D.R. Blake, S. Gao, T.W. Kirchstetter, T. Novakov, and P. Pilewskie (2003), Evolution of gases and

particles from a savanna fire in South Africa, *J. Geophys. Res.*, *108*(D13), 8485, doi:10.1029/2002JD002352.

Holben, B.N., T.F. Eck, and R.S. Fraser (1991), Temporal and spatial variability of aerosol optical depth in the Sahel region in relation to vegetation remote sensing, *Int. J. Remote Sens.*, **12**, 1147-1163.

Holben, B.N., T.F. Eck, I. Slutsker, D. Tanré, J.B. Buis, A. Setzer, E. Vermote, J.A. Reagan, Y.J. Kaufman, T. Nakajima, F. Lavenu, I. Jankowiak, and A. Smirnov (1998), AERONET – a federated instrument network and data archive for aerosol characterization, *Remote Sens. Environ.*, **66**, 1-16.

Holben, B.N., D. Tanré, A. Smirnov, T.F. Eck, I. Slutsker, N. Abuhassan, W.W. Newcomb, J.S. Schafer, B. Chatenet, F. Lavenu, Y.J. Kaufman, J. Vande Castle, A. Setzer, B. Markham, D. Clark, R. Frouin, R. Halthore, A. Kareli, N.T. O'Neill, C. Pietras, R.T. Pinker, K. Voss, and G. Zibordi (2001), An emerging ground-based aerosol climatology: Aerosol optical depth from AERONET, *J. Geophys. Res.*, **106**(D11), 12067-12097.

Hoppel, W.A., J.W. Fitzgerald, G.M. Frick, and R.E. Larson (1990), Aerosol size distributions and optical properties found in the marine boundary layer over the Atlantic Ocean, *J. Geophys. Res.*, **95**(D4), 3659-3686.

Houghton, J.T., L.G. Meira Filho, B.A. Callander, N. Harris, A. Kattenberg, and K. Maskell, Eds. (1996), *Climate Change 1995: The science of climate change.* Intergovenmental Panel on Climate Change, Cambridge University Press, 572pp.

Hsu, N.C., J.R. Herman, P.K. Bhartia, C.J. Seftor, O. Torres, A.M. Thompson, J.F. Gleason, T.F. Eck, and B.N. Holben (1996), Detection of biomass burning smoke from TOMS measurements, *Geophys. Res. Lett*., **23,** 745-748.

Hsu, N.C., J.R. Herman, O. Torres, J.F. Gleason, O. Torres, and C.J. Seftor (1999a), Satellite detection of smoke aerosols over a snow/ice surface by TOMS, *Geophys. Res. Lett*., *26*(8), 1165-1168.

Hsu, N.C., J.R. Herman, O. Torres, B.N. Holben, D. Tanré, T.F. Eck, A. Smirnov, B. Chatenet, and F. Lavenu (1999b), Comparisons of the TOMS aerosol index with sun-photometer aerosol optical thickness: Results and applications, *J. Geophys. Res.*, *104*(D6), 6269-6279.

Hsu, N.C., S.-C. Tsay, M.D. King, and J.R. Herman (2004), Aerosol properties over bright-reflecting source regions, *IEEE Trans. Geosci. Remote Sens.*, **42**(3), 557-569.

Husar, R.B., J.M. Prospero, and L.L. Stowe (1997), Characterization of tropospheric aerosols over the oceans with the NOAA advanced very high resolution radiometer optical thickness operational product, *J Geophys. Res*, **102**, 16889-16909.

Husar, R.B., D.M. Tratt, B.A. Schichtel, S.R. Falke, F. Li, D. Jaffe, S. Gasso, T. Gill, N.S. Laulainen, F. Lu, M.C. Reheis, Y. Chun, D. Westphal, B.N. Holben, C. Gueymard, I. McKendry, N. Kuring, G.C. Feldman, C. McClain, R.J. Frouin, J. Merrill, D. DuBois, F. Vignola, T. Murayama, S. Nickovic, W.E. Wilson, K. Sassen, N. Sugimoto, and W.C. Malm (2001), Asian dust events of April 1998, *J. Geophys. Res.*, *106*(D16), 18317-18330.

Ichoku, C, D.A. Chu, S. Mattoo, Y.J. Kaufman, L.A. Remer, D. Tanré, I. Slutsker, and B.N. Holben (2002), A spatio-temporal approach for global validation and analysis of MODIS aerosol products, *Geophys. Res. Lett*., **29**(12), doi:10.1029/2001GL013206.

Ichoku, C., L.A. Remer, Y.J. Kaufman, R. Levy, D.A. Chu, D. Tanré, and B.N. Holben (2003), MODIS observation of aerosols and estimation of aerosol radiative forcing over southern Africa during SAFARI 2000, *J Geophys. Res*, **108**(D13), 8499, doi:10.1029/2002JD002366.

Ichoku, C., L.A. Remer, T.F. Eck (2005), Quantitative evaluation and intercomparison of morning ad afternoon Moderate Resolution Imaging Spectroradiometer (MODIS) aerosol measurements from Terra and Aqua, *J. Geophys. Res.*, **110**, D10S03, doi:10.1029/2004JD004987.

Ignatov, A., L. Stowe, S. Sakerin, and G. Korotaev (1995), Validation of the NOAA/NESDIS satellite aerosol product over the North Atlantic in 1989, *J. Geophys. Res.*, *100*(D3), 5123-5132.

Ignatov, A., L. Stowe, and R. Singh (1998), Sensitivity study of the Ångström exponent derived from AVHRR over oceans, *Adv. Space Res*., *21*, 439-442.

Ignatov, A. and L. Stowe (2000), Physical basis, premises, and self-consistency checks of aerosol retrievals from TRMM VIRS, *J. Appl. Meteor.*, *39*, 2259-2277.

Ignatov, A. (2002), Sensitivity and information content of aerosol retrievals from AVHRR: Radiometric factors, *Appl. Opt*., *41*, 991-1011.

Ignatov, A. and N.R. Nalli (2002), Aerosol retrievals from multi-year multi-satellite AVHR Pathfinder Atmosphere (PATMOS) dataset for correcting remotely sensed sea surface temperatures, *J. Atmos. Oceanic Technol.*, **19**, 1986-2008.

Ignatov, A. and L. Stowe (2002a), Aerosol retrievals from individual AVHRR channels. Part I: Retrieval algorithm and transition from Dave to 6S radiative transfer model. *J. Atmos. Sci.*, **59**, 313-334.

Ignatov, A. and L. Stowe (2002b), Aerosol retrievals from individual AVHRR channels. Part II: Quality control, probability distribution functions, information content, and consistency checks of retrievals. *J. Atmos. Sci.*, **59**, 335-362.

Ignatov, A. J. Sapper, S. Cox, I. Laszlo, N.R. Nalli, and K.B. Kidwell (2004), Operational aerosol observations (AEROBS) from AVHRR/3 on board NOAA-KLM satellites, *J. Atmos. Oceanic Technol.*, **21**, 3-25.

Intergovernmental Panel on Climate Change (IPCC) (2001), *Climate Change 2001: the scientific basis*, Cambridge Univ. Press, New York.

Iqbal, M. (1983), *An introduction to solar radiation.* Academic Press, pp390.

Kahn, R., P. Banerjee, D. McDonald, and D.J. Diner (1998), Sensitivity of multiangle imaging to aerosol optical depth and to pure-particle size distribution and composition over ocean, *J. Geophys. Res.*, **103**, 32195-32213.

Kahn, R., P. Banerjee, and D. McDonald (2001), Sensitivity of multiangle imaging to natural mixtures of aerosols over ocean, *J. Geophys. Res.*, **106**, 18219-18238.

Kasten, F. (1969), Visibility in the phase of pre-condensation, *Tellus*, **21**, 631-635.

Kasten, F. and A.T. Young (1989), Revised optical air mass tables and approximation formula, *Appl. Opt.*, **28**, 4735-4738.

Kaufman, Y.J., and T. Nakajima (1993), Effect of Amazon smoke on cloud microphysics and albedo – analysis from satellite imagery, *J. Appl. Meteorol.*, **32**, 729-744.

Kaufman, Y.J., A. Gitelson, A. Karnieli, E. Ganor, R.S. Fraser, T. Nakajima, S. Mattoo, and B.N. Holben (1994), Size distribution and phase function of aerosol particles retrieved from sky brightness measurements, *J. Geophys. Res.*, **99**, 10341-10356.

Kaufman, Y.J. and B.N. Holben (1996), Hemispherical backscattering by biomass burning and sulfate particles derived from sky measurements, *J. Geophys. Res.*, **101**, 19433-19445.

Kaufman, Y.J. and R.S. Fraser (1997), Confirmation of the smoke particles effect on clouds and climate, *Science*, **277**, 1636-1639.

Kaufman, Y.J., D. Tanré, L.A. Remer, E.F. Vermote, A. Chu and B.N. Holben (1997), Operational remote sensing of tropospheric aerosol over land from EOS moderate resolution imaging spectroradiometer, *J. Geophys. Res.*, **102**(D14), 17051-17067.

Kaufman, Y.J., P.V. Hobbs, V.W.J.H. Kirchhoff, P. Artaxo, L.A. Remer, B.N. Holben, M.D. King, D.E. Ward, E.M., Prins, K.M. Longo, L.F. Mattos, C.A. Nobre, J.D. Spinhirne, Q. Ji, A.M. Thompson, J.F. Gleason, S.A. Christopher, and S.-C. Tsay (1998), Smoke, Clouds and Radiation – Brazil (SCAR-B) experiment, *J. Geophys. Res.*, **103**, 31783-31808.

Kaufman, Y.J., D. Tanré, and O. Boucher (2002), A satellite view of aerosols in the climate system, *Nature*, **419**, 215-223.

Kaufman, Y.J., L.A. Remer, D. Tanré, R.-R. Li, R. Kleidman, S. Mattoo, R. Levy, T. Eck, B.N. Holben, C. Ichoku, V. Martins, and I. Koren (2005), A critical examination of the residual cloud contamination and diurnal sampling effects on MODIS estimates of aerosol over ocean, Submitted to *IEEE Trans. Geosci. Remote Sens.*

King, M.D., Y.J. Kaufman, W.P. Menzel, and D. Tanré (1992), Remote sensing of cloud, aerosol, and water vapor properties from the Moderate Resolution Imaging Spectrometer (MODIS), *IEEE Trans. Geosci. Remote Sens.*, **30**, 2-27.

King, M.D., S.-C. Tsay, S.A. Ackerman, and N.F. Larssen (1998), Discriminating heavy aerosol, clouds, and fires during SCAR-B: Application of airborne multispectral MAS data, *J. Geophys. Res.*, **103**, 31989-32000.

King, M.D., Y. Kaufman, D. Tanré, and T. Nakajima (1999), Remote sensing of tropospheric aerosols from space: Past, present, and future, *Bull. American Meteorol. Soc*., **11**, 2229-2259.

Kinne, S., T.P. Ackerman, M. Shiobara, A. Uchiyama, A.J. Heymsfield, L. Miloshevich, J. Wendell, E.W. Eloranta, C. Purgold, and R.W. Bergstrom (1997), Cirrus cloud radiative and microphysical properties from ground observations and in situ measurements during FIRE 1991 and their application to exhibit problems in cirrus solar radiative transfer modeling, *J. Atmos. Sci.*, **54**, 2320-2344.

Kinne, S., B. Holben, T. Eck, A. Smirnov., O. Dubovik, I. Slutsker, D. Tanré, et al. (2001), How well do aerosol retrievals from satellites and representation in global circulation models match ground-based AERONET aerosol statistics? Remote sensing and climate modeling: Synergies and limitations. Edited by M. Beniston and M.M. Verstraete, Kuwer Academic Publishers, 103-158, 345pp.

Kinne, S., U. Lohmann, J. Feichter, M. Schulz, C. Timmreck, S. Ghan, R. Easter, M. Chin, P. Ginoux, T. Takemura, I. Tegen, D. Koch, M. Herzog, J. Penner, G. Pitari, B. Holben, T. Eck, A. Smirnov, O. Dubovik, I. Slutsker, D. Tanré, O. Torres, M. Mishchenko, I. Geogdzhayev, D.A. Chu, and Y. Kaufman (2003), Monthly averages of aerosol properties: Aglobal comparison among models, satellite data, and AERONET ground data, *J. Geophys. Res.*, **108**(D20), 4634, doi:10.1029/2001JD001253.

Koren, I., Y.J. Kaufman, L.A. Remer, J.V. Martins (2004), Measurement of the effect of Amazon smoke on inhibition of cloud formation, *Science*, **303**, 1342-1345.

Kotchenruther, R.A. and P.V. Hobbs (1998), Humidification factors of aerosols from biomass burning in Brazil, *J. Geophys. Res.*, **103**(24), 32082-32089.

Kotchenruther, R.A., P.V. Hobbs, and D.A. Hegg (1999), Humidification factors for atmospheric aerosols off the mid-Atlantic coast of the United States, *J. Geophys. Res.*, **104**(2), 2239-2251.

Kuang, Z., and Y.L. Yung (2000), Reflectivity variations off the Peru Coast: evidence for indirect effect of anthropogenic sulfate aerosols on clouds, *Geophys. Res. Lett.*, *27*(16), 2501-2504.

Lenoble, J. (1993), *Atmospheric radiative transfer*, Deepak Publishing, 500pp.

Levy, R.C., L.A. Remer, D. Tanré, Y.J. Kaufman, C. Ichoku, B.N. Holben, J.M. Livingston, P.B. Russell, H. Maring (2003), Evaluation of the MODIS retrievals of dust aerosol over the ocean during PRIDE, *J. Geophys. Res.*, **108**(D19), 8594, doi:10.1029/2002JD002460.

Levy, R.C., L.A. Remer, J.V. Martins, Y.J. Kaufman, A. Plana-Fattori, J. Redemann, and B. Wenny (2005), Evaluation of the MODIS aerosol retrievals over ocean and land during CLAMS, *J. Atmos. Sci.*, **62**, 974-992.

Li-Jones, X., H.B. Maring, and J.M. Prospero (1998), Effect of relative humidity on light scattering by mineral dust aerosol as measured in the marine boundary layer over the tropical Atlantic Ocean, *J. Geophys. Res.*, **103**(23), 31113-31121.

Li, Z. and L. Moreau (1996), A new approach for remote sensing of canopy-absorbed photosynthetically active radiation. I: Total surface absorption, *Remote Sens. Environ.*, *55*, 175-191.

Li, Z., 1998, Influence of absorbing aerosols on the inference of solar surface radiation budget and cloud absorption, J. Climate, 11, 5-17.

Li, Z., and L. Kou, 1998, Atmospheric direct radiative forcing by smoke aerosols determined from satellite and surfase measurements, Tellus (B), 50, 543-554.

Liou, K.N., K.P. Freeman, and T. Sasamori (1978), Cloud and aerosol effects on the solar heating rate of the atmosphere, *Tellus*, **30**, 62-70.

Long, C.N., D.W. Slater, and T. Toonman (2001), Total Sky Imager Model 880 status and testing results, ARM TR-006, 36pp.

Maring, H., D.L. Savoie, M.A. Izaguirre, L. Custals, and J.S. Reid (2003), Mineral dust aerosol size distribution change during atmospheric transport, *J. Geophys. Res.*, **108**(D19), 8592, doi:10.1029/2002JD002536.

Martins, J.V., L. Remer, Y.J. Kaufman, S. Mattoo, and R. Levy (2002), MODIS cloud screening for remote sensing of aerosols over oceans using spatial variability, *Geophys. Res. Lett.*, **29**(12), doi:10.1029/2001GL013252.

Martonchik, J.V., D.J. Diner, R. Kahn, M.M. Verstraete, B. Pinty, H.R. Gordon, and T.P. Ackerman (1998), Techniques for the retrieval of aerosol properties over land and ocean using multiangle imaging, *IEEE Trans. Geosci. Remote Sens.*, 36, 1212-1227.

Masuda, K., H.G. Leighton, and Z. Li (1995), A new parameterization for the determination of solar flux absorbed at the surface from satellite measurements, *J. Clim., 8*, 1615-1629.

McClatchey, R.A., R.W. Fenn, J.E.A. Selby, F.E. Volz, and J.S. Garing (1972), Optical properties of the atmosphere, Air Force Cambridge Research Laboratories, Report AFCRL-72-0497, 110pp., Hanscom Air Force Base, Bedford, Mass.

Meeson, B.W., F.E. Corprew, J.M.P. McManus, D.M. Myers, J.W. Closs, K. -J. Sun, D.J. Sunday, P.J. Sellers (1995), ISLSCP Initiative I-Global Data Sets for Land-Atmosphere Models, 1987-1988. Volumes 1-5. Published on CD by NASA (USA_NASA_GDAAC_ISLSCP_001-USA_NASA_GDDAC_ISLSCP_005).

Mishchenko, M.I., A.A. Lacis, B.E. Carlson, and L.D. Travis (1995), Nonsphericity of dust-like tropospheric aerosols: implications for aerosol remote sensing and climate modeling, *Geophys. Res. Lett.*, *22*, 1077-1080.

Mishchenko, M.I., I.V. Geogdzhayev, B. Cairns, W.B. Rossow, and A.A. Lacis (1999), Aerosol retrievals over the ocean by use of channels 1 and 2 AVHRR data: sensitivity analysis and preliminary results. *Appl. Optics*, **38**, 7325-7341.

Mishchenko, M.I., I.V. Geogdzhayev, L. Liu, J.A. Ogren, A.A. Lacis, W.B. Rossow, J.W. Hovenier, H. Volten, O. Munoz (2003), Aerosol retrievals from AVHRR radiances: effects of particle nonsphericity and absorption and an updated long-term global climatology of aerosol properties, *J. Quantitative Spectroscopy and Radiative Transfer*, **79-80**, 953-972.

Mueller, J., C. McClain, B. Caffrey, and G. Feldman (1998), The NASA SIMBIOS Program, Backscatter, May. (This article can also be found at http://www.ioccg.org/reports/simbios/simbios.html)

Moorthy, K.K., S.S. Babu, S.K. Satheesh (2003), Aerosol spectral optical depths over the Bay of Bengal: Role of transport, *Geophys. Res. Lett.*, **30**(5), 1249, doi:10.1029/2002GL016520.

Murphy, D.M., J.R. Anderson, P.K. Quinn, L.M. McInnes, F.J. Brechtel, S.M. Kreidenweis, A.M. Middlebrook, M. Posfai, D.S. Thomson, and P.R. Buseck (1998), Influence of sea-salt on aerosol radiative properties in the Southern Ocean marine boundary layer, *Nature*, *392*, 62-65.

Myhre, G. F. Stordal, M. Johnsrud, A. Ignatov, M.I. Mishchenko, I.V. Geogdzhayev, D. Tanré, J-L. Deuzé, P. Goloub, T. Nakajima, A. Higurashi, O. Torres, B.N.

Holben (2004), Intercomparison of satellite retrieved aerosol optical depth over ocean, *J. Atmos. Sci.*, **61**, 499-513.

Nakajima, T., M. Tanaka, M. Yamano, M. Siobara, K. Arao, and Y. Nakanishi (1989), Aerosol optical characteristics in the yellow sand events observed in May, 1982 at Nagasaki: Part II Models, *J. Meteorol. Soc. Jpn.*, *67*, 279-291.

Nakajima, T.Y., T. Nakajima, M. Nakajima, H. Fukushima, M. Kuji, A. Uchiyama, and M. Kishino (1998), Optimization of the Advanced Earth Observing Satellite II Global Image channels by use of radiative transfer calculations, *Appl. Opt.*, **37**, 3149-3163.

Nakajima, T. and A. Higurashi (1998), A use of two-channel radiances for an aerosol characterization from space, *Geophys. Res. Lett.*, **25**(20), 3815-3818.

Nakajima, T., A. Higurashi, K. Kawamoto, J.E. Penner (2001), A possible correlation between satellite-derived cloud and aerosol microphysical parameters, *Geophys. Res. Lett*., **28**(7), 1171-1174.

National Aeronautics and Space Administration (2003), Formation flying: The afternoon "A-Train" satellite constellation, *NASA Facts, FS-2003-1-053-GSFC*, 6pp.

O'Neill, N.T. and A. Royer (1993), Extraction of bimodal aerosol-size distribution radii from spectral and angular slope (Ångström) coefficients, *Appl. Opt.*, **32**, 1642-1645.

O'Neill, N.T., T.F. Eck, B.N. Holben, A. Smirnov, A. Royer, and Z. Li (2002), Optical properties of boreal forest fire smoke derived from Sun photometry, *J. Geophys. Res.*, **107**(D11), doi:10.1029/2001JD000877.

Öström, E. and K.J. Noone (2000), Vertical profiles of aerosol scattering and absorption measured in situ during the North Atlantic Aerosol Characterization Experiments, *Tellus, Ser. B*, **52**, 526-545.

Penner, J.E., S.Y. Zhang, M. Chin, C.C. Chuan, J. Feichter, Y. Feng, I.V. Geogdzhayev, P. Ginoux, M. Herzog, A. Higurashi, D. Koch, C. Land, U. Lohmann, M. Mishchenko, T. Nakajima, G. Pitari, B. Soden, I. Tegen, and L. Stowe (2002), A comparison of model- and satellite-derived aerosol optical depth and reflectivity, *J. Atmos. Sci.*, *59*, 441-460.

Platnick, S., M.D. King, S.A. Ackerman, W. P. Menzel, B.A. Baum, J.C. Riedi, and R.A. Frey (2003), The MODIS cloud products: Algorithms and examples from Terra, *IEEE Trans. Geosci. Remote Sens.*, **41**(2), 459-473.

Porter, J.N., M. Miller, C. Pietras, C. Motell (2001), Ship-based sun photometer measurement using Microtops sun photometers, *J. Atmos. Oceanic Technol.*, **18**, 765-774.

Prospero, J.M., and L.S. Savoie (1989), Effect of continental sources on nitrate concentration over the Pacific Oceans, *Nature*, *339*, 687-689.

Prospero, J. M., D. L. Savoie, and R. Arimoto (2003), Long term record of nss-sulfate and nitrate in aerosols on Midway Island, 1981-2000: Evidence of increased (now decreasing?) anthropogenic emissions from Asia, *J. Geophys. Res.*, *108*(D1), 4019, doi: 10.1029/ 2001JD001524.

Rainwater, M. and L. Gregory (2005), *Cimel sunphotometer (CSPHOT) handbook*, ARM TR-056 (available from http://www.arm.gov/instruments/), 14pp.

Ramanathan, V., P.J. Crutzen, J.T. Kiehl, D. Rosenfeld (2001), Aerosols, climate, and the hydrological cycle, *Science*, **294**, 2119-2124.

Rao, C.R.N., L. Stowe, and P. McClain (1989), Remote sensing of aerosols over oceans using AVHRR data: Theory, practice and applications, *Int. J. Remote Sens*., **10**, 743-749.

Reid, J.S., T.F. Eck, S.A. Christopher, P.V. Hobbs, and B. Holben (1999), Use of the Ångström exponent to estimate the variability of optical and physical properties of aging smoke particles in Brazil, *J. Geophys. Res.*, **104**(D22), 27473-27479.

Remer, L.A., S. Gasso, and D.A. Hegg (1997), Urban/industrial aerosol: Ground-based Sun/sky radiometer and airborne in situ measurements, *J. Geophys. Res.*, 102, 16849-16859.

Remer, L.A. and Y.J. Kaufman (1998), Dynamical aerosol model: Urban/industrial aerosol, *J. Geophys. Res.*, **103**, 13859-13871.

Remer, L.A., Y.J. Kaufman, B.N. Holben, A.M. Thompson, and D. McNamara (1998), Biomass burning aerosol size distribution and modeled optical properties, *J. Geophys. Res.*, *103*(D24), 31879-31891.

Remer, L.A., D. Tanré, Y.J. Kaufman, C. Ichoku, S. Mattoo, R. Levy, D.A. Chu, B.N. Holben, O. Dubovik, A. Smirnov, J.V. Martins, R.-R. Li, and Z. Ahmad (2002), Validation of MODIS aerosol retrieval over ocean, *Geophys. Res. Lett*., **29**(12), doi:10.1029/2001GL013204.

Remer, L., et al. (2005), The MODIS aerosol algorithm, products and validation, *J. Atmos. Sci*., **62**, 947-973.

Ricchiazzi, P., S. Yang, C. Gautier, and D. Sowle (1998), SBDART: A research and teaching software toll for plane-parallel radiative transfer in the earth's atmosphere, *Bull.American Meteor. Soc*., **79**(10), 2101-2114.

Rood, M.J., D.S. Covert, and T.V. Larson (1987), Hygroscopic properties of atmospheric aerosol in Riverside, California, *Tellus, Ser. B*, **39**, 383-397.

Rosenfeld, D. (1999), TRMM observed first direct evidence of smoke from forest fires inhibiting rainfall, *Geophys. Res. Lett.* **26**, 3105-3108.

Rosenfeld, D. (2000), Suppression of rain and snow by urban and industrial air pollution, *Science*, **287**, 1793-1796.

Rossow, W.B. and L.C. Garder (1993), Cloud detection using satellite measurements of infrared and visible radiances for ISCCP, *J. Climate*, **6**, 2341-2369.

Rossow, W.B. and R.A. Schiffer (1999), Advances in understanding clouds from ISCCP. *Bull. American Meteor. Soc*., **80**, 2261-2287.

Russell, P.B. and J. Heintzenberg (2000), An overview of the ACE-2 clear sky column closure experiment (CLEARCOLUMN), *Tellus, Ser. B*, **52**, 463-483.

Sakerin, S.M. and D.M. Kabanov (2002), Spatial inhomogeneities and the spectral behavior of atmospheric aerosol optical depth over the Atlantic Ocean, *J. Atmos. Sci.*, **59**(3), 484-500.

Schmid, B., Matzler, C. Heimo, A. and Kampfer, N. (1997), Retrieval of optical depth and particle size distribution of tropospheric and stratospheric aerosols by means of sun photometry, *IEEE Trans. Geosci. Remote Sens.*, **15**, 172-182.

Sheridan, P.J. and J.A. Ogren (1999), Observations of the vertical and regional variability of aerosol optical properties over central and eastern North America, *J. Geophys. Res.*, **104**, 16793-16805.

Sheridan, P.J., D.J. Delene, and J.A. Ogren (2001), Four years of continuous surface aerosol measurements from the Department of Energy's Atmsopheric Radiation Measurement Program Southern Great Plains Cloud and Radiation Testbed site, *J. Geophys. Res.*, 106, 20735-20747.

Sheridan, P.J., A. Jefferson, and J.A. Ogren (2002), Spatial variability of submicrometer aerosol radiative properties over the Indian Ocean during INDOEX, *J. Geophys. Res.*, **107**(D19), 8011, 10.1029/2000JD000166.

Shettle, E.P. and R.W. Fenn (1979), *Models for the aerosols of the lower atmosphere and the effects of humidity variations on their optical properties*, AFGL-TR-79-0214, 94 pp. [Available from AFCRL, Hanscom Field, Bedford, MA 01731.]

Siegel, D.A., M. Wang, S. Maritorena, and W. Robinson (2000), Atmospheric correction of satellite ocean color imagery: the black pixel assumption, *Appl. Optics*, *39*, 3582-3591.

Smirnov, A., B.N. Holben, T.F. Eck, O. Dubovik, and I. Slutsker (2000), Cloud-screening and quality control algorithms for the AERONET database, *Remote Sens. Environ.*, **73**, 337-349.

Stowe, L.L., A. M. Ignatov, R.R. Singh (1997), Development, validation, and potential enhancements to the second-generation operational aerosol product at the National Environmental Satellite, Data, and Information Service of the

National Oceanic and Atmospheric Administration, *J Geophys. Res*, **102**, 16923-16934.

Stowe, L.L., H. Jacobowitz, G. Ohring, K.R. Knapp, and N.R. Nalli (2002), The Advanced Very High Resolution Radiometer (AVHRR) Pathfinder Atmosphere (PATMOS) climate dataset: Initial analyses and evaluations, *J. Clim.*, *15*, 1243-1260.

Tanré, D., C. Deroo, P. Duhaut, M. Herman, J.J. Morcrette, J. Perbos and P.Y. Deschamps (1990), Description of a computer code to simulate the satellite signal in the solar spectrum: the 5S code. *Inter. J. Remote Sensing*, **11**, 659-668.

Tanré, D., Y.J. Kaufman, M. Herman, and S. Mattoo (1997), Remote sensing of aerosol properties over oceans using the MODIS/EOS spectral radiances, *J. Geophys. Res.*, **102**(D14), 16971-16988.

Tanré, D., Y.J. Kaufman, B.N. Holben, B. Chatenet, A. Karneli, F. Lavenu, L. Blarel, O. Dubovik, L.A. Remer, and A. Smirnov (2001), Climatology of dust aerosol size distribution and optical properties derived from remotely sensed data in the solar spectrum, *J. Geophys. Res.*, *106*(D16), 18205-18217.

Tegen, I., P. Hollrig, M. Chin, I. Fung, D. Jacob, and J. Penner (1997), Contribution of different aerosol species to the global aerosol extinction optical thickness: estimates from model results, *J. Geophys. Res.*, *102*(D20), 23895-23915.

Torres, O., P.K. Bhartia, J.R. Herman, Z. Ahmad, and J. Gleason (1998), Derivation of aerosol properties from satellite measurements of backscattered ultraviolet radiation: Theoretical basis, *J. Geophys. Res.*, **103**(D14), 17099-17110.

Torres, O., P.K. Bhartia, J.R. Herman, A. Sinyuk, Paul Ginoux, and B. Holben (2002), A long-term record of aerosol optical depth from TOMS observations and comparison to AERONET measurements, *J. Atmos. Sci.*, **59**, 398-413.

Turner, D.D. and J.E.M. Goldsmith (1999), Twenty-four-hour Raman lidar measurements during the Atmospheric Radiation Measurement program's 1996 and 1997 water vapor intensive observation periods, *J. Atmos. Oceanic Technol.*, **16**, 1062-1076.

Turner, D.D., R.A. Ferrare, and L.A. Brasseur (2001), Average aerosol extinction and water vapor profiles over the Southern Great Plains, *Geophys. Res. Lett.*, **28**(23), 4441-4444.

Turner, D.D., R.A. Ferrare, L.A.H. Brasseur, W.F. Feltz, T.P. Toonman (2002), Automated retrievals of water vapor and aerosol profiles from an operational Raman Lidar, *J. Atmos. Ocean. Tech.*, **19**, 37-50.

Turner, D.D. (2004), *Raman Lidar (RL) handbook*, ARM TR-038 (available at http://www.arm.gov/instruments/), 13pp.

Twomey, S.A. (1977), The influence of pollution on the shortwave albedo of clouds, *J. Atmos. Sci.*, **34**, 1149-1152.

Twomey, S.A., M. Piepgrass and T.L. Wolfe (1984), An assessment of the impact of pollution on the global albedo, *Tellus*, **36B,** 356-366.

van de Hulst, H.C. (1957), *Light scattering by small particles*, John Wiley, 470pp.

Volz, F.E. (1959), Photometer mit Selen-photoelement zurspektralen Messung der Sonnenstrahlung und zer Bestimmung der Wallenlangenabhangigkeit der Dunsttrubung, *Arch. Meteorol. Geophys. Bioklim.*, **B10**, 100-131.

Volz, F.E. (1974), Economical multispectral sun photometer for measurements of aerosol extinction from 0.44μm to 1.6μm and precipitable water, *Appl. Opt.*, **13**, 1732-1733.

Wang M. and H.R. Gordon (1994), Radiance reflected from the ocean-atmosphere system: Synthesis from individual components of the aerosols size distribution, *Applied Optics*, **33**, 7088-7095.

Whitby, K.Y. (1978), The physical characteristics of sulfur aerosols, *Atmos. Environ.*, **12**, 135-159.

Yu, H., R.E. Dickinson, M. Chin, Y.J. Kaufman, B.N. Holben, I.V. Geogdzhayev, and M.I. Mishchenko (2003), Annual cycle of global distributions of aerosol optical depth from integration of MODIS retrievals and GOCART model simulations, *J. Geophys. Res*., *108*(D3), 4128, doi:10.1029/2002JD002717.

Zhang, X.Y., S.L. Gong, Z.X. Shen, F.M. Mei, X.X. Xi, L.C. Liu, Z.J. Zhou, D. Wang, Y.Q. Wang, and Y. Cheng (2003), Characterization of soil dust aerosol in China and its transport and distribution during 2001 ACE-Asia: 1. Network observations, *J. Geophys. Res*., *108*(D9), 4261, doi:10.1029/2002JD002632.

Zhao, T.X.-P., I. Laszlo, O. Dubovik, B.N. Holben, J. Sapper, D. Tanré, and C. Pietras (2003), A study of the effect of non-spherical dust particles on the AVHRR aerosol optical thickness retrievals, *Geophys. Res. Lett*., *30*(6), 1317, doi:10.1029/2002GL016379.

Zhou, J., E. Swielicki, H.C. Hansson, and P. Artaxo (2002), Submicrometer aerosol particle size distribution and hygroscopic growth measured in the Amazon

rain forest during the wet season, *J. Geophys. Res*., *107*(D20), 8055, doi:10.1029/2000JD000203.